Continuous-Flow Chemistry: From the Wavelength Dependence of Photoreactions to Spatial Confinement Effects in Olefin Metathesis

Kumulative Dissertation

Zum Erlangen des akademischen Grades
Doktor der Naturwissenschaften (Dr. rer. nat.)

dem Fachbereich Chemie
der Philipps-Universität Marburg

vorgelegt von

Thomas Roider
geboren in Bad Homburg

Marburg an der Lahn, November 2022

Abgabedatum: _____.

Vom Fachbereich Chemie der Philipps-Universität Marburg (Hochschulkennziffer 1180) als Dissertation angenommen am: _____.

Erstgutachter: Prof. Dr. Ulrich Tallarek
Zweitgutachter: Prof. Dr. Eric Meggers

Tag der mündlichen Prüfung: _____.
Die vorliegende Arbeit wurde in der Zeit von November 2018 bis November 2022 am Fachbereich Chemie der Philipps-Universität Marburg unter Leitung von Herrn Prof. Dr. Ulrich Tallarek angefertigt.

Teile der Dissertation wurden bereits in den folgenden Artikeln veröffentlicht:

1 C. P. Haas,[+] T. Roider,[+] R. W. Hoffmann and U. Tallarek*
„Light as a reaction parameter – systematic wavelength screening in photochemical synthesis"
React. Chem. Eng., **2019**, *4*, 1912–1916. DOI: 10.1039/c9re00339h

2 T. Roider, O. A. Kleykamp, S. I. Ivlev, R. W. Hoffmann and U. Tallarek*
„Catalyst-Free Indirect C–F Activation of 3-Perfluoroalkyl Indoles"
Eur. J. Org. Chem. **2022**, e202201025. DOI: 10.1002/ejoc.202201025

3 T. Roider, N. Frommknecht, A. Höltzel and U. Tallarek*
"Device for automated screening of irradiation wavelength and intensity – investigation of the wavelength dependence of photoreactions with an arylazo sulfone in continuous flow"
React. Chem. Eng., **2022**, *7*, 2035–2044. DOI: 10.1039/d2re00142j

4 F. Ziegler,[+] T. Roider,[+] M. Pyschik, C. P. Haas, D. Wang, U. Tallarek*[+] and M. R. Buchmeiser*[+]
„Olefin Ring-closing Metathesis under Spatial Confinement and Continuous Flow"
ChemCatChem **2021**, *13*, 2234–2241. DOI: 10.1002/cctc.202001993

5 A. Böth,[+] T. Roider,[+] F. Ziegler, X. Xie, M. R. Buchmeiser and U. Tallarek*
„Olefin metathesis under spatial confinement and continuous flow: Investigation of isomeric side reactions with a Grubbs–Hoveyda catalyst"
ChemCatChem **2022**, *under review*.

[+] Die Beiträge dieser Autoren sind gleichwertig.

Danksagung

An dieser Stelle möchte ich mich gerne bei den Menschen bedanken, die mich im Rahmen meiner Promotion und darüber hinaus unterstützt haben

Mein besonderer Dank gilt dabei meinem Doktorvater Herrn Prof. Dr. Ulrich Tallarek, der es mir ermöglicht hat in seinem Arbeitskreis an hochinteressanten und anspruchsvollen Thematiken zu arbeiten. Die uneingeschränkte Freiheit auf diesen spannenden Thematiken sowie die Bereitstellung sämtlicher benötigter Materialien und Mittel habe ich sehr wertgeschätzt. Der gemeinsame Weg hin zu dieser Dissertation war für mich sehr lehrreich.

Des Weiteren möchte ich mich bei Herrn Prof. Dr. Eric Meggers für die Übernahme des Zweitgutachtens bedanken. Außerdem bedanke ich mich bei Frau Prof. Dr. Olalla Vázquez dafür, als drittes Mitglied die Prüfungskommission zu vervollständigen.

Dr. Christian Haas, Dr. Felix Ziegler und André Böth danke ich für die enge und fruchtbare Zusammenarbeit bei der gemeinsamen Arbeit an den Projekten. Frau Dr. Alexandra Höltzel und Herrn Prof. Dr. Reinhard Hoffmann danke ich für die Zusammenarbeit beim wissenschaftlichen Schreiben, wodurch ich selbst viel lernen konnte. Bei den Mitgliedern der Arbeitsgruppe André Böth, Andreas Steinhoff und Nicole Trebel möchte ich mich für die fachlichen und nicht-fachlichen Gespräche sowie für die gute Arbeitsatmosphäre bedanken. Mit Freude durfte ich eine Vielzahl an Studierenden bei Abschlussarbeiten und Forschungspraktika betreuen und möchte mich bei Julia Bihler, André Böth, Regina Busch, Olaf Kleykamp, Christian Priedigkeit, Markus Pyschik und Konstantin Rolheiser für ihre investierte Arbeit, welche diese Dissertation bereichert hat, ganz herzlich bedanken. Kirsten Bubenheim danke ich für die Abnahme vieler bürokratischer und organisatorischer Angelegenheiten, sowie die zügigen und unkomplizierten Bestellungen von Chemikalien und Arbeitsmaterialien.

Tarek Oehler danke ich für die Unterstützung bei der Entwicklung und Herstellung des Mikroreaktors, sowie der guten und präzisen Verarbeitung des Reaktors.

Den Mitarbeitern der feinmechanischen Werkstätten der Universität danke ich für das zügige Abarbeiten der Aufträge.

Norbert Frommknecht danke ich für die Mitarbeit bei der Entwicklung Der LED-Arrays und der Automatisierungseinheit um diese zu wechseln, sowie der Entwicklung der benötigten Software.

Den Mitarbeitern der Informationstechnik und Elektronik der Universität danke ich für die gute Zusammenarbeit und gute Verarbeitung der LED-Arrays im Rahmen des Projektes.

Frau Dr. Xiulan Xie danke ich für die Aufnahme komplexer NMR-Daten sowie ihrer Hilfe bei deren Auswertung.

Den Mitarbeitern der Analytikabteilungen der Kernresonanzspektroskopie, Massenspektrometrie und Einkristallstrukturanalytik danke ich für die stets zügige Messung der Proben.

Zuletzt danke ich von ganzem Herzen meiner Familie für die fortwährende Unterstützung jeglicher Art, ohne die dieses Studium und diese Arbeit nicht möglich gewesen wären.

Contents

I. Zusammenfassung

Untersuchungen im kontinuierlichen Durchfluss (Continuous-Flow Chemistry) gewinnen immer mehr an Bedeutung für die organische Synthese, da sie einige Vorteile gegenüber der klassischen Synthese im Kolben mit sich bringen. Um Reaktionen im kontinuierlichen Durchfluss zu untersuchen, hat sich ein Setup aus zwei miteinander verknüpften HPLC-Anlagen etabliert, wobei die erste HPLC-Anlage für die Reaktionsführung (erste Dimension) und die zweite für die Analytik der Reaktionslösung (zweite Dimension) verwendet wird. In der ersten Dimension befindet sich der Reaktor, auf welchem die Reaktion stattfindet. In dieser Dimension kann die Flussrate und somit die Reaktionszeit auf dem Reaktor eingestellt werden. Ein 2-Positionen/6-Wege Ventil hinter dem Reaktor verbindet die beiden HPLC-Anlagen miteinander und ermöglicht, einen Teil der Reaktionslösung von der ersten in die zweite Dimension zu überführen. In der zweiten Dimension findet die Trennung der Substanzen, sowie deren Quantifizierung statt, welche über eine externe Kalibrierung ermöglicht wird. Reaktionen im kontinuierlichen Durchfluss lassen sich im Vergleich zu der klassischen Synthese im Kolben deutlich einfacher automatisieren. Dadurch wird eine höhere Reproduzierbarkeit erhalten und der Mitarbeiter wird von arbeitsaufwändigen, repetitiven Schritten befreit, wodurch er die Zeit bereits zum Auswerten und Interpretieren der Ergebnisse, oder Planen von weiteren Untersuchungen verwenden kann. In dieser Arbeit werden zwei Gebiete vorgestellt, in denen der kontinuierliche Durchfluss effizient genutzt werden kann.

Bei dem ersten Gebiet handelt es sich um die photochemische Katalyse, beziehungsweise photochemische Reaktionen generell. Hierbei wird ein Katalysator (oder das Substrat) durch Licht einer bestimmten Wellenlänge angeregt, wodurch eine chemische Reaktion gestartet wird. Durch die Synthese im kontinuierlichen Durchfluss wird es ermöglicht, Reaktoren zu verwenden, die einen sehr geringen Kanaldurchmesser haben und somit eine geringe Eindringtiefe für das Licht aufweisen. Dadurch entsteht eine nahezu homogene Bestrahlung der Reaktionslösung, wodurch die Reaktion besser kontrolliert und die Bildung von Nebenprodukten minimiert werden kann. Durch die Fortschritte in der Entwicklung der LED-Technologie haben auch die photochemischen Umsetzungen an Bedeutung gewonnen, da nun vielseitige Lichtquellen zur Verfügung stehen, welche wenig Energie benötigen und kostengünstig in der Anschaffung sind. Viele photochemische Umsetzungen lassen sich auch mit Sonnenlicht durchführen, wodurch sie im Hinblick auf Green Chemistry sehr attraktiv geworden sind. Bei photochemischen Untersuchungen wird jedoch oft vernachlässigt, inwiefern sich die Wellenlänge des emittierten Lichtes auf die Reaktion auswirkt, beziehungsweise wie sich die Reaktion durch Bestrahlung von Licht einer anderen Wellenlänge beeinflussen lässt. Die Kapitel 1 und 3 beschäftigen sich mit der Untersuchung von photochemischen Umsetzungen auf deren Wellenlängenabhängigkeit, wobei es sich bei Kapitel 2 um ein direktes Folgeprojekt aus Kapitel 1 handelt, das durch das gute Zusammenspiel zwischen Reaktionsführung und instrumenteller Analytik ermöglicht wurde.

Das zweite Gebiet, welches sich sehr gut für Untersuchungen im kontinuierlichen Durchfluss eignet, ist die heterogene Katalyse. Hierbei wird ein Katalysator auf einem Trägermaterial (meist Silikapartikel) immobilisiert und das Material in eine Säule gepackt. Diese Säule stellt

nun den Reaktor dar. Da keine weitere Reaktion stattfindet, sobald die Lösung den Reaktor verlassen hat, eignet sich die heterogene Katalyse sehr gut für Untersuchungen im kontinuierlichen Durchfluss. Hierbei muss die Reaktion weder gequencht, noch der Katalysator abgetrennt werden, da er sich lediglich stationär im Reaktor befindet, wodurch sich auch die Reaktionszeit sehr gut über die an den Reaktor angelegte Flussrate steuern lässt. Ein großes Problem bei der heterogenen Katalyse stellt die Katalysatorvergiftung (Katalysatorpoisoning) dar, wodurch die Aktivität des Katalysators und somit der Umsatz der Reaktion bei der mehrfachen Verwendung des Katalysators sinkt. Im kontinuierlichen Durchfluss können relativ schnell hintereinander verschiedene Reaktionsbedingungen mit demselben Reaktor untersucht und der Einfluss der Katalysatorvergiftung minimiert werden. In Kapitel 4 und 5 werden Olefin Metathese Reaktionen mit einem Grubbs Katalysator im kontinuierlichen Durchfluss untersucht. Hierbei wird der Katalysator lediglich innerhalb der Poren (60 Å Innendurchmesser) des Silikas immobilisiert, wodurch der Einfluss der räumlichen Beschränkung der Pore auf die Chemoselektivität der Reaktion untersucht werden kann. Im Folgenden werden die einzelnen Kapitel dieser Arbeit kurz zusammengefasst.

Kapitel 1 bildet den Grundstein für die systematische Untersuchung von photochemischen Reaktionen auf die Abhängigkeit der Wellenlänge des einstrahlenden Lichtes. Für dieses Projekt werden 16 baugleiche LED-Arrays entwickelt, wobei sich auf jedem Array 12 LEDs befinden, welche Licht im selben Wellenlängenbereich emittieren. Mit diesen Arrays ist der Bereich zwischen 365 und 670 nm so kleinschrittig wie möglich abgedeckt, um die höchstmögliche Auflösung bei der Untersuchung der Wellenlängenabhängigkeit der Reaktion zu erhalten. Zusätzlich wird ein Mikroreaktor entwickelt, welcher gut auf die LED-Arrays abgestimmt ist, damit das Licht effizient genutzt werden kann und Untersuchungen bei hohen Lichtintensitäten ermöglicht werden. Darüber hinaus wurde eine geringe Kanaltiefe (0.5 mm) gewählt, um eine möglichst homogene Bestrahlung zu erhalten und zusätzlich die Reaktionszeiten so gering wie möglich zu halten. Als Beispielreaktion wird die Perfluoralkylierung von 2-Methylindol mit Eosin Y als Photoredox Katalysator und Diazabicycloundecen (DBU) als Base gezeigt. Die Reaktion wurde in der Literatur lediglich mit weißem Licht untersucht. In diesem Projekt wird der gesamte Wellenlängenbereich des sichtbaren Lichtes zwischen 365 und 700 nm untersucht, um mögliche Unterschiede bei der Reaktion feststellen zu können. Ein wichtiger Punkt dieser Untersuchungen, welcher diese Arbeit auch deutlich von anderen Wellenlängenuntersuchungen abhebt, ist die Kalibrierung der unterschiedlichen LED Arrays. Es wird eine Methode entwickelt, die es ermöglicht, mit einem Spektroradiometer die Anzahl der Photonen, welche auf den Reaktor auftreffen zu normieren. Dadurch verändert sich bei der Untersuchung nur die Wellenlänge der Photonen, aber die Anzahl der Photonen, die auf den Photoreaktor trifft, bleibt nahezu gleich (Abweichung von ca. 3%). Dadurch kann ausgeschlossen werden, dass ein LED-Array bessere oder schlechtere Ergebnisse aufgrund einer höheren oder niedrigeren Photonenanzahl liefert. In dem Bereich zwischen 430 und 550 nm korreliert der Umsatz der Reaktion mit dem Absorptionsspektrum des Eosin Ys. Es ist allerdings auffällig, dass in dem Wellenlängenbereich unter 400 nm, in welchem Eosin Y keine Absorption aufweist, die höchsten Umsätze erhalten werden. Bei einer weiteren Untersuchung ohne Katalysator konnten die Ergebnisse reproduziert werden, wobei

die Umsätze in dem Bereich, in welchem Eosin Y absorbiert, ausgeblieben sind. Bei einer dritten Untersuchung, die ohne eine Base durchgeführt wird, kann derselbe Trend, wenn auch mit deutlich niedrigeren Umsätzen, festgestellt werden. Zusätzlich kommt es zu einer Änderung der Regioselektivität der Reaktion (zwischen der 3 und 4 Position), was darauf schließen lässt, dass es sich hierbei um unterschiedliche Reaktionsmechanismen handelt. Es können also durch die Wahl der Edukte und der Wellenlänge drei unterschiedliche Reaktionsmechanismen selektiv angesteuert werden. Im Wellenlängenbereich zwischen 430 und 550 nm erfolgt die Reaktion über die Photoredox-Katalyse des Eosin Y Katalysators. In dem Wellenlängenbereich unter 430 nm dominiert der Elektronen-Donor-Akzeptor (EDA) Komplex zwischen der Base DBU und Perfluorbutyliodid, der durch Photoaktivierung freie Perfluoralkylradikale erzeugt. Bei dem dritten Mechanismus handelt es sich um einen EDA Komplex zwischen 2-Methylindol und Perfluorbutyliodid, welcher deutlich schwächer ausgeprägt ist als der EDA Komplex zwischen DBU und Perfluorbutyliodid. Hier wird durch Photoaktivierung ein Radikalpaar im Lösungsmittelkäfig generiert, wodurch auch die Regioselektivität der Reaktion beeinflusst wird. Somit konnten drei unterschiedliche Reaktionsmechanismen durch die systematische Untersuchung der Wellenlängenabhängigkeit der Reaktion aufgezeigt werden.

Das zweite Kapitel ist direkt aus der Thematik des ersten Kapitels entstanden. Bereits im ersten Kapitel konnte beobachtet werden, dass es bei einer längeren Lagerung des Produktgemisches von 1-Methyl-3-(Perfluorbutyl)-1*H*-Indol und 1-Methyl-4-(Perfluorbutyl)-1*H*-Indol zu einer Hydrolyse von 1-Methyl-3-(Perfluorbutyl)-1*H*-Indol an der α-Position des perfluorierten Restes kommt, wohingegen 1-Methyl-4-(Perfluorbutyl)-1*H*-Indol stabil ist. Diese Beobachtung ist sehr ungewöhnlich, da es sich bei der C–F Bindung um eine sehr stabile Bindung handelt, welche in der Regel nur durch harsche Reaktionsbedingungen aktiviert werden kann. Ein weiterer großer Vorteil bei dem Zusammenspiel aus der Reaktionsführung und der instrumentellen Analytik liegt darin, dass alle Daten aufgenommen und gespeichert werden. Somit konnte mit Hilfe der Daten aus Kapitel 1 herausgefunden werden, dass das Hydrolyseprodukt bereits bei allen Untersuchungen mit DBU als Base zu einem sehr geringen Anteil entstanden ist (weniger als 1%). Der geringe Anteil lässt sich dadurch erklären, dass bei den Untersuchungen HPLC-Lösungsmittel verwendet wurden, welche nur einen geringen Wasseranteil besitzen. Die Reaktion ließ sich mit einer Base (Natriumhydrid) und unter Zugabe von Wasser im Kolben reproduzieren, wobei eine Ausbeute von 37% über zwei Stufen erhalten wurde. Durch den elektronenziehenden Rest am 2-Methylindol kann die Aminofunktion deprotoniert werden, wodurch F^- abgespalten und die Addition eines Nukleophils an der α-Position des perfluorierten Restes ermöglicht wird. Durch die Verwendung von Natriumethanolat als Base lässt sich auch der Ethanolatrest in das Molekül einbringen. Analoge Reaktionen lassen sich zudem mit 2-Phenylindol statt 2-Methylindol durchführen, wobei die Ausbeuten mit 44% bis 54% über zwei Stufen etwas höher ausfallen. Die Reaktion lässt sich darüber hinaus auch mit Heptafluor-2-Iodpropan, einem sekundären perfluorierten Iodalkan, durchführen (49% über zwei Stufen). Hierbei wird als Hydrolyseprodukt jedoch der Alkohol und nicht das Keton erhalten. Es konnte eine Methode entwickelt werden, welche die indirekte C–F Aktivierung an der α-Position einer perfluorierten Seitenkette an der $C_{(3)}$ Position von 1*H*-Indolen unter milden Reaktionsbedingungen ermöglicht. Hierbei sind die 3-substituierten 2-

Phenyl Indole hervorzuheben, welche vielversprechende Strukturen für die medizinische Chemie darstellen.

In dem dritten Kapitel, das thematisch ebenfalls an das erste Kapitel anschließt, wird das Setup für die Untersuchung von photochemischen Reaktionen auf ihre Wellenlängenabhängigkeit und die Intensität der Lichtquelle komplettiert. Hierfür wird das Setup um ein selbstentwickeltes Modul erweitert, welches es ermöglicht die LED-Arrays und somit die auf den Reaktor einstrahlende Wellenlänge, sowie auch ihre Intensität automatisiert zu ändern. Bei dem Modul handelt es sich um einen Linearantrieb, auf dem ein Schlitten befestigt ist, der bis zu 10 LED-Arrays tragen kann. Die LED-Arrays lassen sich allerdings problemlos untereinander austauschen. Das LED-Array, das in Betrieb ist, befindet sich immer direkt unter dem Mikroreaktor. Über eine Software lässt sich steuern, welches LED-Array zum jeweiligen Zeitpunkt für eine beliebige Dauer aktiv ist. Anschließend kann die Intensität des LED-Arrays geändert werden, oder es wird ein anderes LED-Array für die nächste Untersuchung verwendet. Somit lassen sich nun in Kombination mit den HPLC-Anlagen sowohl die Reaktionsführung, als auch die Analytik, sowie die Quantifizierung der entstanden Verbindungen von photochemischen Reaktionen im Hinblick auf ihre Wellenlängenabhängigkeit und die Intensität der Lichtquelle vollständig automatisiert untersuchen, was zu einer sehr zeiteffizienten Aufnahme von Reaktionsdaten führt. Als Testreaktion für das System wird die Umsetzung eines Arylazosulfons sowohl mit dem Lösungsmittel (Wasser/Acetonitril 1/9 (v/v)), als auch mit einem Dioxaborolan als Additiv, verwendet. Die Reaktion ist sehr vielversprechend, da sie bereits in der Literatur auf ihre Wellenlängenabhängigkeit untersucht und bei verschiedenen Wellenlängen ein unterschiedliches Verhältnis zwischen den Produkten erhalten wurde. Allerdings wurde die Reaktion lediglich bei zwei unterschiedlichen Wellenlängen (366 nm und 450 nm) und bei weißem Licht bei unterschiedlichen Intensitäten und Bestrahlungsdauern untersucht. In diesem Kapitel wird die Reaktion systematisch in dem Wellenlängenbereich von 373 bis 522 nm (12 LED-Arrays) untersucht. Da bereits durch Bestrahlen des Substrates in dem Lösungsmittel drei unterschiedliche Produkte entstehen sollen, wurde das Additiv zunächst weggelassen, um die Reaktion überschaubarer zu halten. Bei der Untersuchung unter Schutzgas entsteht über alle Wellenlängen lediglich Methoxybenzol als Produkt (max. 60% bei der kürzesten Wellenlänge). Allerdings kann bei der Reaktion in Luftatmosphäre ein weiteres Produkt (4-Methoxybenzoldiazonium Methansulfonat) beobachtet werden, welches durch die Reaktion mit Luft gebildet wird. Diese Verbindung lässt sich nur schwer beobachten, da das Absorptionsspektrum des Produktes sehr ähnlich zu dem des Substrates ist und es ebenfalls zu denselben Produkten umgesetzt wird. Das Absorptionsspektrum des Zwischenproduktes ist gestaucht, wobei sich das Maximum um ungefähr 50 nm in den kürzeren Wellenlängenbereich verschiebt. Dadurch ist es möglich, durch Verwendung eines LED-Arrays, mit welchem lediglich das Substrat aber nicht das Zwischenprodukt, angeregt wird, die Reaktion auf der Stufe des Zwischenproduktes zu stoppen. Nun kann das Zwischenprodukt als Substrat eingesetzt und die Reaktion ebenfalls auf die Abhängigkeit der Wellenlänge untersucht werden. Hierbei ist ein deutlich höherer Anteil an 4-Methoxyacetanilid entstanden (Methoxybenzol 45%, 4-Methoxyacetanilid 15%). Das 4-Methoxyacetanilid wird also lediglich aus dem Zwischenprodukt und nicht direkt aus dem Substrat gebildet. Anschließend stellt sich die Frage,

ob die Reaktion mit dem Dioxaborolan ebenfalls durch das Zwischenprodukt beeinflusst wird. Die Untersuchung unter Schutzgas und in Luftatmosphäre führen zu sehr ähnlichen Ergebnissen (45% Produkt, 22–28% Methoxybenzol), was darauf zurückzuführen ist, dass die Reaktion mit dem Additiv deutlich schneller abläuft, als die Bildung des Zwischenproduktes. Mit dem vorgenerierten Zwischenprodukt werden hingegen nur 38% Produkt, 17% Methoxybenzol und 3–4% des 4-Methoxyacetanilids erhalten. Der Umsatz ist hier allerdings auch etwas geringer, da die Reaktion langsamer abläuft. Zudem ist sehr auffällig, dass die Ausbeute bei höheren Wellenlängen über alle Untersuchungen hinweg sinkt. Allerdings sinkt die Ausbeute, in Bezug auf das Produkt, bei Verwendung des Zwischenproduktes, deutlich langsamer. Bei einer Wellenlänge von 430 nm werden mit dem Zwischenprodukt immer noch 30% Produkt generiert, wobei mit dem Substrat lediglich 17% Produkt bei 430 nm generiert werden. Somit bietet sich der Weg über das Zwischenprodukt vor allem bei Reaktionen an, bei welchen die höhere Energie des kurzwelligen Lichtes vermehrt zu Nebenprodukten, oder zu der Zersetzung des Substrates führt. Zusammenfassend wird in dieser Studie ein Setup präsentiert, das eine photochemische Reaktion bei drei unterschiedlichen Reaktionsbedingungen (unter Schutzgas, in Luftatmosphäre, mit vorgeneriertem Zwischenprodukt) innerhalb von neun Stunden, auf ihre Anhängigkeit gegenüber der Wellenlänge des einfallenden Lichtes, vollständig automatisiert untersuchen kann. Im Rahmen dieser Untersuchungen wurde über das geschickte Wählen der eingesetzten Wellenlänge ein Zwischenprodukt selektiv generiert, welches eine völlig andere Reaktivität als das Substrat aufweist. Somit konnte gezeigt werden, dass der Wellenlänge der verwendeten Lichtquelle deutlich mehr Aufmerksamkeit geschenkt werden sollte und bereits ein geringer Unterschied der Wellenlänge des verwendeten Lichtes einen großen Einfluss auf die Reaktion haben kann.

In Kapitel 4 wird das Gebiet der photochemischen Untersuchungen verlassen und das Gebiet der heterogenen Katalyse betreten. Hierfür wird eine Olefin-Metathese Reaktion mit einem Hoveyda–Grubbs Katalysator untersucht, bei welcher ein Dien als Edukt verwendet wird. Das gewünschte Produkt resultiert aus der intramolekularen Reaktion, bei der ein Ring gebildet wird. Als Konkurrenzreaktion kann es allerdings ebenfalls zu einer intermolekularen Reaktion kommen, wodurch ein Dimer, Trimer oder Oligomer aus dem Substrat erhalten wird. Es ist eine etablierte Methode mit sehr gering konzentrierten Lösungen zu arbeiten, um die intramolekulare Reaktion gegenüber der intermolekularen Reaktion zu begünstigen. Dies hat allerdings den Nachteil, dass eine große Menge an Lösungsmittel verwendet werden muss, um eine geringe Menge an Produkt herzustellen. In diesem Projekt wird ein anderer Ansatz gewählt, um den Ringschluss gegenüber der Oligomerisierung zu priorisieren. Da das Dimer deutlich mehr Platz benötigt um gebildet werden zu können, wird der Katalysator lediglich innerhalb der Poren von Silikapartikeln (60 Å Innendurchmesser) immobilisiert, wodurch die Reaktion räumlich eingeschränkt und die Bildung des Ringes begünstigt wird. Die Silikapartikel werden in eine Säule gepackt, auf welcher die Reaktionen im kontinuierlichen Durchfluss, bei unterschiedlichen Temperaturen und unterschiedlichen Flussraten beziehungsweise Reaktionszeiten, untersucht werden. Dabei lassen sich bei allen Temperaturen ähnliche Trends erkennen. Der Umsatz sinkt erwartungsgemäß bei niedrigeren Reaktionszeiten. Der Verlauf der Selektivität, welche das Verhältnis zwischen dem Produkt aus der

Ringschlussmetathese und den Oligomeren angibt, ist deutlich komplexer. Sowohl bei der Ringschlussmetathese, als auch bei der Oligomerisierung wird Ethen freigesetzt, welches bei einem frei zugänglichen Katalysator in einem Kolben schnell entweichen könnte und somit keinen großen Einfluss auf das Gleichgewicht hätte. In diesem Fall liegt der Katalysator aber in den Poren vor und die Säule ist (bis auf die Anschlüsse) in sich abgeschlossen, wodurch das Ethen deutlich langsamer entweichen kann und in das Gleichgewicht mit einbezogen werden muss. Durch das Ethylen kann der bereits gebildete Ring wieder geöffnet werden, was zu einer geringeren Selektivität führt. Zusätzlich kann das Dimer mit sich selbst reagieren, wodurch ebenfalls das gewünschte Produkt gebildet wird. Diese Reaktion läuft allerdings verhältnismäßig langsam ab, da hierfür zunächst das Dimer gebildet werden muss. Mit diesen Zusammenhängen lässt sich auch der Verlauf der Selektivität in dem Experiment erklären. In dem Bereich in dem die Ausbeuten höher sind (über 2%) steigt die Selektivität mit steigenden Flussraten an. Dies ist darauf zurückzuführen, dass bei höheren Flussraten das Ethen schneller abtransportiert werden kann, wodurch die Rückreaktion (die Ringöffnung) eingeschränkt wird. Bei niedrigen Umsätzen (unter 2%) werden nur geringe Mengen an Ethylen generiert, wodurch die Rückreaktion keinen großen Einfluss auf die Selektivität hat. In diesem Bereich steigt die Selektivität mit sinkender Flussrate (steigender Reaktionszeit), da das Dimer nun genug Zeit hat mit sich selbst zu reagieren und ebenfalls das gewünschte Produkt auszubilden. Unter räumlichem Einschluss können zudem höhere Selektivitäten im Vergleich zu der Reaktion im Kolben erzielt werden (Selektivität von 57% statt 47%). Zusätzlich entstehen deutlich kleinere Oligomere im räumlichen Einschluss. Mittels MALDI-TOF konnte gezeigt werden, dass lediglich das Dimer und Trimer gebildet werden (95% zu 5%), wohingegen bei dem frei zugänglichen Katalysator im Kolben Oligomere bis zum Hexamer beobachtet werden. Zusammenfassend konnte mit der Studie gezeigt werden, dass die räumliche Einschränkung Vorteile für die Selektivität der Reaktion mit sich bringt. Darüber hinaus konnte der Einfluss des entstandenen Ethylens auf den Mechanismus beobachtet und Reaktionsbedingungen gefunden werden, bei welchem die Selektivität der Reaktion maximal ist (ca. 60% Selektivität bei 2% Umsatz).

Das fünfte Kapitel beschäftigt sich ebenfalls mit der Olefin Metathese unter räumlichen Einschluss. Bei diesem Projekt liegt der Schwerpunkt jedoch nicht auf der Selektivität zwischen dem Produkt aus der Ringschlussmetathese und den Oligomeren, sondern auf der Untersuchung einer weiteren Nebenreaktion, der Bildung von Isomeren. Für diese Untersuchung wird derselbe Katalysator wie in Kapitel 4 verwendet (Grubbs–Hoveyda), der auch dafür bekannt ist, dass er Isomere aus dem Edukt bilden kann. In diesem Projekt wird untersucht, welche Isomere bei der Reaktion entstehen können und wie sich die Bildung der Isomere beeinflussen lässt. Im Gegensatz zu Kapitel 4 wird in diesem Fall ein Edukt verwendet, das ein aromatisches System beinhaltet. Dadurch ist es möglich sowohl das Edukt als auch alle Produkte, welche aus diesem entstehen, online mit einem DAD zu verfolgen und zu quantifizieren. Zusätzlich wurde ein Massenspektrometer (ESI-MS) angeschlossen, das dabei hilft einen Überblick über die entstehenden Nebenprodukte zu erhalten. Die Katalysatorvergiftung spielt eine wichtige Rolle für die Isomerisierung. Zunächst reagiert der aktive Rutheniumkatalysator mit Ethylen zu Hydriden, welche wiederum für die Isomerisierung verantwortlich sind. Dazu muss zunächst

genug Ethylen entstehen, damit sich die Hydridspezies ausbilden können. Daher werden bei höheren Flussraten und niedrigeren Eduktkonzentrationen keine Isomere beobachtet. Um den genauen Einfluss der Katalysatorvergiftung auf die Isomerisierung feststellen zu können wird ein Reaktor für 200 Minuten bei einer Eduktkonzentration von 100 mM und der niedrigsten Flussrate (0.01 mL/min beziehungsweise 18.6 Minuten Reaktionszeit), die durch die HPLC-Pumpen eingestellt werden kann, untersucht. In dieser Zeit können 18 Messpunkte aufgenommen werden, wobei drei unterschiedliche Phasen des Reaktors festgestellt werden können. In der ersten Phase bis 100 Minuten ist die Selektivität zu Beginn sehr hoch und nimmt langsam ab. Dies ist darauf zurückzuführen, dass zunächst die Hydridspezies ausgebildet werden müssen, bevor die Isomerisierungsreaktion stattfinden kann. In der zweiten Phase des Reaktors zwischen 100 und 145 Minuten ist die Selektivität konstant. In diesem Bereich befinden sich die Bildung und der Verbrauch von Hydridspezies im Gleichgewicht. Nach 145 Minuten steigt die Selektivität rasch an, da aufgrund der Katalysatorvergiftung der Umsatz mittlerweile niedriger ist und nichtmehr genug Ethylen gebildet wird, um eine ausreichende Menge an Hydridspezies zu bilden. Diese Ergebnisse stimmen sehr gut mit den Ergebnissen aus Kapitel 4 überein, bei denen ebenfalls die besten Selektivitäten erreicht wurden, als die Aktivität des Katalysators sehr gering war. Zusammenfassend konnte in diesem Projekt gezeigt werden, dass der räumliche Einschluss nicht nur Vorteile mit sich bringt, sondern dass auch mit einem höheren Isomerisierungsanteil zu rechnen ist. Darüber hinaus sind die Isomerisierungsprodukte sehr vielseitig, da das Isomer des Substrates ebenfalls einen Ringschluss oder die Ausbildung von Oligomeren durchführen kann. Abschließend konnte mit der Hilfe von NMR-Experimenten gezeigt werden, dass sich die NMR-Analyse aus Reaktionsgemischen der Olefinmetathese, für die Bestimmung von Umsätzen und Selektivitäten, nicht gut eignet, da die Signale der Isomere mit den Signalen des Produktes überlappen können und die NMR-Analyse aus einem Reaktionsgemisch somit falsche Ergebnisse liefert. Dennoch ist dies derzeit eine weit verbreitete Methode, welche überdacht werden sollte. Hierfür würde sich das in Kapitel 4 gezeigte 2D-LC/MS System deutlich besser eignen.

Abschließend lässt sich zusammenfassen, dass diese Arbeit gezeigt hat, wie groß der Einfluss der Wellenlänge auf photochemische Reaktionen sein kann. Bereits kleine Unterschiede in der Wellenlänge können zu deutlich anderen Ergebnissen führen. Um die Reproduzierbarkeit einer photochemischen Untersuchung zu gewährleisten, ist es daher wichtig, die verwendeten Lichtquellen ausreichend zu charakterisieren. Dafür sollte für jede verwendete Lichtquelle zumindest ein Emissionsspektrum angegeben werden. Die Farbe des Lichtes anzugeben ist nicht ausreichend, da hier bereits je nach Wellenlängenbereich unterschiedliche Ergebnisse erhalten werden können. In dem Bereich der Olefin-Metathese mit Grubbs-Katalysatoren konnte gezeigt werden, dass der Katalysatorvergiftung mehr Beachtung geschenkt werden sollte. Diese beeinflusst nicht nur den Umsatz der Reaktion, sondern greift direkt in das Gleichgewicht des Mechanismus ein. Daher ist es nicht trivial, Kinetiken aufzunehmen, da die Katalysatorvergiftung diese verfälschen würde, wenn sie nicht unterdrückt oder deutlich eingeschränkt werden kann. Zusätzlich wird im Kolben bei langen Reaktionszeiten immer ein

Ergebnis über alle Phasen der Katalysatorvergiftung erhalten und es kann keine Phase gezielt angesteuert werden.
Insgesamt konnte gezeigt werden, dass Untersuchungen im kontinuierlichen Durchfluss durchaus ihre Vorteile haben. Gerade im Bereich der photochemischen Untersuchungen und der heterogenen Katalyse können deutlich effizienter Messpunkte aufgenommen werden, wodurch die Ergebnisse schneller erzielt und Mechanismen aufgelöst werden können, welche in der klassischen Synthese im Kolben verborgen geblieben wären.

II. Abstract

Continuous-flow chemistry investigations are becoming increasingly important for organic synthesis, as they offer several advantages over classical synthesis in a flask. In order to investigate reactions in continuous-flow, a setup consisting of two linked HPLC systems has been established, whereby the first HPLC system is used for reaction control (first dimension) and the second for the analysis of the reaction solution (second dimension). The reactor on which the reaction takes place is placed in the first dimension. In this dimension, the flow rate and thus the reaction time on the reactor can be adjusted. A 2-position/6-port valve located behind the reactor connects the two systems and allows to transfer a part of the reaction solution from the first to the second dimension. In the second dimension, the separation of the substances takes place and their quantification is made possible via an external calibration. Therefore, a higher reproducibility is obtained and the employee is freed from labor-intensive, repetitive steps, which means he may use the time to evaluate and interpret the results or plan further investigations. In this thesis, two areas are presented in which continuous-flow can be used efficiently.

The first area deals with photochemical catalysis as well as photochemical reactions in general. Here, a catalyst (or the substrate) is excited by light of a certain wavelength, which starts a chemical reaction. Synthesis in continuous-flow allows to use reactors which have a very small channel diameter and thus a low penetration depth for the light. This results in an almost homogeneous irradiation of the reaction solution, which makes it possible to better control the reaction and minimize the formation of by-products. Due to the progress in the development of LED technology, photochemical reactions have also gained in importance, as versatile light sources are now available that require low energy and are inexpensive to purchase. Many photochemical reactions can also be carried out with sunlight, which has made them very attractive in terms of green chemistry. In photochemical investigations, however, the extent to which the wavelength of the emitted light affects the reaction, or how the reaction can be influenced by irradiation with light of a different wavelength, is often neglected when investigating photochemical reactions. Chapters 1 and 3 deal with the investigation of photochemical reactions regarding their wavelength dependence, whereby chapter 2 is a direct follow-up project from chapter 1, which was made possible by the good interaction between reaction control and instrumental analysis.

The second area which is very well suited for continuous-flow investigations concerns heterogeneous catalysis. Here, a catalyst is immobilized on a carrier material (usually silica particles) and the material is packed into a column. This column represents the reactor. Since no further reaction takes place once the solution has left the reactor, heterogeneous catalysis is very well suited for investigations in continuous-flow. In this case, the reaction does not have to be quenched, nor does the catalyst have to be separated, as it is only stationary in the reactor, which also allows the reaction time to be controlled very well via the flow rate applied to the reactor. A major problem in heterogeneous catalysis lies in catalyst poisoning, whereby the activity of the catalyst and thus the conversion of the reaction decreases when the catalyst is used several times. In continuous-flow, different reaction conditions can be investigated

relatively quickly in succession with the same reactor and the influence of catalyst poisoning can be minimized. In chapters 4 and 5, olefin metathesis reactions with a Grubbs catalyst are investigated in continuous-flow. Here, the catalyst is immobilized only within the pores (60 Å inner diameter) of the silica, allowing the influence of the spatial confinement of the pore on the chemoselectivity of the reaction to be investigated. The individual chapters of this thesis are briefly summarized below.

Chapter 1 lays the foundation for the systematic investigation of photochemical reactions on the dependence of the wavelength of the irradiating light. For this project, 16 identical LED arrays are being developed, with 12 LEDs on each array emitting light in the same wavelength range. These arrays are used to cover the range between 365 and 670 nm in the smallest possible steps to achieve the highest possible resolution when studying the wavelength dependence of the reaction. In addition, a microreactor is being developed that is well matched to the LED arrays so that the light can be used efficiently and investigations at high light intensities are possible. Furthermore, a small channel depth (0.5 mm) was chosen in order to obtain the most homogeneous irradiation possible and to keep the reaction times as short as possible. As an example reaction, the perfluoroalkylation of 2-methylindole with eosin Y as photoredox catalyst and diazabicycloundecene (DBU) as base is shown. The reaction has only been investigated with white light in the literature. In this project, the entire wavelength range of visible light between 365 and 700 nm is investigated to determine possible differences in the reaction. An important point of these investigations, which also sets this work apart from other wavelength investigations, is the calibration of the different LED arrays. A method is developed which makes it possible to normalize the number of photons hitting the reactor using a spectroradiometer. In this way, only the wavelength of the photons changes during the examination, but the number of photons hitting the photoreactor remains almost the same (deviation of approx. 3%). This excludes the possibility that an LED array delivers better or worse results due to a higher or lower number of photons. In the range between 430 and 550 nm, the conversion of the reaction correlates with the absorption spectrum of eosin Y. However, it is noticeable that the highest conversions are obtained in the wavelength range below 400 nm, in which eosin Y shows no absorption. In a further investigation without a catalyst, the results could be reproduced, although the conversions in the range in which eosin Y absorbs were absent. In a third investigation, which is carried out without a base, the same trend can be observed, albeit with significantly lower conversions. In addition, there is a change in the regioselectivity of the reaction (between the 3 and 4 position), which suggests that different reaction mechanisms are involved. Thus, three different reaction mechanisms can be selectively controlled by the choice of the reactants and the wavelength. In the wavelength range between 430 and 550 nm, the reaction takes place via photoredox catalysis of the eosin Y catalyst. In the wavelength range below 430 nm, the electron donor acceptor (EDA) complex between the base DBU and perfluorobutyl iodide dominates, which generates free perfluoroalkyl radicals by photoactivation. The third mechanism is an EDA complex between 2-methylindole and perfluorobutyl iodide, which is much weaker than the EDA complex between DBU and perfluorobutyl iodide. Here, photoactivation generates a radical pair in the solvent cage, which

also influences the regioselectivity of the reaction. Thus, three different reaction mechanisms were revealed by the systematic investigation of the wavelength dependence of the reaction.

The second chapter arose directly from the thematic of the first chapter. It was already observed in the first chapter that if the product mixture of 1-methyl-3-(perfluorobutyl)-1*H*-indole and 1-methyl-4-(perfluorobutyl)-1*H*-indole is stored for a longer period, hydrolysis of 1-methyl-3-(perfluorobutyl)-1*H*-indole occurs at the α-position of the perfluorinated group, whereas 1-methyl-4-(perfluorobutyl)-1*H*-indole is stable. This observation is very unusual, as the C–F bond is a very stable bond that can usually only be activated by harsh reaction conditions. Another great advantage of the interaction between reaction control and instrumental analysis is that all data are recorded and stored. Thus, with the help of the data from chapter 1, it was discovered that the hydrolysis product was already formed in a very small proportion (less than 1%) in all investigations with DBU as the base. The low proportion is explained by the fact that HPLC solvents were used in the investigations, which have only a low water content. The reaction could be reproduced with a base (sodium hydride) and with the addition of water in a flask, whereby a yield of 37% was obtained over two steps. The electron-withdrawing group on the 2-methylindole allows the amino function to be deprotonated, resulting in the cleavage of F^- and the addition of a nucleophile at the *α*-position of the perfluorinated group. By using sodium ethanolate as a base, the ethanolate group can also be introduced into the molecule. Analogous reactions can also be carried out with 2-phenylindole instead of 2-methylindole, with slightly higher yields of 44% to 54% over two steps. The reaction can also be carried out with heptafluoro-2-iodopropane, a secondary perfluorinated iodoalkane (49% over two steps). In this case, however, the alcohol and not the ketone is obtained as the hydrolysis product. A method could be developed which allows the indirect C–F activation at the *α*-position of a perfluorinated side chain at the $C_{(3)}$ position of 1*H*-indoles under mild reaction conditions. Here, the 3-substituted 2-phenyl indoles should be highlighted, which represent promising structures for medicinal chemistry.

In the third chapter, which is linked thematically to the first chapter, the setup for the investigation of photochemical reactions regarding their wavelength dependence and the intensity of the light source is completed. For this purpose, the setup is extended by a self-developed module that enables the LED arrays and thus the wavelength irradiating the reactor as well as the intensity of the light source to be changed automatically. The module consists of a linear drive on which a carriage is mounted that can carry up to 10 LED arrays. However, the LED arrays can be interchanged without any problems. The LED array that is in operation is always located directly under the microreactor. A software is used to control which LED array is active at any given time for any given duration. The intensity of the LED array can then be changed, or another LED array can be used for the next examination. Thus, in combination with the HPLC equipment, both the reaction control and the analysis as well as the quantification of the compounds formed from photochemical reactions can now be investigated in a fully automated manner regarding their wavelength dependence and the intensity of the light source,

resulting in a very time-efficient recording of reaction data. The reaction of an arylazo sulphone with the solvent (water/acetonitrile 1/9 (v/v)) as well as with a dioxaborolane as an additive is used as a test reaction for the system. The reaction is very promising as it has already been studied in the literature for its wavelength dependence and a different ratio between the products has been obtained at different wavelengths. However, the reaction has only been studied at two different wavelengths (366 nm and 450 nm) and with white light at different intensities and irradiation durations. In this chapter, the reaction is systematically investigated in the wavelength range from 373 to 522 nm (12 LED arrays). Since three different products are to be formed by irradiating the substrate in the solvent, the additive was initially omitted in order to keep the reaction simpler. In the investigation under inert gas, only methoxybenzene is formed as a product over all wavelengths (max 60% at the shortest wavelength). However, during the reaction in air atmosphere, another product (4-methoxybenzenediazonium methanesulfonate) can be observed, which is formed by the reaction with air. This compound is difficult to observe because the absorption spectrum of the product is very similar to that of the substrate and it is also converted to the same products. The absorption spectrum of the intermediate product is shifted with a maximum of about 50 nm into the shorter wavelength range. This makes it possible to stop the reaction at the intermediate stage by using an LED array with which only the substrate but not the intermediate is excited. This enables to use the intermediate as substrate and to investigate the reaction for the dependence of the wavelength. Here, a significantly higher proportion of 4-methoxyacetanilide was produced (methoxybenzene 45%, 4-methoxyacetanilide 15%). The 4-methoxyacetanilide is thus only formed from the intermediate and not directly from the substrate. The question which arises subsequently is whether the reaction with the dioxaborolane is also influenced by the intermediate. The investigation under inert gas and in air atmosphere lead to very similar results (45% product, 22-28% methoxybenzene), which is due to the fact that the reaction with the additive proceeds much faster than the formation of the intermediate. With the pre-generated intermediate, on the other hand, only 38% product, 17% methoxybenzene and 3-4% of the 4-methoxyacetanilide are obtained. However, the conversion is also somewhat lower because the reaction proceeds more slowly. In addition, it is very noticeable that the yield decreases at higher wavelengths across all investigations. However, the yield decreases much more slowly when the intermediate is used. At a wavelength of 430 nm, 30% product is still generated with the intermediate, whereas only 17% product is generated with the substrate at 430 nm. Thus, the path via the intermediate is particularly advantageous for reactions in which the higher energy of light at short wavelengths leads increasingly to by-products or to the decomposition of the substrate. In summary, this study presents a setup that can investigate a photochemical reaction under three different reaction conditions (inert gas, in air atmosphere, with pre-generated intermediate product) within nine hours in a fully automated manner for its dependence on the wavelength of the incoming light. During these investigations, an intermediate which shows a completely different reactivity than the substrate was selectively generated by carefully choosing the wavelength used. It could thus be shown that the wavelength of the light source used should be given significantly more attention and that even a small difference in the wavelength of the light used can have a major influence on the reaction.

Chapter 4 leaves the field of photochemical investigations and enters the field of heterogeneous catalysis. For this purpose, an olefin metathesis reaction using a Hoveyda–Grubbs catalyst is investigated, in which a diene is used as the reactant. The desired product results from the intramolecular reaction in which a ring is formed. However, an intermolecular reaction can also occur as a competing reaction, resulting in a dimer, trimer, or oligomer from the substrate. It is an established method to work with very low concentrated solutions to favor the intramolecular reaction over the intermolecular reaction. However, this has the disadvantage that a large amount of solvent must be used to produce a small amount of product. In this project, a different approach is taken to prioritize ring closing over oligomerization. Since the dimer requires significantly more space to be formed, the catalyst is immobilized only within the pores of silica particles (60 Å inner diameter), thus spatially confining the reaction and favoring the formation of the ring. The silica particles are packed into a column on which the reactions are studied in continuous-flow, at different temperatures and different flow rates, which lead to different reaction times. Similar trends can be seen at all temperatures. As expected, the conversion decreases with lower reaction times. The course of the selectivity, which indicates the ratio between the product of ring closing metathesis and the oligomers, is clearly more complex. Both ring closing metathesis and oligomerization release ethene, which could quickly escape if the catalyst were freely accessible in a flask and thus would not have much influence on the equilibrium. In this case, however, the catalyst is present in the pores and the column is sealed (except for the inlet and outlet), which means that the ethene releases much more slowly and must be included in the equilibrium. The ethylene can reopen the ring that has already been formed, which leads to a lower selectivity. In addition, the dimer can react with itself, whereby the desired product is also formed. However, this reaction takes place relatively slowly, since the dimer must first be formed. These processes can also explain the course of the selectivity in the experiment. In the range where the yields are higher (above 2%), the selectivity increases with increasing flow rates. This is because at higher flow rates the ethene can be removed more quickly, limiting the back reaction (the ring opening). At low conversion rates (below 2%), only small amounts of ethylene are generated, so the back reaction does not have much influence on the selectivity. In this range, the selectivity increases with decreasing flow rate (increasing reaction time), as the dimer now has enough time to react with itself and form the desired product. Under spatial confinement, higher selectivities can also be achieved compared to the reaction in the flask (selectivity of 57% instead of 47%). In addition, significantly smaller oligomers are formed in spatial confinement. With MALDI-TOF it was shown that only the dimer and trimer are formed (95% to 5%), whereas with the freely accessible catalyst in the flask oligomers up to the hexamer are observed. In summary, the study showed that the spatial restriction has advantages for the selectivity of the reaction. Furthermore, the influence of the ethylene formed on the mechanism was observed and reaction conditions were found at which the selectivity of the reaction is maximal (approx. 60% selectivity at 2% conversion).

The fifth chapter also deals with olefin metathesis under spatial confinement. In this project, however, the focus is not on the selectivity between the product from ring closing metathesis and the oligomers, but on the investigation of another side reaction, the formation of isomers.

For this investigation, the same catalyst as in chapter 4 is used (Grubbs–Hoveyda), which is also known to form isomers from the reactant. This project investigates which isomers can be formed during the reaction and how the formation of the isomers can be influenced. In contrast to chapter 4, this time a reactant is used that contains an aromatic system. Thus, both the reactant and all the resulting products can be tracked and quantified online with a DAD. In addition, a mass spectrometer (ESI-MS) was connected, which helps to obtain an overview of the by-products formed. Catalyst poisoning plays an important role for isomerization. First, the active ruthenium catalyst reacts with ethylene to form hydrides, which in turn are responsible for isomerization. For isomerization to take place, enough ethylene must first be produced in order to form the hydride species. Therefore, no isomers are observed at higher flow rates and lower reactant concentrations. In order to determine the exact influence of catalyst poisoning on isomerization, a reactor is examined for 200 minutes at a reactant concentration of 100 mM and the lowest flow rate (0.01 mL/min or 18.6 minutes reaction time), which can be set by the HPLC pumps. During this time, 18 measuring points are recorded and three different phases of the reactor are detected. In the first phase up to 100 minutes, the selectivity is very high at the beginning and decreases slowly. The reason for this is that the hydride species must first be formed before the isomerization reaction can take place. In the second phase of the reactor between 100 and 145 minutes, the selectivity is constant. In this range, the formation and consumption of hydride species is in equilibrium. After 145 minutes, the selectivity increases rapidly because the conversion is lower due to catalyst poisoning and not enough ethylene is formed to form enough hydride species. These results fit very well with the results from chapter 4, where the best selectivities were also achieved when the activity of the catalyst was very low. In summary, this project has shown that spatial confinement has not only advantages, but also that a higher isomerization rate can be expected. Furthermore, the isomerization products are very versatile, as the isomer of the substrate can also undergo ring-closing metathesis or the formation of oligomers. Finally, with the help of NMR experiments, it was shown that NMR analysis from reaction mixtures of olefin metathesis, is not well suited for the determination of conversions and selectivities, since the signals of the isomers can overlap with the signals of the product, and NMR analysis from a reaction mixture thus provides false results. Nevertheless, this is currently a widely used method, which should be reconsidered. The 2D-LC/MS system shown in chapter 5 would be much better suited for this purpose.

In conclusion, this work has shown how great the influence of wavelength on photochemical reactions can be. Even small differences in wavelength can lead to significantly different results. In order to ensure the reproducibility of a photochemical investigation, it is therefore important to sufficiently characterize the light sources used. For this purpose, an emission spectrum should be provided at least for each light source used. It is not sufficient to specify the color of the light, as different results can be obtained depending on the wavelength range. In the field of olefin metathesis with Grubbs catalysts, it was shown that more attention should be paid to catalyst poisoning. It does not only influence the conversion of the reaction, but directly interferes with the equilibrium of the mechanism. Therefore, it is also not trivial to record kinetics, because they would be falsified by catalyst poisoning if it cannot be suppressed

or significantly limited. In addition, with long reaction times in the flask, a result is always obtained over all phases of catalyst poisoning and no phase can be specifically targeted.

Overall, it was shown that investigations in continuous-flow do have their advantages. Especially in the area of photochemical investigations and heterogeneous catalysis, measurement points can be recorded much more efficiently, which means that results can be obtained more quickly and mechanisms can be resolved that would have remained hidden in the classical synthesis using a flask.

III. Introduction

III.1 Continuous-flow chemistry

In continuous-flow investigations, the reaction does not take place in a flask, instead one or more reaction solutions are pumped into a reactor, capillary, or polymer tube where the reaction takes place.[1] There are different experimental setups to investigate reactions in continuous-flow. One possibility is to use a syringe pump and a polymer tube.[2] Syringe pumps have the advantage that they are inexpensive to purchase, but cannot be automated that easily. However, HPLC systems can also be used for continuous-flow investigations.[3–6] HPLC systems are normally used to separate and analyze chemical mixtures. A simple HPLC system consists of four modules. One of these modules is a thermostatted column oven in which the chromatography column is located. This is where the separation takes place, as the different analytes interact with the separation column to varying degrees and therefore elute sooner or later. Another module is the pump, which continuously pumps the eluent through the chromatography column. An autosampler between the pump and the column oven enables the analyte to be injected. With a detector behind the chromatography column, the amount of substance or the concentration of the analytes can be quantified by an external calibration. A diode array detector which measures the absorption of light at different wavelengths is suitable for this purpose.

An HPLC system provides everything needed for continuous-flow investigations. The pump is used to transfer the reactant solutions into a reactor. A polymer tube or a reactor milled in stainless steel can be used as a reactor.[7–9] The reactor only needs a connection for the HPLC system. Especially in the field of photochemical catalysis, polymer tubes are very popular because they are cheap to obtain and available in different materials with different inner diameters.[9] Since the reaction solution is only mixed by diffusion, a polymer tube with a small inner diameter is usually chosen. However, polymer tubes have the disadvantage that the temperature cannot be controlled, which makes it difficult to work under isothermal conditions, as the reaction solution heats up over time due to light irradiation and the energy of exothermic reactions is poorly dissipated.

In the field of heterogeneous catalysis, other reactors are known. There is the possibility of immobilizing the catalyst on a carrier material such as silica and sealing the particles in a column.[10,11] Afterwards, the chromatography column located in the temperature-controlled column oven can be replaced by the reactor, allowing direct control of the temperature for the reaction. The reaction time can be determined by the volume of the reactor and the applied flow rate. The DAD behind the reactor monitors the reaction solution by absorbing light at different wavelengths. Although the substances from the reaction solution arrive at the detector together and not separated in time, it can already be seen whether a reaction has taken place. When the reaction solution reaches the DAD, the absorbance of the solution changes because the substrate has a different absorbance than the solvent. When a reaction has occurred in the reactor, the absorbance of the solution changes if the absorbance of the reactants and the product are

different. This may already be sufficient to determine the conversion of the reaction.[12,13] Otherwise, two HPLC systems can be connected with a valve, which is placed behind the reactor of the first HPLC system. The valve contains a capillary that is filled with the reaction solution and can be switched to inject the solution from the capillary into the second HPLC system, replacing the autosampler. The second HPLC system is an ordinary HPLC system, which makes it possible to separate and quantify the reaction substances.[3] The advantage of the HPLC system in the investigation of continuous-flow reaction systems is, that it is operated fully automatically and all data are stored. Timetables can be created which allow the flow rate and thus the reaction time as well as the reaction temperature to be changed at specified times. Furthermore, the setup can be extended with all modules already known from analytical chemistry. This allows to collect substance for NMR experiments with a fraction collector or to obtain further information about the reaction mixture with an ESI-MS. An exemplary setup for continuous-flow investigations, with fraction collector and ESI-MS, is shown in Figure III.1.

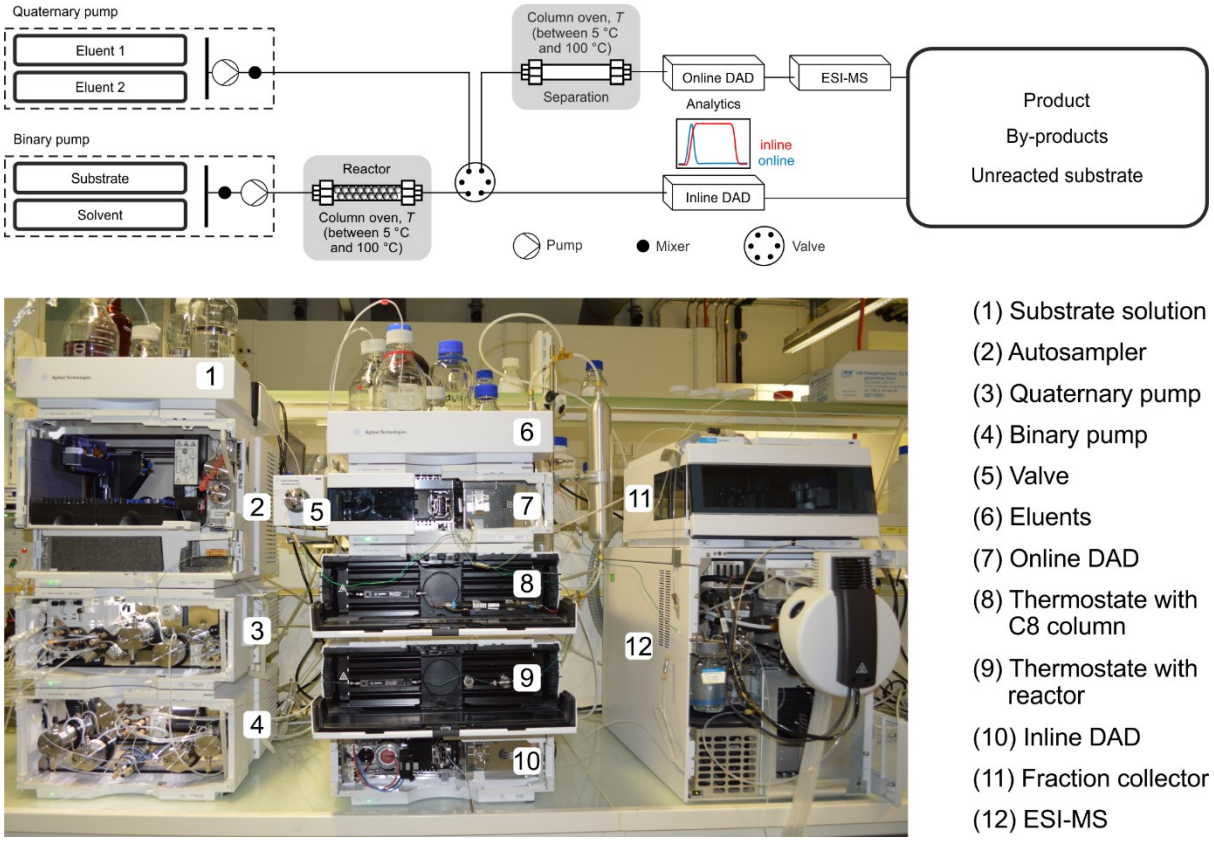

Figure III.1. Top: Schematic drawing of a 2D/LC-MS setup for the investigation of continuous-flow reactions. Bottom: Photograph of the 2D/LC-MS setup. The shown setup is composed of different modules from Agilent Technologies.

III.1.1 Advantages of continuous-flow chemistry

Flow chemistry offers several advantages over classical synthesis in a flask, which is why it is preferable to synthesis in a flask in some aspects.[1] A major advantage is that the temperature of the reaction in microreactors can be better controlled compared to reactions in a flask. The small channel diameter of microreactors leads to a high surface-to-volume ratio between the reaction solution and the channel wall. As a result, the reaction solution can be heated or cooled very quickly,[14] and the heat generated during exothermic reactions is dissipated rapidly. The permanent control of pressure and temperature also provides a higher degree of safety in highly exothermic or potentially explosive reactions.[15] Due to the large surface-to-volume ratio of continuous-flow reactors, very short reaction times are also obtained for the study of reactions between liquids and gases, making them very suitable for their investigations.[16–18] In addition, continuous-flow reactions typically have a higher reproducibility because mixing in the microreactor is much faster due to the small channel diameter,[8] and the reactions can be easily automated,[19] avoiding errors by the operator. Automation also allows more data points to be recorded in a shorter time, making continuous-flow studies very suitable for investigating different input parameters such as reaction times, reaction temperatures or reactant ratios.[1,20] The advantages in the field of photochemical catalysis and heterogeneous catalysis are discussed in detail in chapters III.2.1 and III.3.1.

However, there are also aspects where the investigation in the flask is preferable. The investigation of the influence of the solvent on the reaction cannot be easily automated, so that it is easier to carry out the investigations in a flask. In addition, problems arise in continuous-flow as soon as a substance precipitates during the reaction, as this can lead to clogging of the microreactor. Especially if the precipitation of the substance has a positive effect on the equilibrium of the reaction, it is recommended to carry out the reaction in a flask.[1]

It is most efficient to have both options on the screen and to perform part of the investigation in batch before transferring the system to continuous-flow, where the investigation of input parameters such as temperature and reaction time can be well automated.[1]

III.2 Photochemistry

Photochemical catalysis enables completely new reaction pathways and synthesis possibilities, which is why it is of great interest for organic synthesis.[21] There are a variety of catalysts which can be used for photochemical reactions and adapted to the corresponding synthesis problem.[22] The catalyst system can usually be selected in a manner that only the catalyst absorbs the light and thus the light has no direct influence on the substrate or additive. There are also versatile possibilities in the choice of light source. For example, lasers,[23] LEDs,[24] or even sunlight can be used,[25,26] although all light sources have their advantages and disadvantages. Lasers have a low bandwidth which makes it possible to set an exact wavelength. On the other hand, they irradiate only a small area, making it difficult to upscale reactions with lasers.[23] LEDs irradiate a larger area, but the intensity of the irradiation decreases sharply with the distance of the LED from the reaction solution. Placing the LED close to the reaction solution can in turn lead to thermal problems.[23] Using sunlight is an elegant, energy-saving method, but leads to very long reaction times due to the low light intensity. There are also versatile options in the choice of reactors, which will be discussed in III.2.1.

Photochemical reactions have the advantage that they can usually be carried out under mild reaction conditions, since the activation does not take place by high temperatures but only by excitation by light.[20] Thus, many functional groups can be tolerated, which allows photochemical reactions to be used in higher steps of a longer synthesis route. Therefore, they are very popular for use in natural product synthesis and often form the key step.[27]

Although the potential of photochemical conversions for new reaction pathways and synthesis opportunities has been known for decades,[21,28] photochemical conversions have gained even more importance in recent years.[29–31] This development is due to the fact that great progress has been made in the field of LED development[20,32,33] and in the development of microreactors.[9] LEDs afford the ability to use a relatively inexpensive light source with monochromatic light at a high intensity to specifically excite the catalyst of the reaction, which is why LEDs have become workhorses in modern photochemical synthesis.[34] LEDs are also well suited for studying photochemical reactions for dependence on their light source. For example, Kappe's group has used a commercially available flow reactor to study photochemical reactions for the influence of the wavelength of the light sources used.[24,35–38] However, the reactor used has the disadvantage that with the light at different wavelengths, there are also different light intensities.[24] Therefore, it is possible that the observed correlations are due to the light intensity and not to the wavelength of the light. To avoid this problem, there is a method to measure the photoreactor with spectroradiometers.[39,40] With a spectroradiometer, the light intensity can be measured at different locations in the reactor, allowing the light intensity to be adjusted via the current applied to the LEDs so that the same light intensities are present when using light of different wavelengths.

III.2.1 Advantages of continuous-flow chemistry for photochemical investigations

There are many possibilities when choosing a reactor for carrying out photochemical reactions.[9,41] The reaction can be carried out in a flask or a vial. However, it can also be transferred to continuous-flow.[20] For the implementation of photochemical reactions in continuous-flow, polymer tubes or microreactors milled in stainless steel can be used. In addition, the falling film microreactor is also very well suited for photochemical reactions, especially when reactions between a solvent and a gas are being studied.[17,18] The main difference between the reactors is the diameter of the reactor and thus the distance the light has to travel in the solution for a reaction to take place. In a flask, there is a penetration depth of several centimeters, depending on the charge size, whereas in polymer tubes and microreactors the penetration depth is usually less than one millimeter. The Beer-Lambert-Bouguer law describes how this affects the reaction.[20]

$$A = \log_{10}\frac{1}{T} = \log_{10}\frac{I_0}{I} = \varepsilon \cdot l \cdot c$$

A: Absorbance of the solution at a certain wavelength. T: Transmission at a specific wavelength. I_0: Initial intensity. I: Intensity of the light after crossing the sample. ε: Molar absorption coefficient ($mol^{-1}cm^{-1}$). l: Distance travelled through the solution (cm). c: Concentration of the absorbing species.

The effect of the Beer-Lambert-Bouguer law becomes clear with an example reaction. In a photocatalytic conversion with $Ru(bpy)_3Cl_2$ (c = 0.5, 1 and 2 mM, ε = 13000 $cm^{-1}M^{-1}$), 50% of the photons are already absorbed after 0.47 mm to 0.12 mm, depending on the chosen concentration. The amount the law affects the reaction in the respective reactors can be seen in Figure III.2.

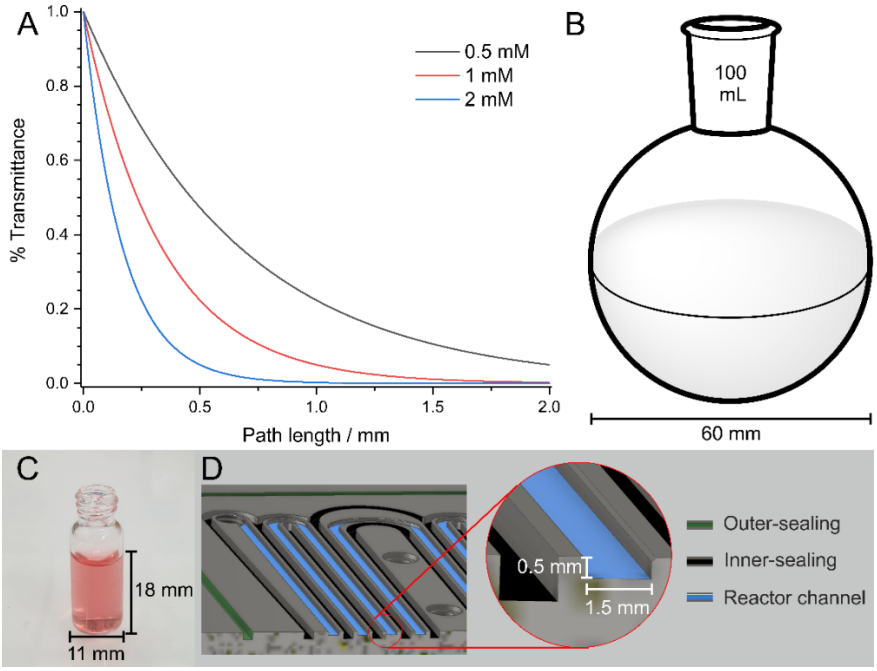

Figure III.2. A: Example system with $Ru(bpy)_3Cl_2$ as catalyst to illustrate the transmission as a function of the solution distance to be penetrated. B: Flask with a volume of 100 mL and a diameter of 60 cm. C: Vial with a diameter of 11 mm and a solvent level of approximately 18 mm. D: Microreactor with a channel depth of 0.5 mm (used in this thesis).

The continuous-flow allows to use reactors with significantly lower irradiation depths (from 60 mm for the flask (Figure III.2 A) to less than 1 mm for the microreactor Figure III.2 D)). As a result, the reaction times of the photochemical reactions are considerably shortened and many more measuring points can be recorded in a shorter time. In addition, better control over the system is achieved, limiting the spectrum of by-products by reducing the probability that products already formed will decay again during prolonged irradiation.[42,43]

III.3 Olefin-metathesis

Olefin metathesis uses a catalytic amount of a metal complex to realkylidate two double bonds. Olefin metathesis is widely used to generate new carbon double bonds since it tolerates many functional groups.[44–47] With the formation of higher oligomers, olefin metathesis has a major impact on the development of petrochemistry.[48] The selection of the catalyst can be very well adapted to the synthesis problem, since there are many different catalysts for olefin metathesis, which differ in their reactivity and sensitivity to oxygen and moisture from the air.[49,50]
In olefin metathesis, initially a carbenoid is formed between the olefin reactant and the catalyst used. Subsequently, the metal-carbene complex forms a metal-cyclobutane complex with another alkene. The cyclobutane complex reopens and the corresponding olefin is obtained. In addition, the use of reactants with terminal double bonds leads to the elimination of ethene. Since the reactant for olefin metathesis only needs to have a double bond, the possible reactions are very diverse. This is illustrated by the scheme in Figure III.3 using a terminal diene.

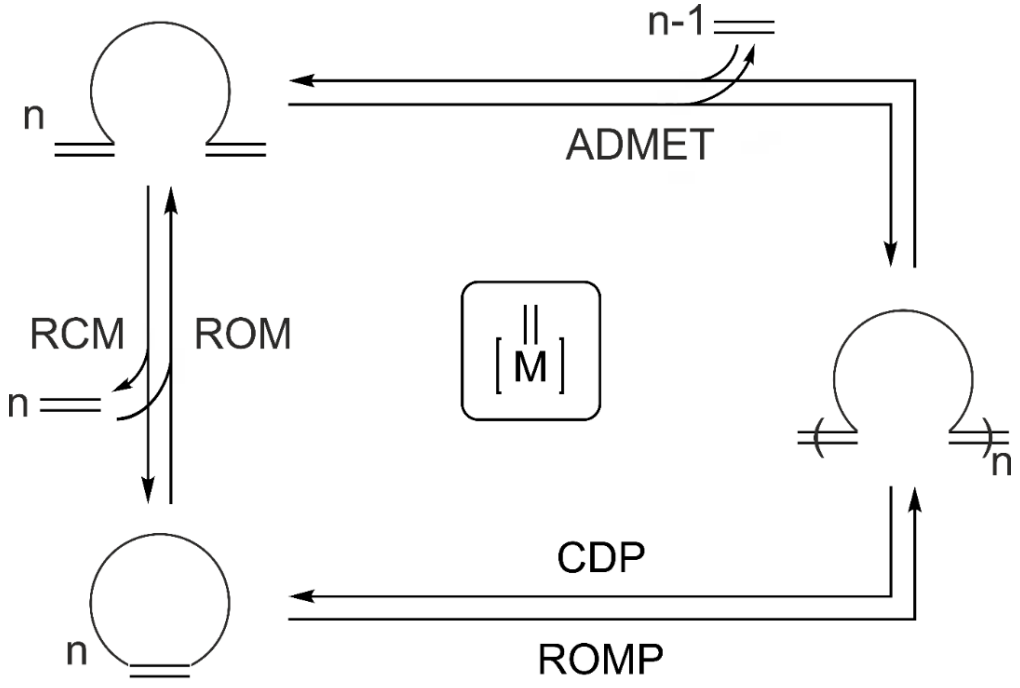

Figure III.3. Reaction scheme of olefin metathesis based on an α,ω-diene. All reaction pathways can proceed in both directions. RCM: Ring-closing metathesis. ROM: Ring-opening metathesis. ADMET: Acyclic diene metathesis. CDP: Cyclodepolymerization. ROMP: Ring-opening metathesis polymerization. Substrate equivalents are indicated with *n*. The catalyst is designated as [M=].

Olefin metathesis can be used for a ring closing of a terminal diene (RCM), forming a mixture of the *E*- and *Z*-isomer. However, depending on the reaction conditions, this ring can also reopen (ROM) (e.g., by increasing the ethene concentration). In addition to intramolecular reactions, there can also be intermolecular reactions with the same or a different reactant, which can occur multiple times and lead to oligomers (ADMET). The resulting oligomers can cleave off the substrate in the form of a closed ring through an intramolecular reaction (CDP). The closed ring can react with another substrate molecule in the presence of the catalyst to form the corresponding oligomer again (ROMP). On the one hand, olefin metathesis can be used in a variety of ways to generate different products, but on the other hand, it is also challenging to selectively generate the desired product. The choice of catalyst is also important. The ^{2}nd-generation Grubbs catalyst,[51] as well as the related ^{2}nd-generation Grubbs–Hoveyda catalyst,[52,53] which are known for their versatility, are prone to the formation of ruthenium hydrides and thus to the isomerization of the double bond of the substrate.[54–57] Since the resulting isomers can also perform the reaction steps shown in Figure III.3, the reaction system becomes complex very quickly.

There are several ways to influence the equilibrium of the reaction. In order to obtain the oligomer, the reaction is usually carried out at very high substrate concentrations, to favor the intermolecular reaction over the intramolecular reaction. Additionally, if the ethene which is formed during the oligomerization can be removed from the equilibrium, there is no threat of a back reaction. However, shifting the equilibrium in the direction of ring-closing metathesis is much more difficult. A proven method is to work with very low concentrations to favor the intramolecular reaction over the intermolecular reaction.[58,59] However, this leads to much longer reaction times at the same catalyst concentration, and a comparatively large amount of solvent is consumed to obtain a small amount of product. Once again, removal of the resulting ethylene from equilibrium is advantageous in suppressing ring-opening metathesis.[59]

III.3.1 Advantages of continuous-flow chemistry for investigations in the field of heterogeneous catalysis

In heterogeneous catalysis, where a solid phase as well as a liquid phase are present, continuous-flow studies are advantageous because the reaction and purification occur simultaneously.[1] For continuous-flow studies, the catalyst is immobilized on a support material (usually silica) and fixed in a column.[60,61] Therefore, the catalyst is unable to leave the column and does not need to be quenched or separated to stop the reaction. In addition, the catalyst is protected from the environment, slowing down the poisoning of the catalyst.[62] This allows more studies to be performed with the same amount of catalyst, making continuous-flow very suitable for studying reaction parameters such as temperature or reaction time.[1]

III.4 Motivation

Although photochemical reactions and their potential to create new reaction possibilities have been known and valued for many years, the investigation of reactions regarding the dependence of the light source used has been rather neglected. Although first studies are known in which photochemical reactions were investigated for their dependence on the wavelength of the light source used, the light sources were not sufficiently characterized. The intensities of the light sources were not adjusted to each other, so that the differences could also be caused by a higher light intensity, i.e. a higher number of photons hitting the reactor. The aim of this work in the field of photochemical catalysis is to develop a setup in which photochemical investigations can be investigated as efficiently as possible regarding the dependence of the light source used. For this purpose, it must be ensured that only the wavelength is changed during the investigations, but the number of photons hitting the reactor remains the same. In order to make full use of the advantages of continuous-flow, the setup is also optimized so that both the wavelength and the light intensity used can be changed automatically. Subsequently, example reactions are used to show how great the influence of the wavelength can be on the photochemical conversions and which additional information can be obtained about the corresponding reaction mechanisms.

Although olefin metathesis is used in a variety of reactions, the possibilities to influence the reaction equilibrium in the direction of ring-closing metathesis are limited. Although it is possible to work at very low reactant concentrations, longer reaction times and a high solvent consumption must be accepted. The aim of this work in the field of olefin metathesis is to find a more efficient way to influence the selectivity of the reaction. For this purpose, the influence of spatial confinement on olefin metathesis is investigated, since oligomerization, which results in larger products, requires significantly more space than ring-closing metathesis. This should make it possible to work with high concentrations and still prefer ring-closing metathesis over oligomerization. The studies are carried out in continuous-flow with a Grubbs catalyst to show the influence of spatial confinement on selectivity and reaction equilibrium in general.

III.5 References

1 M. B. Plutschack, B. Pieber, K. Gilmore, P. H. Seeberger, *Chem. Rev.* **2017**, *117*, 11796–11893.

2 M. Iannone, D. Caccavo, A. A. Barba, G. Lamberti, *HardwareX* **2022**, *11*, e00295.

3 C. P. Haas, T. Müllner, R. Kohns, D. Enke, U. Tallarek, *React. Chem. Eng.* **2017**, *2*, 498–511.

4 C. P. Haas, S. Biesenroth, S. Buckenmaier, T. Van De Goor, U. Tallarek, *React. Chem. Eng.* **2020**, *5*, 912–920.

5 N. Bieniek, C. P. Haas, U. Tallarek, N. Hampp, *Photochem. Photobiol. Sci.* **2021**, *20*, 773–780.

6 C. P. Haas, U. Tallarek, *ChemistryOpen* **2019**, *8*, 606–614.

7 J. P. Mcmullen, K. F. Jensen, Annu. Rev. Anal. Chem. **2010**, *3*, 19–42.

8 R. L. Hartman, J. P. McMullen, K. F. Jensen, *Angew. Chem. Int. Ed.* **2011**, *50*, 7502–7519.

9 Y. Su, N. J. W. Straathof, V. Hessel, T. Noël, *Chem. Eur. J.* **2014**, *20*, 10562–10589.

10 A. Tanimu, S. Jaenicke, K. Alhooshani, *Chem. Eng. J.* **2017**, *327*, 792–821.

11 K. Masuda, T. Ichitsuka, N. Koumura, K. Sato, S. Kobayashi, *Tetrahedron* **2018**, *74*, 1705–1730.

12 M. Baumann, *Org. Biomol. Chem.* **2018**, *16*, 5946–5954.

13 K. Somerville, M. Tilley, G. Li, D. Mallik, M. G. Organ, *Org. Process Res. Dev.* **2014**, *18*, 1315–1320.

14 H. Löwe, V. Hessel, A. Mueller, *Pure Appl. Chem.* **2002**, *74*, 2271–2276.

15 S. Marre, J. Baek, J. Park, M. G. Bawendi, K. F. Jensen, *J. Lab. Autom.* **2009**, *14*, 367–373.

16 S. Han, M. A. Kashfipour, M. Ramezani, M. Abolhasani, *Chem. Commun.* **2020**, *56*, 10593–10606.

17 T. H. Rehm, S. Gros, P. Löb, A. Renken, *React. Chem. Eng.* **2016**, *1*, 636–648.

18 D. Lokhat, A. K. Domah, K. Padayachee, A. Baboolal, D. Ramjugernath, *Chem. Eng. Sci.* **2016**, *155*, 38–44.

19 M. Oelgemöller, O. Shvydkiv, *Molecules* **2011**, *16*, 7522–7550.

20 D. Cambié, C. Bottecchia, N. J. W. Straathof, V. Hessel, T. Noël, *Chem. Rev.* **2016**, *116*, 10276–10341.

21 N. Hoffmann, *Chem. Rev.* **2008**, *108*, 1052–1103.

22 N. A. Romero, D. A. Nicewicz, *Chem. Rev.* **2016**, *116*, 10075–10166.

23 K. C. Harper, E. G. Moschetta, S. V. Bordawekar, S. J. Wittenberger, *ACS Cent. Sci.* **2019**, *5*, 109–115.

24 Y. Chen, O. de Frutos, C. Mateos, J. A. Rincon, D. Cantillo, C. O. Kappe, *ChemPhotoChem* **2018**, *2*, 906–912.

25 G. D. Scholes, G. R. Fleming, A. Olaya-Castro, R. Van Grondelle, *Nat. Chem.* **2011**, *3*, 763–774.

26 T. P. Yoon, M. A. Ischay, J. Du, *Nat. Chem.* **2010**, *2*, 527–532.

27 M. D. Lainchbury, M. I. Medley, P. M. Taylor, P. Hirst, W. Dohle, K. I. Booker-Milburn, *J. Org. Chem.* **2008**, *73*, 6497–6505.

28 H. D. Roth, *Angew. Chem. Int. Ed. Engl.* **1989**, *28*, 1193–1207.
29 D. M. Schultz, T. P. Yoon, *Science* **2014**, *343*, 1239176.
30 T. Bach, J. P. Hehn, *Angew. Chem. Int. Ed.* **2011**, *50*, 1000–1045.
31 J. J. Douglas, K. P. Cole, C. R. J. Stephenson, *J. Org. Chem.* **2014**, *79*, 11631–11643.
32 L. Buglioni, F. Raymenants, A. Slattery, S. D. A. Zondag, T. Noël, *Chem. Rev.* **2022**, *122*, 2752–2906.
33 M. Sender, D. Ziegenbalg, *Chem. Ing. Tech.* **2017**, *89*, 1159–1173.
34 L. Buzzetti, G. E. M. Crisenza and P. Melchiorre, *Angew. Chem. Int. Ed.* **2019**, *58*, 3730–3747.
35 C. Rosso, J. D. Williams, G. Filippini, M. Prato, C. O. Kappe, *Org. Lett.* **2019**, *21*, 5341–5345.
36 Y. Chen, G. Glotz, D. Cantillo, C. O. Kappe, *Chem. Eur. J.* **2020**, *26*, 2973–2979.
37 A. Steiner, O. de Frutos, J. A. Rincón, C. Mateos, J. Williams, C. O. Kappe, *React. Chem. Eng.* **2021**, *6*, 2434–2441.
38 A. Steiner, J. D. Williams, J. A. Rincón, O. de Frutos, C. Mateos, C. O. Kappe, *Eur. J. Org. Chem.* **2019**, *33*, 5807–5811.
39 M. Sender, B. Wriedt, D. Ziegenbalg, *React. Chem. Eng.* **2021**, *6*, 1601–1613.
40 M. Sender, D. Ziegenbalg, *React. Chem. Eng.* **2021**, *6*, 1614–1627.
41 T. H. Rehm, *ChemPhotoChem* **2020**, *4*, 235–254.
42 D. Mazzarella, A. Pulcinella, L. Bovy, R. Broersma, T. Noël, *Angew. Chem. Int. Ed.* **2021**, *60*, 21277–21282.
43 A. V. Nyuchev, T. Wan, B. Cendón, C. Sambiagio, J. J. C. Struijs, M. Ho, M. Gulías, Y. Wang, T. Noël, *Beilstein J. Org. Chem.* **2020**, *16*, 1305–1312.
44 R. H. Grubbs, S. Chang, *Tetrahedron* **1998**, *54*, 4413–4450.
45 K. C Nicolaou, P. G. Bulger, D. Sarlah, *Angew. Chem*. *Int. Ed.* **2005**, *44*, 4490–4527.
46 C. Lecourt, S. Dhambri, L. Allievi, Y. Sanogo, N. Zeghbib, R. Ben Othman, M. I. Lannou, G. Sorin, J. Ardisson, *Nat. Prod. Rep*. **2018**, *35*, 105–124.
47 R. García-Fandiño, M. J. Aldegunde, E. M. Codesido, L. Castedo, J. R. Granja, *J. Org. Chem*. **2005**, *70*, 8281–8290.
48 J. C. Mol, *J. Mol. Catal. A Chem.* **2004**, *213*, 39–45.
49 A. A. Tsedalu, *J. Chem.* **2021**, 3590613.
50 G. C. Vougioukalakis, R. H. Grubbs, *Chem. Rev.* **2010**, *110*, 1746–1787.
51 M. Scholl, S. Ding, C. W. Lee, R. H. Grubbs, *Org. Lett*. **1999**, *1*, 953–956.
52 S. Gessler, S. Randl, S. Blechert, *Tetrahedron Lett*. **2000**, *41*, 9973–9976.
53 S. B. Garber, J. S. Kingsbury, B. L. Gray, A. H. Hoveyda, *J. Am. Chem. Soc.* **2000**, *122*, 8168–8179.
54 V. I. Petkovska, T. E. Hopkins, D. H. Powell, K. B. Wagner, *Macromolecules* **2005**, *38*, 5878–5885.
55 R. Ahuja, S. Kundu, A. S. Goldman, M. Brookhart, B. C. Vicente, S. L. Scott, *Chem. Commun*. **2008**, *2*, 253–255.
56 A. Fürstner, O. R. Thiel, L. Ackermann, H.-J. Schanz, S. P. Nolan, *J. Org. Chem*. **2000**, *65*, 2204–2207.

57 M. Martinez-Amezaga, C. M. L. Delpiccolo, L. Méndez, I. Dragutan, V. Dragutan, E. G. Mata, *Catalysts* **2017**, *7*, 111.
58 S. Monfette, D. E. Fogg, *Chem. Rev*. **2009**, *109*, 3783–3816.
59 J. C. Conrad, M. D. Eelman, J. A. Duarte Silva, S. Monfette, H. H. Parnas, J. L. Snelgrove, D. E. Fogg, *J. Am. Chem. Soc.* **2007**, *129*, 1024–1025.
60 M. Irfan, T. N. Glasnov, C. O. Kappe, *ChemSusChem* **2011**, *4*, 300–316.
61 J. Kobayashi, Y. Mori, S. Kobayashi, *Chem. Asian. J.* **2006**, *1*, 22–35.
62 S. G. Newman, K. F. Jensen, *Green Chem.* **2013**, *15*, 1456–1472.

1. Chapter 1: Light as a reaction parameter – systematic wavelength screening in photochemical synthesis

Authors
C. P. Haas,[+] T. Roider,[+] R. W. Hoffmann and U. Tallarek*
[+]These authors contributed equally to this work.

State of publication
Published 09 September 2019 in *Reaction Chemistry & Engineering*, Vol. 4, pp. 1912–1916.
DOI: 10.1039/c9re00339h

Table of content

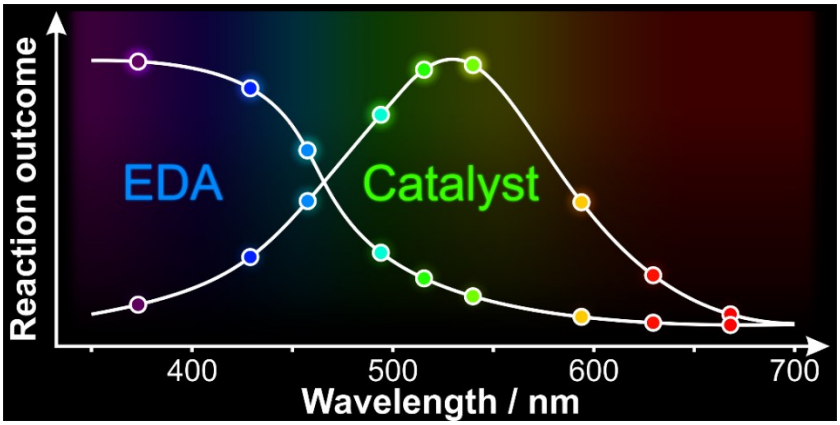

Abstract
We unfold light as reaction parameter in a continuous-flow photoreactor, using 16 LED arrays with different emission bands (350–700 nm) but identical irradiances. For the perfluoroalkylation of 2-methylindole, three reaction mechanisms are revealed wavelength-selectively and subsequently transferred into independent synthetic routes: i) photoredox catalyzed by eosin Y, ii) via amine-based electron donor–acceptor (EDA) complexes (catalyst-free), iii) via indole-based EDA complexes (catalyst- and additive-free). The methodology enables routine and systematic screening of irradiation wavelengths and intensities in photochemical synthesis.

1.1 Main text

The proper selection of light sources represents a valuable asset in synthetic photochemistry to control reaction outcomes. Specific reaction channels can be addressed precisely by using appropriate irradiation wavelengths if the underlying reaction mechanisms are adequately understood.[1,2] Unfortunately, elucidating these reaction mechanisms remains an elaborate and multidisciplinary challenge, especially for complex photochemical reaction systems.[2,3] Therefore, it seems reasonable to discover wavelength selectivities and dependencies of photochemical reactions in their actual synthetic environment by screening different irradiation wavelengths systematically, i.e., with the same number of incident photons per time and area (irradiance).[4] The few reports on wavelength screenings with identical irradiances are limited to the use of tunable laser systems which, even though providing essentially monochromatic emission, are expensive and difficult to combine with typical photoreactor setups.[5]

In contrast, high-power light-emitting diodes (LEDs) have been established as workhorses in modern synthetic photochemistry, since they provide relatively narrow emission bands for many emission maxima.[2] Accordingly, recent reports describe the wavelength selectivities or dependencies of reactions by using different LED light sources.[4] Notably, the group of Kappe could demonstrate wavelength-selective gating of two different reaction channels by screening six different wavelengths, albeit with significantly differing irradiances.[6] In another approach, Noël and co-workers applied luminescent solar concentrators which converted broad solar irradiation to a narrow wavelength range matched with the absorption maximum of the photocatalyst to demonstrate wavelength-selective effects.[7] Here, we present the first systematic wavelength screening with an LED photoreactor using the perfluorobutylation of 2-methylindole as test reaction.

Due to the significance of perfluoroalkylation reactions in drug development, they are well-established in the literature encompassing a variety of photochemical strategies and light sources.[8] Based on previous works (Scheme 1.1 top), we chose the reaction of 2-methylindole (1) with nonafluoro-1-iodobutane (2) in acetonitrile as a test reaction and selected 1,8-diazabicyclo[5.4.0]undec-7-ene (DBU) as a base. This reaction has been previously realized under continuous-flow conditions with eosin Y as metal-free photoredox catalyst and TMEDA (*N*,*N*,*N*′,*N*′-tetramethyl-1,2-ethanediamine) as amine base (Scheme 1.1a).[9] It was also reported that TMEDA as well as DBU act as "amine promoter" in the synthesis of perfluoroalkyl-substituted β-ketoesters involving electron donor–acceptor (EDA) complexes between amine bases and perfluoroalkyl iodides (Scheme 1.1b).[10–12] Moreover, the substrate 2-methylindole itself was shown to form EDA complexes that drive photochemical alkylation reactions (Scheme 1.1c).[13] Finally, the free radical alkylation of indoles may lead to regioisomeric products, as seen in the trifluoromethylation of indoles using Togni's reagent (Scheme 1.1d).[14,15] Considering the various reaction channels of the chosen system and the so far investigated light sources (mostly white light or "blue LED" without further specification of the emission), a systematic study of the wavelength selectivities of the different reaction channels appeared promising.

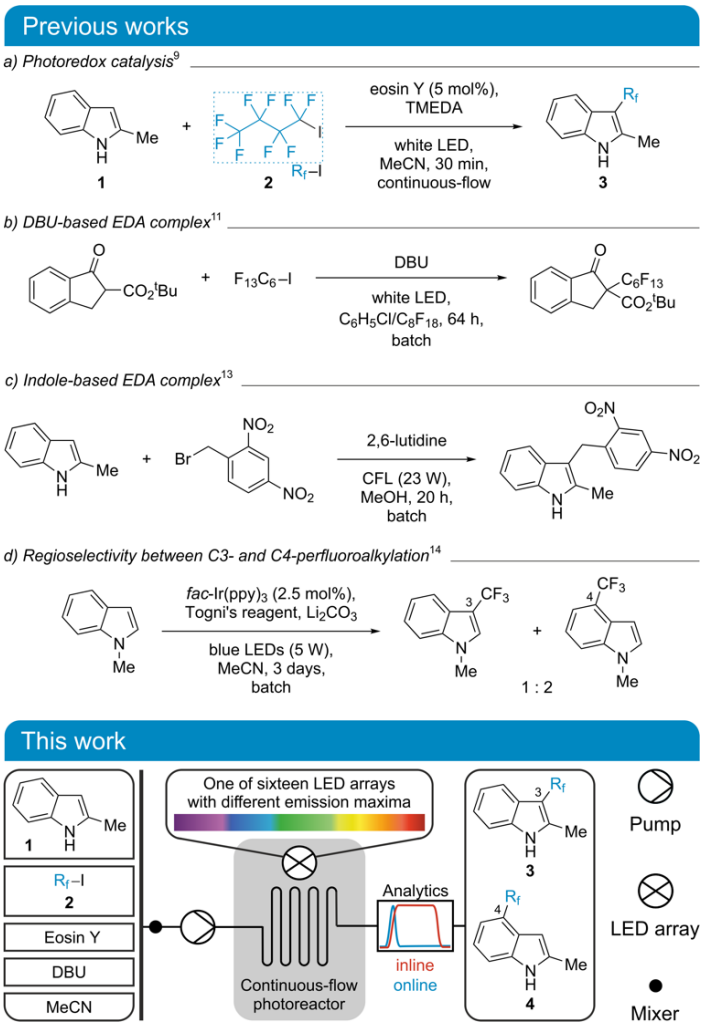

Scheme 1.1. Top: Previous works on (perfluoro)alkylations through photoredox catalysis or EDA complexes.[9–14] Bottom: Schematic experimental setup for the screening of wavelengths on the reaction of 2-methylindole (**1**) and nonafluoro-1-iodobutane (**2**) to yield a mixture of perfluoroalkylated indole regioisomers **3** and **4**.

As experimental setup (Scheme 1.1 bottom), we employed a two-dimensional continuous-flow platform.[16] The pump device in the first dimension precisely controls the flow rate in the photoreactor and enables independent mixing of all substrates and additives with acetonitrile. The online coupled HPLC system allows for the separation as well as the quantification of all reaction partners after external calibration. A detailed description of the setup and the calibration procedure as well as photographs are available in the Electronic Supplementary Information (ESI). The LED arrays and the photoreactor were designed in-house and geometrically matched such that maximum irradiation intensity as well as a high irradiation homogeneity was ensured, representing a hallmark of continuous-flow photochemistry in general.[17] The continuous-flow photoreactor was developed modularly, which allowed a facile exchange of individual components (Figure 1.1). The reaction channel (0.5 mm irradiation depth) was meandered into the reactor plate, resulting in an irradiated reactor volume of 0.85 mL. The heat generated by the LED arrays was efficiently removed by air fans and heat

sinks on the rear sides of the LED arrays and the reactor as well as between reactor and array (ESI).

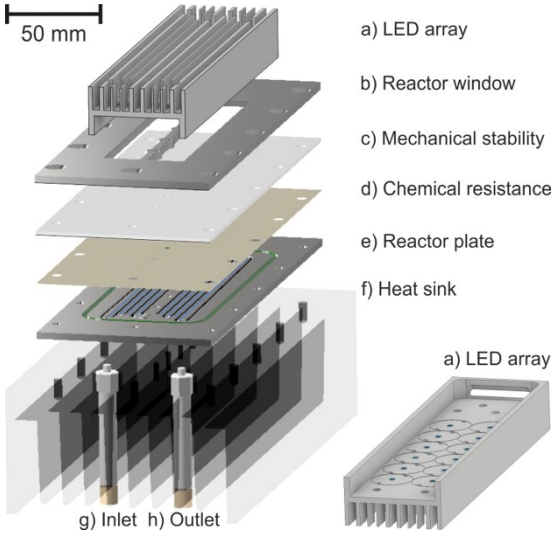

Figure 1.1. Modular design of the employed photoreactor. a) LED array housing with heat sink (aluminum); b) Reactor window (aluminum) for confinement of the irradiated area and mechanical stability; c) polymethylmethacrylate (PMMA) plate for mechanical stability of the pane; d) fluorinated ethylene propylene (FEP) polymer foil providing chemical resistance against organic solvents; e) stainless steel reactor plate; f) heat sink; g) reactor inlet; h) reactor outlet.

LED arrays were each assembled with twelve high-power LEDs (minimum 1.6 W, ESI) for sixteen different emission maxima to cover most of the visible light spectrum (350–700 nm). To match their irradiances, the reactor plate was removed and a calibrated spectroradiometer was used to record emission spectra directly behind the FEP foil. These emission spectra were integrated and the resulting power spectral densities were calibrated as a function of the applied current on the LED array. This allowed the convenient matching of all calibrated LED arrays to any irradiance in the calibrated range. A detailed protocol for the matching can be found in the ESI, where also irradiation intensity profiles over the reactor plate area are shown. To interpret the results (Figure 1.2 bottom), it is crucial to consider the widths of the emission bands after matching the irradiances (Figure 1.2 top) since a wider emission band comes with a lower intensity at the emission maximum.
As a first experiment, the work of Noël and co-workers[9] was reproduced using DBU instead of TMEDA as an amine base (Scheme 1.1a). The 521nm-LED array was applied since it had the largest overlap with the absorption spectrum of the photoredox catalyst eosin Y. Initial screenings revealed that catalyst loading as well as reaction time could be reduced significantly to achieve complete conversion (2 mol%, 4.2 min) compared to the original study where white light was employed (ESI). Our subsequent wavelength screenings were performed with even shorter reaction times (1.7 min, resulting in a conversion of 80% with the 521nm-LED array) to compare the efficiency of the different LED arrays.

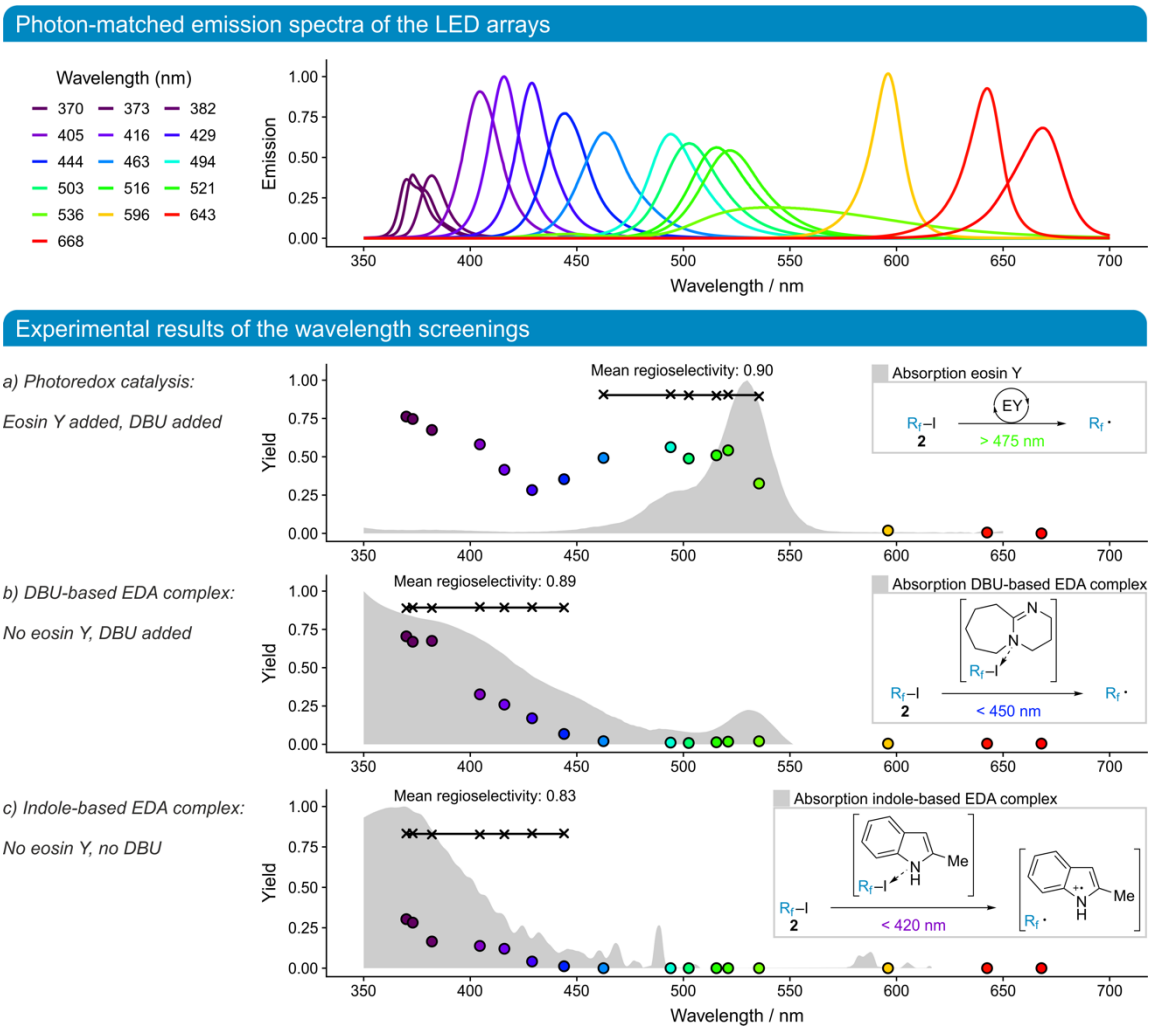

Figure 1.2. Top: Emission of the LED arrays. The light transmission of the pane decreased for wavelengths below 400 nm (ESI). To compensate for the reduced irradiance on the photoreactor (30%), the reaction time was adjusted (ESI for details). Bottom: Experimental results of the wavelength screenings under the following reaction conditions: Flow rate 0.5 mL min^{-1} (reaction time t_{react} = 1.7 min), $[\mathbf{1}]_0$ = 0.0175 mol L^{-1}, 2.0 equiv. **2**, 3.0 equiv. DBU, 2 mol% eosin Y, MeCN, ambient temperature, matched irradiances (except <400 nm, ESI). The yield of the main regioisomer **3** was calculated as [**3**] / $[\mathbf{1}]_0$. The obtained conversions showed the same trend than the here given yields.

The screening of the photoredox catalyzed reaction at wavelengths above 450 nm showed that the product yield of the main regioisomer **3** correlates with the absorption spectrum of eosin Y (Figure 1.2a). Moreover, the regioselectivity between the addition on the indole 3- and 4-position remained constant at 90% in favor of the main regioisomer **3**. At shorter wavelengths (<450 nm) the yield started to increase again, although eosin Y did not show significant absorption in this region. To validate this observation, the same screening was performed without eosin Y (Figure 1.2b). Yields for wavelengths <450 nm showed the same trend as for the screening in Figure 1.2a and became almost identical at <400 nm. Obviously, a second reaction channel was addressed wavelength-selectively that showed almost the same regioselectivity (89%) as the preceding screening. Informed by the previous studies on EDA

complexes (Scheme 1.1b and 1.1c),[10–13] a third screening was performed to determine if the underlying EDA complex is DBU- or indole-based. Therefore, the reaction was run only with the substrates 2-methylindole (**1**) and perfluorobutyl iodide (**2**) – without any bases or other additives. Surprisingly, also this reaction showed significant conversion and yield at wavelengths <420 nm, albeit to a lesser extent than in the screenings before. Moreover, the regioselectivity dropped slightly (yet significantly) to 83%.

These results reveal three different photo-initiated reaction channels of which the first two (Figure 1.2a and 1.2b) deliver the same mixture of the regioisomers **3** and **4** while the third one (Figure 1.2c) leads to a slightly different distribution. These results fit very well to the mechanisms proposed in previous studies. The photo-initiated step of the eosin Y catalyzed reaction results in a free perfluoroalkyl radical via a single electron transfer (SET) to the iodide **2** (Figure 1.2a), which then adds to the 2-methylindole (**1**) with a characteristic regioselectivity.[9] The DBU-based EDA complex also delivers free perfluoroalkyl radicals upon irradiation as evidenced by the same regioselectivity (Figure 1.2b).[11,12] Irradiation of the indole-based EDA complex, in contrast, initiates a SET between the substrate molecules **1** and **2** to a radical pair, where in a different product-determining step radical recombination within the solvent cage takes place prior to a diffusive radical separation out of the solvent cage, leading to a (slightly) different regioselectivity (Figure 1.2c).[13] The results also show that, when both electron donors for the EDA complexes are present (DBU and the indole **1**), the reaction proceeds to a major part via the DBU-based EDA complex as indicated by ^{19}F-NMR experiments (ESI). Finally, the three different reaction channels could be addressed independently under the synthetically relevant conditions of full conversion (Table 1.1). In this way, the systematic screening of irradiation wavelengths using LED arrays could. be directly translated to effect each of three ready-to-use synthetic routes towards the perfluoroalkylated indole **3**.

Table 1.1. Ready-to-use synthetic routes towards the perfluoroalkylated indoles **3** and **4**.[a]

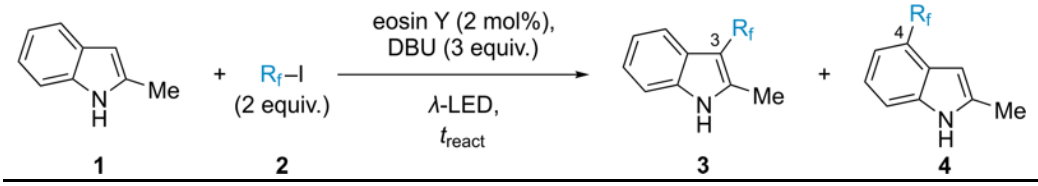

1 **2** **3** **4**

λ (nm)	t_{react} (min)	DBU	Eosin Y	Reaction channel	Yield (%)[c]	Regioselectivity (%)[d]
521	4.2	✓	✓	*a) Photoredox catalysis*	71	90
370[b]	7.1	✓	–	*b) DBU-based EDA complex*	70	89
370[b]	85	–	–	*c) Indole-based EDA complex*	70	83

[a] Conditions: $[\mathbf{1}]_0 = 0.0175$ mol L^{-1}, MeCN, ambient temperature, full conversion. [b] Due to the absorption of the polymer pane, the irradiance was only 30% of that at 521 nm. [c] Yield of the main regioisomer **3**, calculated as [**3**] / $[\mathbf{1}]_0$. [d] Calculated as [**3**] / ([**3**] + [**4**]).

1.2 Conclusions

This study underscores the necessity of wavelength-resolved reaction development in synthetic photochemistry, since light sources with discrete emission bands are essential to trigger discrete photochemical processes. By applying a systematic light source screening with matched irradiances, the reaction outcome can be directly attributed to the irradiated wavelength without interference from differing irradiances. Especially systems with multiple chromophores, such as by the formation of EDA complexes, should be subjected to this type of analysis, because the reactivity of a system under white light irradiation cannot necessarily be attributed exclusively to the reactivity of its photo-catalyst. While the systematic screening of other reaction parameters like solvents, concentrations, reaction times, and substrates is well established in the literature, a routine screening of irradiation wavelengths and intensities is still lacking. The technological advances in LED technology, however, make this analysis affordable and applicable in most synthetic labs. We therefore believe that the presented methodology will play a significant role for photochemical synthesis in the future.

1.3 Supporting Information

1.3.1 General experimental information

All chemicals were received from Sigma–Aldrich (St. Louis, MO) in a purity of at least 98% and were used without further purification. Eosin Y was offered only with a purity of >75% and was bought in its acidic form (CAS number 15086-94-9). Acetonitrile (HiPerSolv CHROMANORM for HPLC) was purchased from VWR Chemicals (Darmstadt, Germany) and water was obtained from a Milli–Q gradient purification system (Millipore, Bedford, MA). The ^{1}H NMR (500 MHz) and ^{13}C NMR (125 MHz) spectra were recorded at ambient temperature on a Bruker Avance 500 NMR spectrometer. ^{19}F NMR spectra (282 MHz) were recorded on a Bruker Avance 300 NMR spectrometer. The chemical shifts are reported in parts per million (ppm) relative to the solvents DMSO-d_6 (^{1}H NMR 2.50 ppm; ^{13}C NMR 39.52 ppm) and $PhCF_3$ (^{19}F NMR −63.2 ppm). Multiplicities are reported using the following abbreviations: s (singlet), d (doublet), t (triplet), m (multiplet).

1.3.2 Two-dimensional reaction–analysis setup

The two-dimensional flow platform, described in detail previously,[S1] was adapted to the test reaction between 2-methylindole (**1**) and nonafluoro-1-iodobutane (**2**) such that the two substrates (**1**, **2**) as well as the amine base 1,8-diazabicyclo[5.4.0]undec-7-ene (DBU) and the photoredox catalyst eosin Y could be mixed independently with acetonitrile. The pump assembly was composed of two HPLC pumps providing five independent channels to precisely control the flow rate on the photoreactor and the starting concentrations of each reactant. Between the pumps and the photoreactor, a back-pressure regulator (adjusted to 50 bar) was mounted to ensure noise-free operation of the HPLC pumps. On the reactor, no back-pressure was applied. Behind the reactor, a 2-position/6-port valve with an injection loop was mounted, which transferred an injection volume of 1.3 µL to an online coupled HPLC system. An inline diode array detector (DAD) was used to verify when the reactor was operating in steady-state. All parts of the system could be programmed depending on the experiment time so that parameter adjustments as well as sampling for the HPLC proceeded fully automated. Scheme 1.S1 illustrates the flow path of the setup.

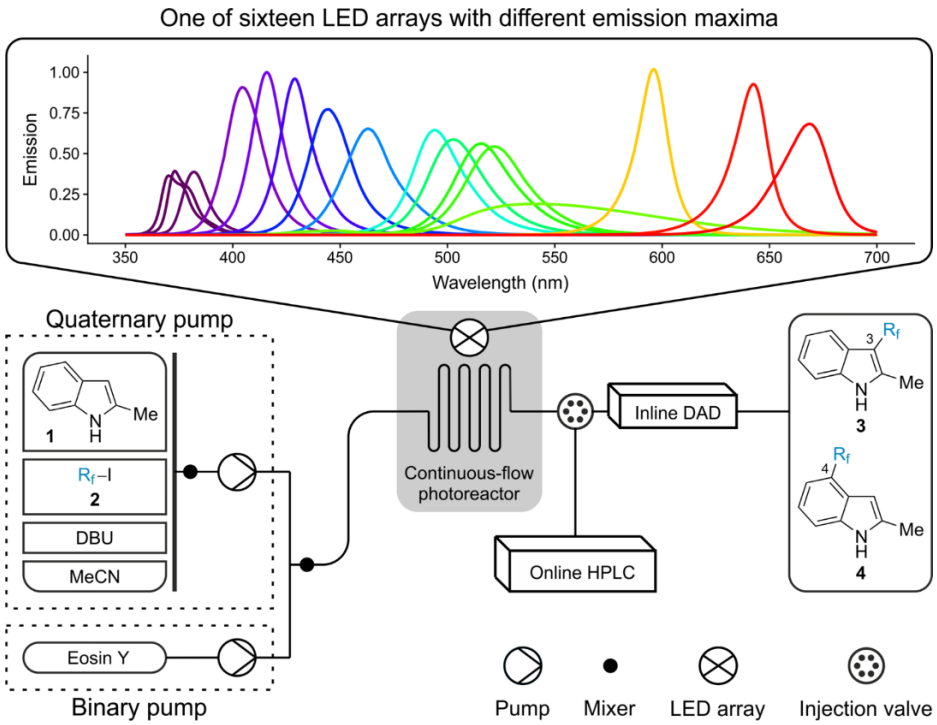

Scheme 1.S1. Flow path of the employed setup and the 16 different irradiance-matched emission spectra of the LED arrays used for the systematic wavelength screenings. R_f–I labels according to the main text the perfluoroalkylated butyl iodide **2**.

A photograph of the employed system (without photoreactor) is shown in Figure 1.S1.. All incorporated hardware components have been received from Agilent Technologies (Santa Clara, CA).

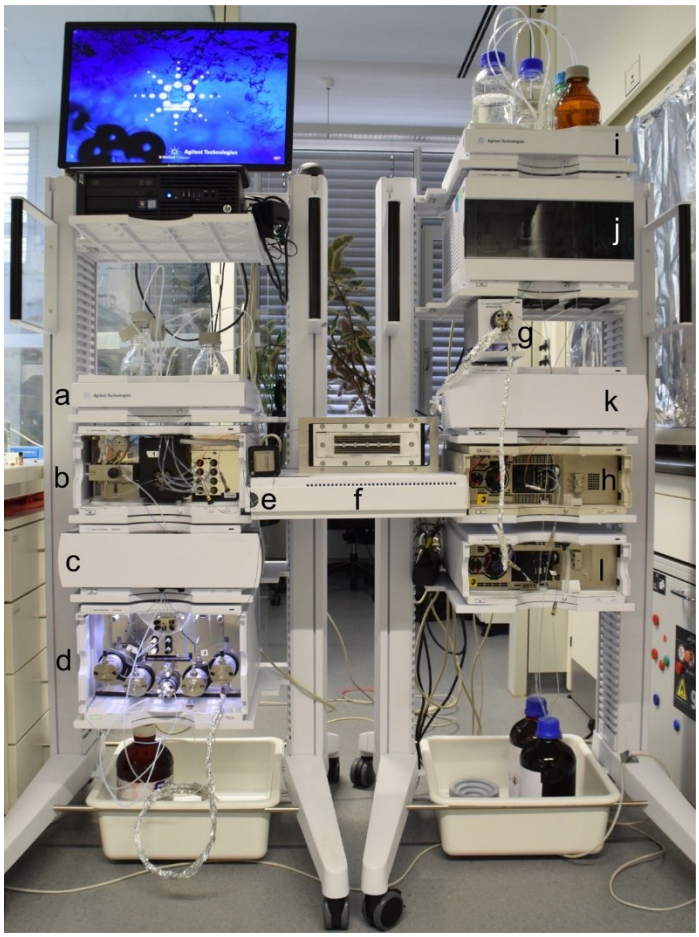

Figure 1.S1. Reaction: a) Substrate solutions; b) quaternary pump (Agilent 1260 Infinity Series, G1311B); c) thermostatted HPLC column compartment (Agilent 1290 Infinity Series, G1316C); d) binary pump (Agilent 1290 Infinity Series, G4220A); e) Jet Weaver V35 Mixer; f) photoreactor; g) 2-position/6-port valve (Agilent 1290er Series, G1170A); h) inline DAD (Agilent 1200 Series, G1315C). HPLC analysis: i) Eluents; j) binary pump (Agilent 1290 Infinity Series, G4220A); k) thermostatted HPLC column compartment (Agilent 1290 Infinity Series, G1316C) with separation column; l) DAD (Agilent 1290 Infinity Series, G4212A).

The chromatographic separation process of the online coupled analytical HPLC system was optimized such that all reactants, additives, products, and side products were baseline-separated in the shortest possible analysis time. Therefore, the separation was performed at 25 °C on a monolithic separation column (C18 Chromolith High Resolution; RP 18-e, 100–4.6 mm) from Merck KGaA (Darmstadt, Germany) with water and acetonitrile (+ 0.1% trifluoroacetic acid) as eluents. Table 1.S1. summarizes the gradient developed for the specific separation problem, resulting in analytical cycles of 14 minutes.

Table 1.S1. Gradient developed for the online coupled HPLC system. The flow rate remained constant at 2 mL min^{-1}.

Time (min)	Water (%)	Acetonitrile (%)
0.00*	80	20
5.00	55	45
7.00	40	60
10.00	40	60
10.90	0	100
12.40	0	100
12.41	80	20
14.00*	80	20

*Injection

However, the separation of the regioisomeric products **3** and **4** remained a challenge, since they persistently coeluted on C18 reversed-phase columns (see further below for more details). A typical chromatogram is shown in Figure 1.S1 with the signals of interest assigned.

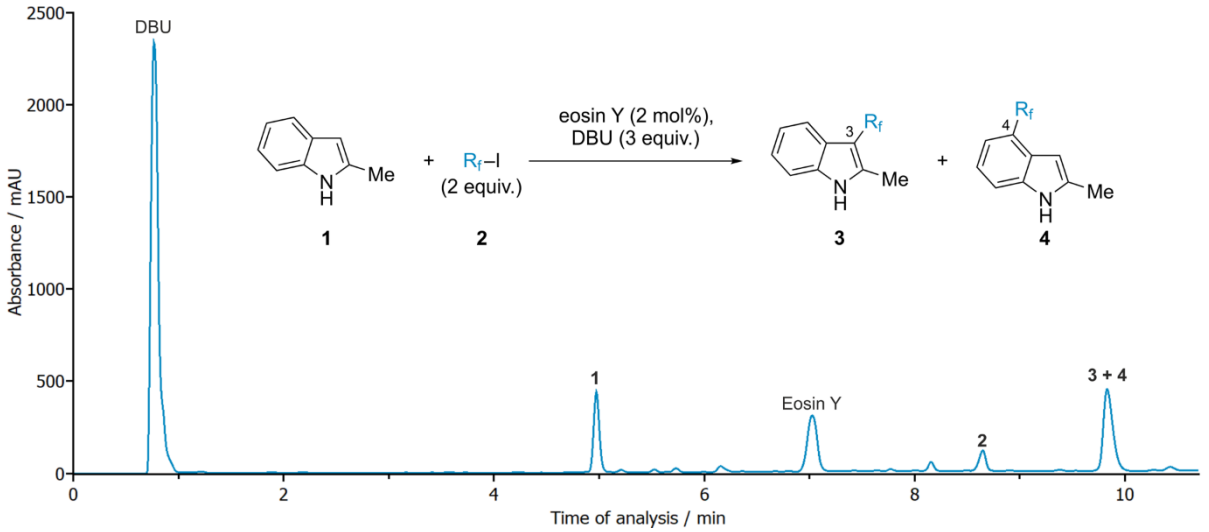

Figure 1.S1. Typical chromatogram obtained at the detection wavelength of 243 nm.

To use the online coupled HPLC system for quantification, it was programmed to calibrate itself fully automized for the two substrates and the product. Therefore, a solution with a known concentration of the respective substrate or product was placed in the first dimension and the system was programmed to mix it in different volumetric ratios with acetonitrile. Programmed switches of the injection valve delivered concentration-dependent HPLC signals in the second dimension using the gradient described in Table 1.S1.. The calibration curves of the substrates 2-methylindole (**1**) and nonafluoro-1-iodobutane (**2**) showed linear behavior in the calibrated

range (illustrated in Figure 1.S2 and 1.S4). These calibration curves also confirm the precision and the high reproducibility of the system, since all ten single-point analyses for each calibration laid almost perfectly on a straight line.

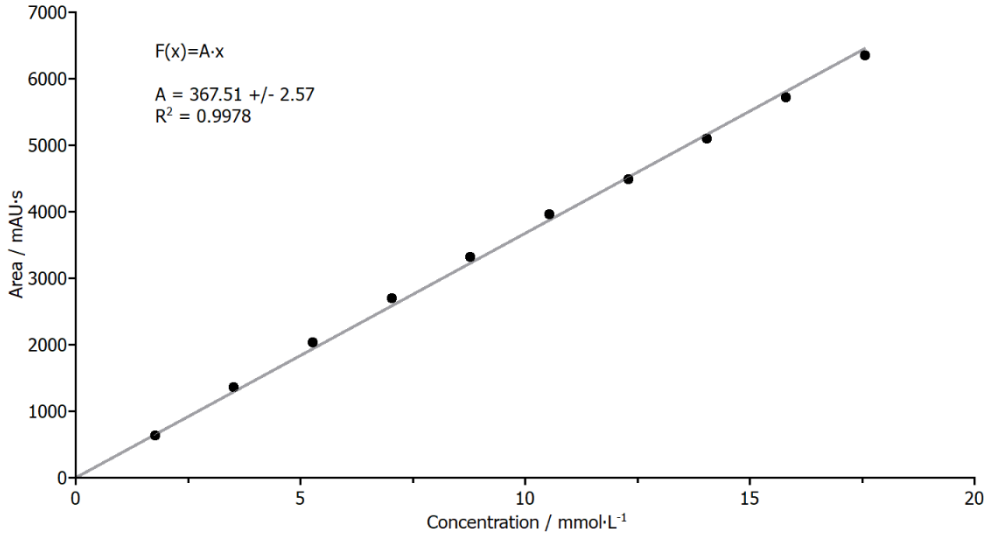

Figure 1.S2. Calibration curve of the substrate 2-methylindole (**1**) at the detection wavelength of 243 nm.

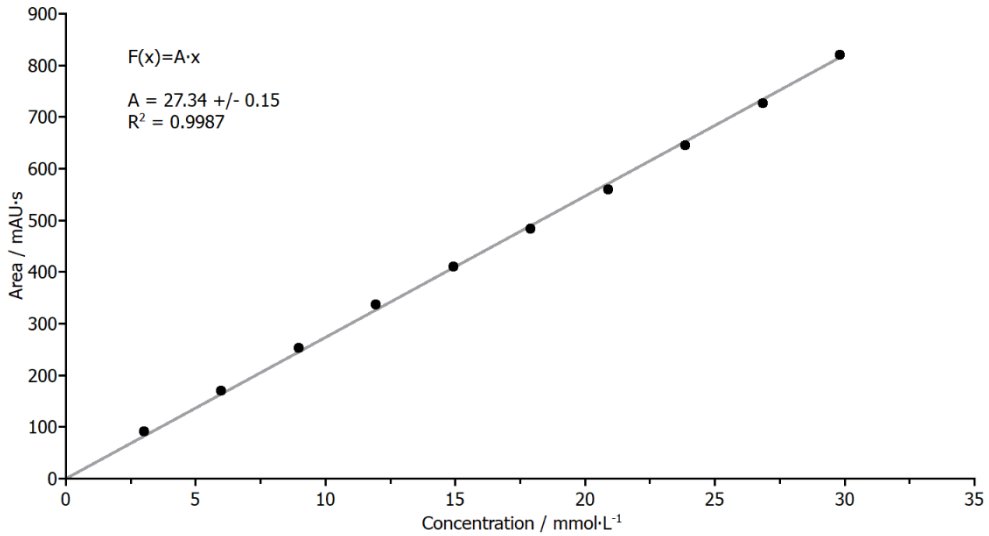

Figure 1.S3. Calibration curve of the substrate nonafluoro-1-iodobutane (**2**) at the detection wavelength of 260 nm.

Since the regioisomeric products **3** and **4** were not separated in the chromatographic process, a new concept for their quantification was used based on the significantly different UV-Vis absorption spectra shown in Figure 1.S4.

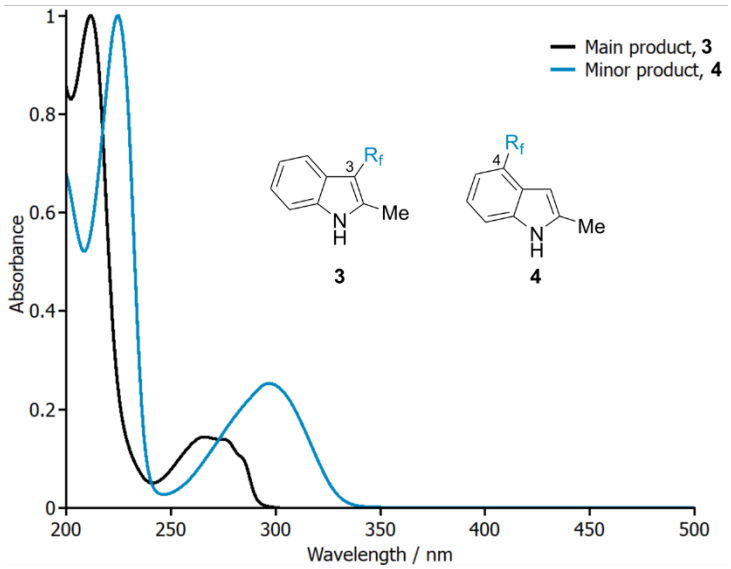

Figure 1.S4. UV-Vis spectra of the regioisomeric perfluorobutylated indoles **3** and **4**.

Quantification is based on the bathochromic shift of the 4-perfluorobutylated indole **4** compared to its regioisomer **3**. Differently composed mixtures of **3** and **4** were calibrated at two different wavelengths, 243 nm and 322 nm. At 322 nm the regioisomer **4** was calibrated in the same manner as the substrates **1** and **2**, since the regioisomer **3** did not show any absorbance at this detection wavelength. The resulting calibration curve is shown in Figure 1.S5.

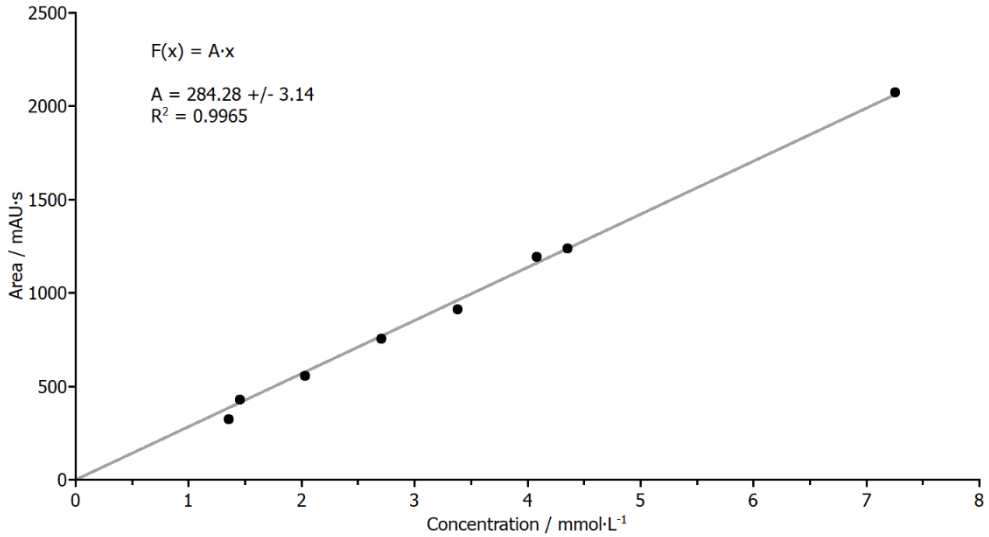

Figure 1.S5. Calibration curve of the 4-perfluorobutylated indole **4** at a detection wavelength of 322 nm.

The calibration at 243 nm (where both regioisomers absorb light) was performed for different molar ratios of **3** and **4**. The fraction of the HPLC signal belonging to the absorbance of regioisomer **3** could be calculated via equations using the defined different molar ratios. The resulting calibration curve of the 3-perfluorobutylated indole **3** is shown in Figure 1.S6.

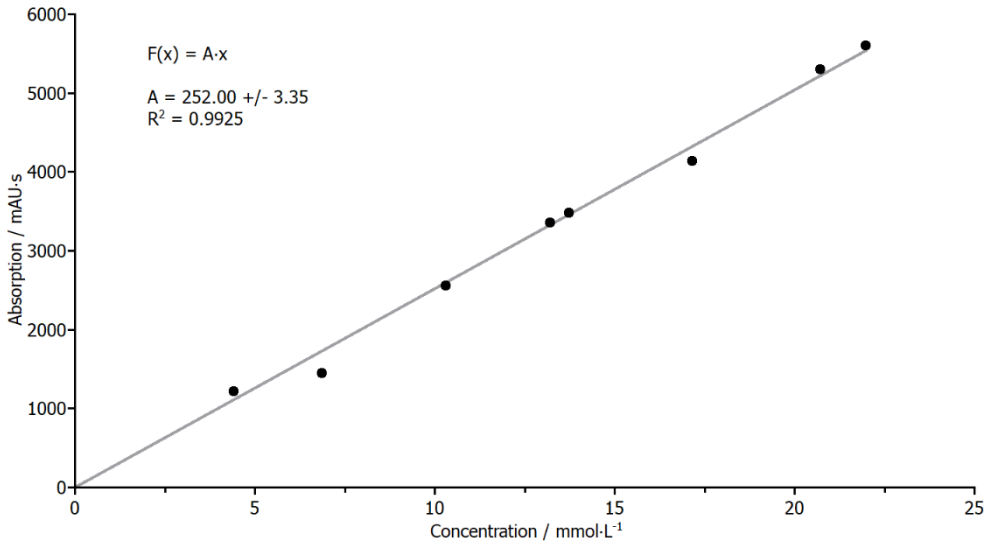

Figure 1.S6. Calibration curve of the 3-perfluorobutylated indole **3** at a detection wavelength of 243 nm.

This calibration allowed to determine unknown concentrations of the regioisomers **3** and **4** via HPLC analysis only by detecting at two different wavelengths (i.e., at 322 nm to determine the concentration of **4** and at 243 nm to determine the concentration of **3** with the concentration of **4** already known), even though the regioisomers could not be separated with the HPLC column.

1.3.3 Photoreactor design

To enable the matching procedure with a spectroradiometer (not possible in tubing photoreactors), a planar photoreactor was designed in-house with geometrically aligned LED array housings. Figure 1.S7 illustrates the modular setup of the reactor. The plates (b–e), which are screwed together, have dimensions of 230 mm length and 90 mm width and thicknesses as given in Figure 1.S7. The reactor window was made of aluminium to provide mechanical stability and confine the irradiated area of the reactor to dimensions of 140 mm length and 40 mm width, with a brace in the middle for added stability. The LED array housing was aligned such that it was seated on the window edges and all LEDs were inside the notched area.

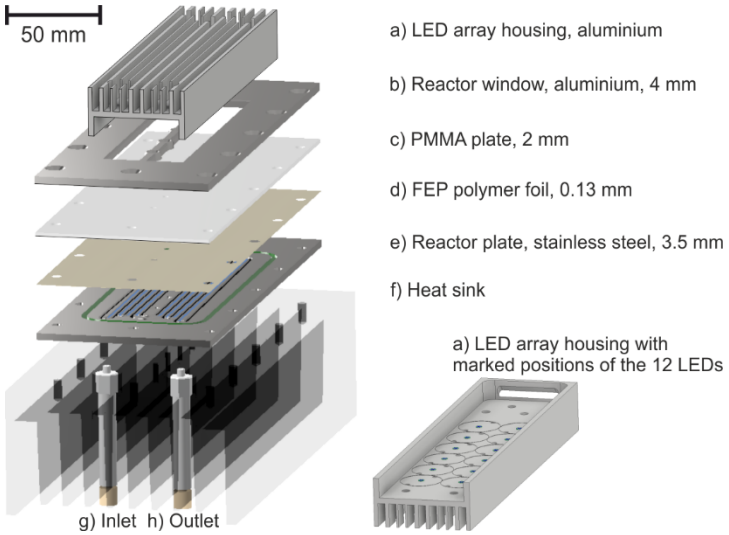

Figure 1.S7. Modularly designed flow photoreactor: a) LED array housing made of aluminium with an integrated heat sink on the rear side; b) reactor window for confinement of the irradiated area and mechanical stability; c) polymethylmethacrylate (PMMA) plate for mechanical stability of the pane; d) fluorinated ethylene propylene (FEP) polymer foil providing chemical resistance against organic solvents; e) stainless steel reactor plate; f) heat sink; g) reactor inlet; h) reactor outlet.

To guarantee highest possible transmission of the window pane combined with a high mechanical stability as well as high chemical resistance, a combination of a thicker polymethylmethacrylate (PMMA) plate and a thinner fluorinated ethylene propylene (FEP) polymer foil (KELUX Kunststoffe GmbH, Geldern, Germany) was assembled. This unique setup delivered a high mechanical stability (PMMA plate) combined with chemical resistance against organic solvents (FEP foil). The transmission of this polymer pane was ~80% for wavelengths >400 nm due to the careful adjustment of the thicknesses of the polymer layers. However, for wavelengths <400 nm the transmission of the pane dropped significantly as shown in Figure 1.S8.

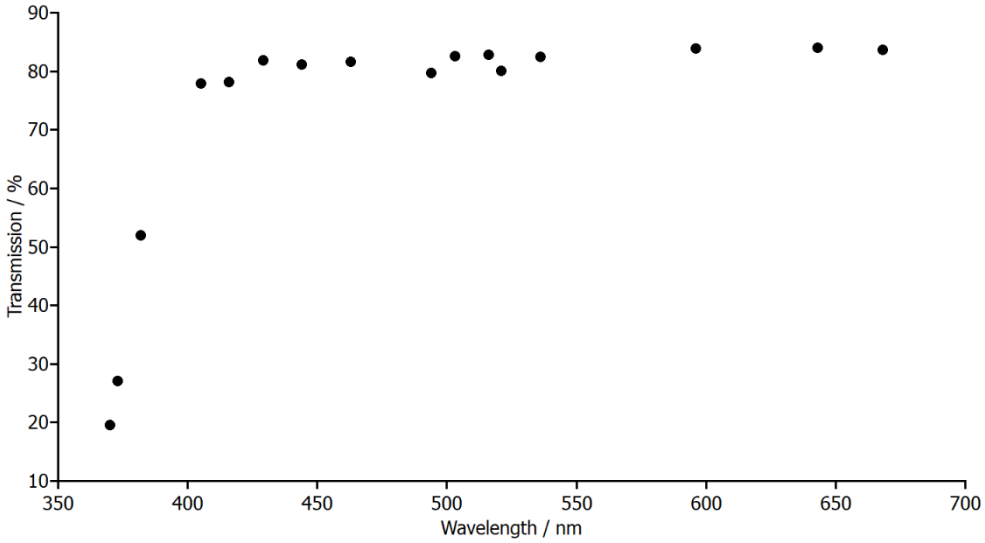

Figure 1.S8. Transmission profile of the polymer layers (2 mm PMMA and 0.13 mm FEP) used as window pane under irradiation of the 16 employed LED arrays.

The heat sink (0.5 K W^{-1}, ABL Components, Birmingham, UK) was fixed on the rear side of the reactor with a heat conduction foil (SFT80-0.15, 0.2 K W^{-1}, AMEC Thermasol, Norfolk, UK) placed between reactor plate and heat sink. With this setup, the maximum measured temperature increase directly behind the photoreactor was ~1 °C using the 370nm-array at maximum current (700 mA). Inlet and outlet of the reactor were equipped with standardized threads to make them compatible with HPLC tubings and fittings. Photographs of the final setup are shown in Figure 1.S9 with the LED array placed on top of the photoflow reactor.

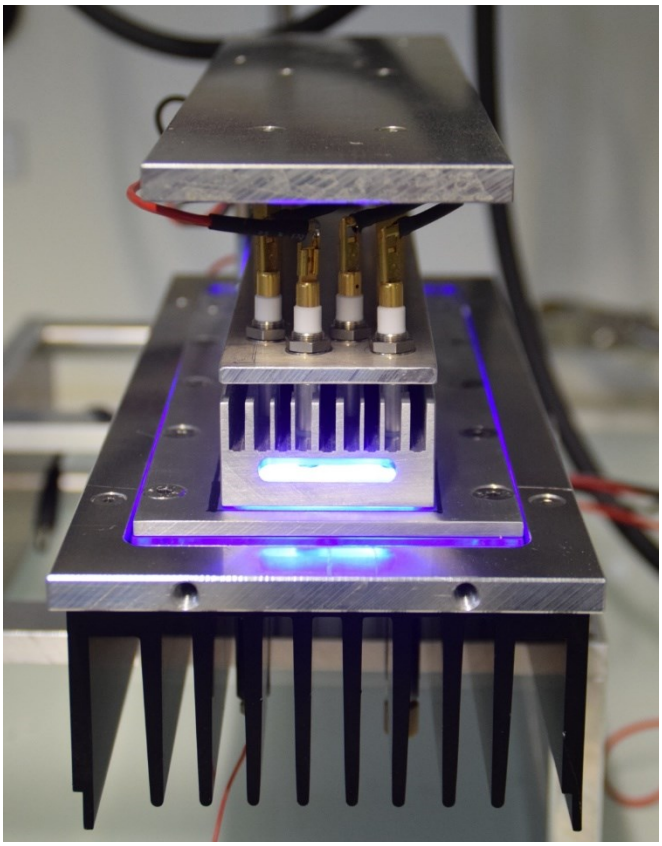

Figure 1.S9. Photograph of the reactor setup ready-to-go.

The centerpiece of this setup was the reactor plate, into which a channel (1.5 mm width and 0.5 mm depth) was milled covering the whole reactor window. Sealing (fluoroelastomer FPM) was purchased from Arcus (Seevetal, Germany) and fixed also between reaction channels to prevent shortcutting between them. A technical drawing with relevant dimensions is given in Figure 1.S10.

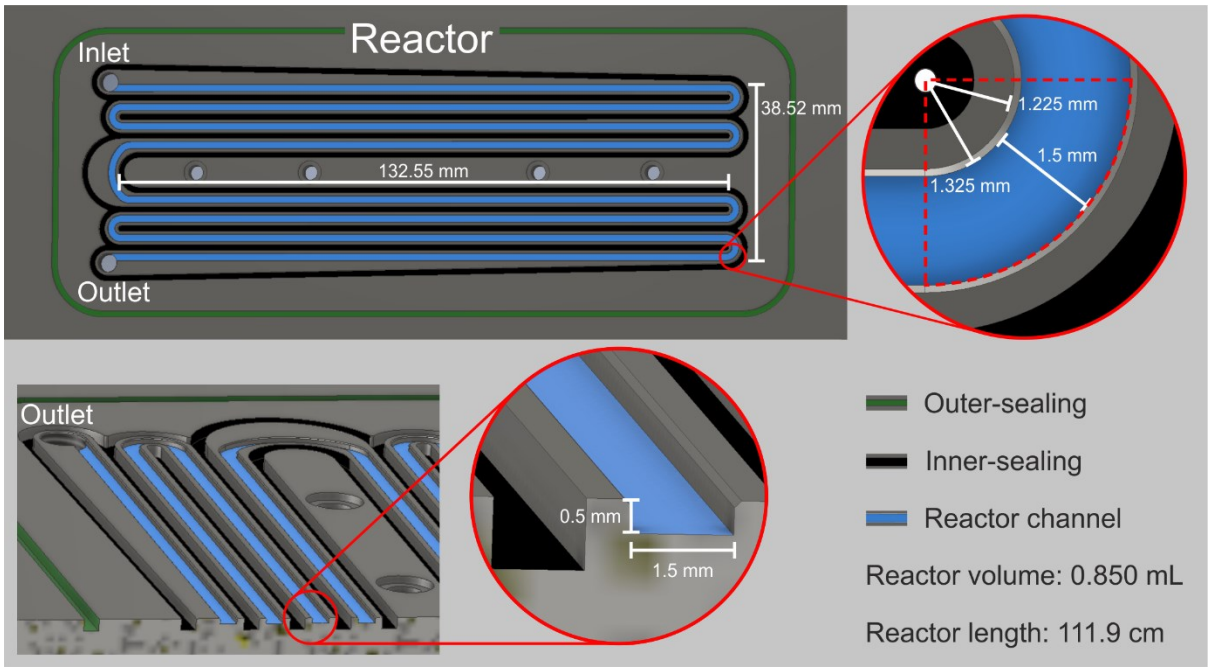

Figure 1.S10. Technical drawing of the reactor plate.

The reactor volume was calculated by adding the irradiated volumes of the different geometrical elements, resulting in a volume of 0.85 mL. A photograph of the reactor plate with the milled channels colored according to Figure 1.S10 is shown in Figure 1.S11 together with a top view onto the closed reactor.

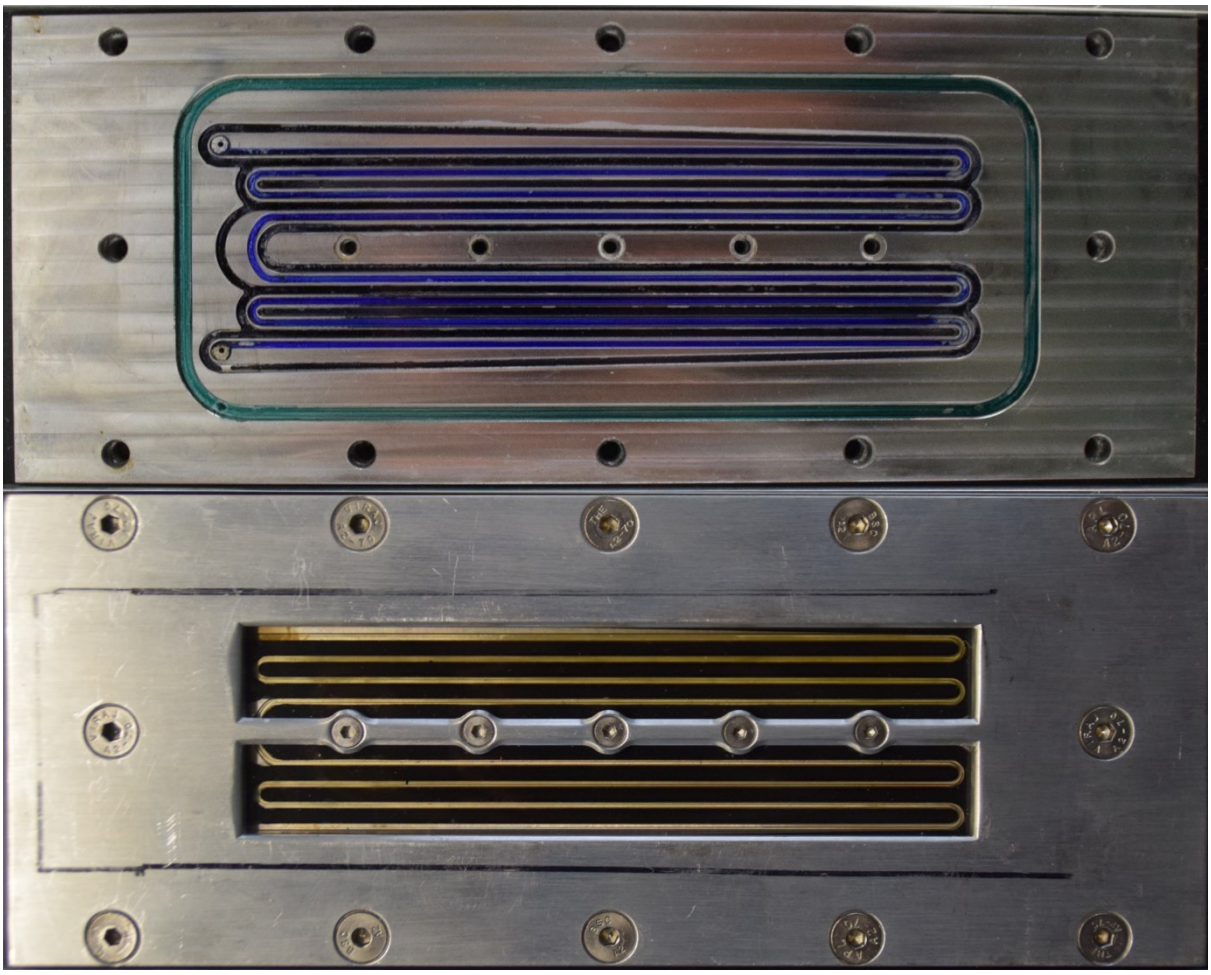

Figure 1.S11. Top: Photograph of the reactor plate. Milled channels are colored according to Figure 1.S10. Bottom: On top view onto the closed reactor.

The housing for the LED arrays was designed based on the reactor window. The electrical connectors were developed in a plug-and-play style so that the arrays could easily be exchanged. Figure 1.S12 shows two photographs of the setup, including the radial fans which directed the air streams on the front and the rear side of the arrays. Cooling of the LED arrays turned out to be crucial to minimize wavelength shifts of the LEDs due to overheating and to make the screening reproducible.

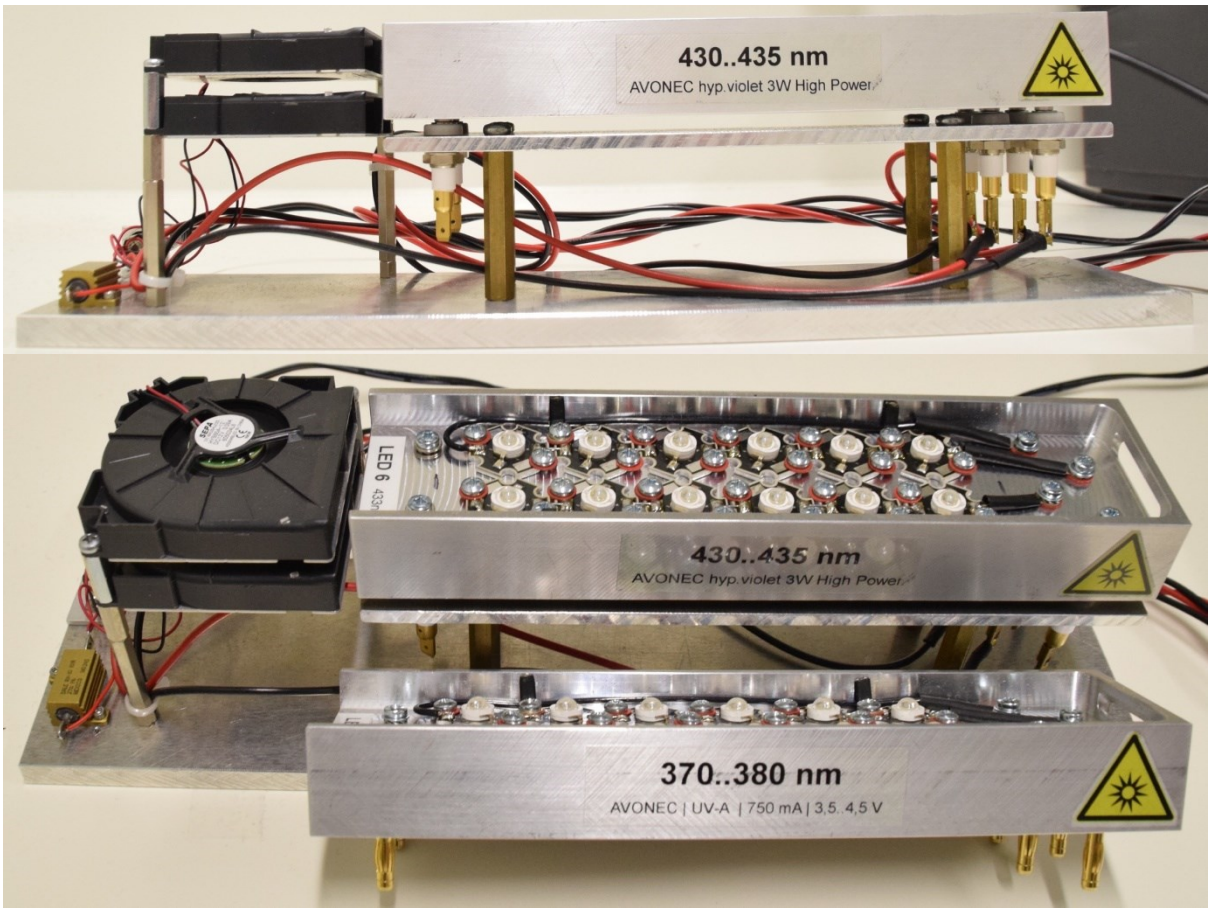

Figure 1.S12. Photographs of the LED setup with radial fans fixed in front of the array.

1.3.4 Irradiance-matching of the LED arrays

LED arrays were assembled for 16 different emission maxima λ aiming to cover most of the visible light spectrum. Each LED array consisted of twelve high-power LEDs of which six each were serially connected in two parallel strings connected to an adjustable power supply with two channels (35 V, 4 A, EX354RT, Aim-TTi, Huntingdon, UK). Table 1.S1 summarizes information about the single LEDs.

Table 1.S1. Employed LEDs which were assembled into LED arrays.

λ (nm)	Power[a] (W)	Product name	Vendor	Costs[b] (€)
370	5.00	Roschwege Star-UV365-05-00-00	Conrad[c]	104.00
373	3.00	3 W High Power LED 370nm–380nm	Avonec[d]	6.05
385	3.00	3 W High Power LED 380nm–390nm	Avonec	4.65
405	3.00	Roschwege Star-UV405-03-00-00	Conrad	18.73
416	3.00	3 W High Power LED 410nm–420nm	Avonec	2.40
429	3.00	3 W High Power LED 430nm–435nm	Avonec	1.85
444	2.17	ILH-OW01-DEBL-SC211-WIR200	RS Components[e]	7.45
463	2.17	ILH-OW01-BLUE-SC211-WIR200	RS Components	6.47
494	3.00	3 W High Power LED 490nm–495nm	Avonec	2.33
503	2.24	ILH-GD01-VEGR-SC201	RS Components	7.01
516	3.00	3 W High Power LED 515nm–525nm	Avonec	1.44
521	2.17	ILH-OW01-TRGR-SC211	RS Components	7.81
536	1.92	ILH-LC01-MINT-SC201-WIR200	RS Components	9.96
596	1.61	ILH-OW01-YELL-SC211-WIR200	RS Components	7.09
643	1.62	ILH-GD01-RED1-SC201	RS Components	4.78
668	1.62	ILH-GD01-HYRE-SC201	RS Components	7.88

[a] Maximal electrical power specified by the vendor. [b] Costs per LED. [c] Conrad Electronic SE (Hirschau, Germany). [d] Avonec (Essen, Germany). [e] RS Components (Corby, UK).

For the irradiance-matching of the 16 LED arrays, a calibrated spectroradiometer PS–200 (Apogee Instruments, Logan, UT) was acquired. Spectroradiometers are calibrated in a specified wavelength range to measure spectral output in absolute units like the photon flux density (in µmol m^{-2} s^{-1} nm^{-1}). Recorded emission spectra can be integrated over a certain area

of wavelengths to obtain a measure of the irradiance, i.e., the power spectral density (PSD, in µmol m^{-2} s^{-1}). For the matching of the irradiances, the PSDs of the LED arrays were calibrated as a function of the applied current adjusted by the power supply. To detect only the photons that pass the reactor window, the reactor plate was removed and the spectroradiometer was placed directly behind the FEP foil. As a first measurement, the area of the reactor window was segmented into squares with 8 mm edge length (according to the outer diameter of the spectroradiometer's detector) to investigate irradiation homogeneity. The window length (140 mm, x coordinate) was divided into 17 segments and the window width (40 mm, y coordinate) into 8 segments. Figure 1.S13 illustrates the irradiation intensity profile over the reactor grid for the 596nm-array, highlighting intensity variations by a factor >2 over the reactor area.

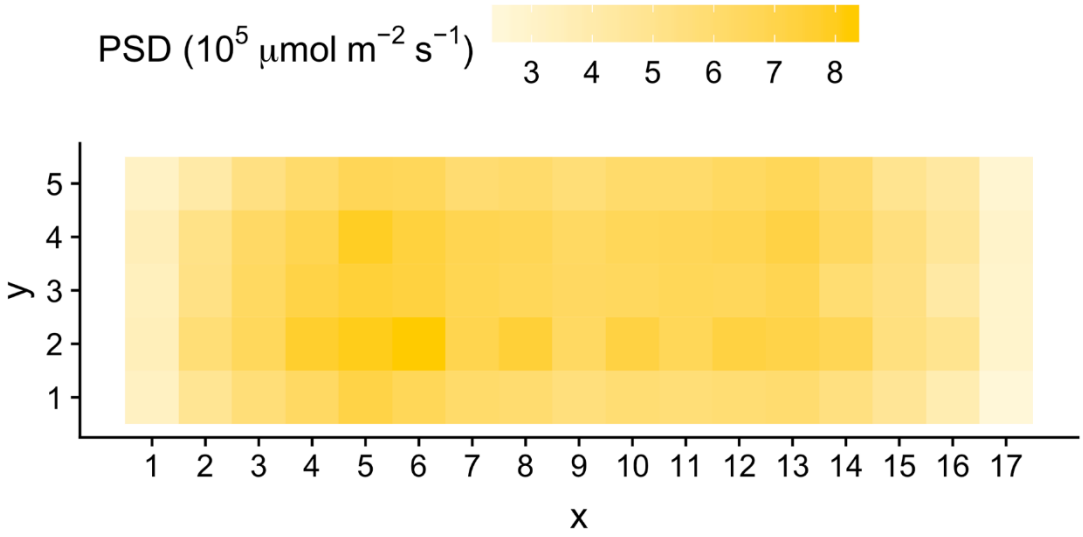

Figure 1.S13. Irradiation intensity profile over the reactor area using the 596nm-array at a current of 700 mA.

Considering the nonuniform intensity profile, ten measurement points were distributed over the segmented grid. Moreover, ten control points were introduced where the matching of the LED arrays could be confirmed. Figure 1.S14 shows the measurement and the control points on the reactor window grid.

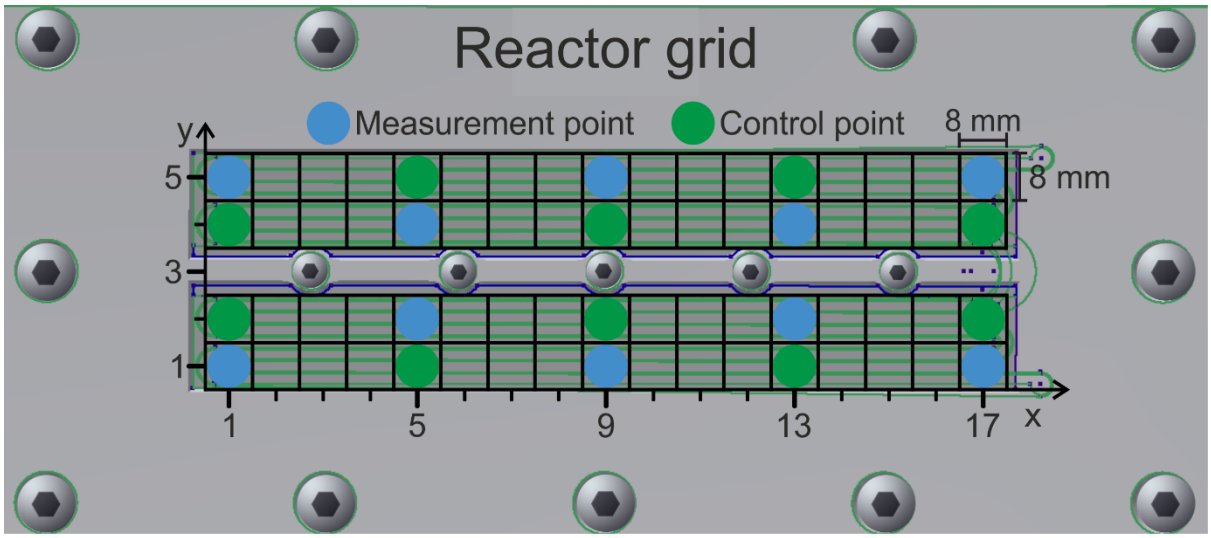

Figure 1.S14. Position of the measurement and control points on the reactor grid for the matching of the LED arrays.

To gate the measurement and control points precisely and highly reproducible with the spectroradiometer, scaffolds were 3D-printed using an Ultimaker 2+ (Ultimaker, Utrecht, The Netherlands). Figure 1.S15 shows the scaffold for the measurement points and for the control points considering that the detector itself had an outer diameter of 31.5 mm while the light collecting area only had a diameter of 8 mm.

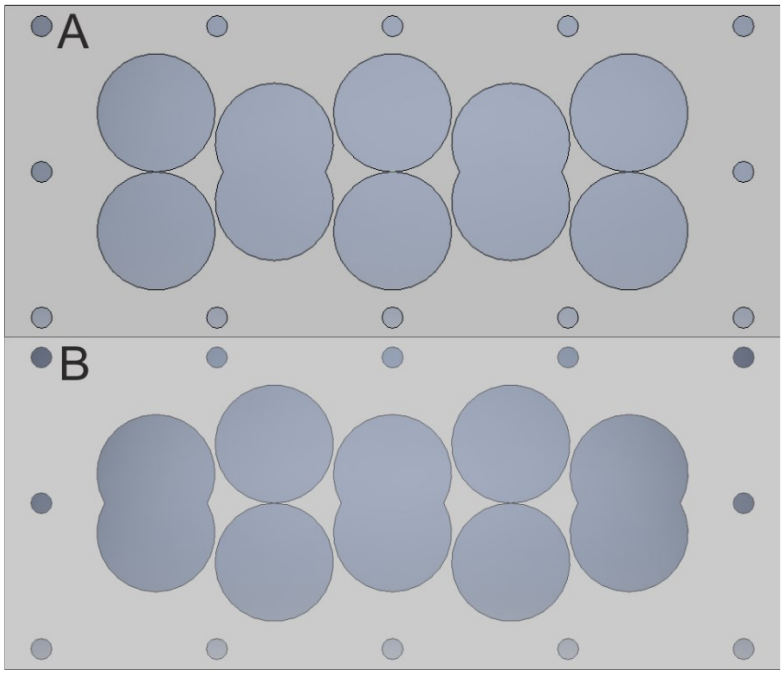

Figure 1.S15. Scaffolds to precisely locate the measurements of irradiances. A: Measurement points. B: Control points.

The scaffolds could be screwed directly onto the FEP foil and the detector of the spectroradiometer fitted exactly to the holes. Figure 1.S16 shows a photograph of the final matching setup.

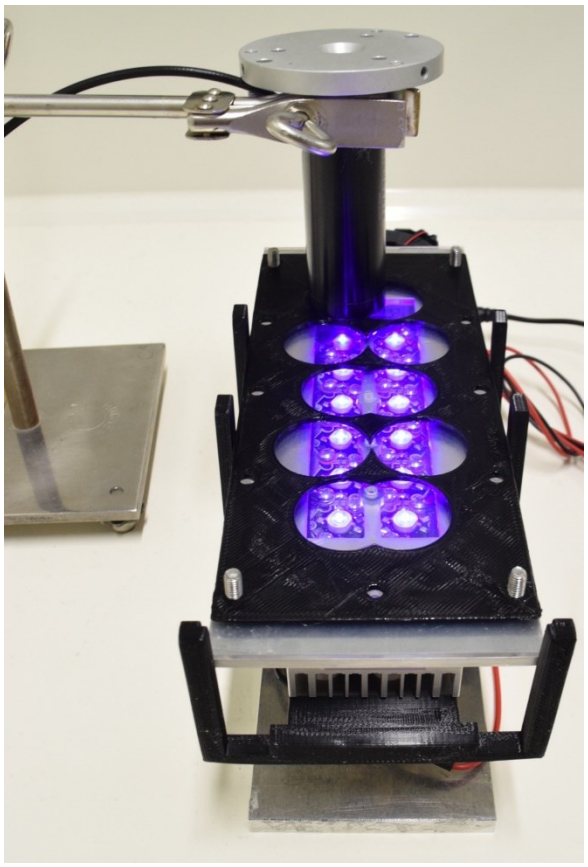

Figure 1.S16. Photograph of the final matching setup with the spectroradiometer fixed directly on the FEP foil and positioned by the 3D-printed scaffold.

To match the LED arrays conveniently to any desired irradiance, the PSD of the arrays was calibrated as a function of the applied current. Therefore, the PSDs of all ten measurement points were added and the summed PSD value was plotted against the applied current. As an example, Figure 1.S17B illustrates the calibration curve for the 569nm-array, fitted by a fifth-grade polynomial. The normalized emission spectrum of the array is shown in Figure 1.S17A.

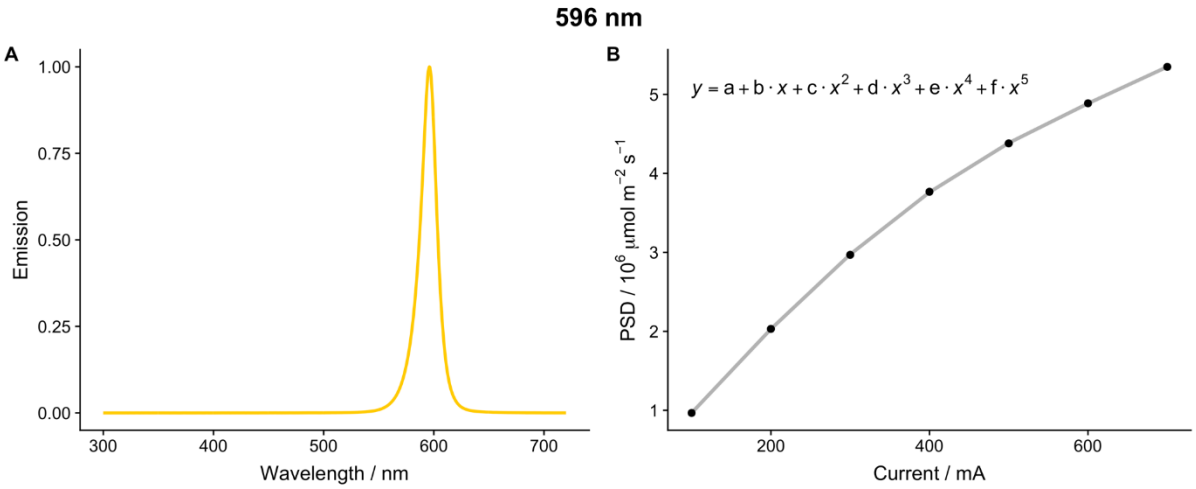

Figure 1.S17. A: Normalized emission spectrum of the 596nm-array; B: Calibration curve for the sum of the ten PSDs recorded at the measurement points as a function of the applied current.

This calibration procedure was carried out for all LED arrays with an emission maximum >400 nm. Of these 13 LED arrays, the 596nm-array exhibited the lowest irradiance at maximum current (700 mA). Thus, the other 12 LED arrays were matched to the maximum PSD value of this array. The currents *I* needed to match the irradiance of the arrays could be conveniently calculated from the calibration curves. To validate this approach of matching, the irradiances at the control points of all LED arrays with the matching current *I* applied were measured and compared to the 596nm-array. The deviations are summarized in Table 1.S2. With a maximum deviation of only 2% in the summed PSD values, the accuracy of the method was verified to prove that all LED arrays irradiate almost the same amount of photons per time on the reactor area.

Table 1.S2. Deviations of the summed PSDs of the control points compared to the 596nm-array.

λ (nm)	I (mA)	Deviation (%)
405	277	2
416	216	2
429	182	< 1
444	177	1
463	185	< 1
494	137	1
503	174	< 1
516	159	1
521	174	< 1
536	168	2
596	700	—
643	249	< 1
668	328	< 1

Due to the observation of another wavelength-selective reaction channel at wavelengths <450 nm (see main text, Figure 1.2), we decided to acquire three more LED arrays with emission maxima <400 nm. However, the combination of the PMMA plate and the FEP foil used as a pane for the window (Figure 1.S7) exhibited significantly decreasing transmissions for light near the UV-A spectrum (Figure 1.S8). Since the high irradiances of the high-power LEDs provided the advantages of very short reaction times and high process efficiencies, we decided to not push down the irradiance of all LED arrays by a factor ~3 but instead perform a new matching. The procedure of the calibration process was adapted from the one described above. The three LED arrays were matched to the irradiance of the 373nm-array, which showed the lowest irradiance at maximum current. This value was only ~30% of the matched irradiance above. Therefore, also the 405 nm array was matched to this lower intensity and the reaction time was adjusted such that the reaction with the 405nm-array showed the same conversion and yield as above (7.1 min reaction time instead of 1.7 min above). For the screenings in the main text (Figure 1.2) the prolonged reaction times were used for the three LED arrays with emission maxima <400 nm. Table 1.S3 summarizes the deviation of the matching recorded on the control points.

Table 1.S3. Deviations of the summed PSDs of the control points compared to the 373nm-array.

λ (nm)	I (mA)	Deviation (%)
370	385	1
373	700	—
382	461	< 3
405	82	< 2

1.3.5 Reaction time screening

As described in the main text, the work of Noël and co-workers was reproduced using DBU instead of TMEDA as an amine base (Scheme 1.1a, main text).[S2] Due to the here employed high irradiance of the 521nm-array, which irradiates directly into the absorption band of eosin Y, the catalyst loading could be reduced to 2 mol%. With this catalyst loading, the reaction provides reasonable conversions in short reaction times. Figure 1.S18 illustrates the results of the reaction time screening, which decided over the reaction conditions for the subsequent wavelength screenings

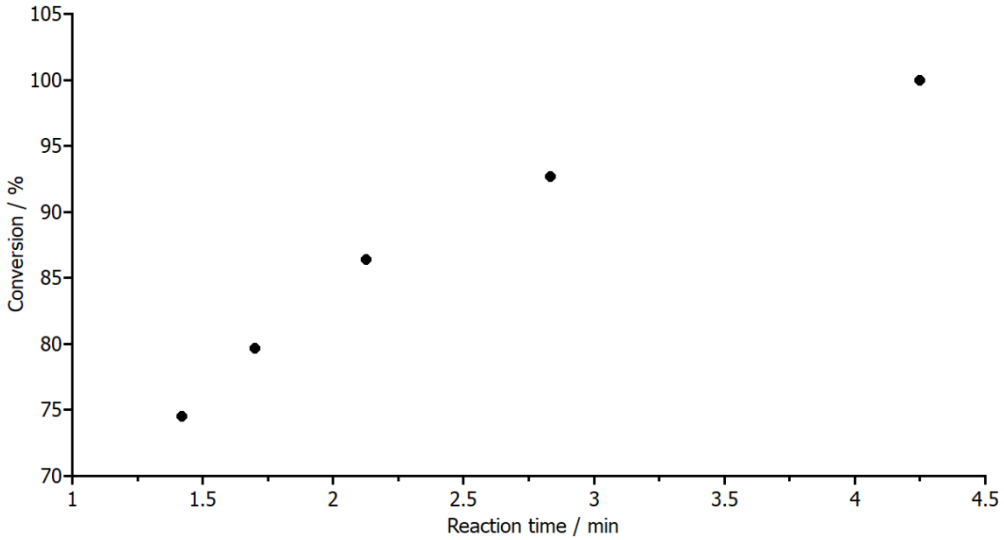

Figure 1.S18. Reaction time screening under the following reaction conditions: $[\mathbf{1}]_0 = 0.0175$ mol L^{-1}, 2.0 equiv. **2**, 3.0 equiv. DBU, 2 mol% eosin Y, MeCN, ambient temperature, irradiance-matched 521nm-array.

During the reaction time (Figure 1.S18) and wavelength screenings (Figure 1.2, main text), we observed an issue already described by Noël and co-workers, that is, the use of DBU led to black, non-transparent reaction solutions at long reaction times.[S2] This issue could be overcome by utilizing the reaction channel via the EDA complex between the substrates **1** and **2** which, however, came at the price of longer reaction times (Table 1.1, main text).

1.3.6 Offline NMR analysis

Since it was not possible to separate the single regioisomers **3** and **4** from each other (neither by flash chromatography nor by preparative RP chromatography), a mixture of regioisomers was isolated. In this mixture, the molecular ion peak was found using mass spectrometry (HRMS, ESI^+, m/z calculated for $C_{13}H_7F_9N$ $[M]^+$: 348.0440; m/z found: 348.0443). Nuclear magnetic resonance (NMR) spectroscopy was used to determine the exact chemical structure of the substances. Besides one-dimensional NMR experiments (^1H, ^{13}C, ^{19}F), the two-dimensional NMR experiments DQF-COSY, HSQC, and HMBC were used for structural elucidation. Due to the two signal sets visible in the spectra, all meaningful signals were assigned by their according atom number (Scheme 1.S2).

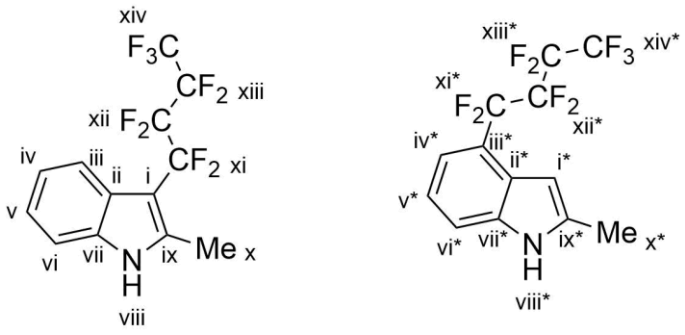

3 **4**

Scheme 1.S2. Regioisomeric perfluoroalkylated indoles **3** and **4** with enumberated atoms. The positions in the minor product **4** are marked with an asterisk.

The NMR signals of the main product **3** were found to be in good agreement with the previous report.[S2] All signals were assigned according to Scheme 1.S2.

<u>1-methyl-3-(perfluorobutyl)-1*H*-indole (**3**):</u>

^1H NMR (500 MHz, DMSO-d_6) δ = 11.87 (s, 1H, H_{viii}), 7.45 (d, J = 7.9 Hz, 1H, H_{iii}), 7.42–7.38 (m, 1H, H_{vi}), 7.17–7.13 (m, 1H, H_v), 7.11–7.06 (m, 1H, H_{iv}), 2.47 (m, 3H, H_x).

^{13}C NMR (125 MHz, DMSO-d_6) δ = 138.8 (t, J = 4.9 Hz, C_{ix}), 134.8 (s, C_{vii}), 125.6 (t, J = 3.5 Hz, C_{ii}), 121.7 (s, C_v), 120.7 (s, C_{iv}), 118.1 (s, C_{iii}), 111.5 (s, C_{vi}), 97.5 (t, J = 27.3 Hz, C_i), 12.3 (s, C_x).

^{19}F NMR (282 MHz, DMSO-d_6) δ = −82.6 (m, 3F, F_{xiv}), −105.3 (m, 2F, F_{xi}), −124.8 (m, 2F, F_{xii}), −127.6 (m, 2F, F_{xiii}).

<u>1-methyl-4-(perfluorobutyl)-1*H*-indole (**4**):</u>

^1H NMR (500 MHz, DMSO-d_6) δ = 11.44 (s, 1H, H_{viii*}), 7.57 (d, J = 7.8 Hz, 1H, H_{vi*}), 7.23–7.17 (m, 2H, H_{iv*}, H_{v*}), 6.22 (s, 1H, H_{i*}), 2.42 (s, 3H, H_{x*}).

^{13}C NMR (125 MHz, DMSO-d_6) δ = 138.6 (s, C_{ix*}), 136.7 (s, C_{vii*}), 125.8 (t, J = 3.4 Hz, C_{ii*}), 119.4 (s, C_{v*}), 118.1 (s, C_{iv*}), 116.6 (C_{iii*}, from HMBC), 114.9 (s, C_{vi*}), 98.3 (s, C_{i*}), 13.2 (s, C_{x*}).

^{19}F NMR (282 MHz, DMSO-d_6) δ = −82.6 (m, 3F, F_{xiv*}), −110.0 (m, 2F, F_{xi*}), −124.2* (m, 2F, F_{xii*}), −127.4* (m, 2F, F_{xiii*}).

C_{iii*} of the minor product **4** could not be found in the ^{13}C NMR spectrum, which is due to the low sensitivity of the method combined with the ^{2}J coupling to the fluorine atoms splitting the signal into a triplet. However, a HMBC cross peak to H_{v*} could be found to assign a chemical shift to the signal. In the NMR spectra, moreover, traces of another regioisomer could be found. The signal intensities, though, were too low to elucidate its structure. The NMR spectra with assigned signals are attached. Thereafter, the ^{19}F-NMR experiments are presented which were used to characterize the EDA complexes.

^{1}H NMR

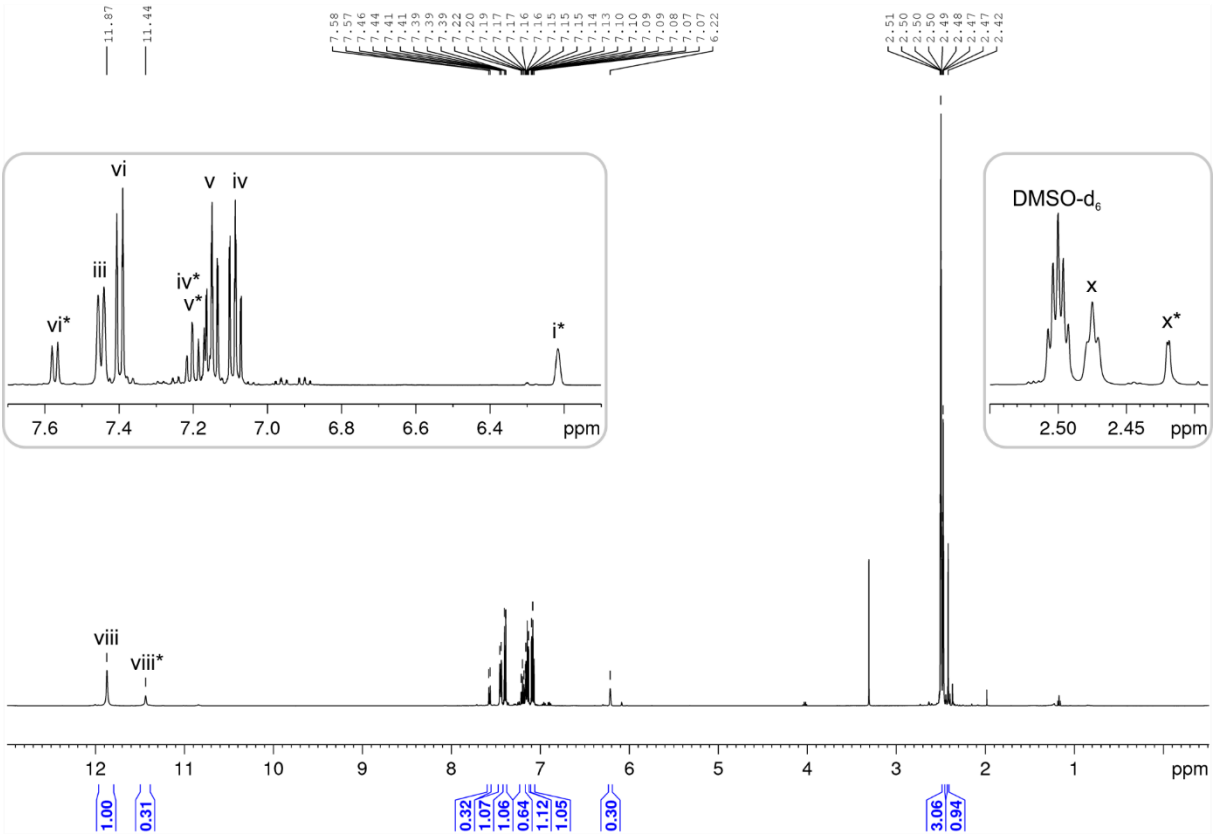

^{13}C NMR

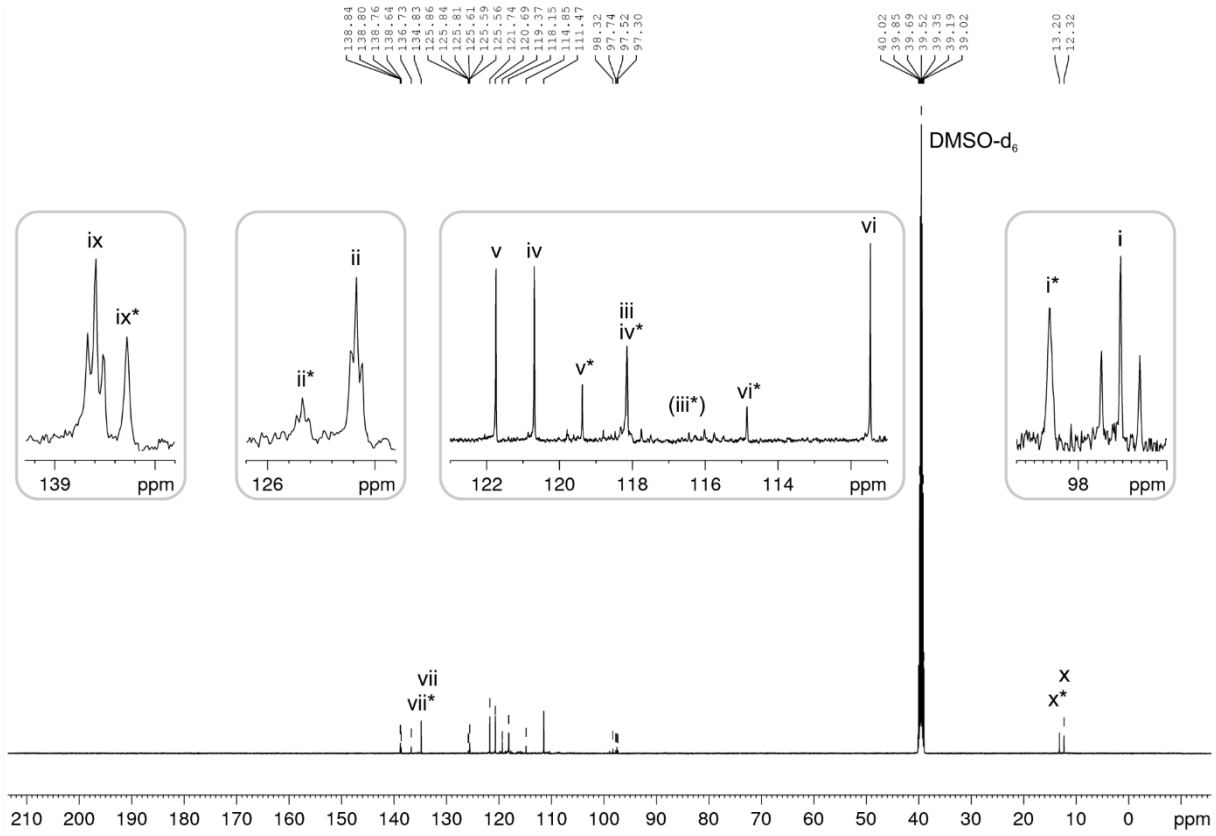

^{19}F NMR

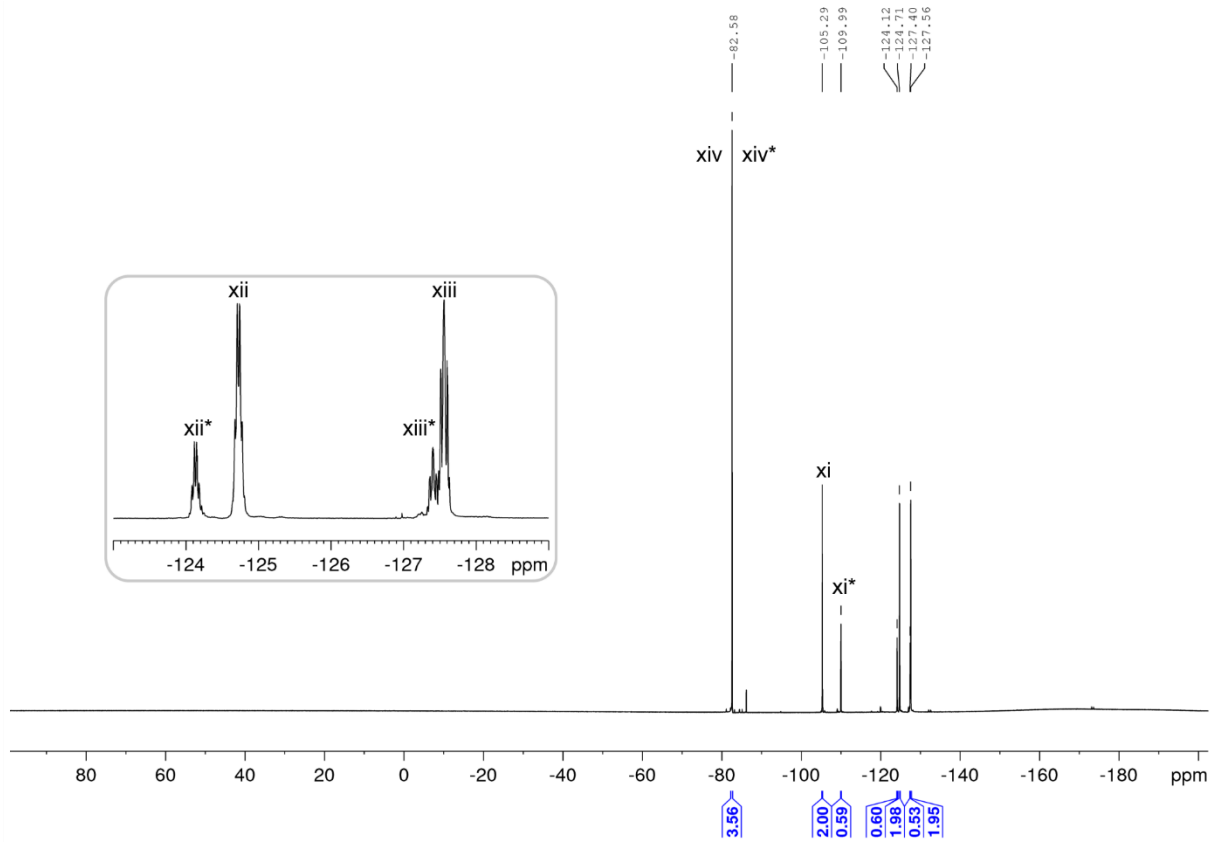

DQF-COSY

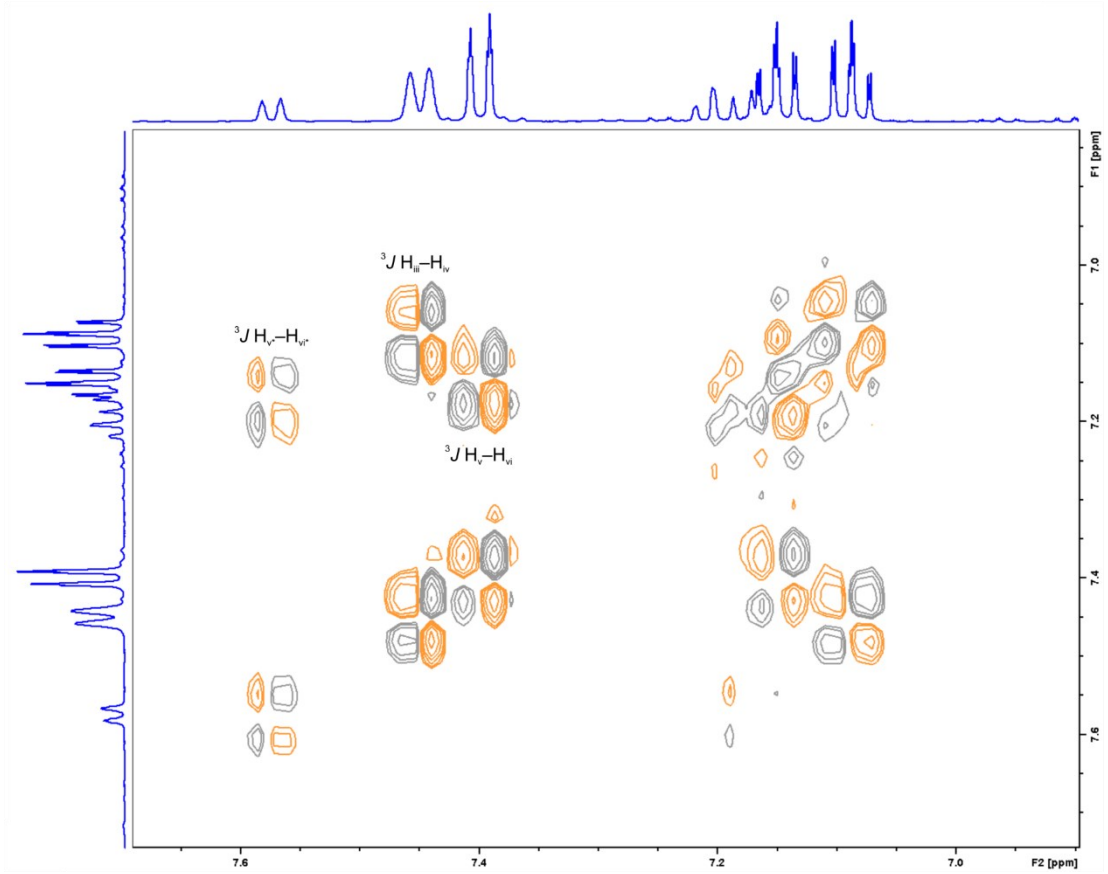

HSQC

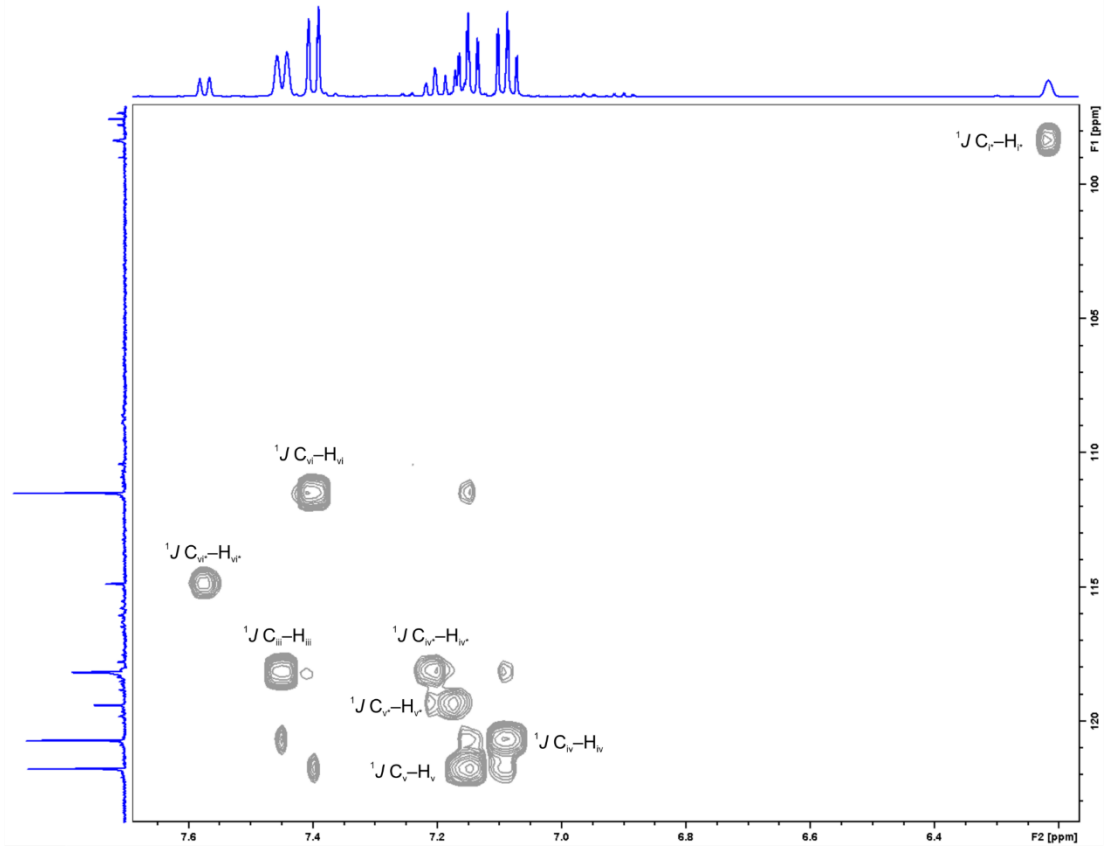

HMBC

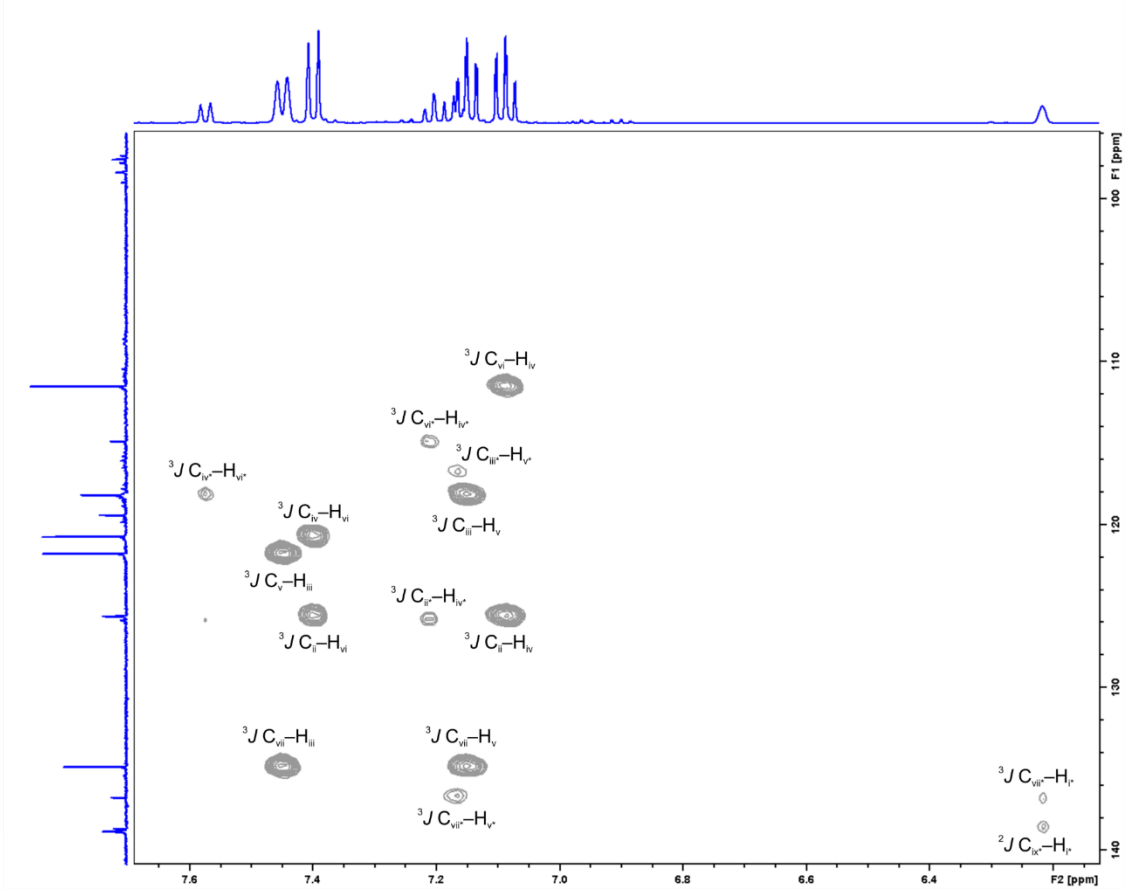
F1 [ppm]
100
110
120
130
140
F2 [ppm]
7.6
7.4
7.2
7.0
6.8
6.6
6.4
$^3J\ C_{vi}–H_{iv}$
$^3J\ C_{vi*}–H_{iv*}$
$^3J\ C_{iii*}–H_{v*}$
$^3J\ C_{iv*}–H_{vi*}$
$^3J\ C_{iv}–H_{vi}$
$^3J\ C_{iii}–H_{v}$
$^3J\ C_{v}–H_{iii}$
$^3J\ C_{ix*}–H_{iv*}$
$^3J\ C_{ii}–H_{vi}$
$^3J\ C_{ii}–H_{iv}$
$^3J\ C_{vii}–H_{iii}$
$^3J\ C_{vii}–H_{v}$
$^3J\ C_{vii*}–H_{v*}$
$^3J\ C_{vii*}–H_{i*}$
$^2J\ C_{ix*}–H_{i*}$

To characterize the EDA complexes of this work, ^{19}F-NMR experiments were performed in the actual synthetic environment, i.e., with the given standard conenctrations in acetonitrile. (Trifluoromethyl)benzene ($PhCF_3$) was added as internal standard. The results show, that the displacement of the chemical shift of the CF_2-group next to the iodide (marked blue) of the DBU-based EDA complex is much bigger than the displacement of the indole-based EDA complex, which is only very little. If both electron donors (indole and DBU) are present in the solution, the displacement is very similar to the DBU-based EDA complex which means that the DBU-EDA complex is almost exclusively present in the reaction solution.

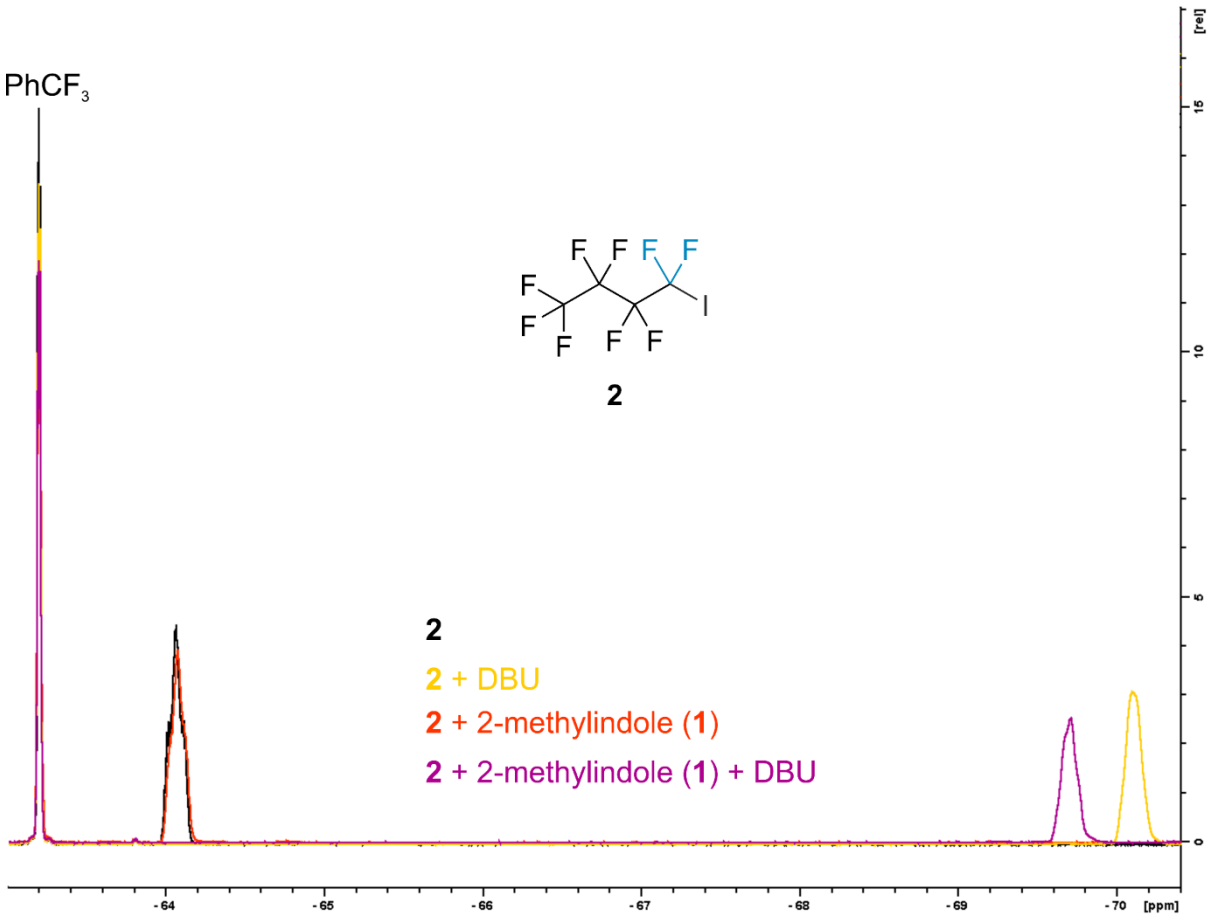

1.4 References

1 H. Frisch, D. E. Marschner, A. S. Goldmann and C. Barner-Kowollik, *Angew. Chem. Int. Ed.*, 2018, **57**, 2036–2045; *Angew. Chem.*, 2018, **130**, 2054–2064.

2 L. Buzzetti, G. E. M. Crisenza and P. Melchiorre, *Angew. Chem. Int. Ed.*, 2019, **58**, 3730–3747; *Angew. Chem.*, 2019, **131**, 3768–3786.

3 (*a*) I. Ghosh, R. S. Shaikh and B. König, *Angew. Chem. Int. Ed.*, 2017, **56**, 8544–8549; *Angew. Chem.*, 2017, **129**, 8664–8669. (*b*) M. Marchini, G. Bergamini, P. G. Cozzi, P. Ceroni and V. Balzani, *Angew. Chem. Int. Ed.*, 2017, **56**, 12820–12821; *Angew. Chem.*, 2017, **129**, 12996–12997. (*c*) I. Ghosh, J. I. Bardagi and B. König, *Angew. Chem. Int. Ed.*, 2017, **56**, 12822–12824; *Angew. Chem.*, 2017, **129**, 12998–13000.

4 (*a*) I. Ghosh and B. König, *Angew. Chem. Int. Ed.*, 2016, **55**, 7676–7679; *Angew. Chem.*, 2016, **128**, 7806–7810. (*b*) S. Protti, D. Ravelli and M. Fagnoni, *Photochem. Photobiol. Sci.*, 2019, DOI 10.1039/c8pp00512e.

5 (*a*) S. Tschierlei, M. Karnahl, M. Presselt, B. Dietzek, J. Guthmuller, L. González, M. Schmitt, S. Rau and J. Popp, *Angew. Chem. Int. Ed.*, 2010, **49**, 3981–3984; *Angew. Chem.*, 2010, **122**, 4073–4076. (*b*) D. E. Fast, A. Lauer, J. P. Menzel, A. M. Kelterer, G. Gescheidt and C. Barner-Kowollik, *Macromolecules*, 2017, **50**, 1815–1823. (*c*) B. T. Tuten, J. P. Menzel, K. Pahnke, J. P. Blinco and C. Barner-Kowollik, *Chem. Commun.*, 2017, **53**, 4501–4504. (*d*) K. C. Harper, E. G. Moschetta, S. V. Bordawekar and S. J. Wittenberger, *ACS Cent. Sci.*, 2019, **5**, 109–115.

6 (*a*) Y. Chen, O. de Frutos, C. Mateos, J. A. Rincon, D. Cantillo and C. O. Kappe, *ChemPhotoChem*, 2018, **2**, 906–912. (*b*) C. Rosso, J. D. Williams, G. Filippini, M. Prato and C. O. Kappe, *Org. Lett.*, 2019, **21**, 5341–5345.

7 (*a*) D. Cambié, F. Zhao, V. Hessel, M. G. Debije and T. Noël, *Angew. Chem. Int. Ed.*, 2017, **56**, 1050–1054; *Angew. Chem.*, 2017, **129**, 1070–1074. (*b*) D. Cambié, J. Dobbelaar, P. Riente, J. Vanderspikken, C. Shen, P. H. Seeberger, K. Gilmore, M. G. Debije and T. Noël, *Angew. Chem. Int. Ed.*, 2019, DOI 10.1002/anie.201908553.

8 S. Barata-Vallejo, S. M. Bonesi and A. Postigo, *Org. Biomol. Chem.*, 2015, **13**, 11153–11183.

9 N. Straathof, D. Osch, A. Schouten, X. Wang, J. Schouten, V. Hessel and T. Noël, *J. Flow Chem.*, 2014, **4**, 12–17.

10 E. Arceo, I. D. Jurberg, A. Álvarez-Fernández and P. Melchiorre, *Nat. Chem.*, 2013, **5**, 750–756.

11 Ł. Woźniak, J. J. Murphy and P. Melchiorre, *J. Am. Chem. Soc.*, 2015, **137**, 5678–5681.

12 Y. Wang, J. Wang, G. X. Li, G. He and G. Chen, *Org. Lett.*, 2017, **19**, 1442–1445.

13 S. R. Kandukuri, A. Bahamonde, I. Chatterjee, I. D. Jurberg, E. C. Escudero-Adán and P. Melchiorre, *Angew. Chem. Int. Ed.*, 2015, **54**, 1485–1489; *Angew. Chem.*, 2015, **127**, 1505–1509.

14 G. L. Gao, C. Yang and W. Xia, *Chem. Commun.*, 2017, **53**, 1041–1044.

15 C. Bottecchia, R. Martín, I. Abdiaj, E. Crovini, J. Alcazar, J. Orduna, M. J. Blesa, J. R. Carrillo, P. Prieto and T. Noël, *Adv. Synth. Catal.*, 2019, **361**, 945–950.

16 C. P. Haas, T. Müllner, R. Kohns, D. Enke and U. Tallarek, *React. Chem. Eng.*, 2017, **2**, 498–511.

17 (*a*) M. H. Shaw, J. Twilton and D. W. C. MacMillan, *J. Org. Chem.*, 2016, **81**, 6898–6926. (*b*) D. Cambié, C. Bottecchia, N. J. W. Straathof, V. Hessel and T. Noël, *Chem. Rev.*, 2016, **116**, 10276–10341. (*c*) M. Sender and D. Ziegenbalg, *Chem. Ing. Tech.*, 2017, **89**, 1159–1173. (*d*) A. Roibu, R. Bharadwaj Morthala, M. E. Leblebici, D. Koziej, T. Van Gerven and Simon Kuhn, *React. Chem. Eng.*, 2018, **3**, 849–865.

S1 C. P. Haas, T. Müllner, R. Kohns, D. Enke and U. Tallarek, *React. Chem. Eng.*, 2017, **2**, 498–511.

S2 N. Straathof, D. Osch, A. Schouten, X. Wang, J. Schouten, V. Hessel and T. Noël, *J. Flow Chem.*, 2014, **4**, 12–17.

2. Chapter 2: Catalyst-Free Indirect C–F Activation of 3-Perfluoroalkyl Indoles

Authors
T. Roider, O. A. Kleykamp, S. I. Ivlev, R. W. Hoffmann and U. Tallarek*

State of publication
Published 10 September 2022 in *European Journal of Organic Chemistry*, e202201025. DOI: 10.1002/ejoc.202201025

Table of content

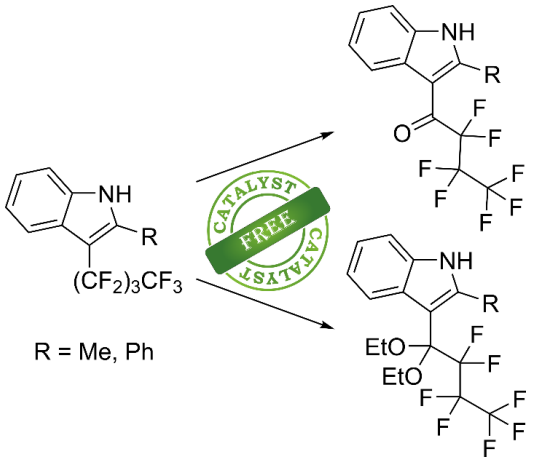

Abstract
We present a catalyst-free method for indirect C–F activation of a perfluorinated side chain in $C_{(3)}$ position of 1*H*-indoles with moderate-to-good yields, which allows the introduction of a nucleophile at the α-CF_2-group of the perfluorinated chain. By adapting this approach, it is also possible to modify 3-perfluorobutyl-2-phenyl-1*H*-indole to generate privileged structures for medicinal chemistry.

2.1 Introduction

The unique properties of fluorine-containing organic compounds have caused them to receive increased attention in recent decades.[1–4] For this reason, it has also become increasingly important to develop new synthetic routes to introduce fluorine species into organic frameworks, or to modify fluorinated substructures.[5–10] The modification of such substructures often represents a challenge, because the high C–F bond energy resulting from the large difference in electronegativities usually requires harsh reaction conditions for bond activation.[10] In Scheme 2.1, typical synthetic routes for C–F bond activation are illustrated. The three most common methods are two-electron reduction via transition metals,[10–13] single-electron reduction via low-valent transition metals[10,14] (or electrochemistry[15,16]), and fluoride abstraction via strong main-group Lewis acids (Scheme 2.1a).[10,17,18] For these methods, harsh reaction conditions or the use of expensive catalysts are often unavoidable.

In contrast, an indirect activation of C–F groups next to vinyl groups can already be achieved under mild conditions.[19] As illustrated in Scheme 2.1b, cleavage of the C–F bond occurs by a nucleophilic attack on the adjacent vinyl group, because fluoroalkenes are electron-deficient and facilitate a nucleophilic attack on the carbon in γ-position with respect to the fluorine substituents.[10,20] The resulting vinylic CF_2 group has a high reactivity toward another nucleophilic attack and allows *e.g.* the cyclization of the product.

C–F groups in β-position to carbonyl functions can be activated under mild conditions and without catalysts (Scheme 2.1c).[21] Besides carbonyl groups, also carboxylic groups,[22–24] a tetrahydrofuryl substituent,[25] sulfonyl groups,[26] and thioethers[26] were described to activate β-C–F bonds.

In this work, we advance previously reported routes and present a new method for an indirect activation of the α-CF_2-group in 3-position of an indole under mild reaction conditions (Scheme 2.1d). A strong base deprotonates the NH function of 2,3-disubstituted indoles, leading to subsequent nucleophilic addition of OH^- or sodium ethoxide at the activated group to generate the corresponding ketones or acetals.

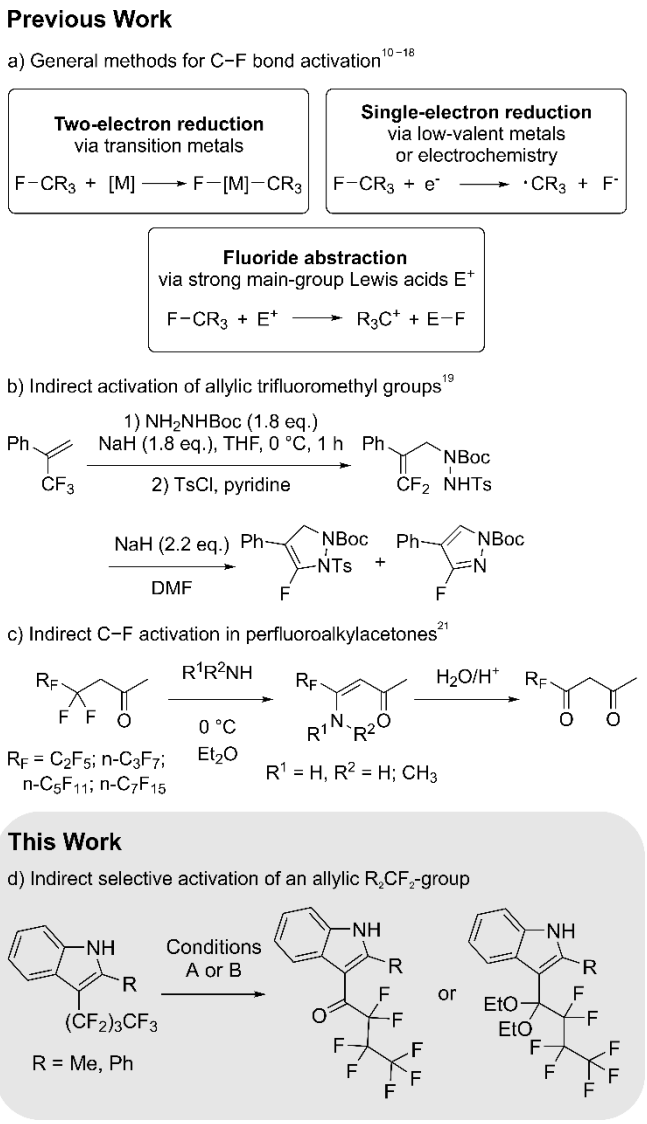

Scheme 2.1. Top: Previous work on C–F bond activation in organic synthesis.[10,19,21] Bottom: Reaction scheme for indirect selective activation of an allylic R_2CF_2-group. Conditions A: With NaH (15 eq.) in H_2O/MeCN (1:5), 30 min at room temperature. Conditions B: With NaOEt (1.5 eq.) in EtOH, 30 min at room temperature.

The obtained products can be used as building blocks for further modification toward drugs or drug candidates, as found in the literature.[27–29] So far, perfluorinated carboxylic anhydrides are used to generate perfluoroalkyl-aryl-ketones,[30] but they are significantly more expensive than the nonafluoro-1-iodobutane employed in this work. Therefore, the synthetic route presented here offers a new and cheap alternative for the generation of perfluoroalkyl-aryl-ketones, based on the corresponding 1*H*-indoles.

2.2 Results and Discussion

First of all, the 3-substituted indoles mentioned in Scheme 2.1d had to be synthesized, starting with the indole derivatives **1a** and **1b** (Scheme 2.2). For that purpose, the electron donor–acceptor complex between diazabicycloundecene (DBU) and nonafluoro-1-iodobutane (**2**) was exploited.[31–33] To perform this photochemical reaction, we relied on a two-dimensional continuous-flow setup (reaction–separation/analysis) as experimental platform, which is indicated in Scheme 2.2.

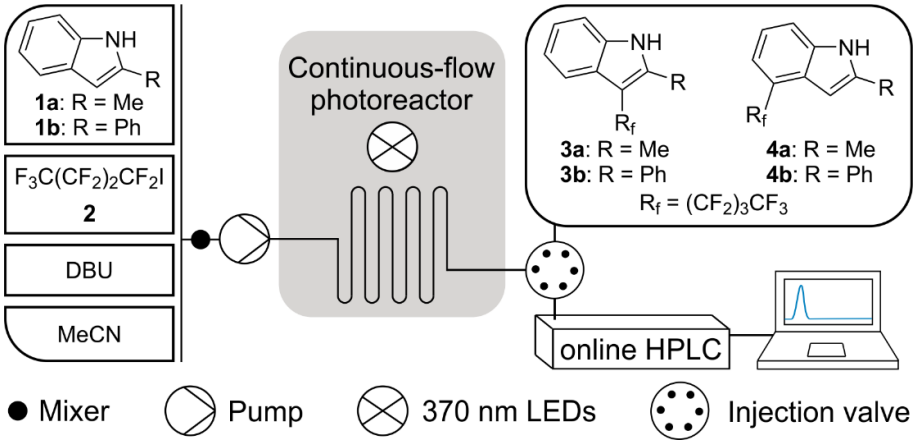

Scheme 2.2. For the perfluoroalkylation reaction, an HPLC system was adapted and the reaction took place in a custom-made stainless-steel reactor described in the Supporting Information (Section 2.4.2, Figure 2.S2 and 2.S3).

The adapted continuous-flow platform has been described in detail before[34] and was used to optimize the reaction with respect to reaction times, equivalents of perfluorobutyliodide (**2**), and the intensity of the light source. The HPLC pump arrangement allows precise control of the flow rate and initial concentrations of each reactant in the photoreactor. Further, it allows to analyze product solutions and determine the amount of generated product online. To make this possible, the chromatographic separation process of the online-coupled analytical HPLC system (cf. Scheme 2.2) was optimized such that all reactants, additives, products, and side products could be baseline-separated in the shortest possible analysis time (see Supporting Information, Table 2.S1 and 2.S2). A detailed description of the employed HPLC hardware of the two-dimensional continuous-flow platform as well as a photograph are available in the Supporting Information (Figure 2.S1). A custom-made LED array with 12 high-power LEDs was used as the light source. Additional information about this LED array as well as an emission spectrum of the LEDs are provided in the Supporting Information (Figure 2.S4 and 2.S5).
At a set volumetric pump flow rate of 0.2 mL·min^{-1}, which translates into a (residence and thus) reaction time of 4.25 min on the photoreactor, 2-methyl-3-(perfluorobutyl)-1*H*-indole (**3a**) was obtained with 59% yield. Applying the same conditions, 2-phenyl-3-(perfluorobutyl)-1*H*-indole (**3b**) was obtained in a yield of 54%. Optimized reaction conditions and the relevant NMR spectra can be found in the Supporting Information (Section 2.4.4 and 2.4.5). Besides the expected 2-substituted-3-(perfluorobutyl)-1*H*-indole **3**, another regioisomer (**4**) was detected.
Storage of the mixture at room temperature over a period of three weeks resulted in the conversion of 2-methyl-3-(perfluorobutyl)-1*H*-indole (**3a**) to the hydrolysis product **5a** (Table

2.1, Entry 1). It was observed that only 2-methyl-3-(perfluorobutyl)-1*H*-indole (**3a**) was hydrolysed and the regioisomer **4a** was stable at room temperature. Moreover, it was possible to detect the hydrolysis product already in the reaction solution with a yield of less than 1%. Even though the amount of the generated side product **5a** was extremely low, the outcome was reproducible in all experiments. In addition, it was observed that during column chromatographic purification of **3a** on silica gel, the hydrolysis product **5a** was increasingly formed. To find out how **5a** is generated, several batch experiments were performed. The results are summarized in Table 2.1.

Table 2.1. Hydrolysis of 2-methyl-3-(perfluorobutyl)-1*H*-indole (**3a**).

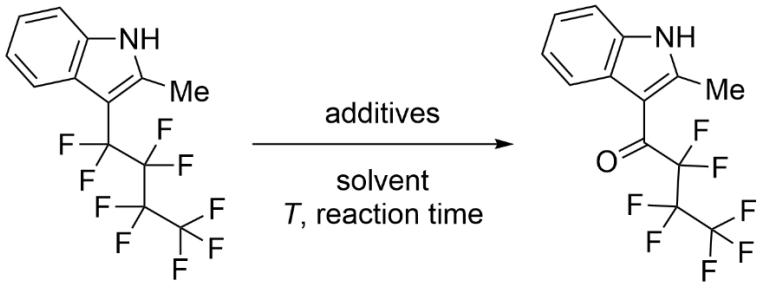

3a **5a**

Entry	Additives	Solvent	*T*	Reaction time	Conversion[a]
1	—	—	r.t.	3 weeks	100%
2	SiO_2, DBU	MeCN/H_2O 5/1	40 °C	16 h	100%
3	SiO_2	MeCN/H_2O 5/1	40 °C	16 h	—
4	SiO_2, DBU	MeCN/H_2O 5/1 degassed	r.t.	20 min	100%
5	DBU	MeCN/H_2O 5/1	r.t.	5 min	100%

a: Determined with HPLC analysis.

In order to reproduce the reaction conditions on the separation column, SiO_2 was added to the reaction solution. To further speed up the reaction, water and a base (DBU) were added, and also the temperature was increased up to 40 °C, resulting in 100% conversion after 16 hours (Entry 2 in Table 2.1). It turned out that the usage of a base was critical for the generation of the side product **5a** (Entry 3). The reaction could also be carried out under inert gas conditions, which means that water is the oxygen supplier for the reaction (Entry 4). This also explains the low yield of **5a** in the initial reaction solution. For the reaction in continuous-flow, HPLC grade solvents were used, which contain only a very low amount of water. In a final experiment, it could be shown that SiO_2 is not necessary for the hydrolysis of **3a** and complete conversion could already be achieved after a reaction time of five minutes (Entry 5). This optimized reaction could also be reproduced with 2-phenyl-3-(perfluorobutyl)-1*H*-indole (**3b**) instead of **3a**.

With consideration of the results from Table 2.1 and the literature mentioned in Scheme 2.1b and 2.1c, the following mechanism is proposed (Scheme 2.3).

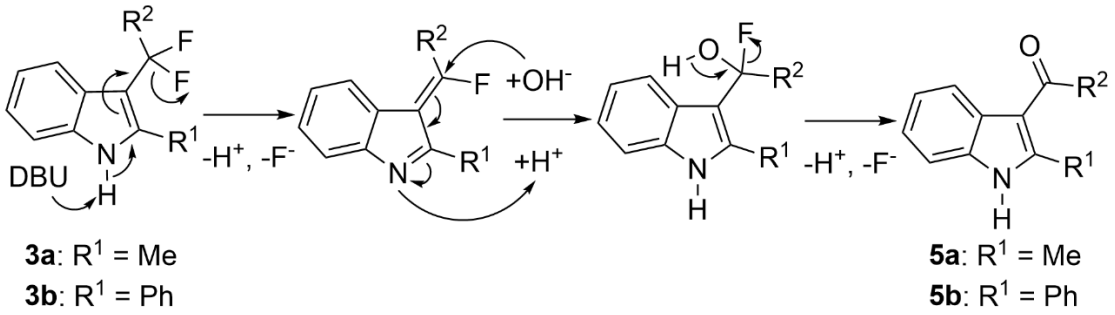

Scheme 2.3. Proposed mechanism for hydrolysis of 3-perfluorobutyl indoles **3**.

First, the amino function of the indole is deprotonated by the base and an alkene is generated, allowing nucleophilic attack of hydroxide at the formerly fluorinated carbon. In a subsequent step, the ketone **5** is produced.
The deprotonation of indoles seems to be difficult due to the high pK_a values. Indole is a weak acid (pK_a = 16.97), but the pK_a value changes significantly with electron withdrawing groups at the $C_{(3)}$ position.[35] Indole-3-CHO, for example, has a pK_a value of 12.36 and deprotonation with lithium aluminium hydride has already been described in the literature.[36] The perfluorobutyl side chain at the $C_{(3)}$ position represents a very strong electron withdrawing group, which facilitates deprotonation of the indole.

The utilization of DBU as base leads to another side product next to the ketone. Therefore, we tried some different non-nucleophilic bases and analyzed the reaction using the HPLC system. With *N,N,N',N'*-tetramethylethylendiamine (TMEDA) no conversion was observed due to the lower basicity compared to DBU (pK_a value of the conjugate acids; DBU: 11.9,[37] TMEDA: pK_{a1} = 5.85, pK_{a2} = 8.97).[38] However, changing the base to (in situ (NaH) generated) hydroxide prevented the formation of the side product and led to complete conversion. To verify the mechanism, another control experiment was carried out with 1,2-dimethyl-3-(perfluorobutyl)-1*H*-indole (**6**) to shut down the deprotonation of the amino function (Scheme 2.4). Even with a prolonged reaction time, no conversion could be detected.

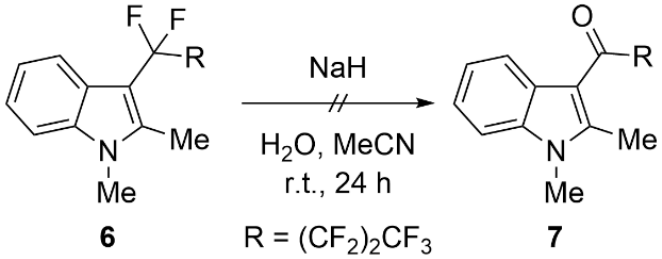

Scheme 2.4. Control experiment to indicate the critical step of the mechanism.

If the reaction proceeds via nucleophilic attack, it should also work with another nucleophile. We decided to use sodium ethoxide, because it reacts as nucleophile and can additionally

deprotonate the indole derivative. The results are summarized in Table 2.2, presenting the yields over two steps.

Table 2.2. Results of the perfluoroalkylation of indoles followed by nucleophilic attack in *α*-position of the activated perfluorinated alkyl chain.

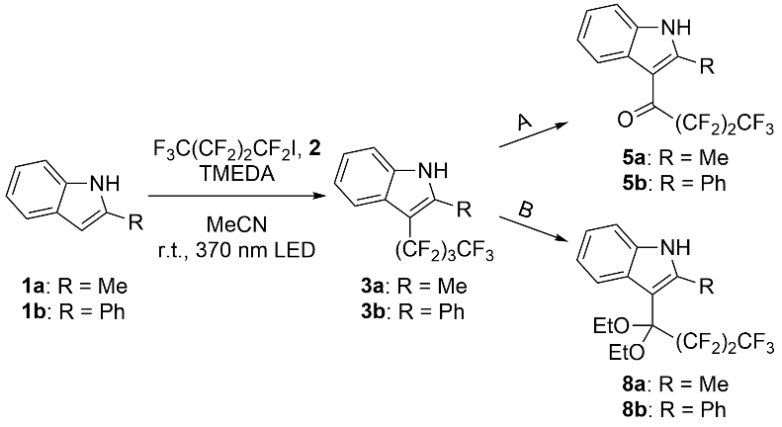

Entry	R	Conditions[a]	Yield over two steps
1	Me (**5a**)	A	37%[b]
2	Me (**8a**)	B	41%
3	Ph (**5b**)	A	54%[b]
4	Ph (**8b**)	B	44%

[a] Conditions A: With NaH (15 eq.) in H_2O/MeCN (1:5), stirred for 25 minutes at room temperature. Conditions B: With NaOEt (1.5 eq.) in EtOH, stirred for 30 minutes at room temperature.
[b] Without purification of the resulting intermediate from the first step.

As the formation of the ketone **5a** could already be observed in small amounts during the generation of **3a**, the development of a method to obtain **5** without further purification of the intermediate **3** appeared promising (Entry 1). For the first step, TMEDA was used instead of DBU to avoid formation of side products. TMEDA has already been used for photochemical perfluoroalkylations.[39] We were able to generate **5a** in a moderate yield of 37% in two steps. But to generate the corresponding ketal **8a**, purification of the intermediate **3a** was necessary in order to achieve a yield of 41% (Entry 2). Without purification no conversion was detected after the second step of the reaction (see Supporting Information, Scheme 2.S1). The use of 2-phenylindole (**1b**) instead of 2-methylindole (**1a**, Entry 3 and 4) provided similar results with higher yields. Furthermore, the corresponding ketal **8b** could be obtained as single crystal. Its X-ray analysis as well as the yields of all individual steps of the reaction are presented in the Supporting Information (Scheme 2.S1 and 2.S2).

The reaction can be carried out with primary as well as with secondary perfluorinated iodoalkanes. This was demonstrated by the reaction of 2-phenyl-1*H*-indole with heptafluoro-2-iodopropane followed by solvolysis, leading to the expected alcohol **10** and the ether **11**

(Scheme 2.5). With 49% over two steps, the yields are very similar compared to the reaction with primary perfluorinated iodoalkanes.

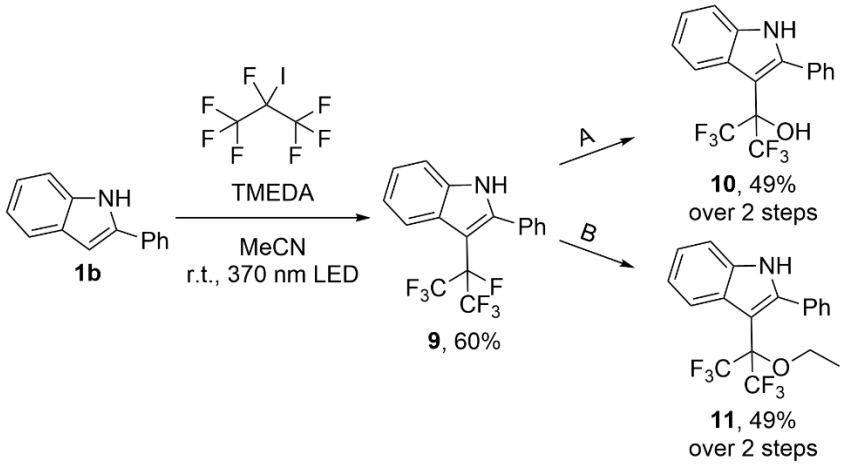

Scheme 2.5. Reaction with a secondary perfluorinated iodoalkane. Conditions A: With NaH (15 eq.) in H_2O/MeCN (1:5), stirred for 25 minutes at room temperature. Conditions B: With NaOEt (1.5 eq.) in EtOH, stirred for 30 minutes at room temperature.

2.3 Conclusion

We presented a catalyst-free method for an indirect selective C–F activation of a perfluorinated side chain in $C_{(3)}$ position of 1*H*-indoles under mild reaction conditions. This, in turn, opened an alternative pathway for the generation of heptafluoro-1-indol-butan-1-ones using inexpensive reagents. The reaction pathway also allows for the addition of other nucleophiles in the *α*–position of the perfluorinated side chain of indoles. It provides access to building blocks for the synthesis of biologically active molecules, and especially 3-substituted 2-phenyl indoles are promising structures for medicinal chemistry.[28] Togni's group has already presented a method for the asymmetric hydrogenation of perfluoroalkyl aryl ketones (suitable for the ketones in this work) and mentioned the potential of 3-substituted 2-phenyl indoles for the modulation of G-protein-coupled receptors.[27,28,40]

2.4 Supporting Information

2.4.1 General experimental information

2-Phenylindole was received from Carl Roth (Karlsruhe, Germany) with a purity of 94.5%. Perfluorobutyliodide was received from Acros Organics (New Jersey, United States) with a purity of 99%. All other chemicals were received from Sigma–Aldrich (St. Louis, MO) with a purity of >98%. All chemicals were used as received, without further purification. Acetonitrile (HiPerSolv CHROMANORM for HPLC) and ethanol absolute (AnalaR NORMAPUR) were purchased from VWR Chemicals (Darmstadt, Germany). Water was obtained from a Milli–Q gradient purification system (Millipore, Bedford, MA).

^{1}H NMR (500 MHz) and ^{13}C NMR (125 MHz) spectra were recorded at ambient temperature on a Bruker Avance 500 NMR spectrometer. ^{19}F NMR spectra (282 MHz) were recorded on a Bruker Avance 300 NMR spectrometer. Chemical shifts are reported in parts per million (ppm) relative to the solvents DMSO-d_6 (^{1}H NMR 2.50 ppm; ^{13}C NMR 39.52 ppm) and $PhCF_3$ (^{19}F NMR −63.2 ppm). Multiplicities are reported using the following abbreviations: s (singlet), d (doublet), t (triplet), q (quartet), m (multiplet).

Infrared spectra were recorded on a Bruker Alpha-P FT-IR spectrometer. The spectra were measured neat. The bonds are characterized using the following abbreviations: s (strong), m (medium), w (weak), b (broad).

TLC analysis was carried out on aluminium TLC plates with silica gel 60 F245 from Merck (Darmstadt, Germany). Column liquid chromatography was performed on MN Kieselgel 60 M (Macherey-Nagel, Düren, Germany; 0.040-0.063 mm). Detection was realized by fluorescence quenching with UV-light (λ = 254 nm) or HPLC analysis. Melting points were determined on a BÜCHI Melting Point B-540 instrument.

2.4.2 Reaction setup for the perfluoroalkylation

To optimize the perfluoroalkylation reaction, a two-dimensional (reaction–separation/analysis) continuous-flow platform, described in detail previously,[S1] was used. A photograph of the flow platform is shown in Figure 2.S1. All integrated hardware components have been received from Agilent Technologies (Santa Clara, CA).

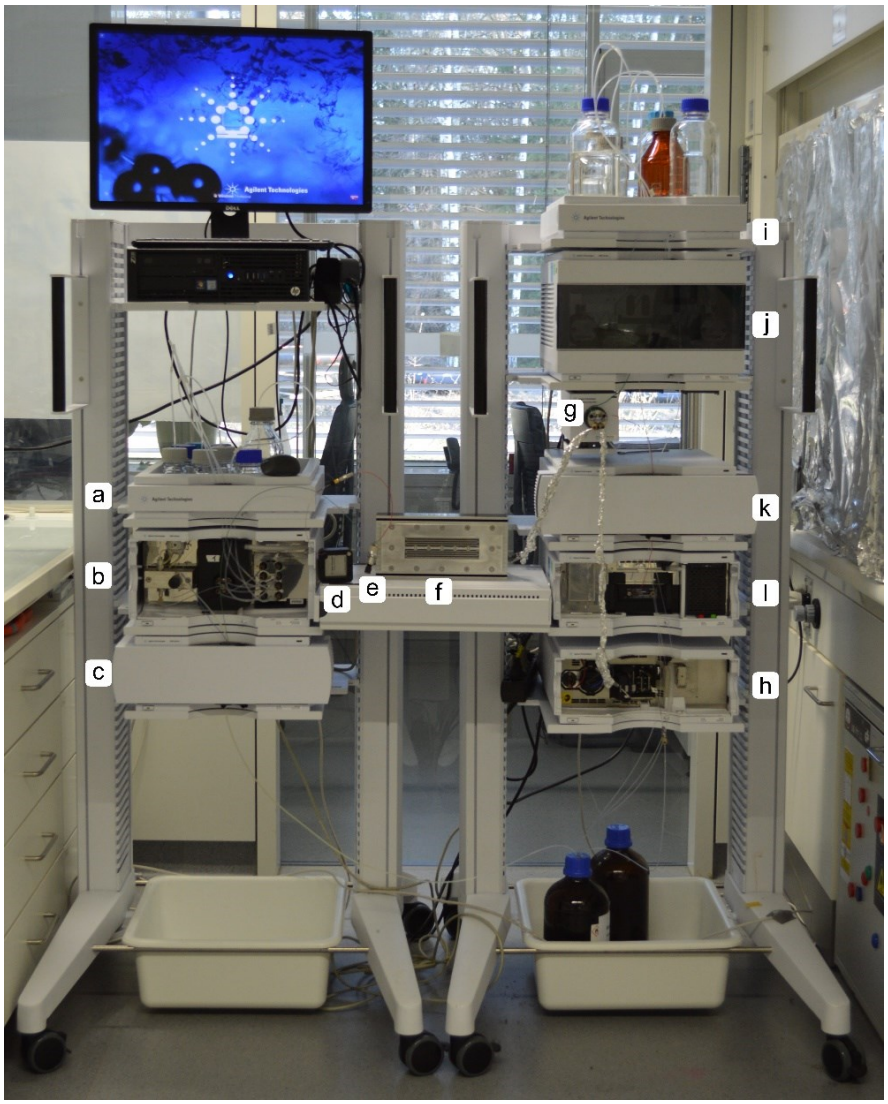

Figure 2.S1.
Two-dimensional continuous-flow platform for coupled reaction–separation/analysis. Hardware components used for the reaction: a) Substrate solutions; b) quaternary pump (Agilent 1260 Infinity Series, G1311B); c) thermostatted HPLC column compartment (Agilent 1290 Infinity Series, G1316C); d) Jet Weaver V35 Mixer; e) back-pressure regulator; f) photoreactor; g) 2-position/6-port valve (Agilent 1290 Series, G1170A); h) inline DAD (Agilent 1200 Series, G1315C).
Hardware components used for HPLC analysis: i) eluents; j) binary pump (Agilent 1290 Infinity Series, G4220A); k) thermostatted HPLC column compartment (Agilent 1290 Infinity Series, G1316C) with separation column; l) DAD (Agilent 1290 Infinity Series, G4212A).

The chemical reaction (first dimension of the setup in Figure 2.S1) was optimized in terms of reaction time, equivalents of perfluorobutyliodide used, and light source intensity. The pump assembly corresponds to the configuration already used in a wavelength-resolved analysis and was previously described in detail.[S2] The assembly of the HPLC pumps allows a precise control of the flow rate (thus, residence and reaction time) and starting concentrations of each reactant in the photoreactor. It also allows product solutions to be analyzed and yields to be determined online. To make this possible, the chromatographic separation process of the online coupled analytical HPLC system (second dimension of the setup in Figure 2.S1) was optimized to baseline-separate all reactants, additives, products and side-products in the shortest possible analysis time. The gradient developed for the separation depends on the indole derivative used (i.e., Me or Ph at the $C_{(2)}$ position). All separations were carried out at 25 °C on a monolithic, silica-based separation column (C18 Chromolith High Resolution; RP 18-e, 100–4.6 mm) from Merck KGaA (Darmstadt, Germany) with water and acetonitrile (+ 0.1% trifluoroacetic acid) as eluents. Table 2.S1 summarizes the gradient developed for the specific separation problem of the 2-methylindole derivatives, resulting in analysis cycles of 14.00 minutes.

Table 2.S1. Elution gradient for the 2-methylindole derivatives in the online coupled HPLC system. Flow rate: 2 mL min^{-1}.

Time (min)	Water (vol %)	Acetonitrile (vol %)
0.00*	80	20
5.00	55	45
7.00	40	60
10.00	40	60
10.90	0	100
12.40	0	100
12.41	80	20
14.00	80	20

*Point of injection.

Table 2.S2 summarizes the elution gradient developed for the specific separation problem of the 2-phenylindole derivatives, resulting in analysis cycles of 17.20 minutes.

Table 2.S2. Elution gradient for the 2-phenylindole derivatives in the online coupled HPLC system. Flow rate: 2 mL min^{-1}.

Time (min)	Water (vol %)	Acetonitrile (vol %)
0.00*	80	20
3.00	40	60
9.00	40	60
9.90	20	80
11.40	20	80
13.70	10	90
13.71	0	100
15.20*	0	100
15.21	80	20
17.20	80	20

*Point of injection.

The adapted photoreactor and light source were custom-made and described previously.[S2] The reactor has a modular design and consists of several components illustrated in Figure 2.S2.

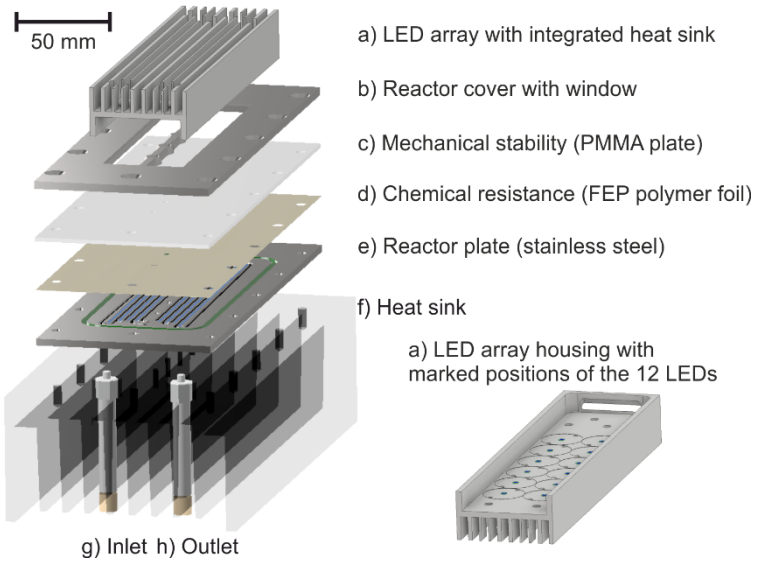

Figure 2.S2. Modular design of the employed photoreactor, highlighting its individual components.

The reaction takes place on the reactor plate (Figure 2.S2, e), into which a reaction channel with a total volume of 0.85 mL was milled (1.5 mm wide, 0.5 mm deep). Above the reactor plate is a FEP polymer foil (Figure 2.S2, d), which is essential for chemical resistance. Because FEP strongly absorbs light at larger layer thickness, the foil was chosen to be as thin as possible

(0.13 mm). Above the FEP polymer foil is a PMMA plate, necessary to provide mechanical stability (Figure 2.S2, c, 2 mm). On top of the PMMA plate, another steel plate with a window defines the irradiated area of the reactor (Figure 2.S2, b).
The LED array (Figure 2.S2, a) is placed directly on the reactor cover with window (Figure 2.S2, b) to keep the light intensity on the reactor plate as high as possible. On the rear side of the reactor plate there is a heat sink (Figure 2.S2, f), which allows to work under isothermal reaction conditions. Between the cooling fins are the inlet (Figure 2.S2, g) and outlet (Figure 2.S2, h) for the reactor plate.

A photograph of the reactor is shown in Figure 2.S3.

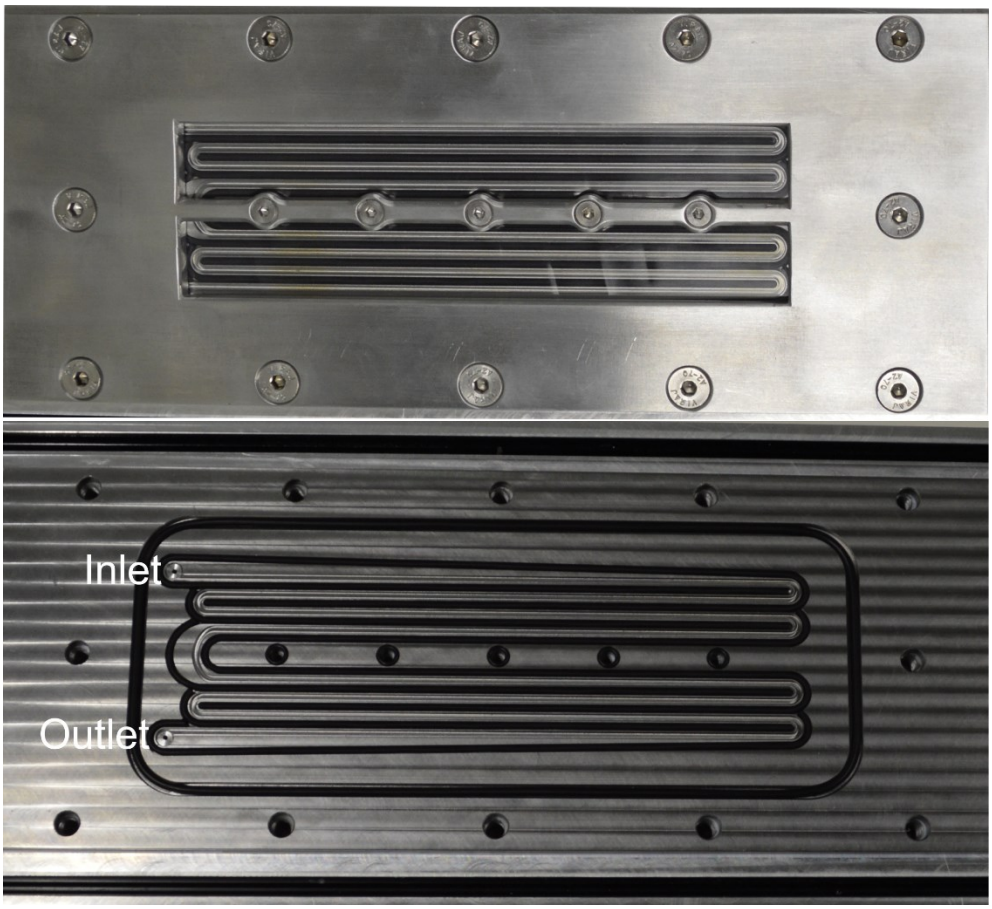

Figure 2.S3. Top: Photograph of the closed reactor. Bottom: View onto the reactor plate.

The light source was designed based on the reactor window to achieve efficient irradiation. It consists of twelve LEDs of the same type and is shown in Figure 2.S4.

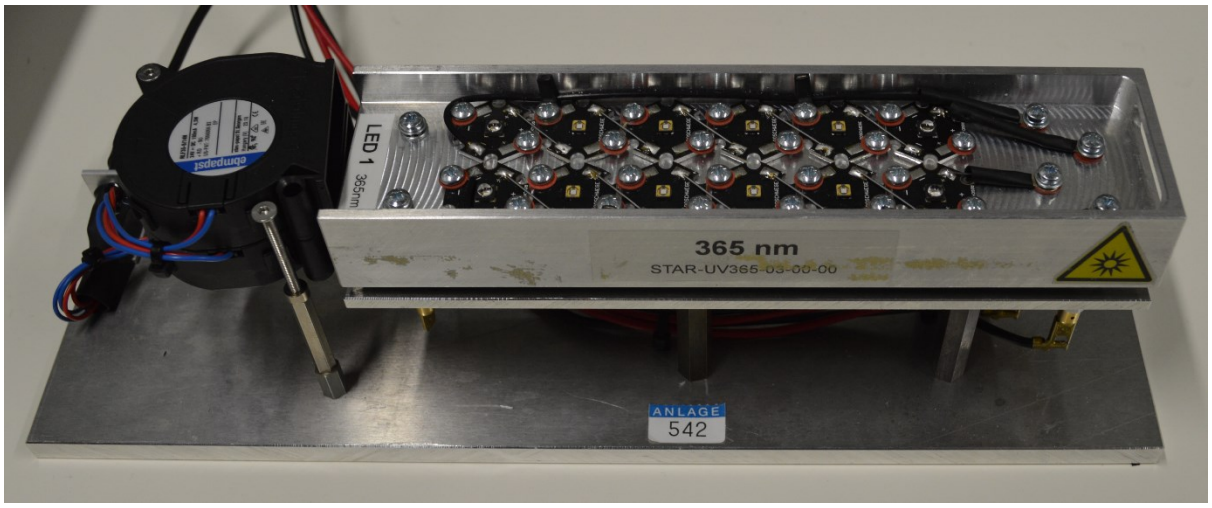

Figure 2.S4. Photograph of the LED-setup with fixed radial fans in front of the array.

The 370 nm LEDs (Roschwege Star-UV365-05-00-00 UV-LED 365 nm SMD manufactured by Roschwege, Greifenstein, Germany) were purchased from Conrad Electronic SE (Hirschau, Germany) and have a power rating of 5 watts each. Cooling of the LEDs turned out to be crucial for archieving reproducible results. Therefore, radial fans and a heat sink on the rear side of the LED array had to be implemented.
The emission spectrum of the light source was measured using a calibrated spectroradiometer PS–200 from Apogee Instruments (Logan, UT) and is shown in Figure 2.S5. The spectrum was measured with consideration of the absorption of the PMMA plate and FEP polymer foil.

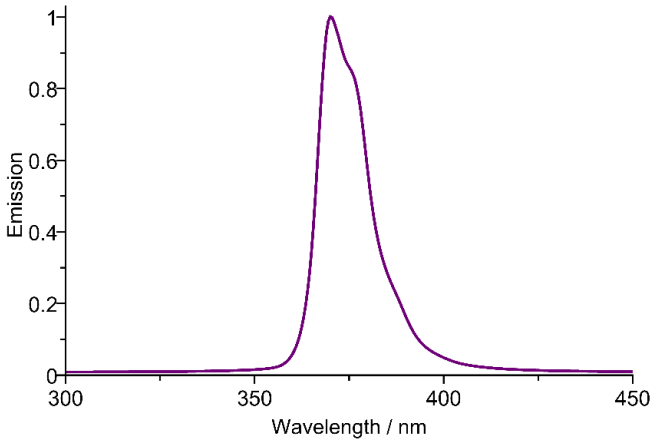

Figure 2.S5. Normalized emission spectrum of the light source (Roschwege Star-UV365-05-00-00, 5 watt, 370 nm) under the actual reaction conditions.

Normalized emission spectrum of the light source (Roschwege Star-UV365-05-00-00, 5 watt, 370 nm) under the actual reaction conditions.[S2]

2.4.3 Overview of the yields from each reaction step

Individual yields of the perfluoroalkylation as well as the corresponding reaction conditions are summarized in Scheme 2.S1 and 2.S2.

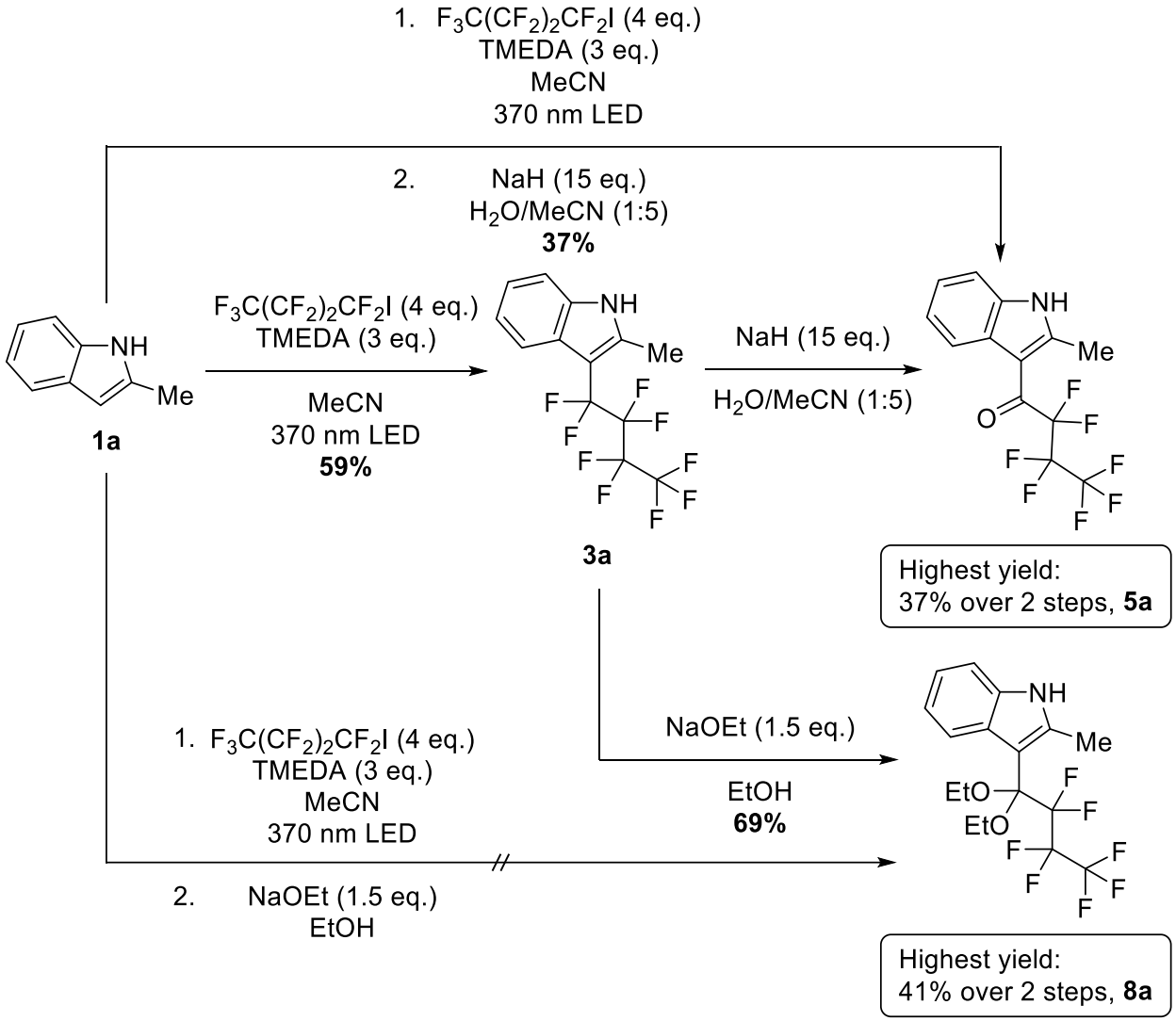

Scheme 2.S1. Summary of yields and reaction conditions for the 2-methylindole-system.

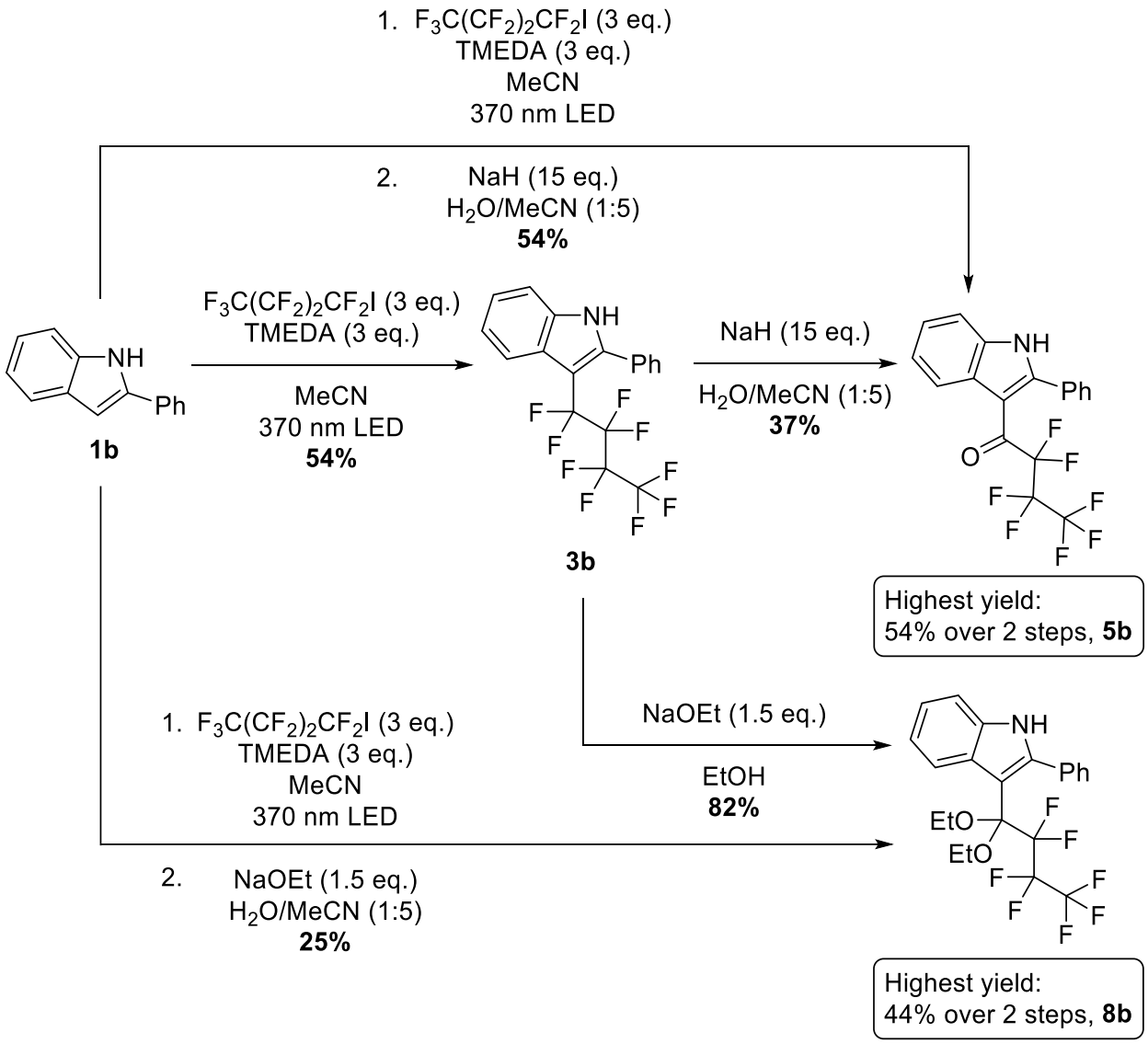

Scheme 2.S2. Summary of yields and reaction conditions for the 2-phenylindole-system.

For both reaction systems, the highest yield of ketone was obtained without further purification of the intermediate. However, purification of the intermediate became necessary to achieve a higher yield of the corresponding ketal.

2.4.4 Synthesis of 3-perfluoroalkyl indole derivatives

General procedure for the synthesis of 3-perfluorobutyl-1*H*-indoles (3)

1: The respective indole derivative (**1**, 7 mmol), perfluorobutyliodide (**2**, 21 mmol) and TMEDA (21 mmol) were dissolved in 100 mL acetonitrile each. An additional pure acetonitrile solution was connected to the pump to be able to increase the concentration of a particular reactant as part of the reaction optimization. All four solutions were continuously pumped into the photoreactor at an equal volume of 25% of each solution and a total flow rate of 0.2 mL min^{-1}, resulting in a reaction time of 4.25 minutes. The flow rate was held for 788 minutes and the collected solution was concentrated under reduced pressure.

General procedure for the synthesis of 2,2,3,3,4,4,4-heptafluoro-1*H*-indol-butan-1-ones (5)

2a: The respective 3-perfluoroalkyl indole (**3**, 919 µmol) was dissolved in acetonitrile (50 mL) and sodium hydride (60% dispersion in mineral oil, 15 eq.) was added. Water (10 mL) was added over a period of 2 minutes and the solution was stirred for 25 minutes at room temperature. Brine (30 mL) was added and the aqueous layer extracted with dichloromethane (3 x 30 mL). The organic layer was dried over sodium sulfate and concentrated under reduced pressure.

General procedure for the synthesis of 3-(1,1-diethoxy-2,2,3,3,4,4,4-heptafluorobutyl)-1*H*-indoles (8)

2b: The respective 3-perfluoroalkyl indole (**3**, 286 µmol) was dissolved in ethanol (3.8 mL) and a sodium ethoxide solution in ethanol (21% wt., 1.5 eq., 0.16 mL, 429 µmol) was added. The solution was stirred at room temperature for 30 minutes, before it was quenched with saturated NH_4Cl solution (5 mL). The aqueous layer was extracted with dichloromethane (3 x 5 mL) and the organic layer was dried over sodium sulfate and concentrated under reduced pressure.

Synthesis of 2-methyl-3-(perfluorobutyl)-1*H*-indole (3a)

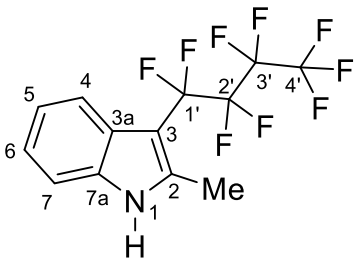

Prepared according to GP 1 with 2-methyl-1*H*-indole (**1a**, 70 mmolar in acetonitrile). Purification by column chromatography over silica gel (dichloromethane/toluene 1:3) yielded **3a** as a yellow oil (572 mg, 1.64 mmol, 59%). The NMR spectroscopic data were in accordance with those reported in the literature.[S3]

^{1}H NMR (500 MHz, DMSO-d_6) δ = 11.90 (s, 1H, N-H), 7.44 (d, *J* = 8.0 Hz, 1H, 4-H), 7.42–7.38 (m, 1H, 7-H), 7.17–7.12 (m, 1H, 6-H), 7.11–7.06 (m, 5-H), 2.48–2.46 (m, 3H, Me). —**^{13}C NMR** (126 MHz, DMSO-d_6) δ = 138.9 (t, *J* = 5.0 Hz, 2-C), 134.9 (s, 7a-C), 125.6 (t, *J* = 3.3 Hz, 3a-C), 121.8 (s, 6-C), 120.8 (s, 5-C), 118.2 (s, 4-C), 111.5 (s, 7-C), 97.5 (t, *J* = 27.4 Hz, 3-C), 12.4 (s, Me). — **^{19}F NMR** (282 MHz, DMSO-d_6) δ = –82.5 (tt, *J* = 9.6, *J* = 3.2 Hz, 3F, 4'-F), –105.1 – –105.4 (m, 2F, 3'-F), –124.5 – –124.8 (m, 2F, 2'-F), –127.4 – –127.7 (m, 2F, 1'-F). **ESI (HR-MS)** calcd. for $C_{13}H_7F_9N$: 348.0440; found 348.0443.

Synthesis of 2-phenyl-3-(perfluorobutyl)-1*H*-indole (3b)

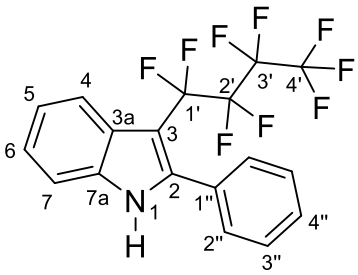

Prepared according to GP 1 with 2-phenyl-1*H*-indole (**1b**, 70 mmolar in acetonitrile) and DBU instead of TMEDA (210 mmolar in acetonitrile). A flowrate of 0.2 mL/min was held for 700 min. Purification by column chromatography over silica gel (dichloromethane/toluene 1:3) yielded **3b** as a yellow oil (544 mg, 1.64 mmol, 54%).

^{1}H NMR (500 MHz, DMSO-d_6) δ = 12.28 (s, 1H, N-H), 7.59 (d, *J* = 8.1 Hz, 1H, 4-H), 7.57–7.50 (m, 5H, 2''-H, 3''-H, 4''-H), 7.50–7.46 (m, 1H, 7-H), 7.29–7.24 (m, 1H, 6-H), 7.22–7.17

(m, 1H, 5-H). —**^{13}C NMR** (126 MHz, DMSO-d_6) δ = 141.2 (t, J = 4.6 Hz, 2-C), 135.5 (s, 7a-C), 131.3 (s, 1''-C), 129.6 (s, 2C, 2''-C or 3''-C), 129.2 (s, 1-C, 4''-C), 128.1 (s, 2C, 2''-C or 3''-C), 125.5 (t, J = 3.3 Hz, 3a-C), 122.8 (s, 6-C), 121.3 (s, 5-C), 119.3 (s, 4-C), 112.1 (s, 7-C), 98.2 (t, J = 27.2 Hz, 3-C). — **^{19}F NMR** (282 MHz, DMSO-d_6) δ = –82.5 (tt, J = 9.6, 3.3 Hz, 3F, 4'-F), –102.3 – –102.5 (m, 2F, 3'-F), –123.2 – –123.5 (m, 2F, 2'-F), –127.4 – –127.7 (m, 2F, 1'-F). — **IR (neat):** $\tilde{\nu}$ = 3404 b, 3063 w, 1608 w, 1557 w, 1492 w, 1458 m, 1449 m, 1430 m, 1351 m, 1295 w, 1229 s, 1202 s, 1130 s, 1092 m, 1057 m, 1044 m, 1029 m, 1002 w, 984 m, 952 w, 925 w, 900 m, 854 s, 813 s, 744 s, 733 s, 697 s, 652 w, 638 w, 611 m, 585 m, 562 m, 532 m, 439 w, 414 w cm^{-1}. — **EI (HR-MS)** calcd. for $C_{18}H_{10}F_9N$: 411.06695; found 411.06626.

Synthesis of 1,2-dimethyl-3-(perfluorobutyl)-1*H*-indole (6)

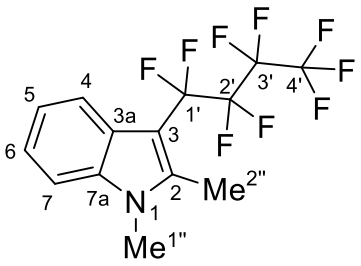

Prepared according to GP 1 with 1,2-dimethyl-1*H*-indole (70 mmolar in acetonitrile), DBU instead of TMEDA (210 mmolar in acetonitrile) and perfluorobutyliodide (140 mmolar in acetonitrile). A flowrate of 0.2 mL/min was held for 200 min. Purification by column chromatography over silica gel (pentane/EtOAc 7:1) yielded **6** as a yellow oil (130 mg, 0.37 mmol, 53%). The NMR spectroscopic data were in accordance with those reported in the literature.[S3]

^{1}H NMR (500 MHz, DMSO-d_6) δ = 7.56 (d, J = 8.3 Hz, 1H, 7-H), 7.49 (d, J = 8.0 Hz, 1H, 4-H), 7.25–7.20 (m, 1H, 6-H), 7.16–7.12 (m, 1H, 5-H), 3.75 (s, 3H, 1''-H), 2.50 (s, 3H, 2''-H). —**^{13}C NMR** (126 MHz, DMSO-d_6) δ = 140.0 (t, J = 4.8 Hz, 2-C), 136.2 (s, 7a-C), 124.6 (t, J = 3.1 Hz, 3a-C), 121.9 (s, 6-C), 121.1 (s, 5-C), 118.3 (s, 4-C), 97.5 (t, J = 27.4 Hz, 3-C), 29.8 (s, 1''-C), 11.0 (s, 2''-C). — **^{19}F NMR** (282 MHz, DMSO-d_6) δ = –82.5 (tt, J = 9.6, 3.2 Hz, 3F, 4'-F), –104.4 – –104.6 (m, 2F, 3'-F), –124.5 – –124.7 (m, 2F, 2'-F), –127.3 – –127.5 (m, 2F, 1'-F). — **EI (HR-MS)** calcd. for $C_{14}H_{10}F_9N$: 363.06695; found 363.06640.

3-(perfluoropropan-2-yl)-2-phenyl-1*H*-indole (9)

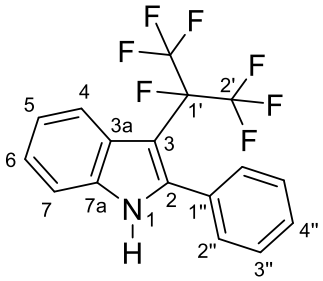

Prepared according to GP 1 with 2-phenyl-1*H*-indole (**1b**, 70 mmolar in acetonitrile), TMEDA (210 mmolar in acetonitrile) and heptafluoro-2-iodopropane (210 mmolar in acetonitrile). A flowrate of 0.2 mL/min was held for 740 min. Purification by column chromatography over silica gel (dichloromethane/toluene 7:1) yielded **9** as a yellow solid (756 mg, 2.09 mmol, 60%).

Mp = 97 °C. — **^{1}H NMR** (500 MHz, DMSO-d_6) δ = 12.20 (s, 1H, N-H), 7.57 (d, J = 8.3 Hz, 1H, 4-H), 7.52–7.44 (m, 6H, 7-H, 2''-H, 3''-H, 4''-H), 7.29–7.23 (m, 1H, 6-H), 7.20–7.15 (m, 1H, 5-H). —**^{13}C NMR** (126 MHz, DMSO-d_6) δ = 140.6 (s, 1''-C), 135.9 (s, 7a-C), 132.7 (d, J = 3.0 Hz, 2-C), 129.6 (d, J = 3.2 Hz, 2''-C), 128.9 (s, 4''-C), 127.9 (s, 3''-C), 124.0 (s, 3a-C), 122.6 (s, 6-C), 121.0 (s, 5-C), 119.6 (s, 4-C), 112.1 (s, 7-C), 95.3 (d, J = 19.9 Hz, 3-C), 94.3–91.4 (m, 1'-C). — **^{19}F NMR** (282 MHz, DMSO-d_6) δ = –75.0 (d, J = 8.3 Hz, 6F, 2'-F), –175.7 (s, 1F, 1'-F). — **IR (neat):** $\tilde{\nu}$ = 3397 m, 3055 w, 1608 w, 1551

w, 1491 w, 1459 m, 1452 m, 1424 m, 1360 w, 1323 w, 1295 s, 1270 m, 1214 s, 1191 s, 1160 s, 1134 s, 1119 m, 1080 m, 1051 m, 1029 m, 1019 m, 966 s, 916 s, 846 w, 829 w, 785 w, 771 m, 751 s, 724 m, 695 s, 640 w, 630 m, 588 m, 569 m, 539 s, 495 m, 468 w, 443 w, 412 w cm^{-1}.— **EI (HR-MS)** calcd. for $C_{17}H_{10}F_7N$: 361.07015; found 361.07172.

Synthesis of 2,2,3,3,4,4,4-heptafluoro-1-(2-methyl-1*H*-indol-3-yl)butan-1-one (5a)

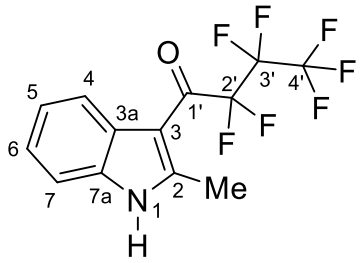

Prepared according to GP 2a with 2-methyl-3-(perfluorobutyl)-1*H*-indole (**3a**, used without further purification). Purification by column chromatography over silica gel (dichloromethane/toluene 1:3) yielded **5a** as a yellow solid (111 mg, 339 µmol, 37% via two steps).

Mp = 99 °C. — **^{1}H NMR** (500 MHz, DMSO-d_6) δ = 12.71 (s, 1H, N-H), 7.89–7.83 (m, 1H, 4-H), 7.50–7.44 (m, 1H, 7-H), 7.28–7.21 (m, 2H, 5-H and 6-H), 2.68 (s, 3H, Me). —**^{13}C NMR** (126 MHz, DMSO-d_6) δ = 176.7 (t, J = 27.4 Hz, 2-C), 151.0 (s, 2-C), 135.1 (s, 7a-C), 125.5 (s, 3a-C), 123.2 (s, 6-C), 122.9 (s, 5-C), 120.3 (t, J = 5.8 Hz, 4-C), 112.2 (s, 7-C), 108.2 (s, 3-C), 15.7 (s, Me). — **^{19}F NMR** (282 MHz, DMSO-d_6) δ = –81.5 (t, J = 9.0 Hz, 3F, 4'-F), –115.4 – –115.6 (m, 2F, 3'-F), –126.6 – –126.7 (m, 2F, 2'-F). — **IR (neat):** $\tilde{\nu}$ = 3293 b, 1617 m, 1458 m, 1421 m, 1343 m, 1262 m, 1225 s, 1201 s, 1182 s, 1165 s, 1141 m, 1116 s, 1076 m, 1030 w, 1006 m, 985 w, 975 m, 961 m, 871 w, 849 m, 795 w, 746 s, 723 s, 692 m, 676 m, 636 m, 614 m, 592 w, 582 w, 529 m, 509 w, 493 w, 452 m, 435 m, 401 w cm^{-1}. — **EI (HR-MS)** calcd. for $C_{13}H_8F_7NO$: 327.04941; found 327.04985.

Synthesis of 2,2,3,3,4,4,4-heptafluoro-1-(2-phenyl-1*H*-indol-3-yl)butan-1-one (5b)

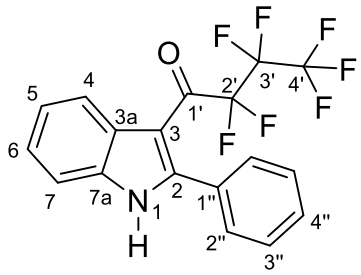

Prepared according to GP 2a with 2-phenyl-3-(perfluorobutyl)-1*H*-indole (**3b**, 875 µmol, used without further purification). Purification by column chromatography over silica gel (dichloromethane/toluene 1:10) yielded **5b** as an orange solid (185 mg, 475 µmol, 54% via two steps).

Mp = 109 °C. — **^{1}H NMR** (500 MHz, DMSO-d_6) δ = 12.86 (s, 1H, N-H), 7.96–7.92 (m, 1H, 4-H), 7.63–7.59 (m, 2H, 3''-H), 7.57–7.52 (m, 4H, 7-H, 2''-H, 4''-H), 7.36–7.29 (m, 2H, 5-H, 6-H). —**^{13}C NMR** (126 MHz, DMSO-d_6) δ = 179.3 (t, J = 27.2 Hz, 1'-C), 148.7 (s, 1''-C), 135.8 (s, 7a-C), 131.7 (s, 2-C), 129.8 (s, 4''-C), 129.5 (s, 2C 3''-C), 128.3 (s, 2C, 2''-C), 126.8 (s, 3a-C), 124.1 (s, 6-C), 123.2 (s, 5-C), 120.3 (s, 4-C), 112.6 (s, 7-C), 108.3 (s, 3-C). — **^{19}F NMR** (282 MHz, DMSO-d_6) δ = –79.5 (t, J = 9.0 Hz, 3F, 4'-F), –113.4 – –113.6 (m, 2F, 3'-F), –124.6 – –124.7 (m, 2F, 2'-F). — **IR (neat):** $\tilde{\nu}$ = 3256 b, 3063 w, 1632 m, 1531 w, 1494 w, 1479 w, 1451 m, 1418 m, 1337 m, 1280 w, 1222 s, 1180 s, 1158 m 1118 s, 1071 w, 1028 w, 1000 w, 977 m, 959 w, 917 w, 908 w, 862 m, 828 m, 798 w, 759 m, 740 s, 723 s, 689 s, 674 m, 630 m, 597 m, 582 m, 565 m, 533 m, 493 w, 451 m, 429 w, 410 w cm^{-1}. — **EI (HR-MS)** calcd. for $C_{18}H_{10}F_7NO$: 389.06506; found 389.06640.

1,1,1,3,3,3-hexafluoro-2-(2-phenyl-1*H*-indol-3-yl)propan-2-ol (10)

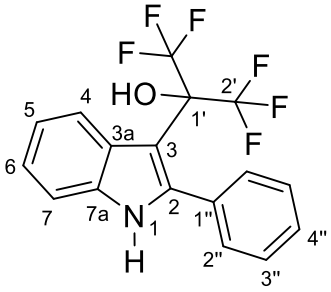

Prepared according to GP 2a with 3-(perfluoropropan-2-yl)-2-phenyl-1*H*-indole (**9**, 1.40 mmol, used without further purification). Purification by column chromatography over silica gel (dichloromethane/toluene 1:3) yielded **10** as a yellow solid (246 mg, 685 µmol, 49% via two steps).

Mp = 135 °C. — **^{1}H NMR** (500 MHz, DMSO-d_6) δ = 11.67 (s, 1H, N-H), 8.00 (s, 1H, O-H), 7.79 (d, J = 8.3 Hz, 1H, 4-H), 7.47–7.41 (m, 5H, 2''-H, 3''-H, 4''-H), 7.39–7.35 (m, 1H, 7-H), 7.19–7.13 (m, 1H, 6-H), 7.12–7.05 (m, 1H, 5-H). —**^{13}C NMR** (126 MHz, DMSO-d_6) δ = 139.6 (s, 1''-C), 135.4 (s, 7a-C), 134.6 (s, 2-C), 130.1 (s, 2C, 2''-C), 128.0 (s, 4''-C), 127.1 (s, 2C, 3''-C), 125.7 (s, 3a-C), 121.6 (s, 6-C), 121.2 (s, 4-C), 119.8 (s, 5-C), 111.3 (s, 7-C), 101.2 (s, 3-C), 78.0–76.9 (m, 1'-C). — **^{19}F NMR** (282 MHz, DMSO-d_6) δ = –71.4 (s, 6F, 2'-F). — **IR (neat):** $\tilde{\nu}$ = 3533 w, 3465 m, 3063 w, 1604 w, 1547 w, 1486 w, 1458 w, 1447 w, 1419 w, 1362 w, 1329 w, 1308 w, 1261 m, 1245 m, 1220 s, 1193 s, 1144 s, 1119 s, 1077 w, 1038 m, 1022 m, 999 w, 976 w, 952 s, 895 s, 853 w, 825 w, 769 m, 750 s, 723 m, 702 s, 695 s, 628 w, 616 w, 592 w, 581 w, 569 w, 538 m, 502 s, 489 s, 440 m 411 m cm^{-1}. — **EI (HR-MS)** calcd. for $C_{17}H_{11}F_6NO$: 359.07448; found 359.07630.

Synthesis of 3-(1,1-diethoxy-2,2,3,3,4,4,4-heptafluorobutyl)-2-methyl-1*H*-indole (8a)

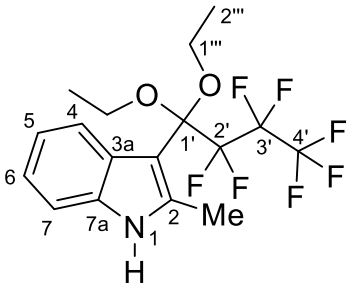

Prepared according to GP 2b with 2-methyl-3-(perfluorobutyl)-1*H*-indole (**3a**). Purification by column chromatography over silica gel (gradient pentane/EtOAc 30:1 to 20:1) yielded **8a** as a yellow solid (77.3 mg, 193 µmol, 69%).

Mp = 94 °C. — **^{1}H NMR** (500 MHz, DMSO-d_6) δ = 11.21 (s, 1H, N-H), 7.61 (d, J = 7.9 Hz, 1H, 4-H), 7.26 (d, J = 7.9 Hz, 1H, 7-H), 7.03–6.98 (m, 1H, 6-H), 6.98–6.93 (m, 1H, 5-H), 3.67–3.53 (m, 4H, 1'''-H), 2.46 (s, 3H, Me), 1.24 (t, J = 7.0 Hz, 6H, 2'''-H). —**^{13}C NMR** (126 MHz, DMSO-d_6) δ = 137.1 (s, 2-C), 134.7 (s,7a-C), 126.8 (s, 3a-C), 120.3 (s, 6-C), 120.1 (s, 4-C), 119.2 (s, 5-C), 110.5 (s, 7-C), 103.2 (s, 3-C), 100.2 (t, J = 21.8 Hz 1'-C), 57.9 (s, 1'''-C), 14.8 (s, 2'''-C), 13.5 (s, Me). — **^{19}F NMR** (282 MHz, DMSO-d_6) δ = –82.3 (t, J = 11.6 Hz, 3F, 4'-F), –117.6 – –118.2 (m, 2F, 3'-F), –127.3 – –127.5 (m, 2F, 2'-F). **IR (neat):** $\tilde{\nu}$ = 3388 m, 2986 w, 2933 w, 2893 w, 1615 w, 1556 w, 1482 w, 1458 m, 1430 w, 1395 w, 1342 m, 1304 w, 1289 w, 1213 s, 1185 s, 1140 m, 1116 s, 1068 s, 1034 s, 1014 m, 972 m, 923 m, 900 m, 874 w, 846 m, 831 w, 811 m, 759 s, 748 m, 723 m, 682 m, 667 w, 657 w, 630 w, 598 m, 588 w, 524 m, 440 w cm^{-1}. — **EI (HR-MS)** calcd. for $C_{17}H_{18}F_7NO_2$: 401.12258; found 401.12328.

Synthesis of 3-(1,1-diethoxy-2,2,3,3,4,4,4-heptafluorobutyl)-2-phenyl-1*H*-indole (8b)

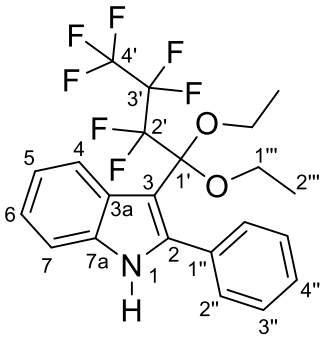

Prepared according to GP 2b with 2-phenyl-3-(perfluorobutyl)-1*H*-indole (**3b**, 729 µmol) dissolved in 7.0 mL ethanol. Purification by column chromatography over silica gel (pentane/EtOAc 7:1) yielded **8b** as a yellow solid (280 mg, 605 µmol, 83%).

Mp = 140 °C. — **^{1}H NMR** (500 MHz, DMSO-d_6) δ = 11.58 (s, 1H, N-H), 7.67 (d, J = 8.1 Hz, 1H, 4-H), 7.48–7.40 (m, 5H, 2''-H, 3''-H, 4''-H), 7.34 (d, J = 8.0 Hz 1H, 7-H), 7.15–7.10 (m, 1H, 6-H), 7.10–7.04 (m, 1H, 5-H), 3.57–3.43 (m, 1'''-H), 1.1–0.7 (m, 6H, 2'''-H). —**^{13}C NMR** (126 MHz, DMSO-d_6) δ = 140.4 (s, 1''-C), 135.4 (s,7a-C), 134.4 (s, 2-C), 130.3 (s, 2C, 3''-C), 127.8 (s, 4''-C), 127.1 (s, 2C, 2''-C), 126.2 (s, 3a-C), 121.5 (s, 5-C), 120.9 (t, J = 4.0 Hz, 4-C), 119.8 (s, 6-C), 111.3 (s, 7-C), 104.1 (s, 3-C), 100.4 (t, J = 23.1 Hz, 1'-C). — **^{19}F NMR** (282 MHz, DMSO-d_6) δ = –82.1 (t, J = 10.9 Hz, 3F, 4'-F), –117.0 (s, 2F, 3'-F), –126.3 (s, 2F, 2'-F). — **IR (neat):** $\tilde{\nu}$ = 3392 w, 2985 w, 2929 w, 1613 w, 1554 w, 1488 w, 1455 w, 1428 w, 1393 w, 1342 w, 1305 w, 1290 w, 1238 m, 1216 s, 1203 s, 1183 s, 1137 m, 1115 s, 1083 m, 1059 m, 1036 s, 1015 m, 962 m, 918 m, 871 w, 846 w, 810 m, 761 m, 745 s, 724 m, 699 s, 657 w, 633 m, 619 m, 601 m, 568 m, 524 m, 473 w, 438 w cm^{-1}. — **EI (HR-MS)** calcd. for $C_{22}H_{20}F_7NO_2$: 463.13823; found 463.13951.

3-(2-ethoxy-1,1,1,3,3,3-hexafluoropropan-2-yl)-2-phenyl-1*H*-indole (11)

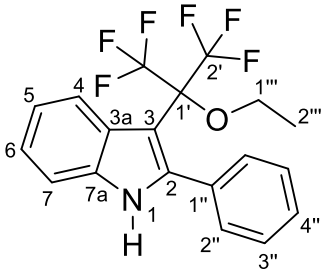

Prepared according to GP 2b with 3-(perfluoropropan-2-yl)-2-phenyl-1*H*-indole (**9**, 286 µmol) dissolved in 3.8 mL ethanol. Purification by column chromatography over silica gel (dichloromethane/toluene 1:10) yielded **11** as white solid (91.2 mg, 235 µmol, 82%).

Mp = 114 °C. — **^{1}H NMR** (500 MHz, DMSO-d_6) δ = 11.89 (s, 1H, N-H), 7.80 (d, J = 8.2 Hz, 1H, 4-H), 7.52–7.40 (m, 5H, 2''-H, 3''-H, 4''-H), 7.40–7.36 (m, 1H, 7-H), 7.22–7.17 (m, 1H, 6-H), 7.17–7.11 (m, 1H, 5-H), 3.49 (q, J = 6.9 Hz, 2H, 1'''-H), 1.04 (t, J = 6.9 Hz, 3H, 2'''-H). —**^{13}C NMR** (126 MHz, DMSO-d_6) δ = 139.9 (s, 1''-C), 135.1 (s,7a-C), 133.0 (s, 2-C), 130.4 (s, 2C, 2''-C), 128.9 (s, 4''-C), 127.5 (s, 2C, 3''-C), 126.3 (s, 3a-C), 122.1 (s, 6-C), 120.9 (s, 4-C), 120.4 (s, 5-C), 111.5 (s, 7-C), 98.0 (s, 3-C), 82.6–81.6 (m, 1'-C), 61.8 (s, 1'''-C), 14.5 (s, 2'''-C). — **^{19}F NMR** (282 MHz, DMSO-d_6) δ = –71.3 (s, 6F, 2'-F). — **IR (neat):** $\tilde{\nu}$ = 3398 m, 3060 w, 3004 w, 2913 w, 1547 w, 1487 w, 1456 m, 1421w, 1356 w, 1331 w, 1298 w, 1279 m, 1259 s, 1241 m, 1212 s, 1183 m, 1172 s, 1145 m, 1116 m, 1090 s, 1072 s, 1025 m, 979 s, 918 m, 892 m, 848 w, 820 w, 774 m, 764 m, 752 s, 729 m, 702 s, 662 m, 626 m, 619 m, 605 m, 589 m, 571 m, 549 m, 542 m, 514 m, 479 w, 455 w, 423 w, 409 w cm^{-1}. — **EI (HR-MS)** calcd. for $C_{19}H_{15}F_6NO$: 387.10578; found 387.10791.

2.4.5 Offline NMR analysis

2-Methyl-3-(perfluorobutyl)-1*H*-indole (3a)

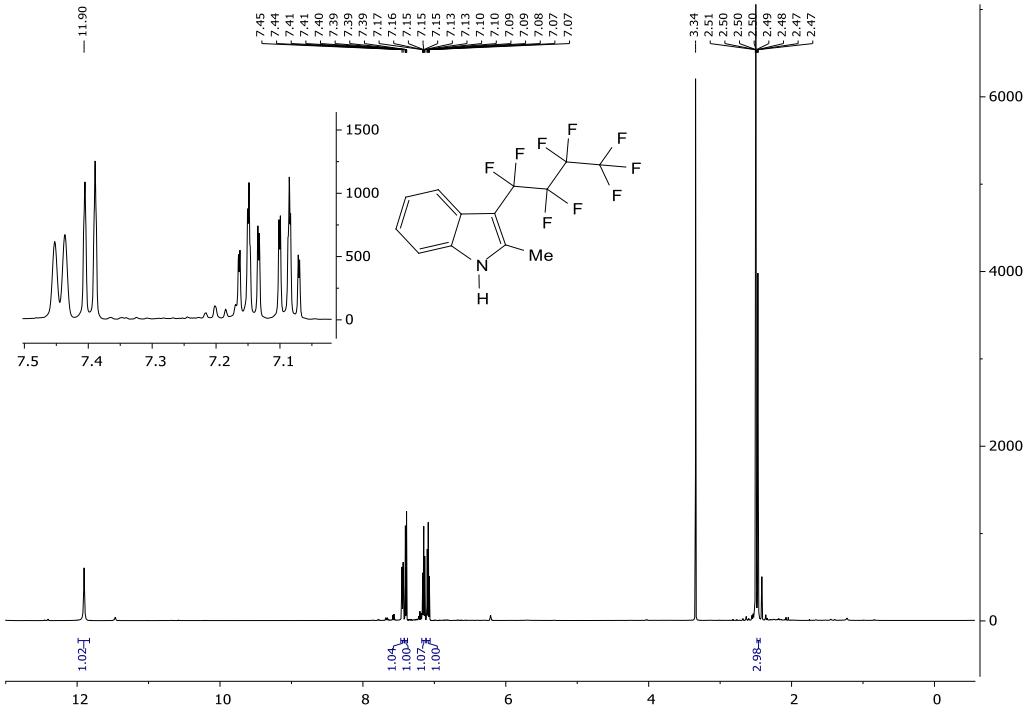

^{1}H–NMR: (500 MHz, DMSO-d_6).

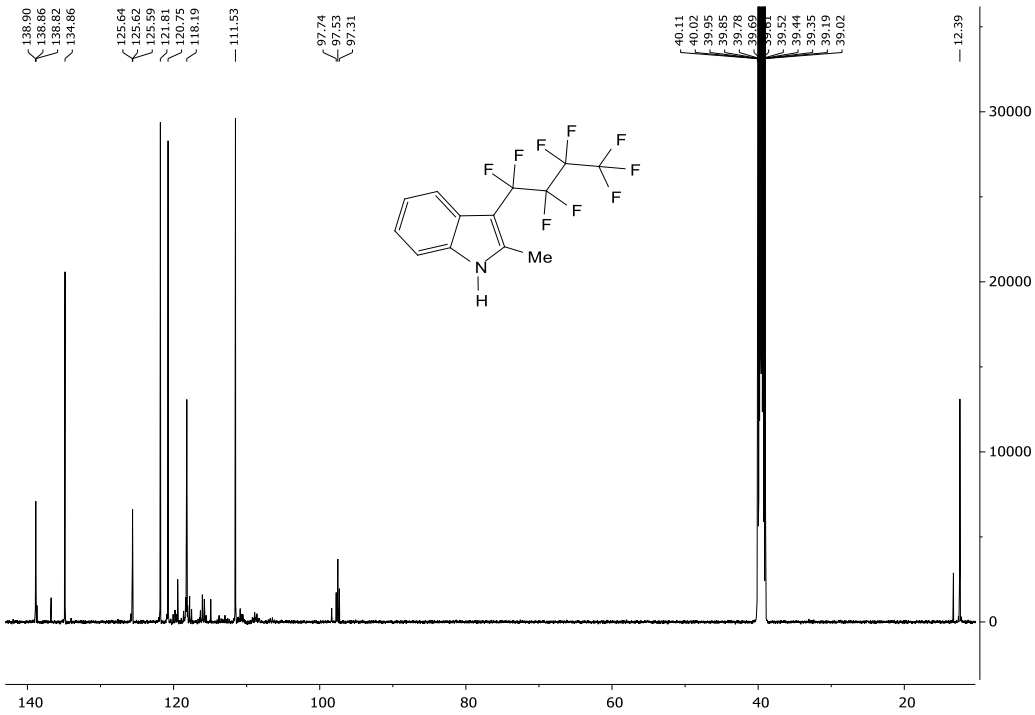

^{13}C–NMR: (126 MHz, DMSO-d_6).

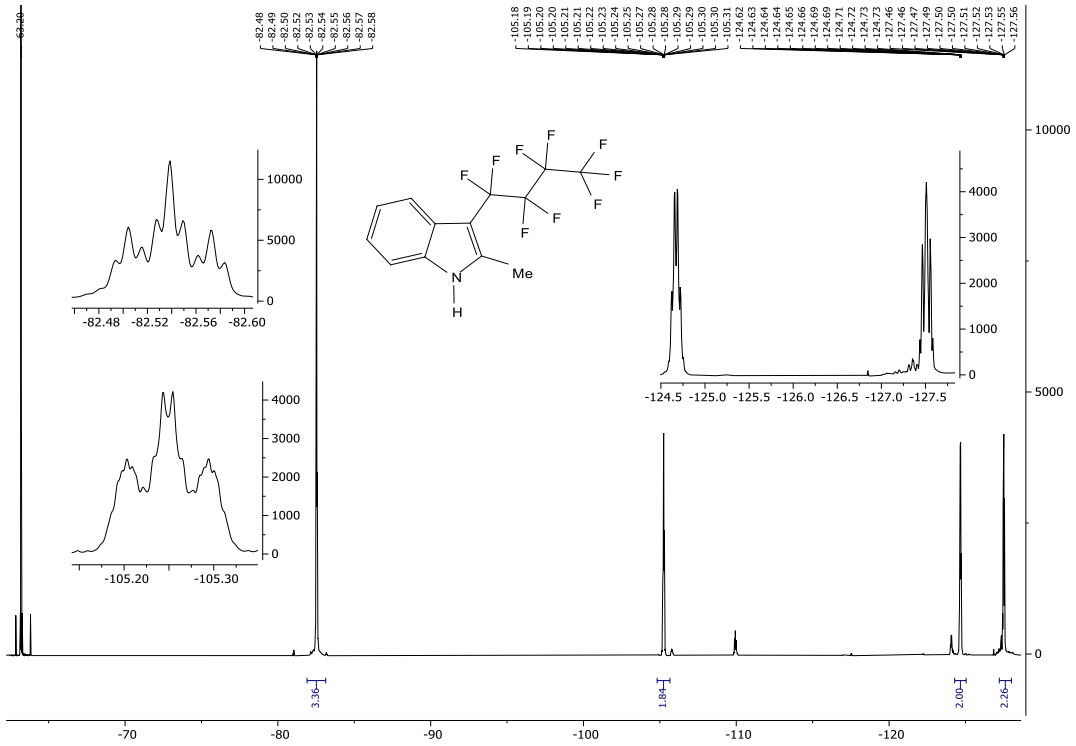

^{19}F–NMR: (282 MHz, DMSO-d_6).

3-(Perfluorobutyl)-2-phenyl-1*H*-indole (3b)

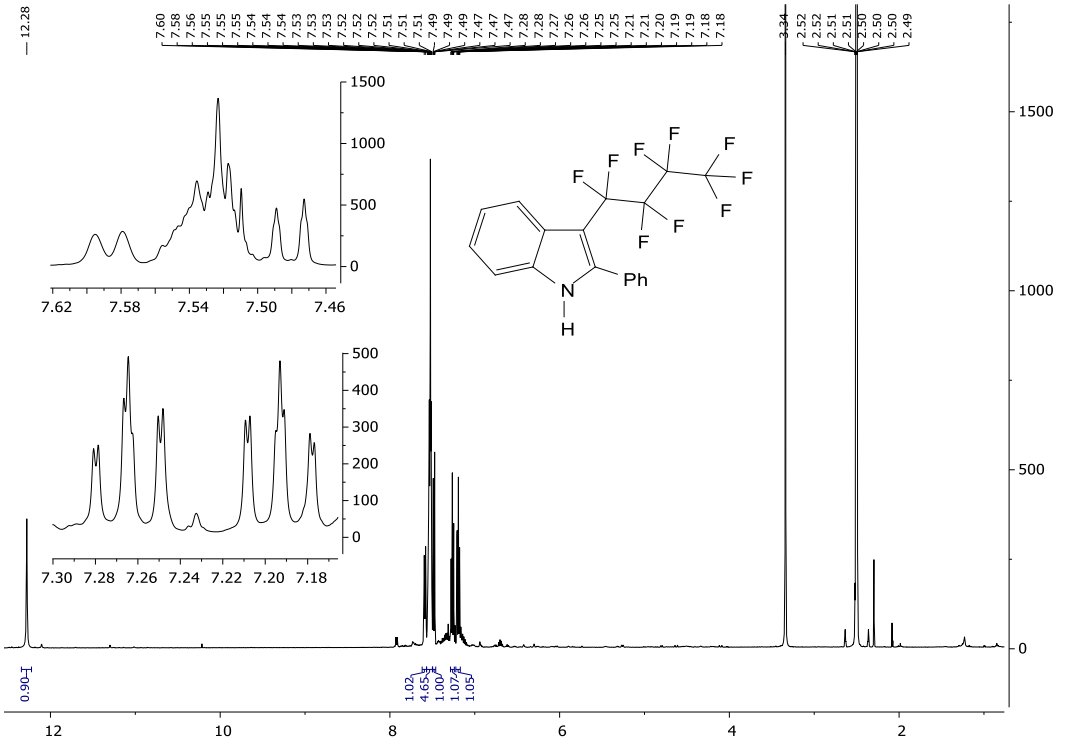

^{1}H–NMR: (500 MHz, DMSO-d_6).

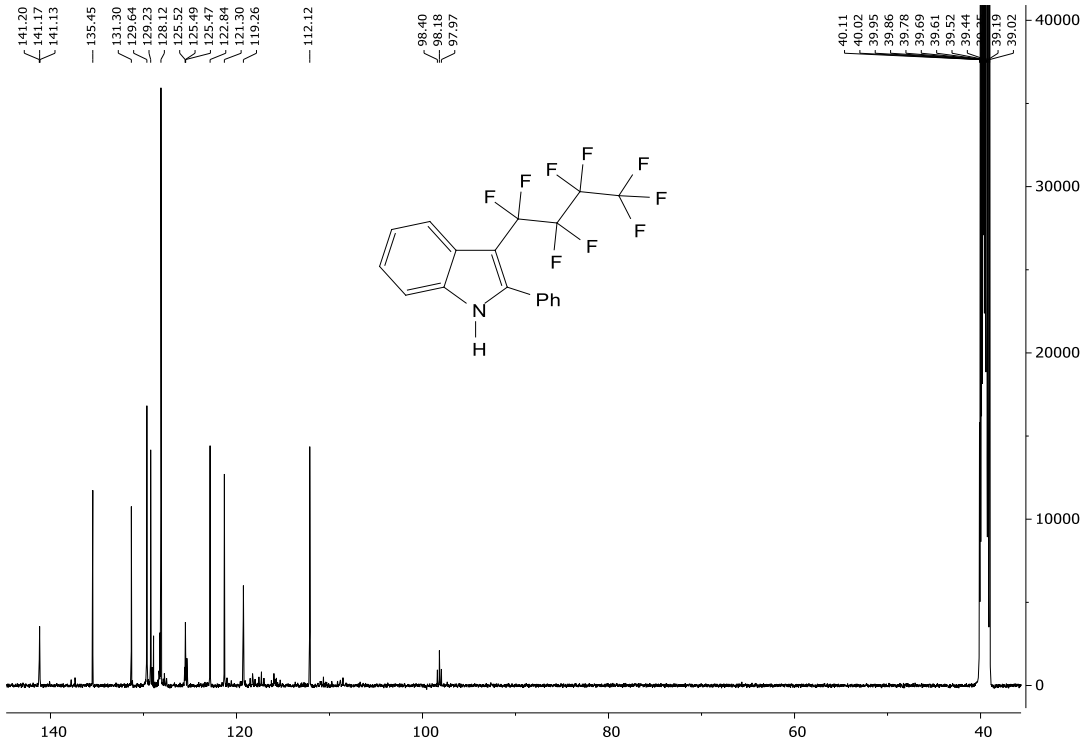

^{13}C–NMR: (126 MHz, DMSO-d_6).

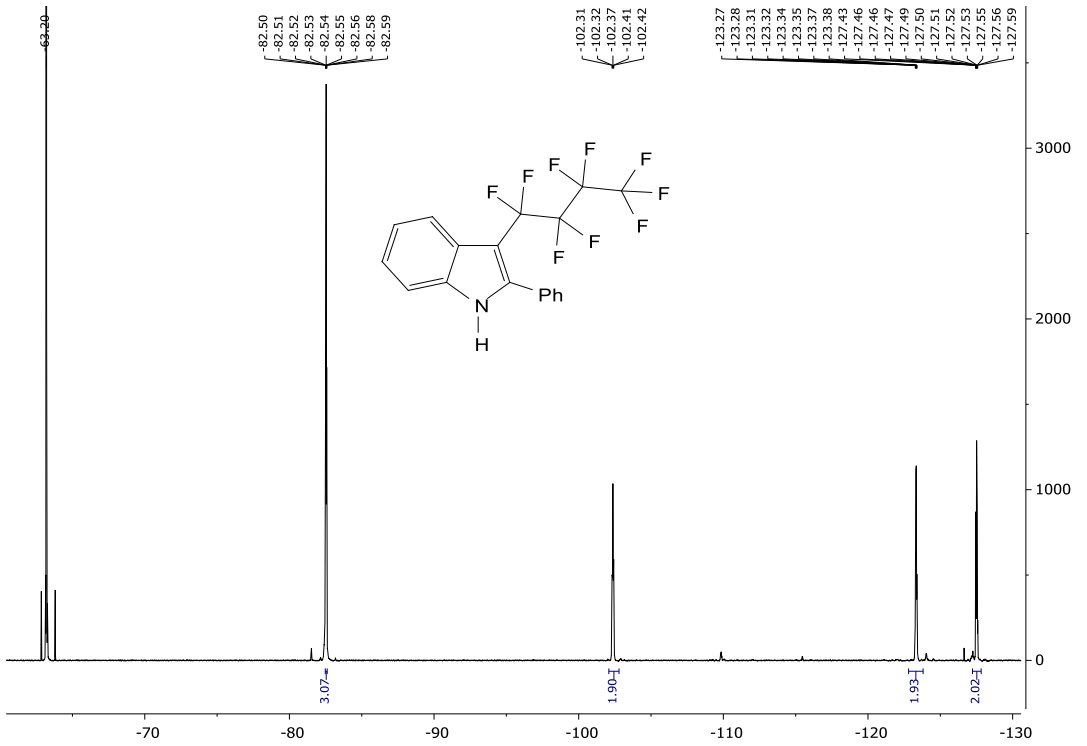

^{19}F–NMR: (282 MHz, DMSO-d_6).

1,2-Dimethyl-3-(perfluorobutyl)-1*H*-indole (6)

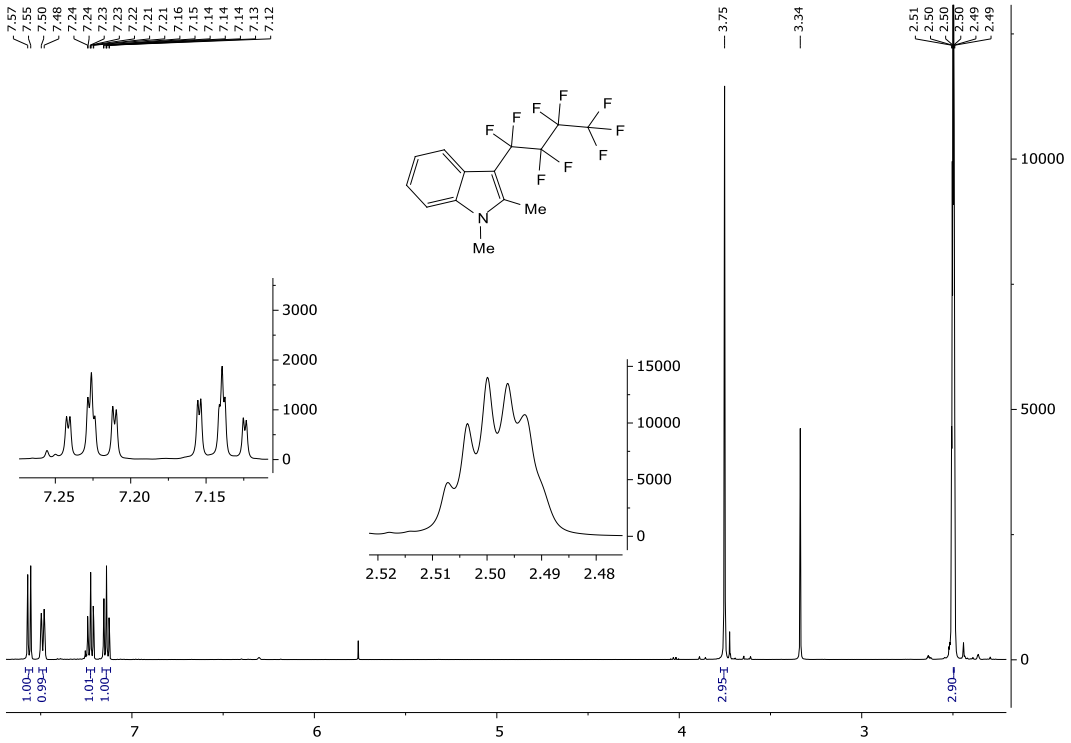

^{1}H–NMR: (500 MHz, DMSO-d_6).

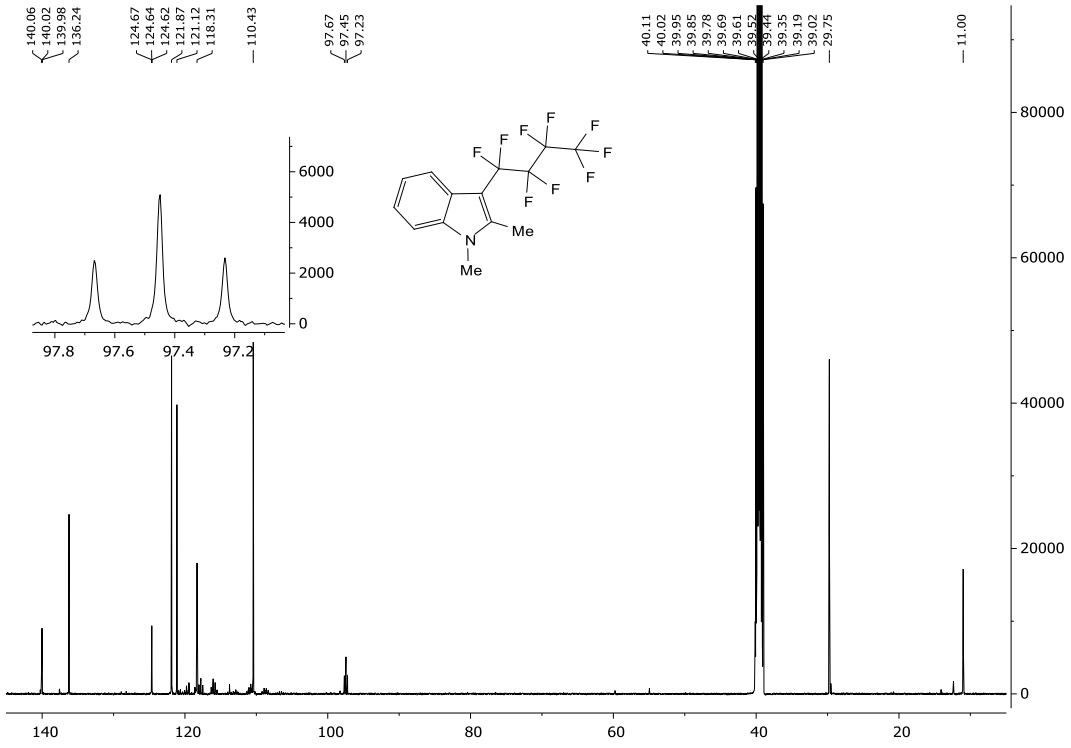

^{13}C–NMR: (126 MHz, DMSO-d_6).

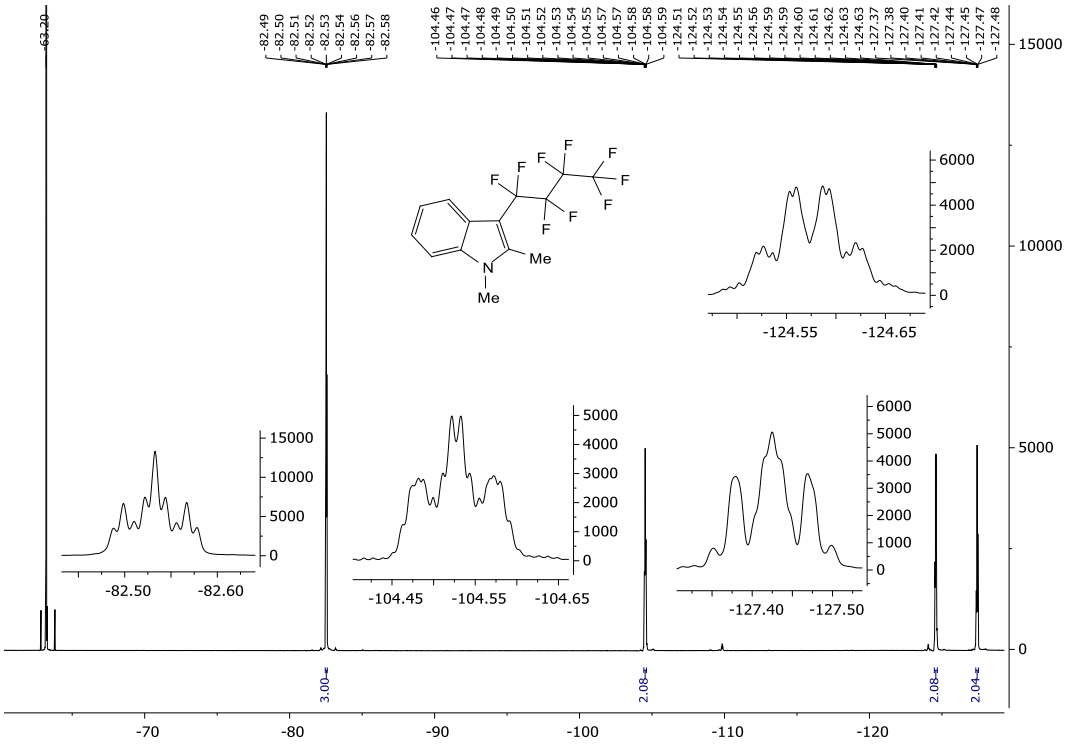

^{19}F–NMR: (282 MHz, DMSO-d_6).

3-(perfluoropropan-2-yl)-2-phenyl-1H-indole (9)

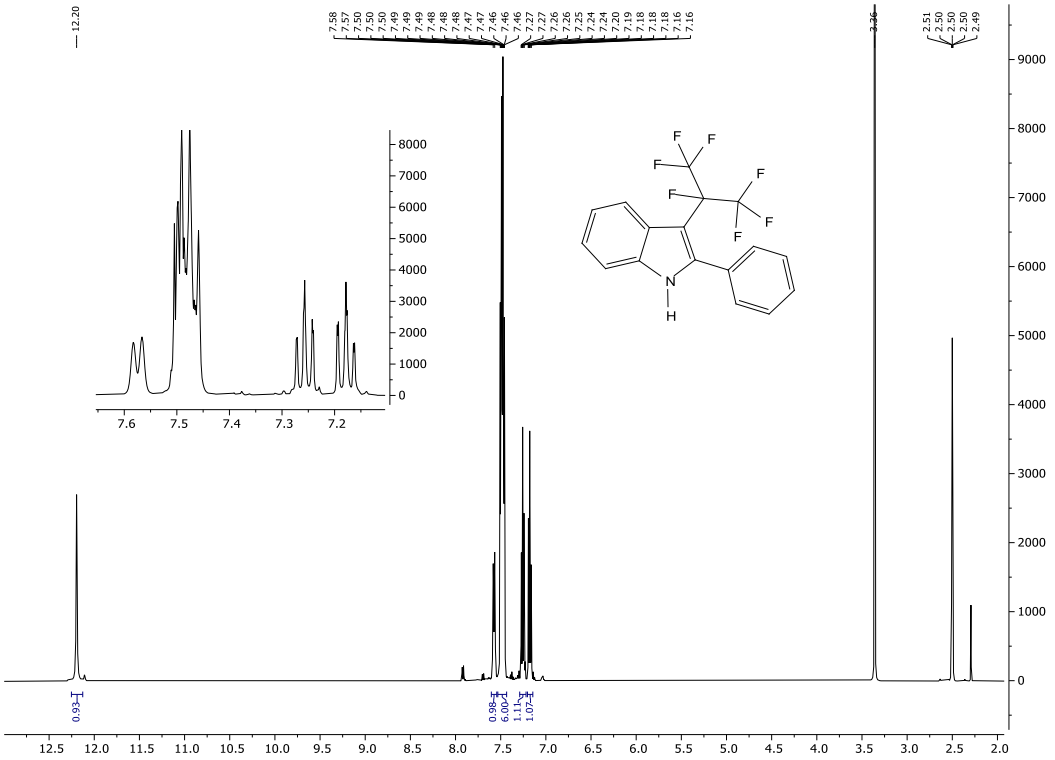

^{1}H–NMR: (500 MHz, DMSO-d_6).

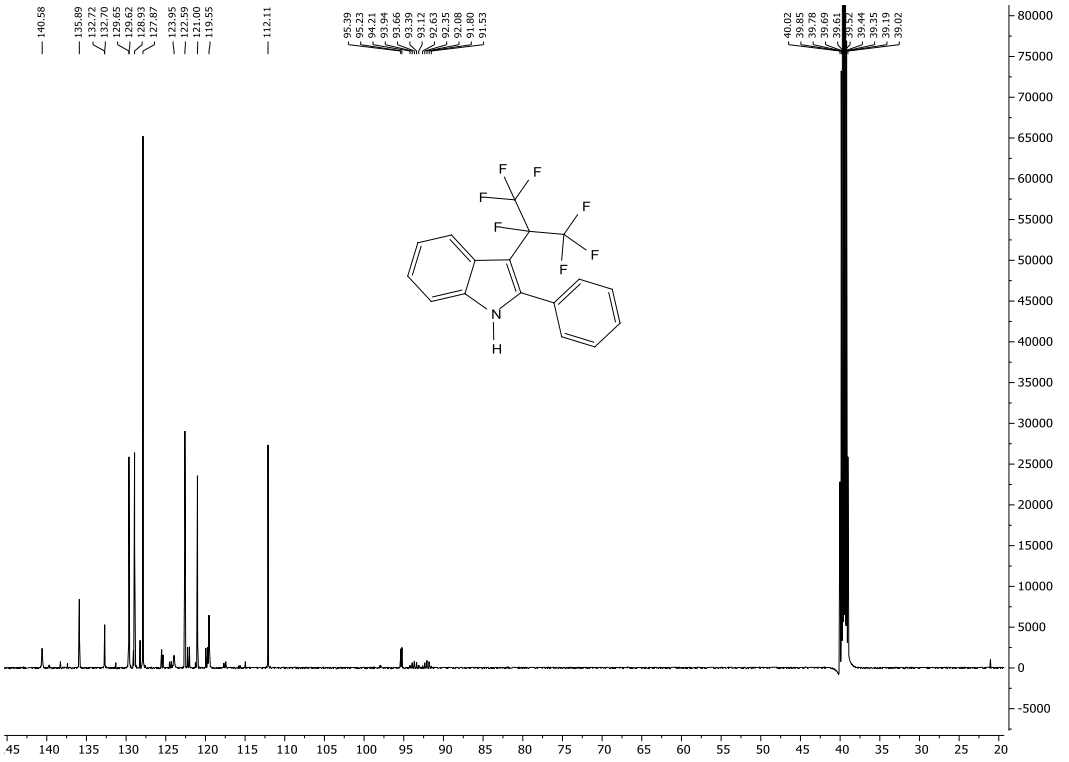

^{13}C–NMR: (126 MHz, DMSO-d_6).

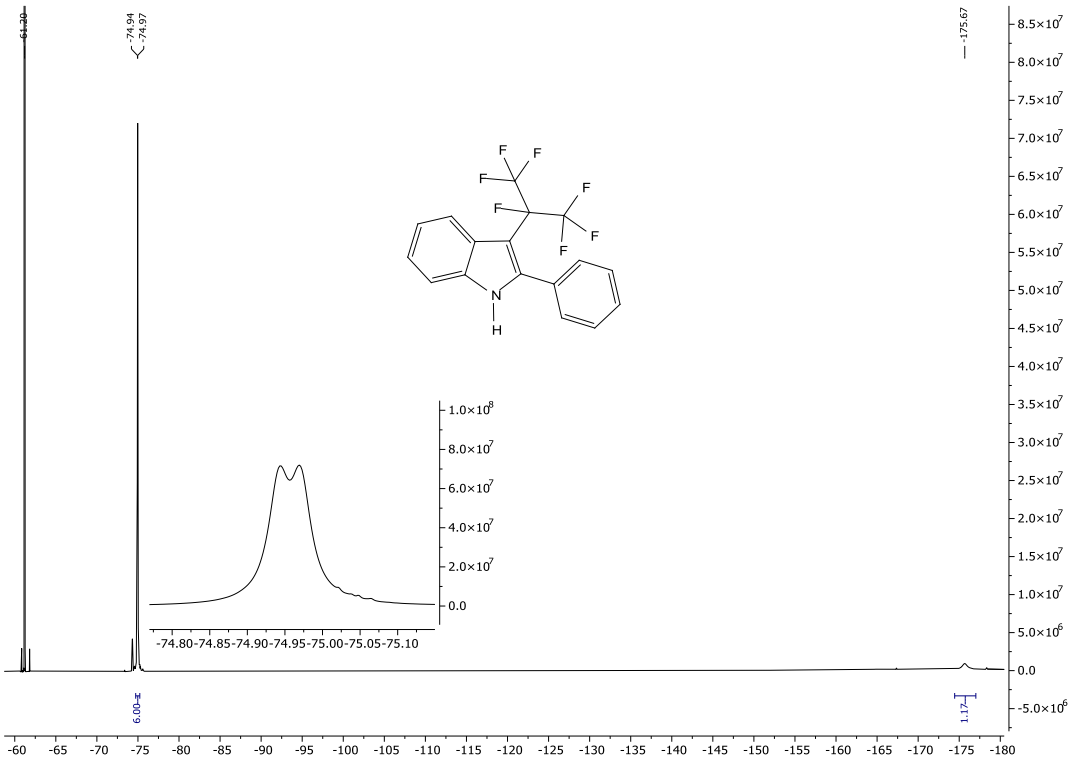

^{19}F–NMR: (282 MHz, DMSO-d_6).

2,2,3,3,4,4,4-Heptafluoro-1-(2-methyl-1*H*-indol-3-yl)butan-1-one (5a)

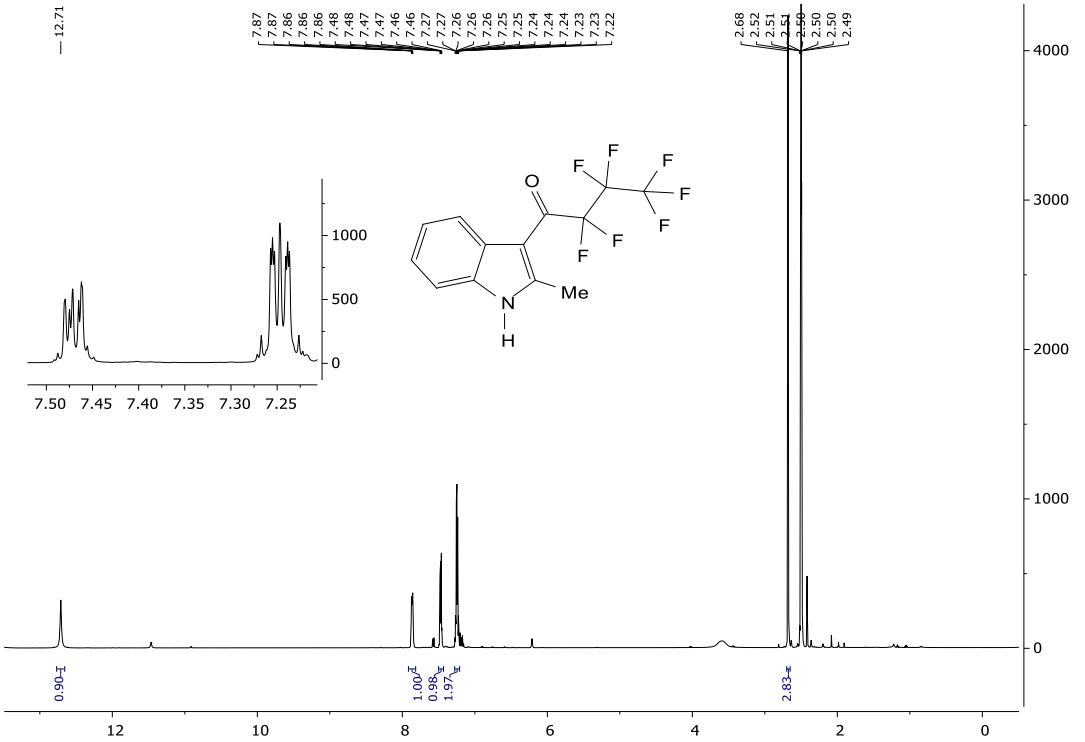

^{1}H–NMR: (500 MHz, DMSO-d_6).

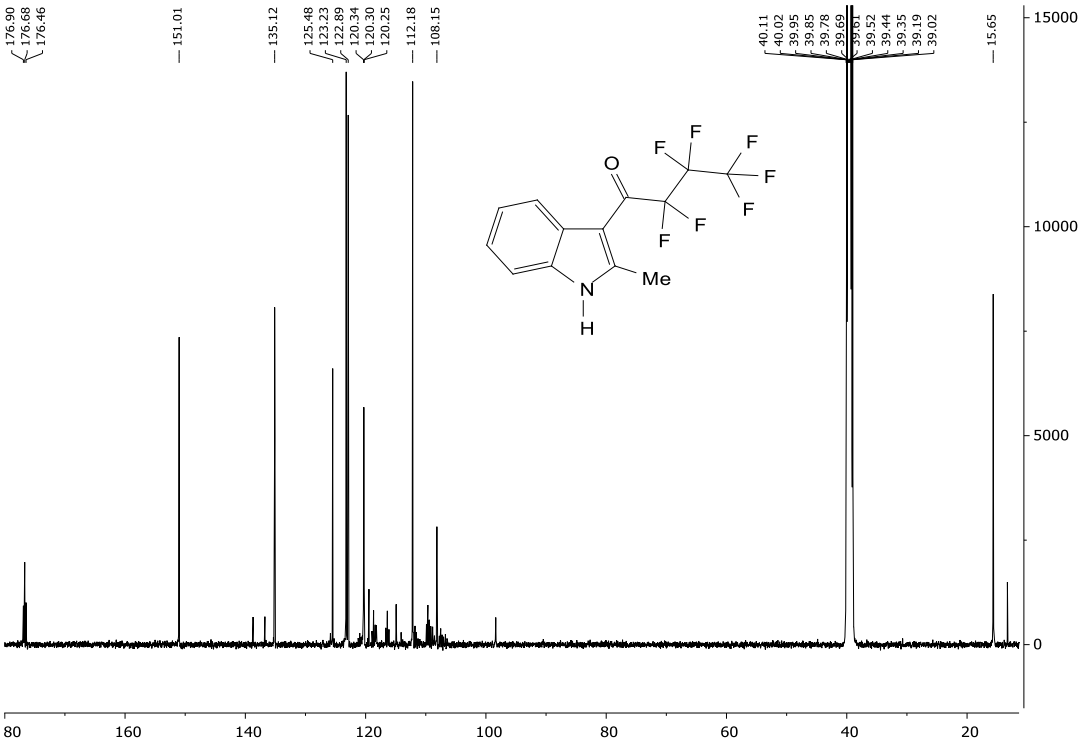

^{13}C–NMR: (126 MHz, DMSO-d_6).

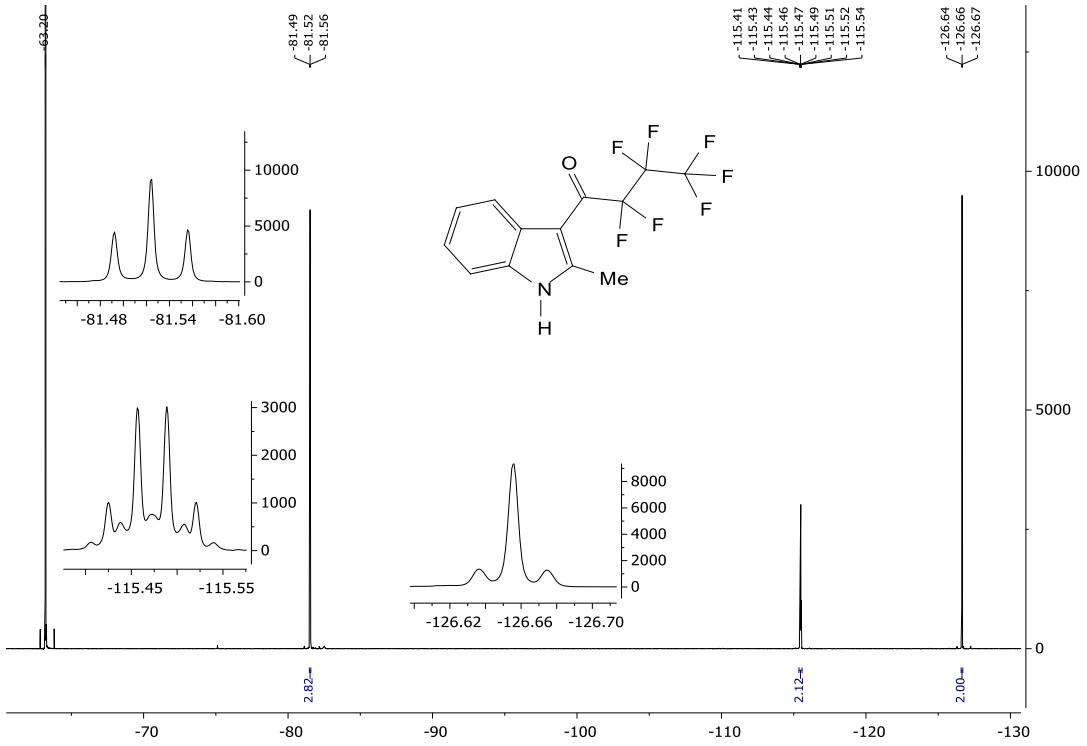

^{19}F–NMR: (282 MHz, DMSO-d_6).

2,2,3,3,4,4,4-Heptafluoro-1-(2-phenyl-1*H*-indol-3-yl)butan-1-one (5b)

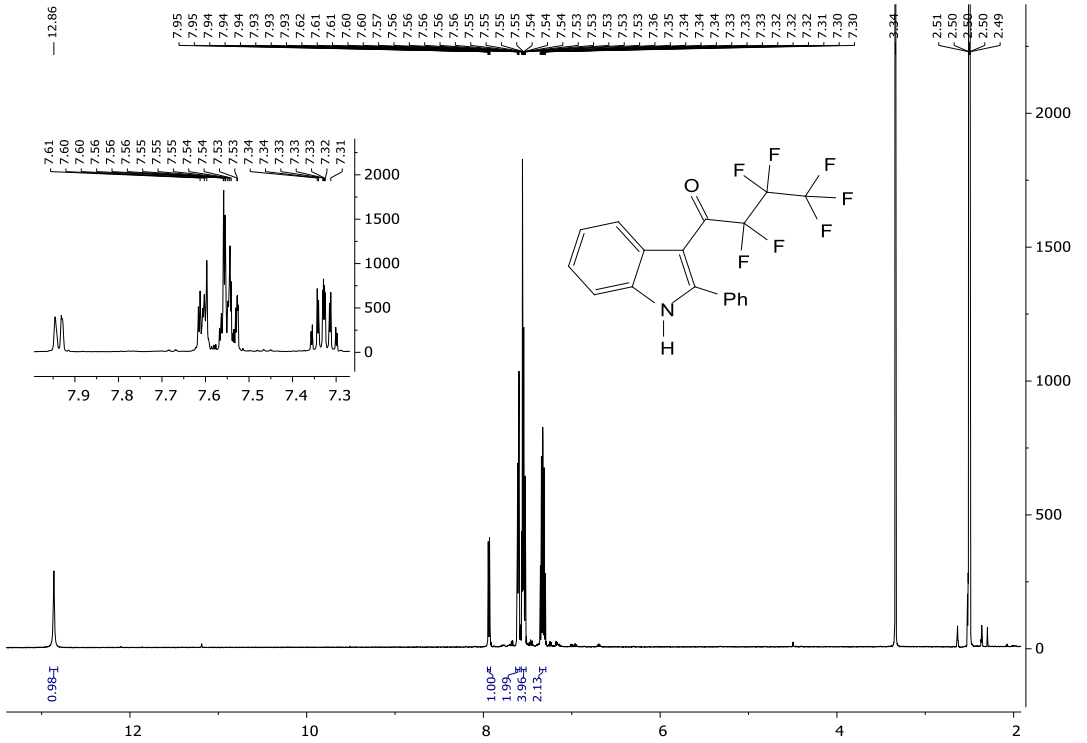

^{1}H–NMR: (500 MHz, DMSO-d_6).

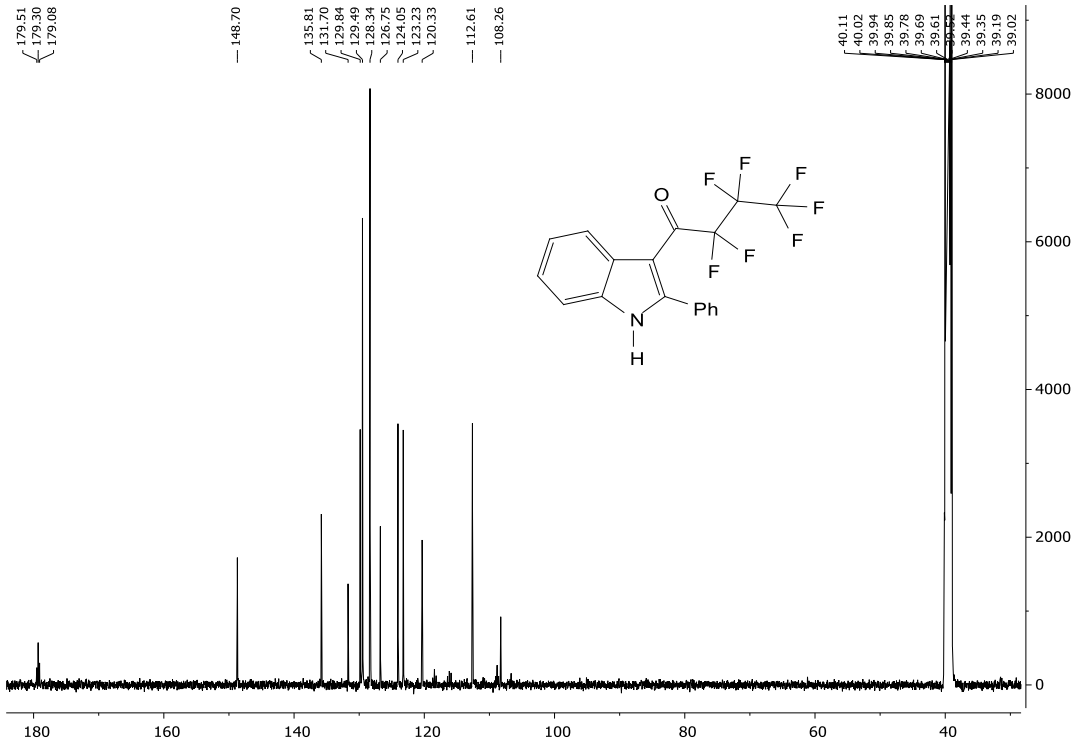

^{13}C–NMR: (126 MHz, DMSO-d_6).

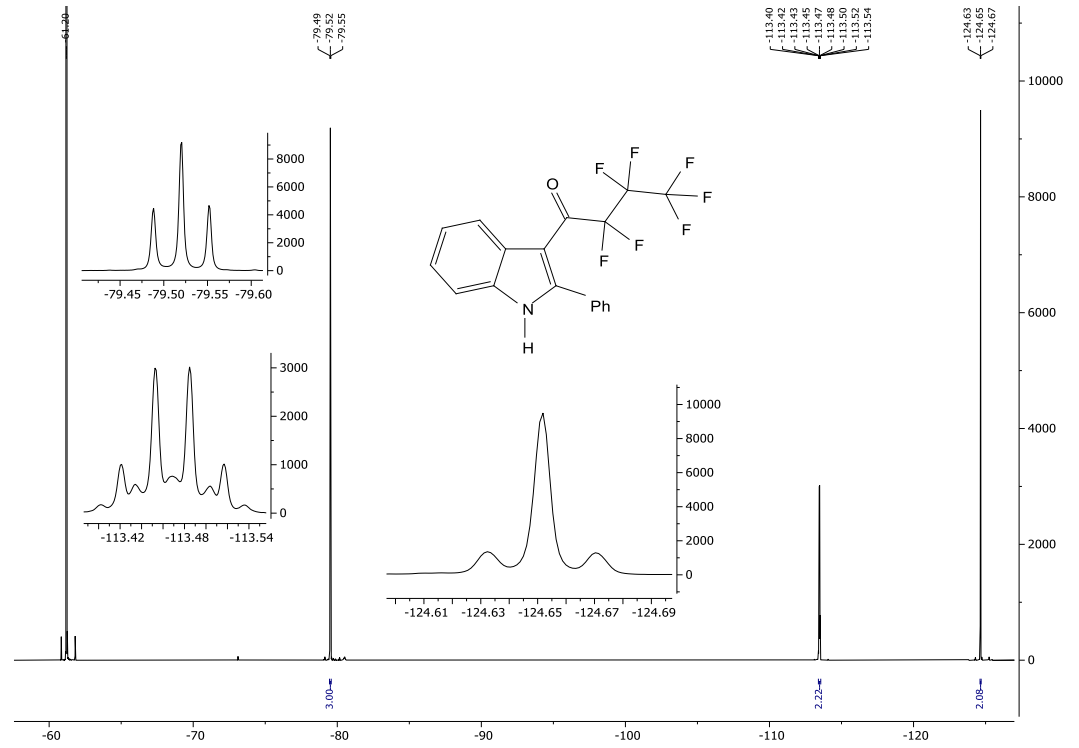

^{19}F–NMR: (282 MHz, DMSO-d_6).

1,1,1,3,3,3-hexafluoro-2-(2-phenyl-1H-indol-3-yl)propan-2-ol (10)

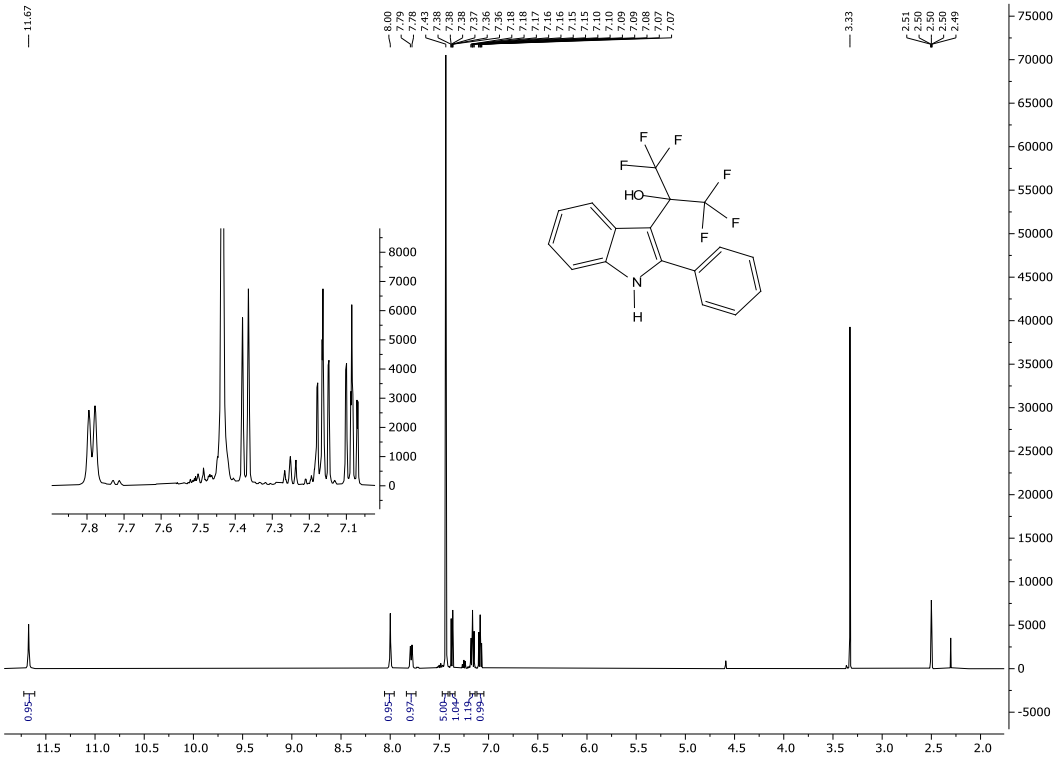

^{1}H–NMR: (500 MHz, DMSO-d_6).

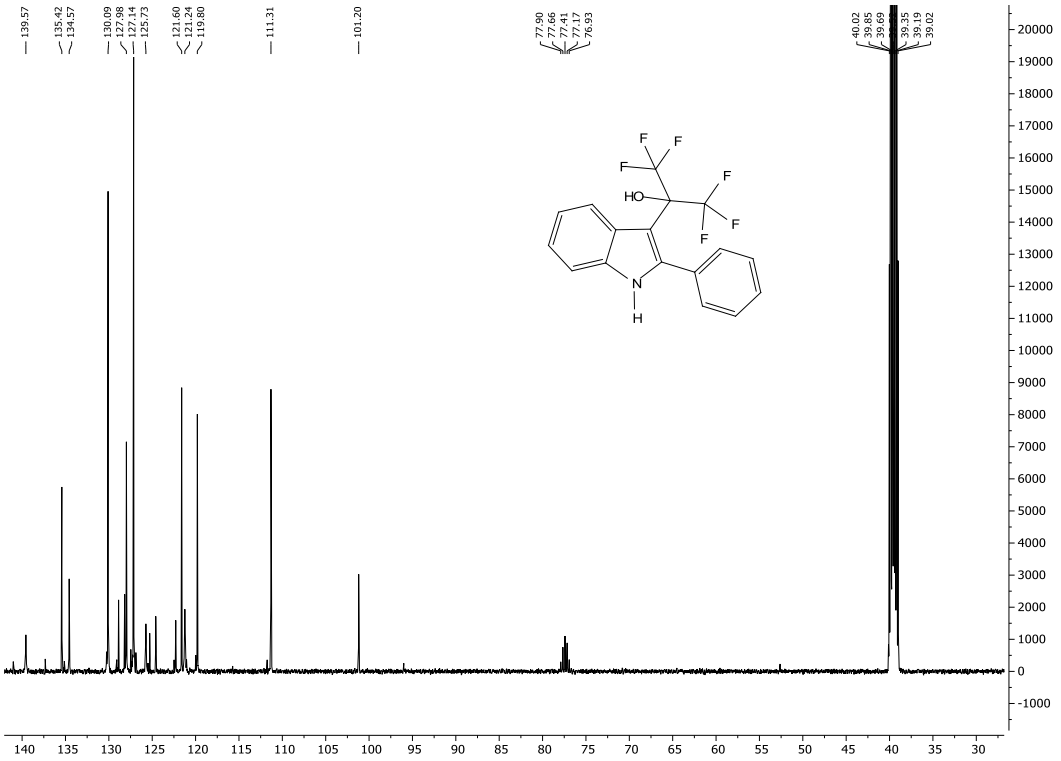

^{13}C–NMR: (126 MHz, DMSO-d_6).

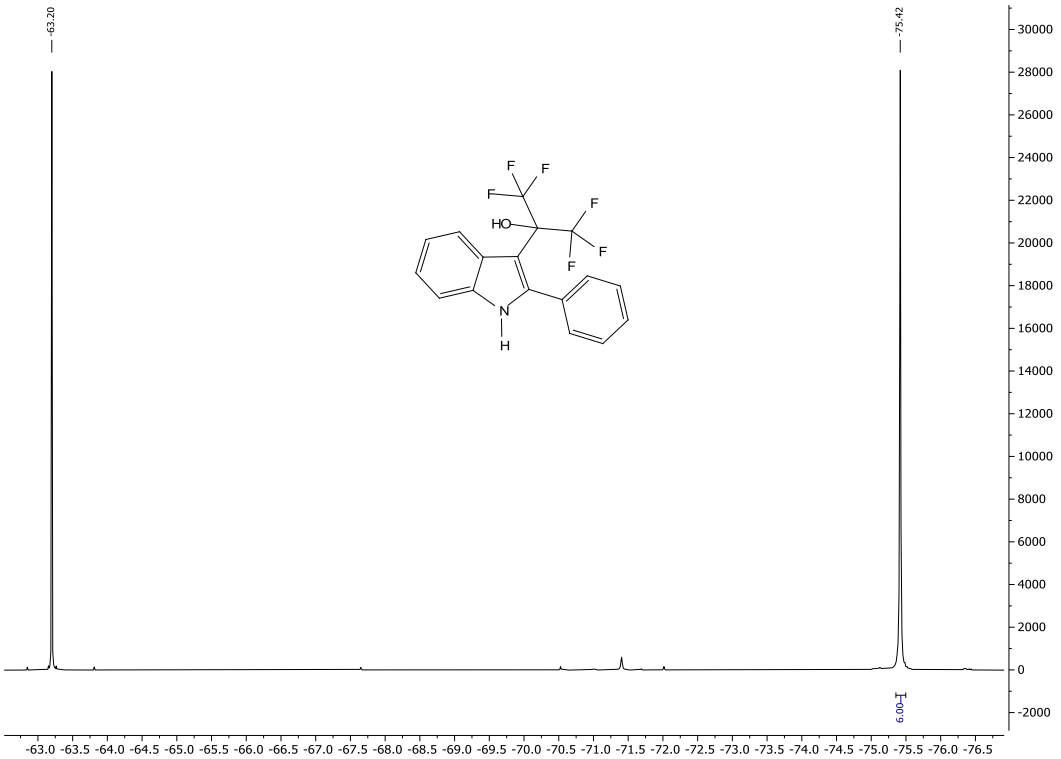

^{19}F–NMR: (282 MHz, DMSO-d_6).

3-(1,1-Diethoxy-2,2,3,3,4,4,4-heptafluorobutyl)-2-methyl-1*H*-indole (8a)

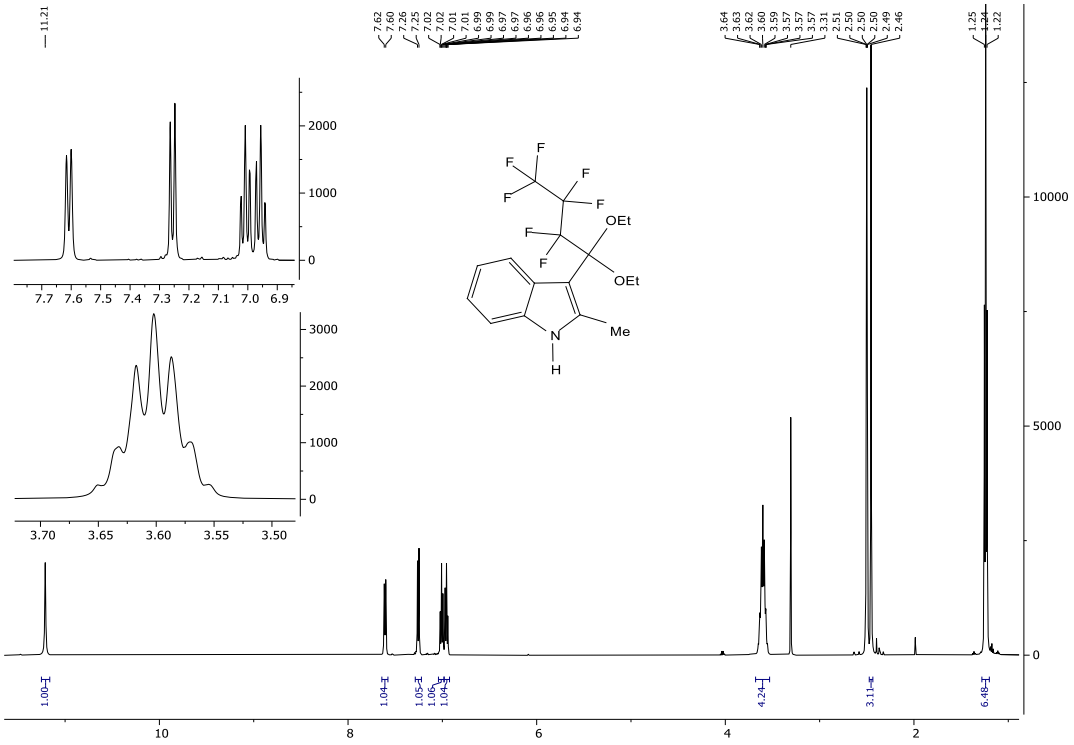

^{1}H–NMR: (500 MHz, DMSO-d_6).

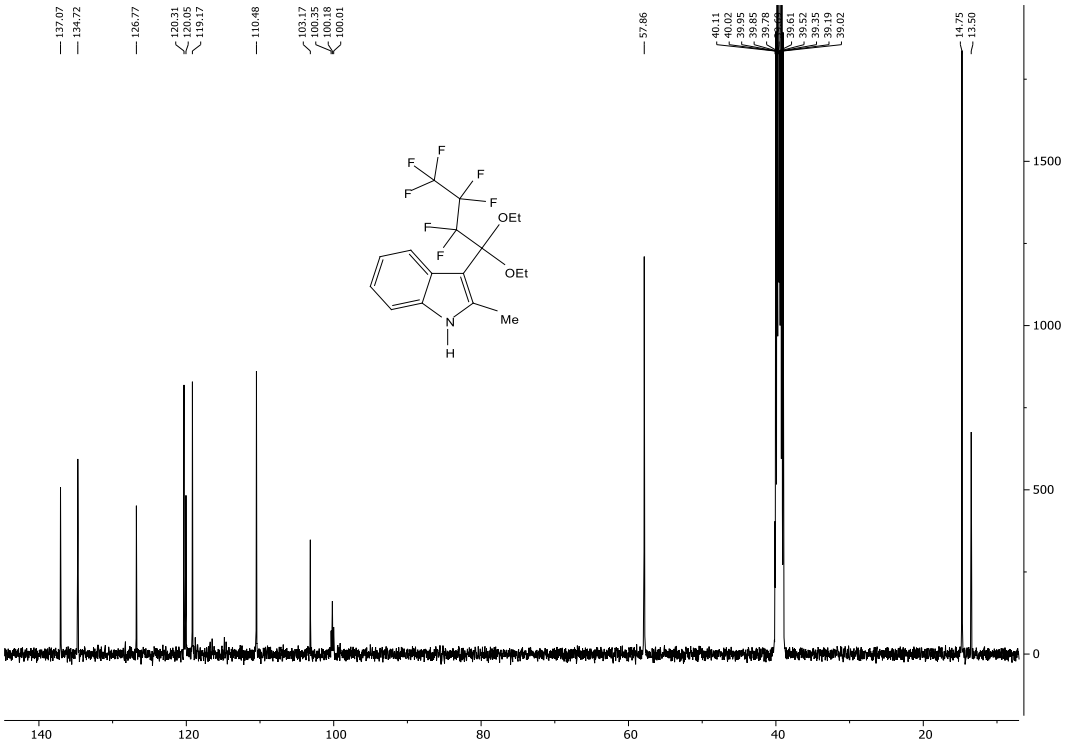

^{13}C–NMR: (126 MHz, DMSO-d_6).

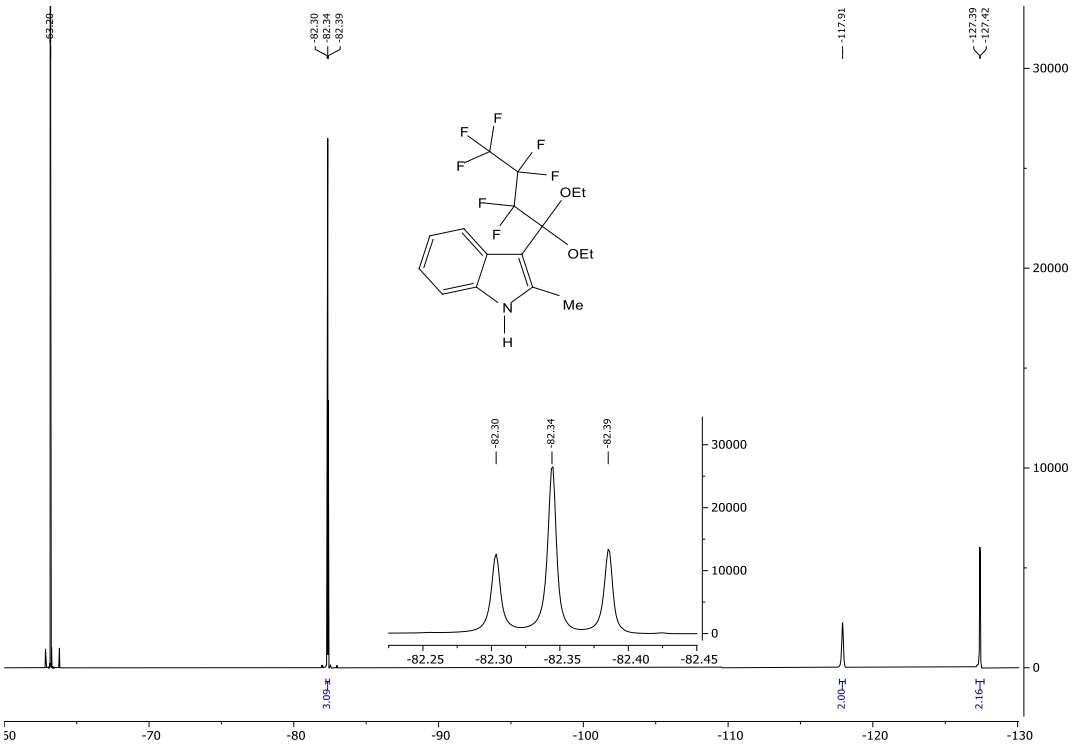

^{19}F–NMR: (282 MHz, DMSO-d_6).

3-(1,1-Diethoxy-2,2,3,3,4,4,4-heptafluorobutyl)-2-phenyl-1*H*-indole (8b)

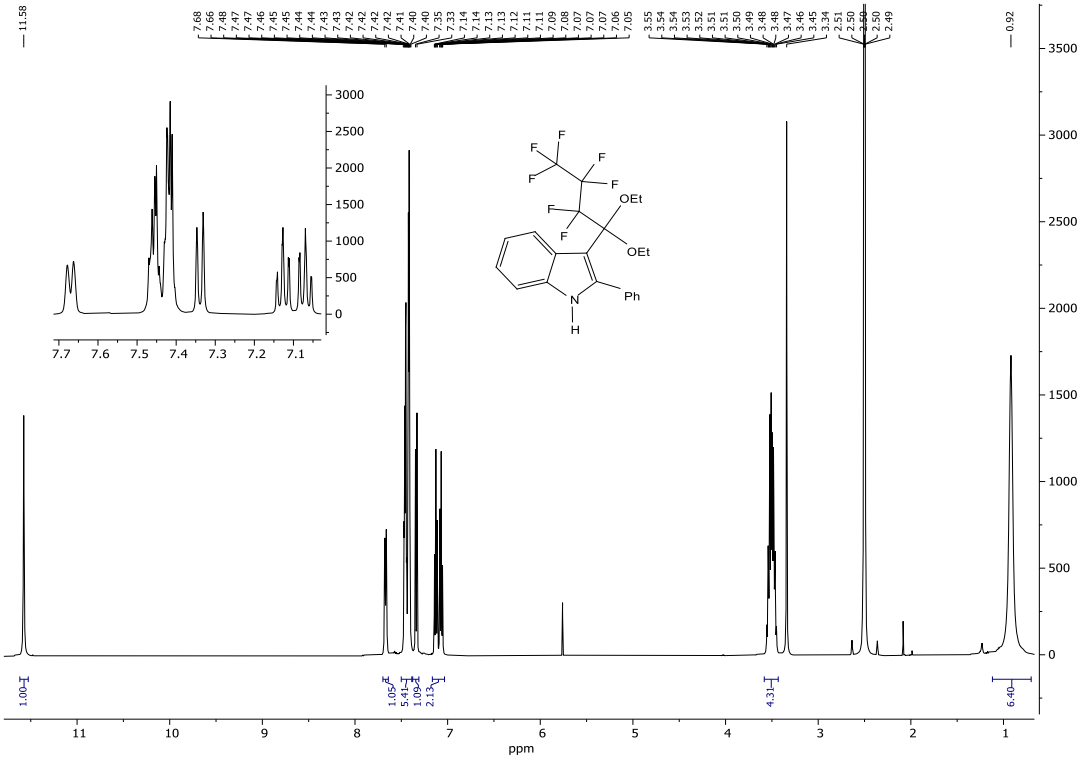

^{1}H–NMR: (500 MHz, DMSO-d_6).

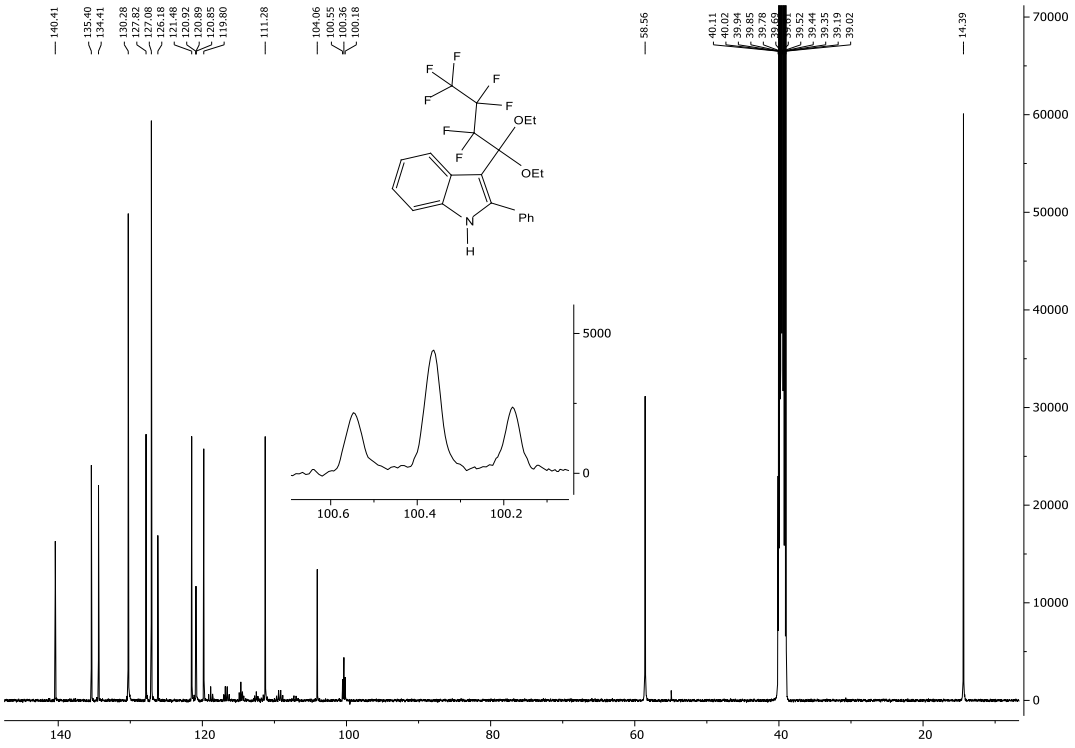

^{13}C–NMR: (126 MHz, DMSO-d_6).

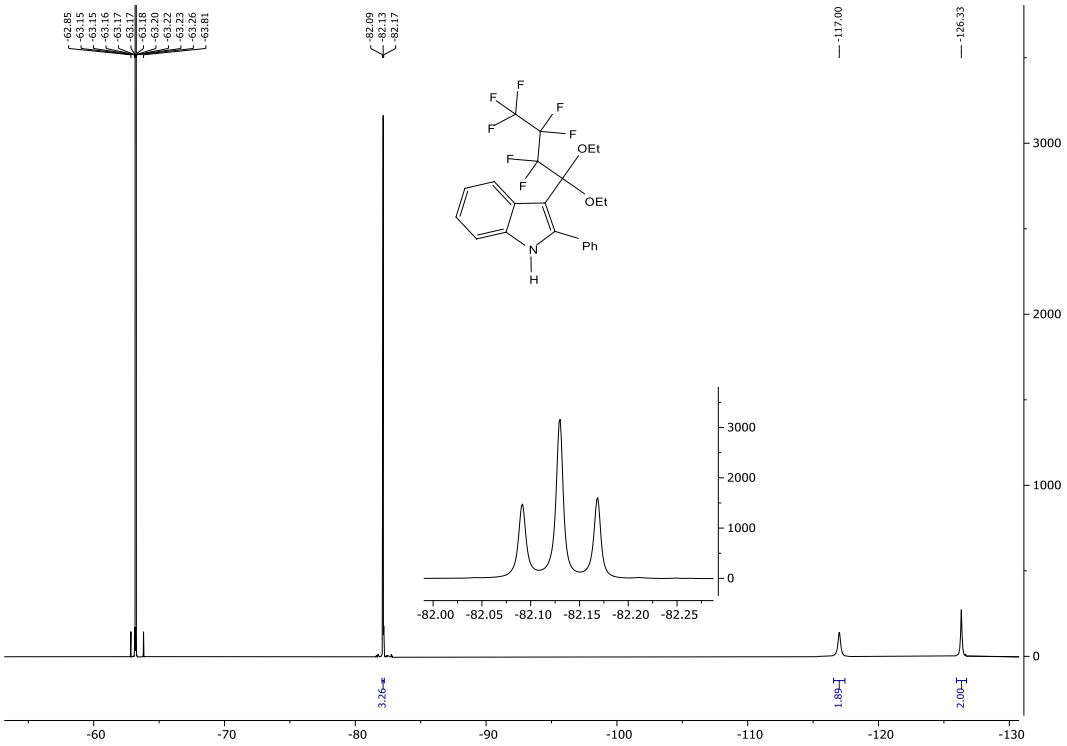

^{19}F–NMR: (282 MHz, DMSO-d_6).

3-(2-ethoxy-1,1,1,3,3,3-hexafluoropropan-2-yl)-2-phenyl-1H-indole (11)

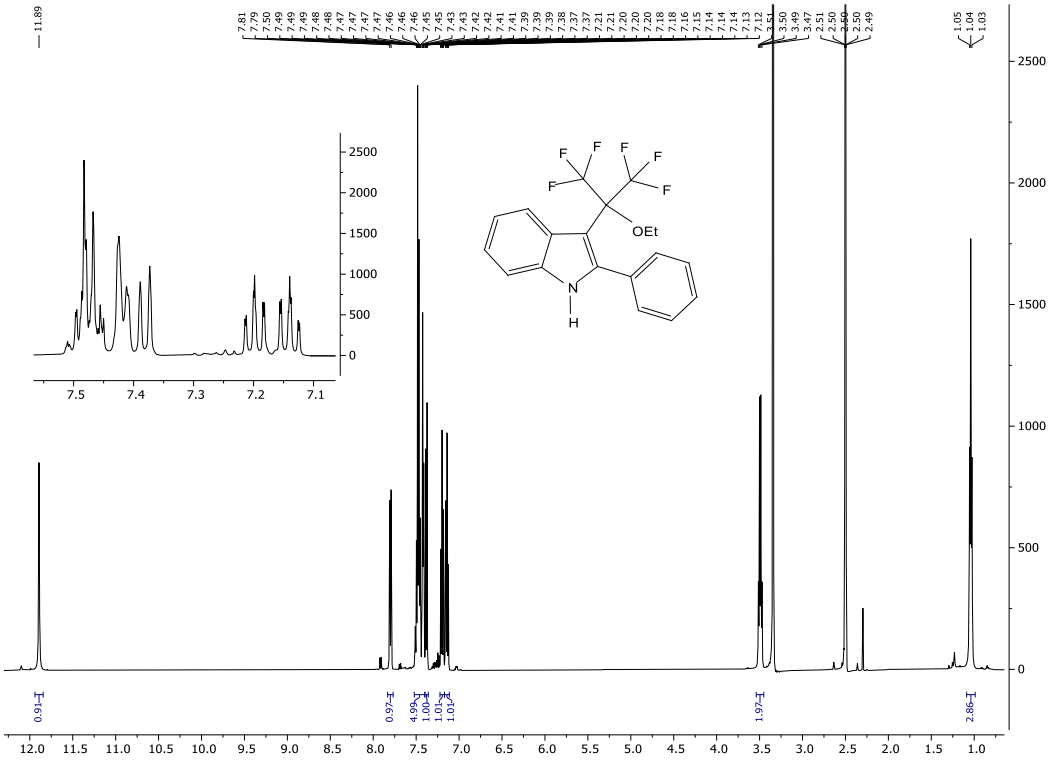

^{1}H–NMR: (500 MHz, DMSO-d_6).

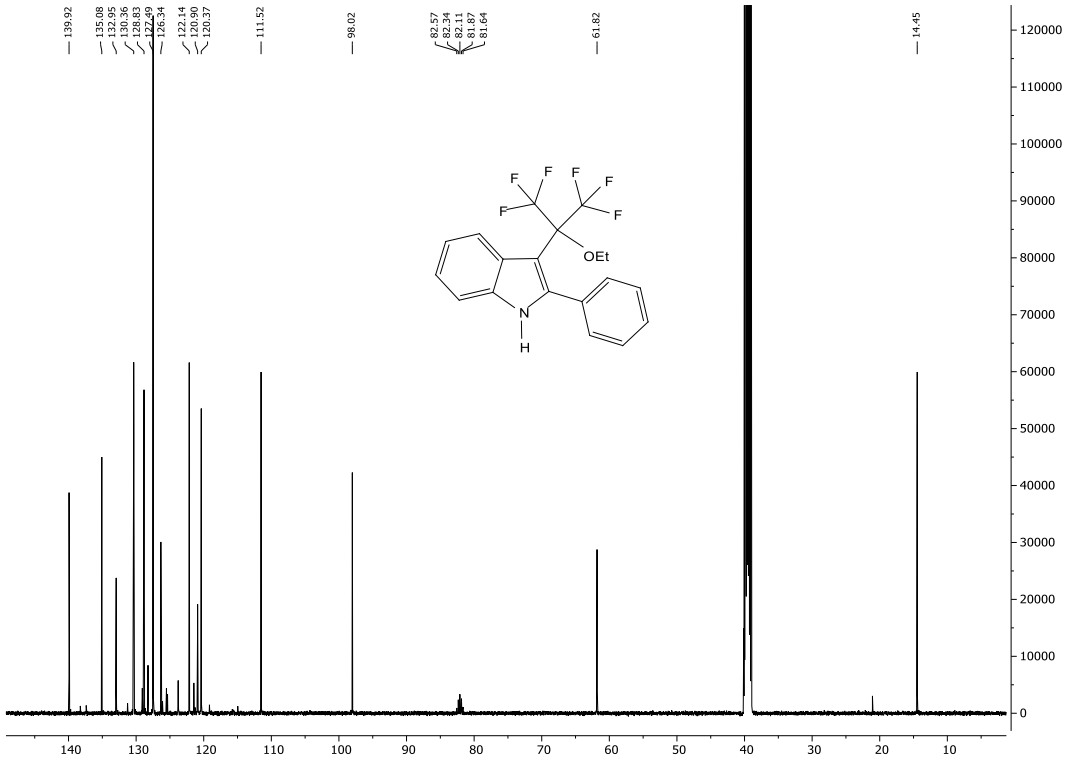

^{13}C–NMR: (126 MHz, DMSO-d_6).

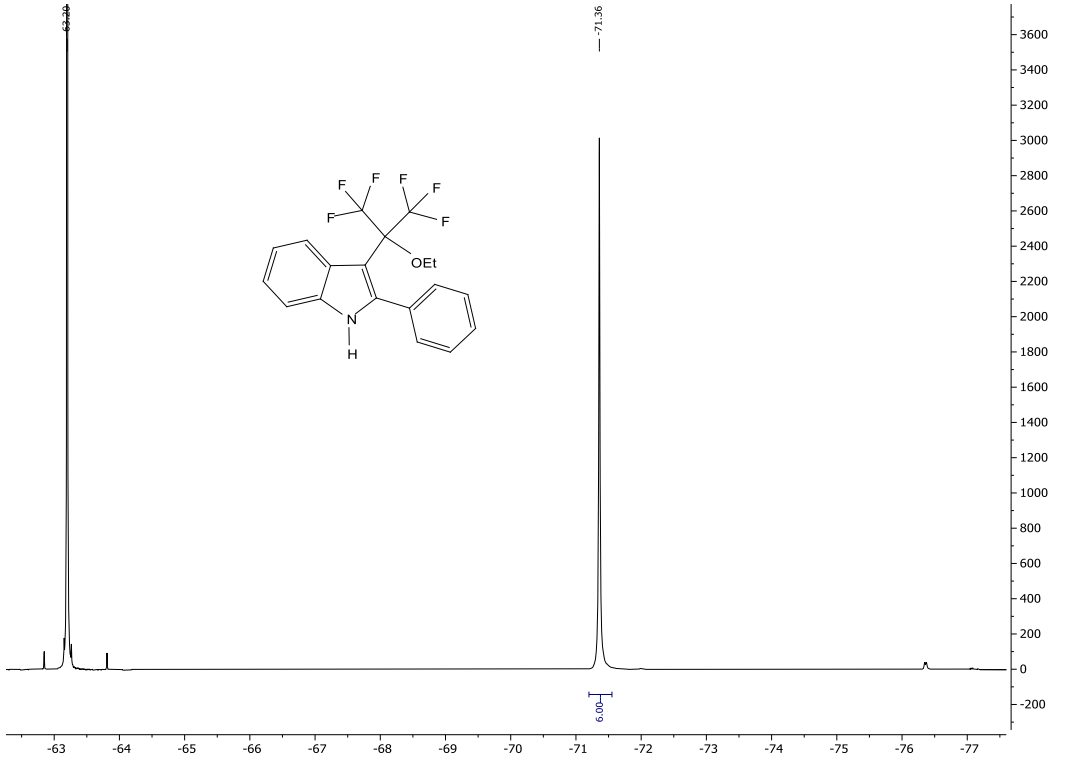

^{19}F–NMR: (282 MHz, DMSO-d_6).

2.4.6 X-ray crystallography

A suitable crystal of $C_{22}H_{20}F_7NO_2$ was selected under inert oil and mounted using a MiTeGen loop. Intensity data of the crystal were recorded with a STADIVARI diffractometer (Stoe & Cie). The diffractometer was operated with Cu-Kα radiation (1.54186 Å, microfocus source) and equipped with a Dectris PILATUS 300K detector. Evaluation, integration and reduction of the diffraction data was carried out using the X-Area software suite.[S4] Multi-scan and numerical absorption corrections were applied with the X-Red32 and LANA modules of the X-Area software suite.[S5,S6] The structure was solved using dual-space methods (SHELXT-2014/5) and refined against F^2 (SHELXL-2018/3).[S7,S8] All non-hydrogen atoms were refined with anisotropic displacement parameters. The hydrogen atom bonded to the nitrogen atom was refined unrestrained. The other hydrogen atoms were refined using the "riding model" approach with isotropic displacement parameters 1.2 times (for CH_3 groups 1.5 times) of that of the preceding carbon atom. CCDC 2180131 contains the supplementary crystallographic data for this paper. These data can be obtained free of charge from The Cambridge Crystallographic Data Centre via www.ccdc.cam.ac.uk/structures.

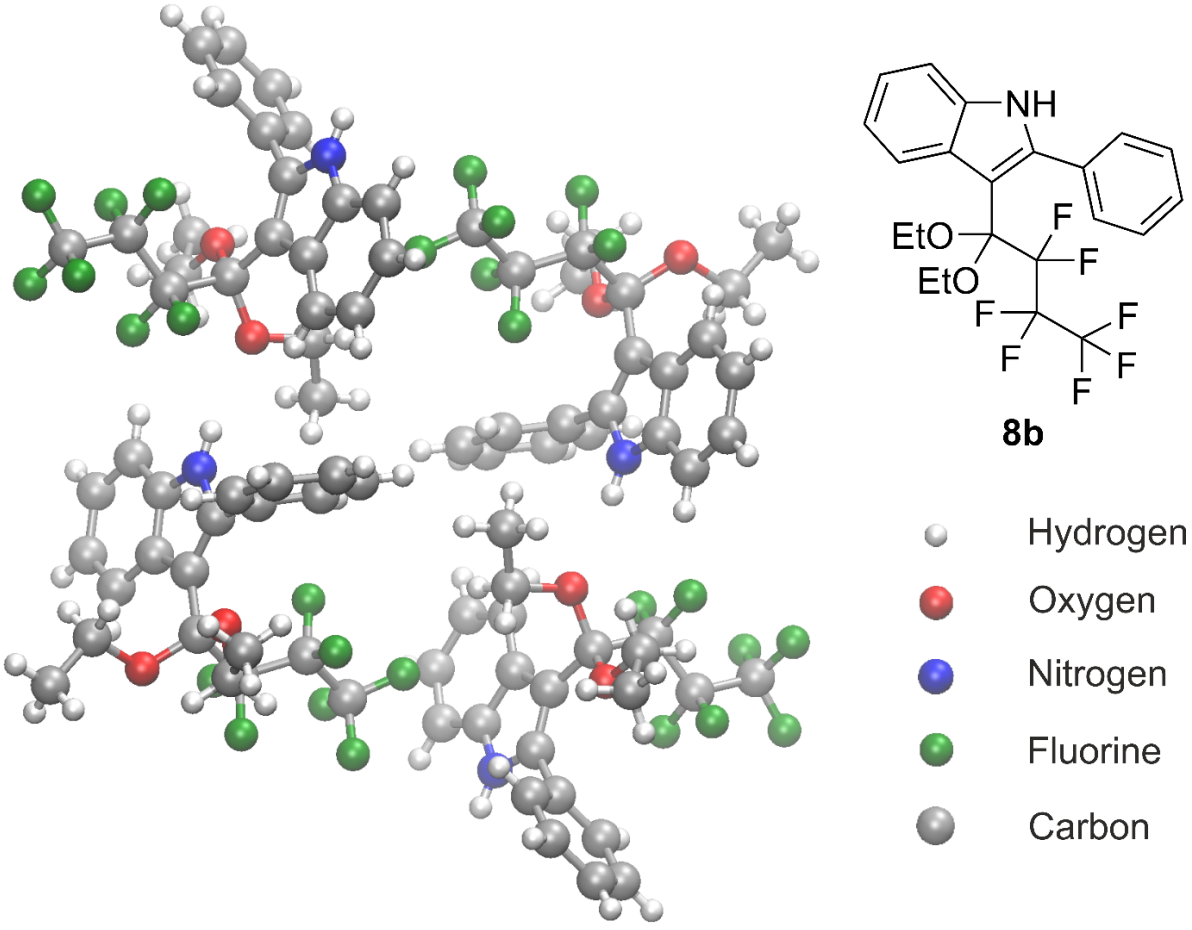

Table 2.S3. Selected crystallographic data and details of the structure determination for $C_{22}H_{20}F_7NO_2$.

Empirical formula	$C_{22}H_{20}F_7NO_2$
Molar mass / g·mol^{-1}	463.39
Space group (No.)	$P2_1/n$ (14)
a / Å	10.2135(2)
b / Å	14.8407(2)
c / Å	13.5890(3)
β / °	90.146(2)
V / Å^3	2059.75(7)
Z	4
$\rho_{calc.}$ / g·cm^{-3}	1.494
μ / mm^{-1}	1.215
Color	colorless
Crystal habitus	block
Crystal size / mm^3	0.464 x 0.135 x 0.123
T / K	100
λ / Å	1.54186 (Cu-K$_\alpha$)
θ range / °	4.412 to 75.641
Range of Miller indices	$-12 \leq h \leq 12$
	$-18 \leq k \leq 11$
	$-15 \leq l \leq 17$
Absorption correction	multi-scan
T_{max}, T_{min}	0.3941, 0.7953
R_{int}, R_σ	0.0144, 0.0078
Completeness of the data set	0.997
No. of measured reflections	24977
No. of independent reflections	4233
No. of parameters	316
No. of restrains	50
S (all data)	1.030
$R(F)$ ($I \geq 2\sigma(I)$, all data)	0.0314, 0.0332
$wR(F^2)$ ($I \geq 2\sigma(I)$, all data)	0.0774, 0.0787
Extinction coefficient	0.00127(10)
$\Delta\rho_{max}$, $\Delta\rho_{min}$ / e·Å^{-3}	0.441, –0.218

Table 2.S4. Bond lengths [Å] and angles [°] for **8b**.

C(1)-N(1)	1.3740(14)
C(1)-C(2)	1.3967(15)
C(1)-C(6)	1.4119(15)
C(2)-C(3)	1.3777(17)
C(2)-H(2)	0.9500
C(3)-C(4)	1.4044(17)
C(3)-H(3)	0.9500
C(4)-C(5)	1.3837(16)
C(4)-H(4)	0.9500
C(5)-C(6)	1.4072(15)
C(5)-H(5)	0.9500
C(6)-C(7)	1.4473(15)
C(7)-C(8)	1.3778(15)
C(7)-C(15)	1.5085(15)
C(8)-N(1)	1.3740(14)
C(8)-C(9)	1.4871(15)
C(9)-C(14)	1.3888(17)
C(9)-C(10)	1.3906(17)
C(10)-C(11)	1.3926(18)
C(10)-H(10)	0.9500
C(11)-C(12)	1.379(2)
C(11)-H(11)	0.9500
C(12)-C(13)	1.382(2)
C(12)-H(12)	0.9500
C(13)-C(14)	1.3912(17)
C(13)-H(13)	0.9500
C(14)-H(14)	0.9500
C(15)-O(1)	1.3950(13)
C(15)-O(2)	1.4198(13)
C(15)-C(16)	1.5669(15)
C(16)-F(1)	1.3539(12)
C(16)-F(2)	1.3617(12)
C(16)-C(17)	1.5473(15)
C(17)-F(3)	1.3437(14)
C(17)-F(4)	1.3453(13)
C(17)-C(18)	1.5505(16)
C(18)-F(5)	1.3159(14)
C(18)-F(7)	1.3232(14)

C(18)-F(6)	1.3253(14)
C(19)-O(1)	1.4443(13)
C(19)-C(20)	1.5040(17)
C(19)-H(19A)	0.9900
C(19)-H(19B)	0.9900
C(20)-H(20A)	0.9800
C(20)-H(20B)	0.9800
C(20)-H(20C)	0.9800
C(21A)-O(2)	1.4517(18)
C(21A)-C(22A)	1.503(3)
C(21A)-H(21A)	0.9900
C(21A)-H(21B)	0.9900
C(22A)-H(22A)	0.9800
C(22A)-H(22B)	0.9800
C(22A)-H(22C)	0.9800
C(21B)-O(2)	1.481(17)
C(21B)-C(22B)	1.501(18)
C(21B)-H(21C)	0.9900
C(21B)-H(21D)	0.9900
C(22B)-H(22D)	0.9800
C(22B)-H(22E)	0.9800
C(22B)-H(22F)	0.9800
N(1)-H(1)	0.855(17)
N(1)-C(1)-C(2)	129.15(11)
N(1)-C(1)-C(6)	107.81(9)
C(2)-C(1)-C(6)	123.02(10)
C(3)-C(2)-C(1)	117.42(11)
C(3)-C(2)-H(2)	121.3
C(1)-C(2)-H(2)	121.3
C(2)-C(3)-C(4)	120.87(11)
C(2)-C(3)-H(3)	119.6
C(4)-C(3)-H(3)	119.6
C(5)-C(4)-C(3)	121.66(11)
C(5)-C(4)-H(4)	119.2
C(3)-C(4)-H(4)	119.2
C(4)-C(5)-C(6)	118.89(11)
C(4)-C(5)-H(5)	120.6
C(6)-C(5)-H(5)	120.6
C(5)-C(6)-C(1)	118.13(10)

C(5)-C(6)-C(7)	135.52(10)
C(1)-C(6)-C(7)	106.31(9)
C(8)-C(7)-C(6)	107.08(9)
C(8)-C(7)-C(15)	126.25(10)
C(6)-C(7)-C(15)	126.64(10)
N(1)-C(8)-C(7)	108.97(9)
N(1)-C(8)-C(9)	117.75(10)
C(7)-C(8)-C(9)	133.25(10)
C(14)-C(9)-C(10)	119.14(11)
C(14)-C(9)-C(8)	119.92(10)
C(10)-C(9)-C(8)	120.92(11)
C(9)-C(10)-C(11)	120.19(12)
C(9)-C(10)-H(10)	119.9
C(11)-C(10)-H(10)	119.9
C(12)-C(11)-C(10)	120.30(12)
C(12)-C(11)-H(11)	119.9
C(10)-C(11)-H(11)	119.9
C(11)-C(12)-C(13)	119.81(11)
C(11)-C(12)-H(12)	120.1
C(13)-C(12)-H(12)	120.1
C(12)-C(13)-C(14)	120.19(12)
C(12)-C(13)-H(13)	119.9
C(14)-C(13)-H(13)	119.9
C(9)-C(14)-C(13)	120.34(12)
C(9)-C(14)-H(14)	119.8
C(13)-C(14)-H(14)	119.8
O(1)-C(15)-O(2)	112.82(9)
O(1)-C(15)-C(7)	106.52(9)
O(2)-C(15)-C(7)	113.23(9)
O(1)-C(15)-C(16)	111.50(9)
O(2)-C(15)-C(16)	101.35(8)
C(7)-C(15)-C(16)	111.54(9)
F(1)-C(16)-F(2)	106.33(8)
F(1)-C(16)-C(17)	106.87(9)
F(2)-C(16)-C(17)	106.48(9)
F(1)-C(16)-C(15)	109.83(8)
F(2)-C(16)-C(15)	109.94(8)
C(17)-C(16)-C(15)	116.84(9)
F(3)-C(17)-F(4)	108.72(10)
F(3)-C(17)-C(16)	109.94(9)

F(4)-C(17)-C(16)	109.82(9)
F(3)-C(17)-C(18)	105.97(9)
F(4)-C(17)-C(18)	105.94(9)
C(16)-C(17)-C(18)	116.15(9)
F(5)-C(18)-F(7)	108.52(10)
F(5)-C(18)-F(6)	108.65(10)
F(7)-C(18)-F(6)	107.84(10)
F(5)-C(18)-C(17)	111.69(9)
F(7)-C(18)-C(17)	108.32(9)
F(6)-C(18)-C(17)	111.70(10)
O(1)-C(19)-C(20)	106.87(10)
O(1)-C(19)-H(19A)	110.3
C(20)-C(19)-H(19A)	110.3
O(1)-C(19)-H(19B)	110.3
C(20)-C(19)-H(19B)	110.3
H(19A)-C(19)-H(19B)	108.6
C(19)-C(20)-H(20A)	109.5
C(19)-C(20)-H(20B)	109.5
H(20A)-C(20)-H(20B)	109.5
C(19)-C(20)-H(20C)	109.5
H(20A)-C(20)-H(20C)	109.5
H(20B)-C(20)-H(20C)	109.5
O(2)-C(21A)-C(22A)	108.51(15)
O(2)-C(21A)-H(21A)	110.0
C(22A)-C(21A)-H(21A)	110.0
O(2)-C(21A)-H(21B)	110.0
C(22A)-C(21A)-H(21B)	110.0
H(21A)-C(21A)-H(21B)	108.4
C(21A)-C(22A)-H(22A)	109.5
C(21A)-C(22A)-H(22B)	109.5
H(22A)-C(22A)-H(22B)	109.5
C(21A)-C(22A)-H(22C)	109.5
H(22A)-C(22A)-H(22C)	109.5
H(22B)-C(22A)-H(22C)	109.5
O(2)-C(21B)-C(22B)	104.1(15)
O(2)-C(21B)-H(21C)	110.9
C(22B)-C(21B)-H(21C)	110.9
O(2)-C(21B)-H(21D)	110.9
C(22B)-C(21B)-H(21D)	110.9
H(21C)-C(21B)-H(21D)	109.0

C(21B)-C(22B)-H(22D)	109.5
C(21B)-C(22B)-H(22E)	109.5
H(22D)-C(22B)-H(22E)	109.5
C(21B)-C(22B)-H(22F)	109.5
H(22D)-C(22B)-H(22F)	109.5
H(22E)-C(22B)-H(22F)	109.5
C(1)-N(1)-C(8)	109.83(9)
C(1)-N(1)-H(1)	125.3(10)
C(8)-N(1)-H(1)	124.9(10)
C(15)-O(1)-C(19)	120.14(9)
C(15)-O(2)-C(21A)	114.16(11)
C(15)-O(2)-C(21B)	106.6(10)

2.5 References

1 Y. Zhou, J. Wang, Z. Gu, S. Wang, W. Zhu, J. L. Acenã, V. A. Soloshonok, K. Izawa, H. Liu, *Chem. Rev.* **2016**, *116*, 422–518.

2 D. O'Hagan, *J. Fluorine Chem.* **2010**, *131*, 1071–1081.

3 H. Mei, J. Han, S. Fustero, M. Medio-Simon, D. M. Sedgwick, C. Santi, R. Ruzziconi, V. A. Soloshonok, *Chem. Eur. J.* **2019**, *25*, 11797–11819.

4 P. Shah, A. D. Westwell, *J. Enzym. Inhib. Med. Chem.* **2007**, *22*, 527–540.

5 K. Markakis, P. T. Lowe, L. Davison-Gates, D. O'Hagan, S. J. Rosser, A. Elfick, *ChemBioChem* **2020**, *21*, 1856–1860.

6 L. Hintermann, M. Perseghini, A. Togni, *Beilstein J. Org. Chem.* **2011**, *7*, 1421–1435.

7 N. Santschi, A. Togni, *CHIMIA* **2014**, *68*, 419–424.

8 A. Togni, *Adv. Synth. Catal.* **2010**, *352*, 2689–2690.

9 H. J. Böhm, D. Banner, S. Bendels, M. Kansy, B. Kuhn, K. Müller, U. Obst-Sander, M. Stahl, *ChemBioChem* **2004**, *5*, 637–643.

10 H. Amii, K. Uneyama, *Chem. Rev.* **2009**, *109*, 2119–2183.

11 M. F. Kuehnel, D. Lentz, T. Braun, *Angew. Chem. Int. Ed.* **2013**, *52*, 3328–3348.

12 H. Torrens, *Coord. Chem. Rev.* **2005**, *249*, 1957–1985.

13 T. Fujita, K. Fuchibe, J. Ichikawa, *Angew. Chem. Int. Ed.* **2019**, *58*, 390–402.

14 K. Uneyama, H. Amii, *J. Fluorine Chem.* **2002**, *114*, 127–131.

15 P. Clavel, M-P. Léger-lambert, C. Biran, F. Serein-Spirau, M. Bordeau, N. Roques, H. Marzouk, *Synthesis* **1999**, *5*, 829–834.

16 P. Clavel, G. Lessene, C. Biran, M. Bordeau, N. Roques, S. Trévin, D. de Montauzon, *J. Fluorine Chem.* **2001**, *107*, 301–310.

17 T. Stahl, H. F. T. Klare, M. Oestreich, *ACS Catal.* **2013**, *3*, 1578–1587.

18 K. Fuchibe, R. Oki, H. Hatta, J. Ichikawa, *Chem. Eur. J.* **2018**, *24*, 17932–17935.

19 K. Fuchibe, M. Takahashi, J. Ichikawa, *Angew. Chem. Int. Ed.* **2012**, *51*, 12059–12062.

20 J. Ichikawa, H. Fukui, Y. Ishibashi, *J. Org. Chem.* **2003**, *68*, 7800–7805.

21 M. A. Kurykin, I. M. Vol'pin, L. S. German, *J. Fluorine Chem.* **1996**, *80*, 9–12.

22 M. Iznaden, C. Portella, *J. Fluorine Chem.* **1989**, *43*, 105–118.
23 C. Portella, M. Iznaden, *Synthesis* **1991**, *11*, 1013–1014.
24 Y. Wang, S. Zhu, *Tetrahedron Lett.* **2001**, *42*, 5741–5744.
25 W. Dmowski, *J. Fluorine Chem.* **1980**, *15*, 299–313.
26 V. M. Timoshenko, Ya. V. Nikolin, N. P. Kolesnik, Yu. G. Shermolovich, *Russ. J. Org. Chem.* **2001**, *37*, 624–632.
27 F. Brüning, H. Nagae, D. Käch, K. Mashima, A. Togni, *Chem. Eur. J.* **2019**, *25*, 10818–10822.
28 H. Johansson, T. B. Jørgensen, D. E. Gloriam, H. Bräuner-Osborne, D. S. Pedersen, *RSC Adv.* **2013**, *3*, 945–960.
29 S. L. Garland, D. E. Gloriam, *Curr. Top. Med. Chem.* **2011**, *11*, 1872–1881.
30 C. J. Thomas, M. A. Wolak, R. R. Birge, W. J. Lees, *J. Org. Chem.* **2001**, *66*, 1914–1918.
31 C. P. Haas, T. Roider, R. W. Hoffmann, U. Tallarek, *React. Chem. Eng.* **2019**, *4*, 1912–1916.
32 L. Buzzetti, G. E. M. Crisenza, P. Melchiorre, *Angew. Chem. Int. Ed.* **2019**, *58*, 3730–3747.
33 S. R. Kandukuri, A. Bahamonde, I. Chatterjee, I. D. Jurberg, E. C. Escudero-Adán, P. Melchiorre, *Angew. Chem. Int. Ed.* **2015**, *54*, 1485–1489.
34 C. P. Haas, T. Müllner, R. Kohns, D. Enke, U. Tallarek, *React. Chem. Eng.* **2017**, *2*, 498–511.
35 W. A. Remers, R. K. Brown, in *lndoles Part I* (Ed.: W. J. Houlihan), Heterocyclic compounds; Wiley-Interscience: New York, 1972; pp. 13–14.
36 E. Leete, *J. Am. Chem. Soc.* **1959**, *81*, 6023–6026.
37 R. Srivastava, *J. Mol. Catal. A: Chem.* **2007**, *264*, 146–152.
38 L. Spialter, R. W. Moshier, *J. Am. Chem. Soc.* **1957**, *79*, 5955–5957.
39 N. J. W. Straathof, D. J. G. P. van Osch, A. Schouten, X. Wang, J. C. Schouten, V. Hessel, T. Noël, *J. Flow Chem.* **2014**, *4*, 12–17.
40 E. von Angerer, J. Strohmeier, *J. Med. Chem.* **1987**, *30*, 131–136.
S1 C. P. Haas, T. Müllner, R. Kohns, D. Enke, U. Tallarek, *React. Chem. Eng.* **2017**, *2*, 498–511.
S2 C. P. Haas, T. Roider, R. W. Hoffmann, U. Tallarek, *React. Chem. Eng.* **2019**, *4*, 1912–1916.
S3 N. Straathof, D. Osch, A. Schouten, X. Wang, J. Schouten, V. Hessel, T. Noël, *J. Flow Chem.* **2014**, *4*, 12–17.
S4 X-Area, STOE & Cie GmbH, Darmstadt, Germany, **2018**.
S5 X-RED32, STOE & Cie GmbH, Darmstadt, Germany, **2018**.
S6 LANA - Laue Analyzer, STOE & Cie GmbH, Darmstadt, Germany, **2019**.
S7 G. M. Sheldrick, *Acta Crystallogr., Sect. A: Found. Adv.* **2015**, *71*, 3–8.
S8 G. M. Sheldrick, *Acta Crystallogr., Sect. C: Struct. Chem.* **2015**, *71*, 3–8.

3. Chapter 3: Device for Automated Screening of Irradiation Wavelength and Intensity – Investigation of the Wavelength Dependence of Photoreactions with an Arylazo Sulfone in Continuous Flow

Authors
T. Roider, N. Frommknecht, A. Höltzel and Ulrich Tallarek

State of publication
Published 14 June February 2021 in *Reaction Chemistry & Engineering*, Vol. 7, pp.2035–2044.
DOI: 10.1039/D2RE00142J

Table of content

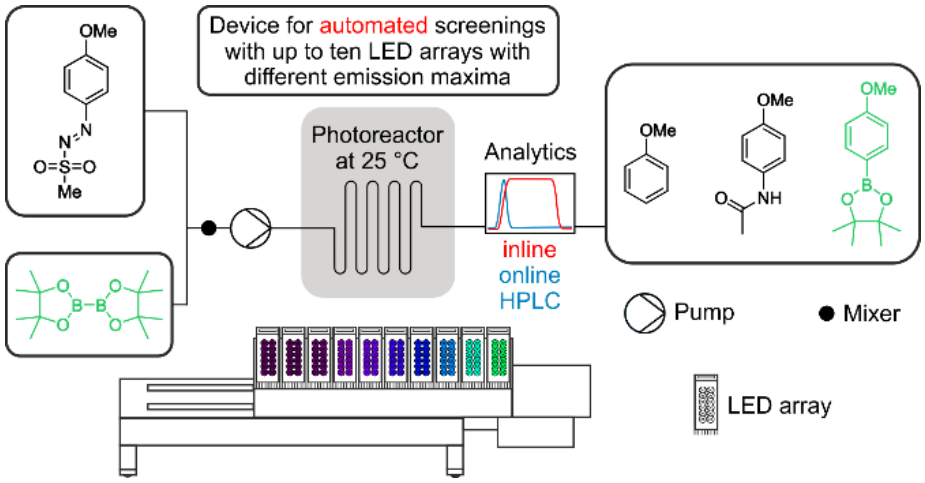

Abstract
We introduce a device that allows programmable, automated changes of the irradiation wavelength and intensity for use with a continuous-flow photoreactor. Combined with parallel chromatographic analysis, the set-up enables systematic screening of photoreactions in a remarkably short time frame. This is demonstrated by investigating the photoconversion of an arylazo sulfone under different reaction conditions, with and without the use of an additive. Data obtained from a series of systematic wavelength screenings at defined irradiation intensity reveal a previously unknown intermediate and disclose a new, wavelength-dependent reaction pathway. Our study shows how systematic screening of the wavelength and irradiation intensity can contribute to the fundamental understanding of photochemical reactions

3.1 Introduction

Although the potential of photochemistry for new reaction pathways and synthesis possibilities has been recognized for decades,[1,2] the enormous interest in photochemical reactions is a rather recent phenomenon.[3–5] The main drivers of this rapid evolution are the advances in LED technology[6–8] and the emergence of continuous-flow reactors.[9] LEDs provide energy-efficient irradiation with a narrow wavelength band, and continuous-flow reactors can often considerably reduce reaction times compared to batch synthesis at conserved or even improved yield.[10–13] For example, in photoreactions catalyzed by $Ru(bpy)_3Cl_2$, 95% of the photons hitting the reaction solution are absorbed after a distance of 0.5 mm, assuming a catalyst concentration of 2 mmol/L.[8] In batch synthesis, this translates to inhomogeneous irradiation of the reaction solution, which can result in catalyst losses due to inactivation or product loss through decomposition from overexposure to irradiation. The high surface-to-volume ratio in continuous-flow reactors, on the other hand, allows the best possible homogeneous irradiation of the reaction solution. Combined with high-power LEDs, continuous-flow reactors can reduce the reaction time from days to minutes and narrow the by-product spectrum,[14,15] making photochemical reactions attractive synthesis options for academic and industrial laboratories.[9,16–20]

With light as a reaction parameter, wavelength and intensity of the irradiation influence the outcome of the reaction, yet in the literature this information is rarely provided.[21] The importance of wavelength definition has received a bit more attention than the correlated intensity aspect.[22–28] Kappe's group, for example, performed wavelength screenings of photochemical reactions using a commercial flow reactor.[22–26] This reactor handles up to six wavelengths, but these are emitted at different intensities.[24] The PhotoGreen Lab around Fagnoni and Protti used narrow wavelength band irradiation as well the solar-light simulating broadband emission from a Xe lamp to study the formation of aryl radicals and aryl cations in the photoconversion of an arylazo sulfone.[27] The irradiation intensities at the different wavelengths and the irradiation times of the experiments varied.

If wavelength, intensity, and irradiation time are varied at the same time, the observed effects could result from either of the parameters or a combination of them. To enable wavelength studies of photochemical reactions at comparable irradiation intensity, we previously introduced a library of 16 LED arrays that emitted quasi-identical photon flux densities over the visible light range onto a custom-built photo–flow reactor.[29] In this work, we present a device for automated changes of the LED arrays. Automation plays an increasingly important role in laboratories, because it offers higher efficiency, improved reproducibility and safer handling of chemicals.[30–32] The novel device completes the equipment for systematic, time-efficient and programmable screening of photochemical reactions in continuous flow at defined irradiation wavelength, intensity and time.

The performance of the automated set-up is demonstrated in wavelength screenings of the photoconversion of an arylazo sulfone. This reaction was selected for several reasons. First, it is easy to control, as no further reactants or catalysts are needed. Second, earlier results obtained by the PhotoGreen Lab suggest this reaction as a promising candidate for systematic wavelength screening.[27] If carried out in aqueous acetonitrile, the reaction yields three products whose ratio depends on the irradiation wavelength. Third, arylazo sulfones are versatile and

enable a wide range of reactions through additives.[33–39] Through automated wavelength screening, supplemented by batch experiments, we investigate the wavelength dependence of the photoconversion of the arylazo sulfone **1** in aqueous acetonitrile under different reaction conditions, with and without a borylation additive (Figure 3.1).

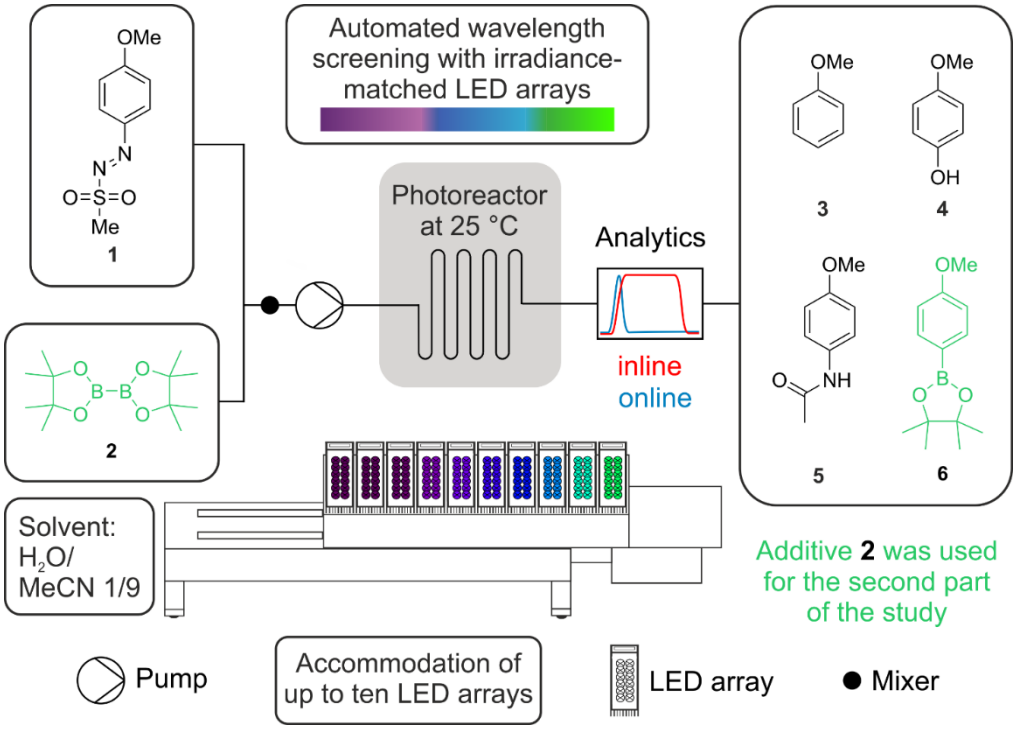

Figure 3.1. Schematic experimental setup for automated wavelength screening of the photoconversion of the arylazo sulfone **1** in aqueous acetonitrile, with and without the dioxaborolane **2** as additive. Online analytics refers to quantitative analysis of the reaction solution by reversed-phase liquid chromatography with UV detection to determine product ratios and the conversion rate. Inline analytics refers to monitoring the steady state of the photoreactor through measuring the total UV absorbance of the reaction solution.

3.2 Experimental

A two-dimensional Agilent HPLC system was used for parallel reaction and analysis. The components and advantages of the platform were described in detail previously,[29] which is why only the most relevant information is given here. An extensive description of the platform, with photographs, can be found in Section 3.5.5 of the ESI.† The HPLC pump of the first system feeds the reactant solution continuously and precisely into the photoreactor (Figure 3.1). The reaction time is thus determined by the flow rate and the reactor volume. The reaction solution is transferred through a valve behind the reactor to the second HPLC system for online chromatographic analysis. Conversion rate and product ratios are determined directly from the chromatographic peaks of the compounds. Quantitative analysis relies on the UV absorption of the compounds using external calibration. The chromatographic separation conditions (Table 3.S2–3.S3) and UV absorption calibration curves for the compounds (Figure 3.S24–3.S32) are compiled in Section 3.5.5 of the ESI.† To acquire the calibration curves, the respective

compounds were bought or, if commercially unavailable, synthesized as described in Section 3.5.1 and 3.5.6 of the ESI.†

For this work, we developed a device for automated changes of the LED array in operation (Figure 3.2) together with the software for programming the sequence of LED arrays as well as their irradiation intensity and time (Section 3.5.4 of the ESI†). The wavelength change is effected by the linear actuator (Figure 3.2D), which moves a carriage on which up to ten custom-built LED arrays (Figure 3.2B) can be mounted. The device is attached via the reactor bracket (Figure 3.2b) to the photo–flow reactor. The reactor (Figure 3.2A) features a modular design intended to keep the distance between the operative LED array and the reaction solution as short as possible (14 mm).[29] Two radial fans (Figure 3.2C) placed directly under the reactor are used to actively cool the LED array in operation. This is important, as the emission spectrum as well as the irradiance of LEDs are temperature sensitive. At the core is the reactor plate (stainless steel, Figure 3.2f) with the channel in which the photoreaction takes place. A large heat sink is placed below the reactor plate (Figure 3.2g) for isothermal conditions. The heat elements are placed on the rear side of the reactor, where the inlet and outlet for the reaction solution (Figure 3.2h and 3.2i) are also located.

The reactor plate is covered by a FEP foil (fluorinated ethylene propylene, 0.13 mm, Figure 3.2e) with high chemical resistance. The thinnest commercially available FEP foil was used, because light absorption strongly increases with the material thickness. Above the FEP foil, a PMMA plate (poly(methyl methacrylate), 2.0 mm, Figure 3.2d) provides mechanical stability. PMMA decomposes on contact with common solvents (e.g., ethanol and acetonitrile), but has the advantage to absorb light only below 375 nm, even with thicker layers. The reactor window above the PMMA plate defines the irradiated area and is attached to the heat sink with several screws to fix the reactor. Detailed information about the reactor plate and the channel dimensions (Figure 3.S3) is given in Section 3.5.2 of the ESI.†

All LED arrays are identically constructed. Twelve LEDs per array are arranged in two parallel rows of six LEDs connected in series (Figure 3.2k). Each array has a ventilation slit on the front (Figure 3.2j) and a passive cooling system (heat sink fins, Figure 3.2l) on the rear side. Also on the rear side are connectors for mounting the array onto the carriage. Through these connectors the array is also supplied with power (Figure 3.2m). In operation, the LED array is cooled by one radial fan blowing over the LEDs and the other radial fan blowing over the heat sink fins (Figure 3.S2, ESI†).

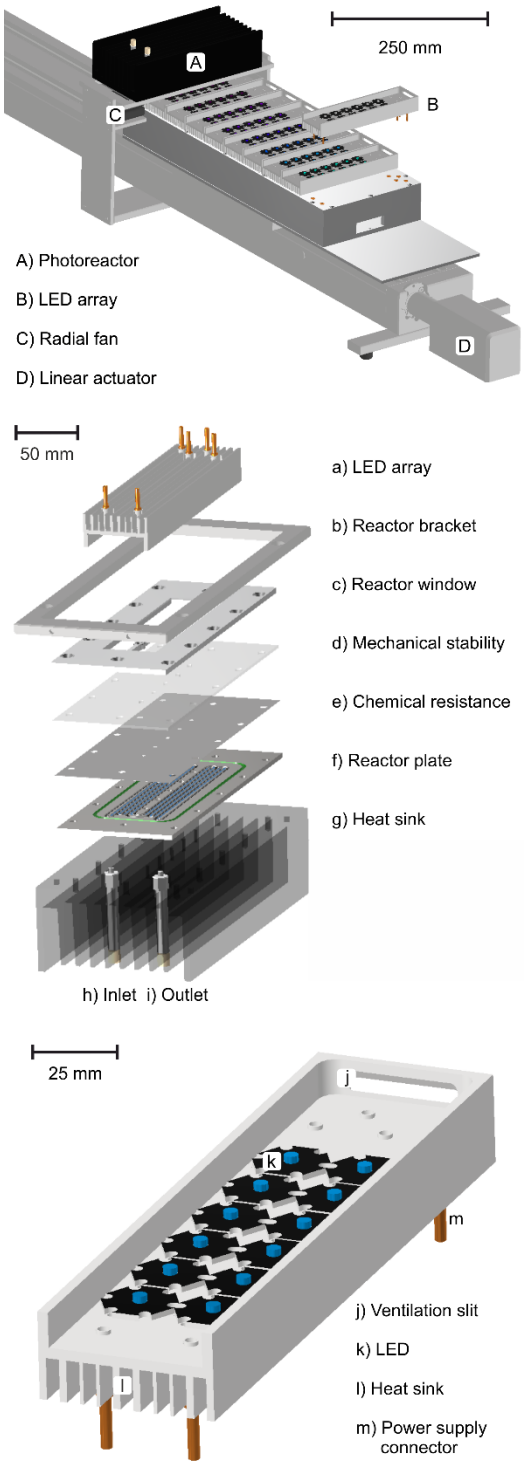

Figure 3.2. Top: 3D drawing of the device for automated wavelength changes. Middle: Modular design of the custom-built photo–flow reactor. Bottom: LED array construction.

For wavelength screenings at identical irradiation intensity, the photon flux density on the reactor solution must remain the same with each LED array. Chemical actinometers are commonly used to measure the photon flux density.[40] It is, however, practically impossible to find an actinometer that can be used over the entire wavelength range represented by the LED array library.[21] Several actinometers, with different quantum yields, would have to be used to

measure the photon flux density of the 16 LED arrays, with different emission bandwidths, making a sufficiently accurate irradiance matching of the LED arrays unlikely. Additionally, chemical actinometers are incompatible with the high irradiances realized by our photoreactor design. We therefore pursued the elaborate, but increasingly popular, spectroradiometer approach[41,42] to determine the photon flux density of the LED arrays (Section 3.5.3 of the ESI†). To ensure that the same locations on the reactor plate are measured for each LED array, a template of the reactor plate was obtained from a 3D printer. The template divided the reactor plate into a grid of squares whose edge length matched the diameter (8 mm) of the spectroradiometer detector (Figure 3.3A). Ten squares each were defined as measurement points and control points. These are distributed evenly over the grid to obtain representative values for the entire area. Reactor window, FEP film and PMMA plate were removed from the modular reactor and screwed to the template. This arrangement was placed between the LED array and the spectroradiometer detector (Figure 3.3D). A holder obtained from the 3D printer attached the arrangement to the LED array carrier to fix the positions of reactor and LED array.

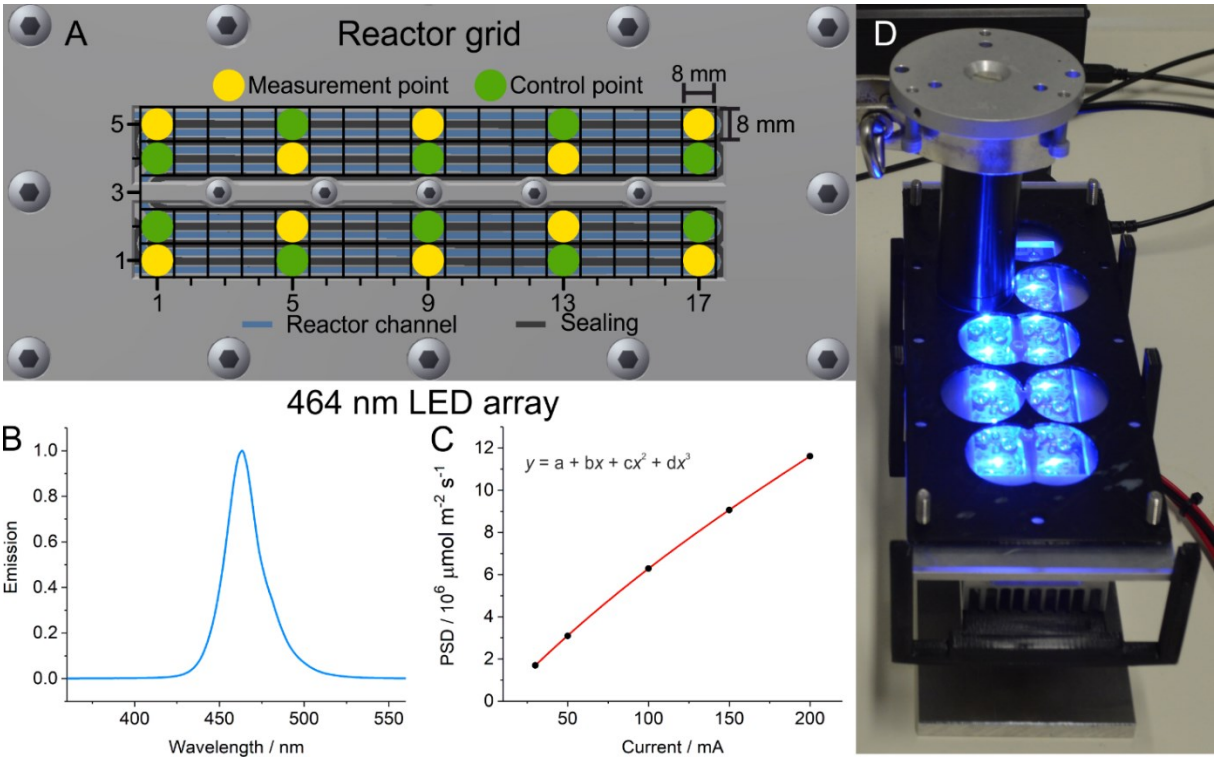

Figure 3.3. A) Distribution of measurement and control points over the reactor plate for characterization of the LED arrays. B) Normalized emission spectrum of the 464 nm LED array. C) Total amount of photons hitting the spectroradiometer detector at the measurement points per time unit (power spectral density, PSD) depending on the applied current for the 464 nm LED array. D) The spectroradiometer measures the photon flux density emitted by each LED array at defined measurement points on a 3D template of the reactor plate.

Currents between 100 and 700 mA (operation limit of the LED arrays) were then applied to the LEDs. The signals received from the individual measurement points were added to yield the power spectral density (PSD) at a given applied current (Figure 3.3C). The PSD gives the photon flux density (the amount of photons that hit the detector per unit area and time)

integrated over all emitted wavelengths. A linear correlation between the applied current and the PSD was only observed for 4 of 12 LED arrays; for the other 8 LED arrays, the curves flattened at higher currents (Figure 3.S5–3.S16, ESI†). This behavior reflects the temperature sensitivity of the LED arrays.[43] The passive and active cooling systems protect the LED arrays from temporary overheating and permanent heat damage, but cannot prevent a rise in their core temperature at higher currents.

Of the twelve LED arrays used in this study, the 375 nm LED array has the lowest PSD value at the maximum applicable current (cf. Figure 3.S6, ESI†; $2.97 \cdot 10^6$ µmol m^{-2} s^{-1} at 700 mA). This PSD value was taken as the reference and the respective current to achieve the reference PSD value was determined from the current sensitivity curves of the other LED arrays. Then, the PSD values at the determined current values were measured again for each array at the measurement and the control points of the reactor grid to determine the deviation of the measured PSD from the reference value (Table 3.1). The maximum deviation was 3% (observed for the 518 nm LED array).

Table 3.1. Current applied to each LED array for identical irradiation intensity on the reaction solution in the photo–flow reactor.

λ_{max} (nm)	I (mA)	Deviation (%)
373	379	<1
375	700	–[a]
383	436	~1
403	80	<1
416	65	<1
430	53	<2
442	49	<1
464	48	<1
495	37	<1
504	44	~1
518	44	~3
522	50	<1

a: Set as reference.

The current sensitivity curves of all LED arrays in the library are stored in the software, which calculates the current to apply to a given LED array for the desired irradiation intensity.

The spectroradiometer-based characterization of the LEDs is laborious. Each array needs to be characterized over the full current range. It must also be considered that as the LEDs age, their emission spectra and photon output changes. The time frame for the aging process depends on the particular LED as well as its overall operating time and conditions. Therefore, the accuracy of the current sensitivity curves of the LED arrays must be checked periodically and eventually reacquired after a longer time period.

In return, the spectroradiometer approach delivers superior accuracy and the data base that allows to select the irradiation intensity. For this study, we used the maximum PSD (100%) of

the weakest LED array as reference. Table 3.1 shows that the shorter-wavelength LED arrays require considerably higher currents for the same PSD than the LED arrays with emission wavelengths above 400 nm. Therefore, wavelength screenings at higher irradiation intensities are possible when LED arrays with emission wavelength below 400 nm can be omitted. The acquired data base and software further enable automated screening of the irradiation intensity at a given wavelength as well as the repetition of wavelength screenings at varied intensities or irradiation times.

3.3 Results and Discussion

From preliminary batch experiments of the photoconversion of the arylazo sulfone **1** in aqueous acetonitrile, we knew that the product spectrum of the reaction depends on the absence or presence of O_2. Therefore, two wavelength screenings were performed for the reaction, one when carried out under inert gas conditions and one when carried out in air atmosphere.
For the screenings, nine LED arrays with emission maxima between 373 and 495 nm (Figure 3.4A) were selected from the library based on sufficient overlap of their emission spectra with the UV–vis absorption spectrum of the arylazo sulfone **1**. The flow rate was set to 0.1 mL min^{-1} to obtain approximately 60% conversion with the shortest irradiation wavelength. This leaves a sufficient margin for higher or lower conversion rates with longer irradiation wavelengths. With the reactor volume of 0.845 mL, the chosen flow rate yields a reaction time of 8.45 minutes. The chromatographic separation conditions were tuned for an analysis time of only seven minutes (Figure 3.5). Because reaction and analysis run in parallel, the time-determining step of the screening was the run-in time of the reactor, which is the time span (10–15 min) after which the operating LED array has reached a constant photon emission rate. Acquisition of the data shown in Figure 3.4 required an overall screening time of 13.5 hours.

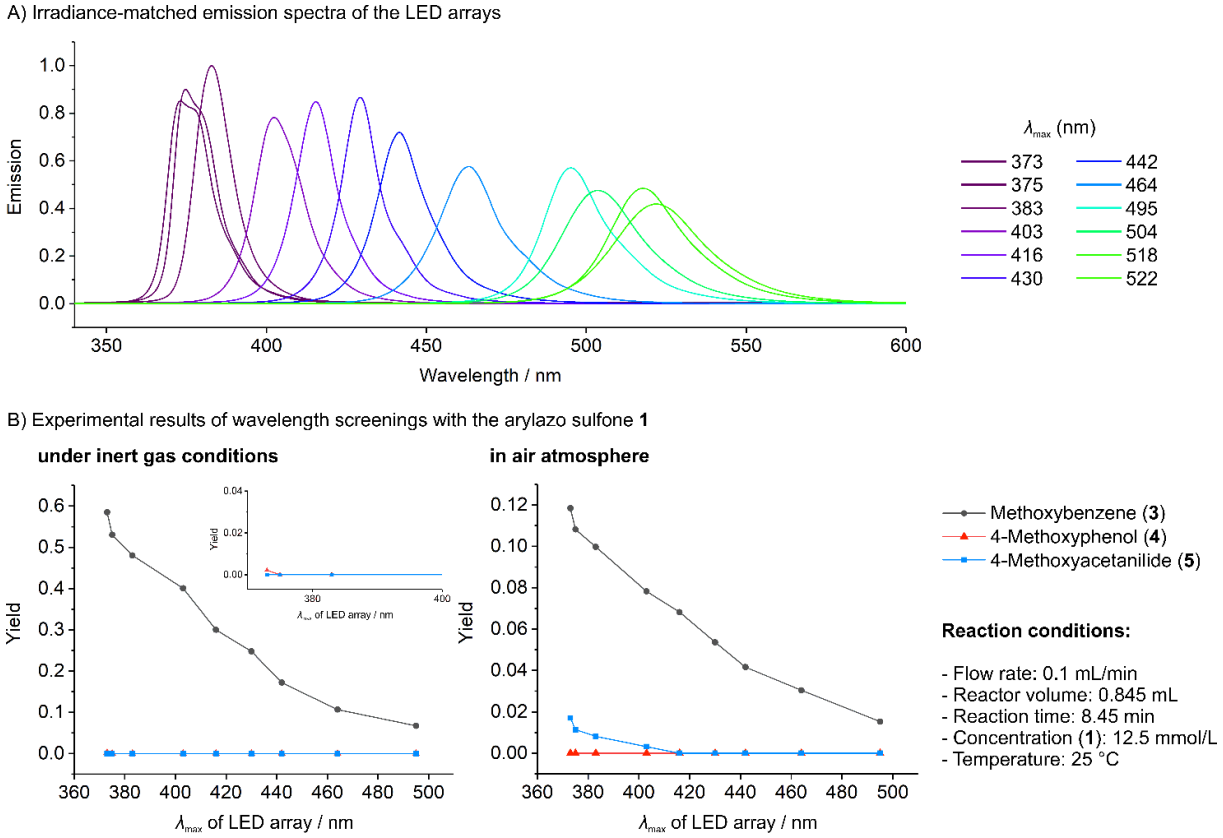

Figure 3.4. A) Irradiance-matched emission spectra of the nine LED arrays selected for the wavelength screening of the photoconversion of the arylazo sulfone **1** in aqueous acetonitrile. Light absorption by the PMMA plate causes the asymmetric shape of the emission spectra of the 373 nm and the 375 nm LED arrays.[29] B) Comparison of data obtained from wavelength screenings of the reaction when carried out under inert gas conditions or in air atmosphere. Yields were calculated as c_p/c_0, where c_p represents the concentration of the products (p = **3**, **4**, **5**) and c_0 is the initial concentration of **1** (12.5 mmol/L).

When the reaction was carried out under inert gas conditions, only one of the three expected products, methoxybenzene (**3**), was found in major amounts (Figure 3.4B). A tiny amount of 4-methoxyphenol (**4**), well below 1%, was detected with the 373 nm LED array, but 4-methoxyacetanilide (**5**) could not be detected at all. When the reaction was carried out in air atmosphere, a 2% yield of **5** was obtained with the 373 nm LED array (Figure 3.4B). In return, the yield of **3** as well as the total product yield (14%) were significantly reduced compared to inert gas conditions (60%). The observed product loss in the presence of O_2 can be explained by the formation of another, previously unknown compound. The chromatograms obtained with the 373 nm LED array show that the reaction mainly produces compound **7** when carried out in air atmosphere (Figure 3.5). Interestingly, **7** can be converted to the known products at long reaction times without formation of new by-products in significant amounts, as shown below. Thus, 4-methoxyacetanilide (**5**) is produced only via the intermediate **7**, which, in turn, is only formed in the presence of O_2. Consequently, there are two reaction pathways: direct conversion of **1** to **3** and the conversion of **1** to the intermediate **7**, which subsequently reacts to 4-methoxyacetanilide (**5**) and possibly to methoxybenzene (**3**).

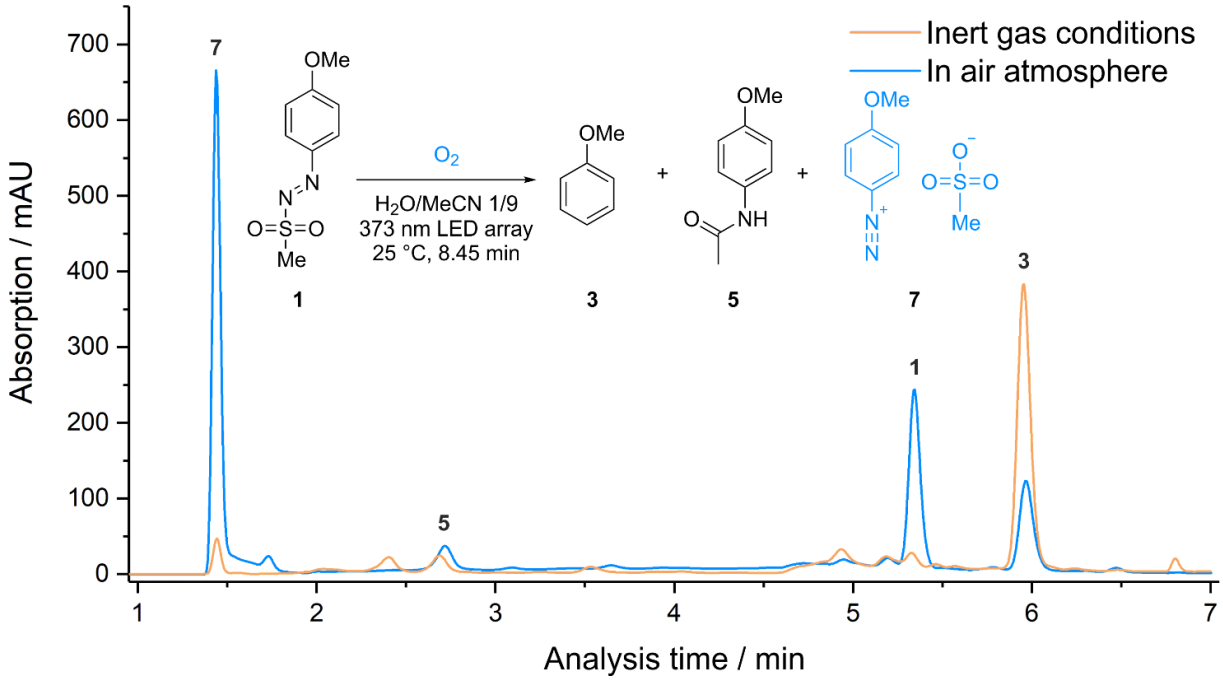

Figure 3.5. Chromatograms obtained for the photoconversion of the arylazo sulfone **1** in aqueous acetonitrile when carried out under inert gas conditions or in air atmosphere and irradiation with the 373 nm LED array. (Separation conditions are given in Table 3.S2 of the ESI,† the detection wavelength is 261 nm.) Comparison of the chromatograms shows that the presence of O_2 lowers the conversion of **1** and decreases the yield of the main product **3** in favour of formation of the intermediate **7**.

Identification of the intermediate required a sufficient amount for structure elucidation. Reaction conditions that deliver **7** as the main product were easily found, but the compound could not be purified from the reaction solution by column chromatography without decomposition. We therefore used wavelength screening to find reaction conditions for the selective synthesis of **7**. The previous wavelength screening had shown that the intermediate is formed quickly, whereas its conversion to the follow-on products is much slower. In addition, comparison of the UV–vis absorption spectra showed that **1** absorbs up to 490 nm, whereas **7** absorbs only up to 380 nm (Figure 3.6). This suggested that with longer irradiation wavelengths the reaction could be halted at the intermediate stage, with only **7** and **3** remaining in the reaction solution. The latter compound can be removed by evaporation under reduced pressure, eliminating the need for purification of **7**.

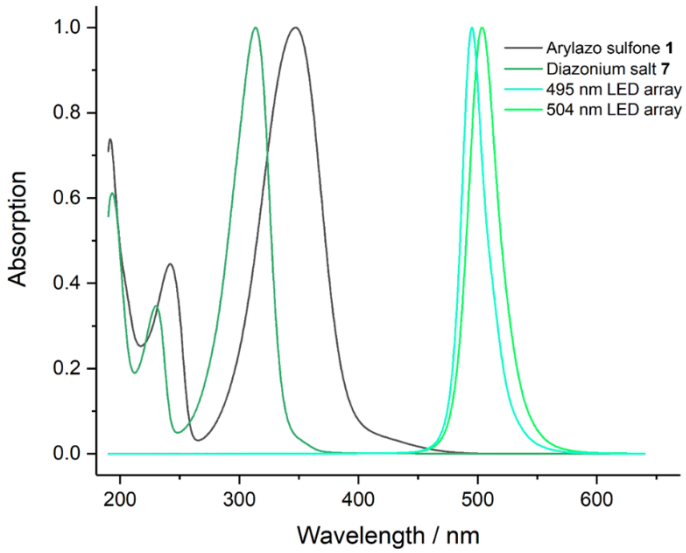

Figure 3.6. Comparison of the UV–vis absorption spectra of the arylazo sulfone **1** and the intermediate **7** with the emission spectra of the 495 nm and 504 nm LED arrays.

To test this hypothesis, we performed a wavelength screening of the reaction in air atmosphere (Figure 3.7A) using five LED arrays with emission maxima between 464 and 522 nm. This wavelength range was selected because irradiation below 464 nm favors formation of **3** (Figure 3.4B), whereas the emission spectra of LED arrays with maxima above 522 nm have too little overlap with the UV–vis absorption spectrum of **1** (Figure 3.6). The screening was done as a batch experiment (one vial per LED array) to increase the O_2 supply. In the vial, the reaction solution has continuous air contact, whereas the O_2 source in the flow reactor is limited to the amount of air dissolved in the reaction solution. The irradiation intensity was set to 900% of the reference PSD (Table 3.S1). The batch experiment also allowed to extend the irradiation and reaction time for increased yield. Subsequent chromatographic analysis of the reaction solution from each vial (Figure 3.7A) showed that the 495 nm and 504 nm LED arrays returned the best yields of **7**. Shorter irradiation wavelengths increase the amount of **3** in the reaction solution, as expected; longer wavelengths slow the reaction down, which leads to decomposition of **7** into several unknown by-products. A batch experiment where the reaction solution was irradiated for 3h with the 504 nm LED array delivered **7** with 91% yield. The structure of **7** was then elucidated by NMR spectroscopy and ESI-MS (Section 3.5.6 and 3.5.7 in the ESI†).

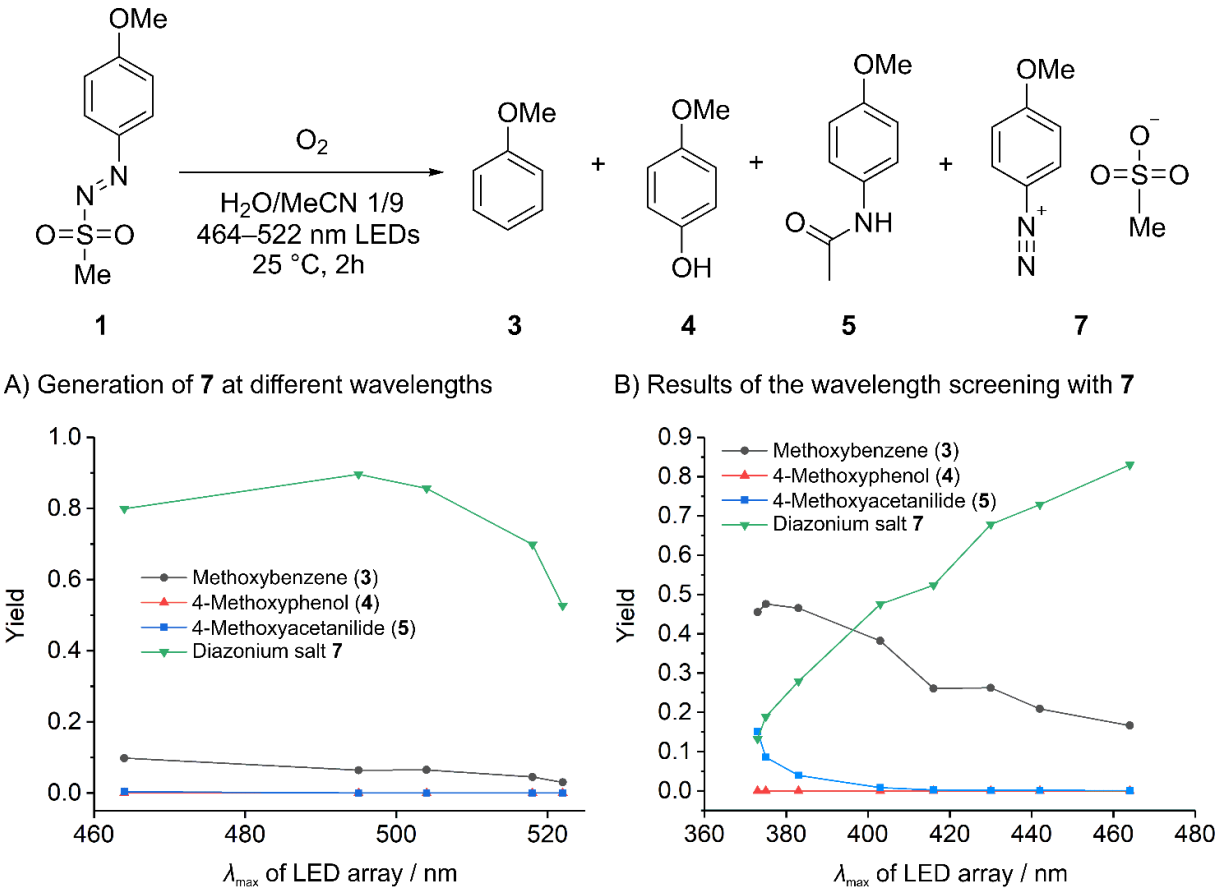

Figure 3.7. A) Reaction conditions for selective generation of the intermediate **7** as a batch experiment of five vials containing the reaction solution. Yields were calculated as c_p/c_0, where c_p represents the concentration of the products (p = **3**, **4**, **5**, **7**) and c_0 is the initial concentration of **1** (12.5 mmol/L). B) Wavelength screening of the reaction with **7** instead of the arylazo sulfone **1** as substrate. In this case, the yields refer to substrate **7** and were calculated as c_p/c_0, where c_p represents the concentration of the products (p = **3**, **4**, **5**) and c_0 is the initial concentration of **7** (12.5 mmol/L).

To determine the product ratio of the reaction pathway via the intermediate, the wavelength screening of the reaction in air atmosphere was repeated with **7** as substrate (Figure 3.7B). With shorter irradiation wavelengths, the photoconversion of **7** produced a significantly higher yield of 4-methoxyacetanilide (**5**) than the photoconversion of **1**: the highest yield of **5** with **7** as substrate was 15% (Figure 3.7B) compared with 2% with **1** as substrate (Figure 3.4B). Methoxybenzene (**3**) remained the main product, confirming that the reaction pathway via the intermediate produces the same main product as the direct conversion of **1**.

At last, we addressed the question how the pathway via the intermediate affects the reaction when an additive is used. Crespi et al. proposed an excitation wavelength-dependent reaction mechanism for the photoconversion of **1**.[27] At 366 nm, a $^1\pi\pi^*$ excitation occurs, followed by a two-step heterolytic cleavage of first the S–N and then the C–N bond. The resulting aryl carbocation can react to the main product **3** or the by-products **4** and **5**. At 450 nm, $^1n\pi^*$ excitation occurs, followed by homolytic cleavage of the S–N bond and elimination of N_2. Without additive, the resulting aryl radical can react only to **3**. With an appropriate additive,

the carbocation and the aryl radical can both react to the desired product.[27] Although the carbocation route entails more by-products than the aryl radical route, the former route is not necessarily more favorable for the main product yield than the latter, as this depends on the respective product ratios of the two pathways.

To determine the product ratio for each reaction pathway, the wavelength screening of the photoconversion of **1** in aqueous acetonitrile was repeated with the dioxaborolane **2** as additive to generate **6** as the desired product (cf. Figure 3.4). The screening was carried out first under inert gas conditions, then in air atmosphere, and finally with the previously generated intermediate **7** instead of the arylazo sulfone **1** as substrate (Figure 3.8).

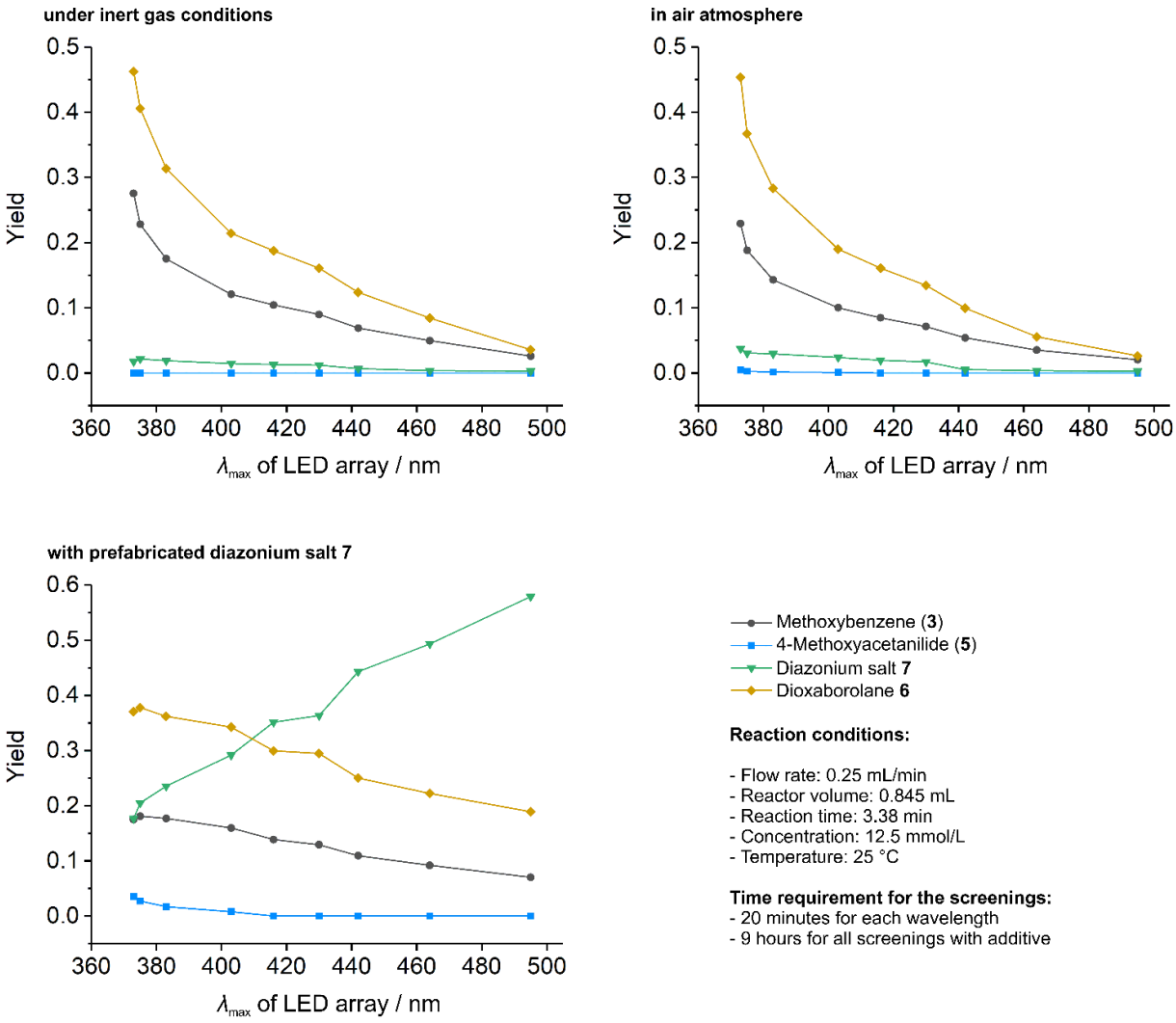

Figure 3.8. Wavelength screenings of the photoconversion of the arylazo sulfone **1** in aqueous acetonitrile with the dioxaborolane **2** as additive under inert gas conditions (top left), in air atmosphere (top right), and with the previously generated intermediate **7** instead of the arylazo sulfone **1** as substrate (bottom panel). For the reactions under inert gas conditions and under air atmosphere, the yield refers to substrate **1** and is calculated as c_p/c_0, where c_p represents the concentration of the products (p = **3**, **5**, **6**, **7**) and c_0 is the initial concentration of **1** (12.5 mmol/L). For the screening with prefabricated diazonium salt **7**, the yield refers to substrate **7**, where c_0 represents the initial concentration of **7** (12.5 mmol/L).

To adapt to the higher reaction rate observed with the additive, the reaction time was reduced via the flow rate to 3.38 minutes. Chromatographic separation conditions were found that essentially conserved the analysis time of the reaction without additive (Figure 3.S23). The time-determining step of the screening remained thus the run-in time of the reactor. Screening the reaction with additive required only 20 minutes per wavelength, resulting in a total screening time of nine hours to generate the data in Figure 3.8. It should also be considered that in none of the screenings complete conversion is achieved. For the screening with **1** as substrate the maximum conversion is 85% and with **7** as substrate the maximum conversion is 82%. In this respect, applying a lower flow rate, or increasing the number of photons with which the reaction solution is irradiated (up to 1.93 times the number of photons used for the screening would be possible with the 373 nm array) would further increase the yields of **6**, and full conversion would probably be achieved.

Under inert gas conditions (Figure 3.8, top left panel), the desired product **6** and 4-methoxybenzene (**3**) show a highly similar wavelength dependence of their yields. The highest yields (47% for **6** and 28% for **3**) were obtained with the shortest irradiation wavelength. Towards longer wavelengths, the yield curves of **3** and **6** flatten out at the same rate. **7** was detected as an additional by-product, also preferentially with short irradiation wavelengths. As **7** is only generated at O_2 presence, small amounts of O_2 must be able to enter the reactor via diffusion through the PMMA plate and/or the FEP foil. This explains why the wavelength screenings under inert gas conditions and in air atmosphere gave highly similar results (Figure 3.8, top right panel). Because the reaction of **1** with the dioxaborolane **2** is faster than the reaction with O_2, the higher O_2 concentration present in air atmosphere has no major effect on the product spectrum. With the pre-fabricated compound **7** as substrate, however, significant changes in the wavelength dependence of the yield curves are attained (Figure 3.8, bottom panel). With the 373 nm LED array, the yield of **6** is lower (37%) than in the reaction with **1** as substrate (47%, Figure 3.8, top left panel). But the yield curve of **6** flattens out much more slowly towards longer wavelengths with **7** as substrate. Irradiation with the 430 nm LED array, for example, returns a 30% yield with **7** as substrate compared with less than 18% yield with **1** as substrate (Figure 3.8). Thus, using the intermediate **7** as substrate in combination with longer irradiation wavelengths is a way to boost the main product formation. Generally, irradiation with longer wavelengths may be key to significantly increased product yields and the avoidance of by-products for reactions of compounds with larger aromatic systems.

3.4 Conclusions

We introduced a device for programmable, automated changes of the irradiation wavelength, intensity and time for use with photo–flow reactors. Paired with a parallel reaction and analysis system, the introduced device enables systematic screening of photochemical reactions in a remarkably short time. Overall, the study has shown how systematic wavelength screening can contribute to the fundamental understanding of photochemical reactions. In particular, we discovered a previously unknown intermediate of the photoconversion of an arylazo sulfone in aqueous acetonitrile as well as a new reaction pathway through a series of automated wavelength screenings at defined irradiation intensity.

In general, this study has confirmed that comparatively small differences between irradiation wavelengths can have major consequences for the product spectrum. Therefore, the emission spectra and irradiation intensities of the light sources as well as the irradiation times of the reaction solution must be specified to guarantee the reproducibility of a photochemical reaction.

3.5 Supporting Information

3.5.1 Materials

4'-Methoxyacetanilide was received from abcr GmbH (Karlsruhe, Germany) in a purity of 98%. Sodium nitrite ($NaNO_2$) was received from Carl Roth (Karlsruhe, Germany) in a purity of ≥98%. Sodium methanesulfinate was received from TCI Deutschland GmbH (Eschborn, Germany) in a purity of >90%. Acetonitrile (HiPerSolv CHROMANORM for HPLC) was purchased from VWR Chemicals (Darmstadt, Germany). Water was obtained from a Milli–Q gradient purification system (Millipore, Bedford, MA). All other chemicals were received from Sigma–Aldrich (St. Louis, MO) in a purity of at least 98%. All chemicals were used without further purification.

3.5.2 Photoreactor design

The design of the custom-built photoreactor has been described previously.[S1] The LED arrays are also custom-built and were matched to the geometry of the photoreactor. Figure 3.S1 repeats Figure 3.2 for easy reference of the description below.

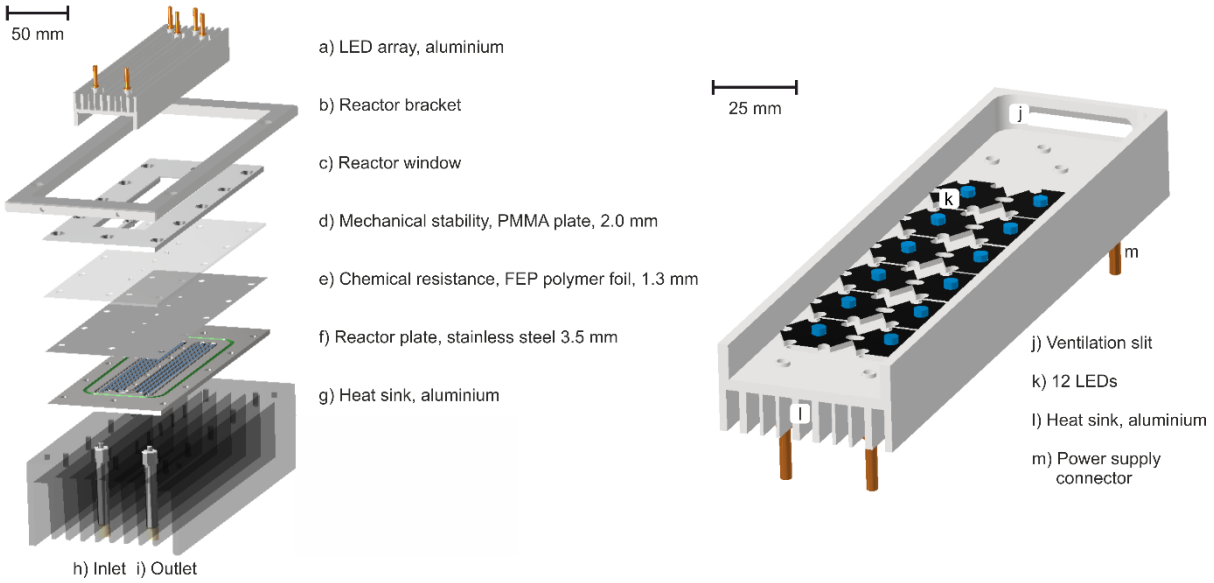

Figure 3.S1. Modular design of the custom-built photo–flow reactor (left side) and the LED arrays (right).

The reactor plate (f) is made of stainless steel to provide chemical resistance and to dissipate reaction heat. A heat sink (0.5 K W^{-1}, ABL Components, Birmingham, UK, g) and a heat-conducting foil (SFT80-0.15, 0.2 K W^{-1}, AMEC Thermasol, Norfolk, UK) are attached on the rear side of the reactor. The heat-conducting foil provides good heat transfer between the reactor plate and the heat sink. The 48 mm cooling fins ensure that reactions take place under isothermal conditions. The inlet (h) and outlet (i) for the reaction solution are also placed on the rear side of the reactor to allow connection to the HPLC system. A chemically resistant FEP polymer foil (fluorinated ethylene propylene, 1.3 mm, e) is placed on top of the reactor plate, and a PMMA plate (poly(methyl methacrylate)), 2.0 mm, d) is placed over the FEP foil to provide mechanical stability. Via the reactor window (c) above the PMMA plate, the reactor is

fixed with twelve screws. In the center of the reactor window, a cross bar with another five screws is attached to prevent spilling between parallel segments of the reactor channel. In addition, the reactor window defines the area that is irradiated by the LED arrays. A reactor bracket (b) connects the reactor to the automation system. The LED array is positioned as close as possible to the reactor to minimize irradiation losses. Each LED array holds twelve identical LEDs (k) mounted on an aluminium housing with a heat sink (l) on the rear side. Power for the LEDs is supplied through the power supply connectors (m) on the rear side of the housing. A ventilation slit (j) assists in cooling the LEDs. Two radial fans placed next to the LED array in operation prevent overheating (Figure 3.S2): one radial fan blows over the LEDs, the other over the heat sink fins.

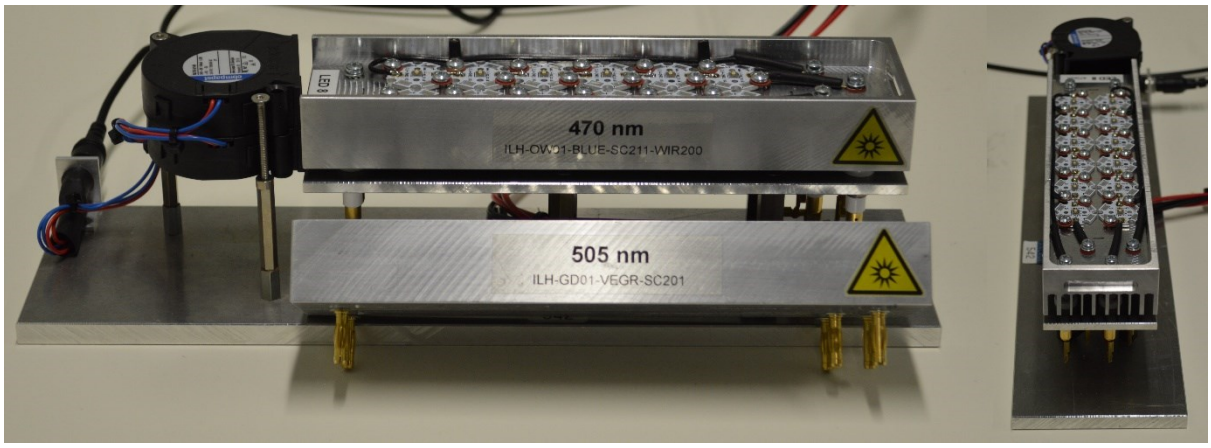

Figure 3.S2. Photograph of an LED array with radial fan.

The reactor plate (Figure 3.S3) contains a 1.5 mm wide and 0.5 mm deep channel for the reaction solution. The shallow channel depth minimizes the penetration depth of the LEDs. (A shallower channel could not be milled into the plate for technical reasons.) The reaction channel is flanked by a deeper channel lined with fluoroelastomer FPM (inner sealing) to prevent spilling between parallel sections of the channel. As an additional safety feature, a deep surrounding channel lined with fluoroelastomer FPM (outer sealing) ensures that spilled reaction solution cannot leave the reactor plate.

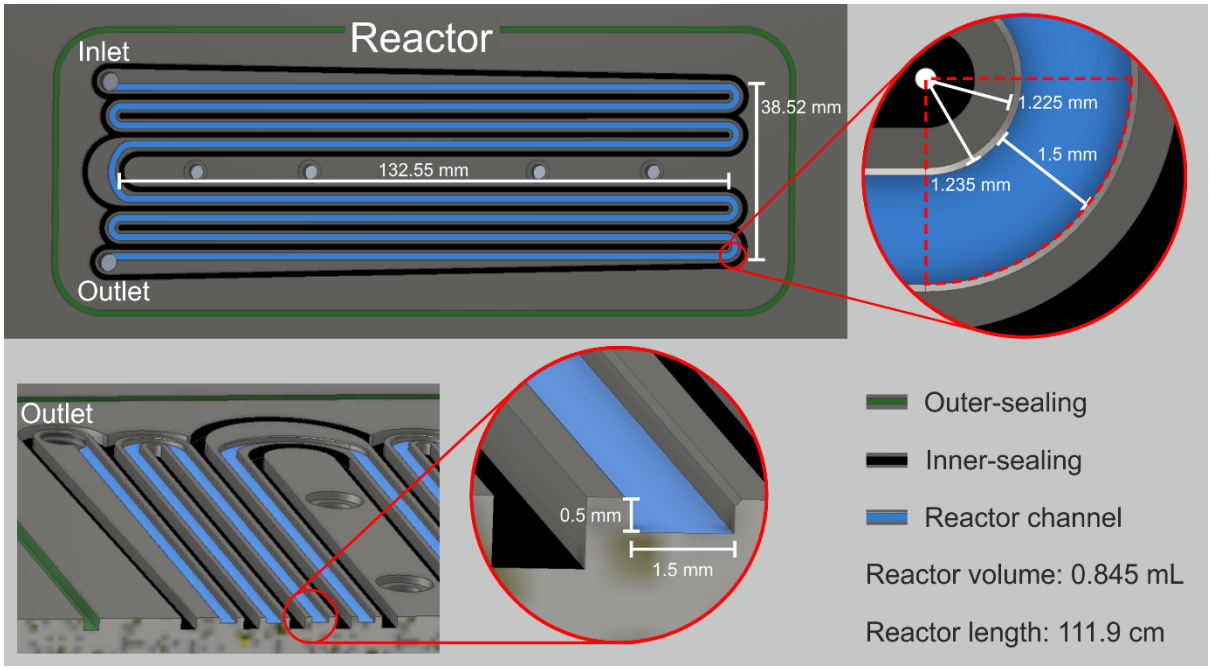

Figure 3.S3. Technical drawing of the reactor plate.

The reactor volume determines the reaction time at different flow rates. All irradiated volumes of the different geometrical elements contribute to the reactor volume of 0.845 mL. A photograph of the reactor plate with coloring as in Figure 3.S3 is shown in Figure 3.S4 besides a top view onto the closed reactor.

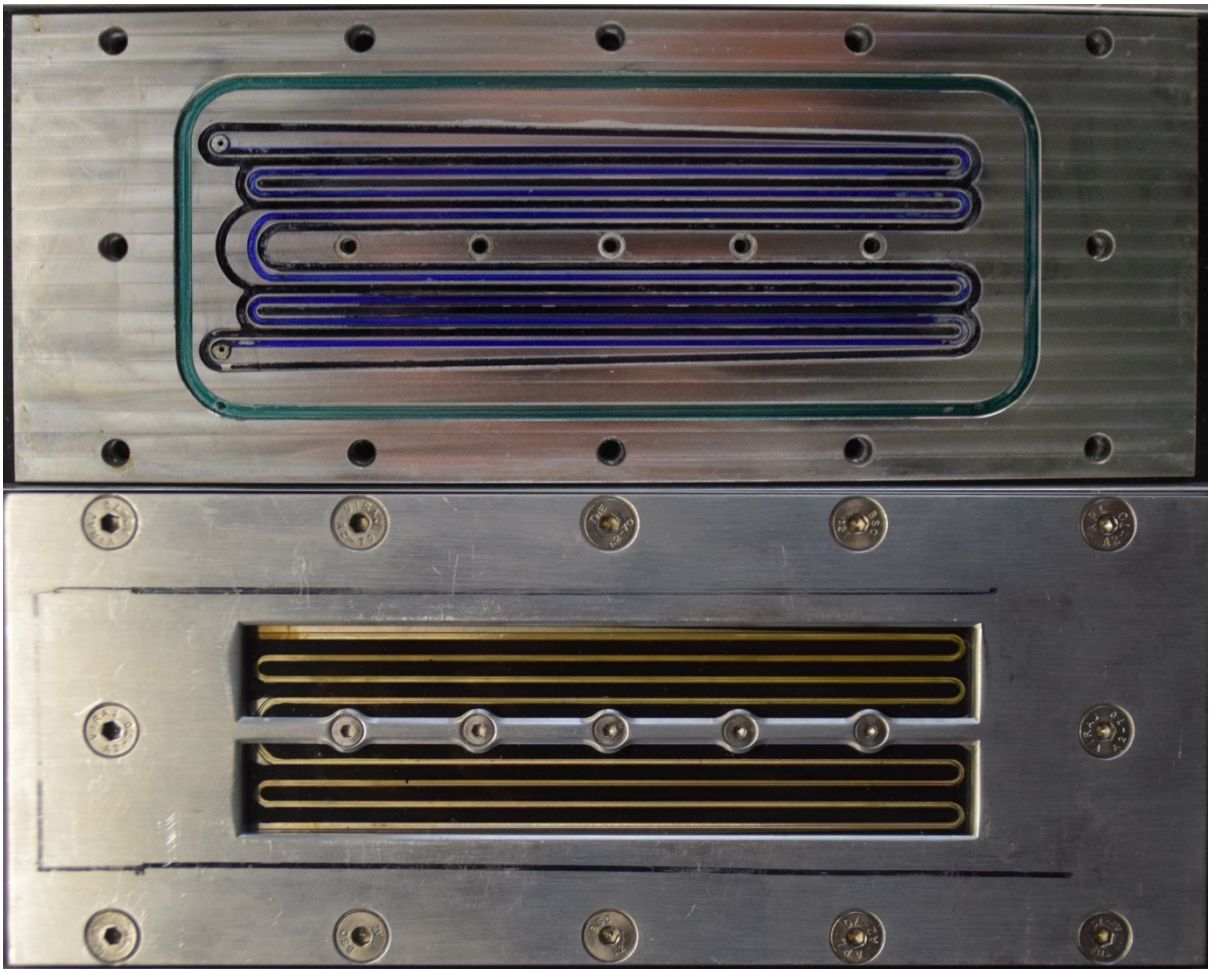

Figure 3.S4. Top: Reactor plate with colored channels. Bottom: Top view onto the closed reactor.

3.5.3 LED arrays characterization

Table 3.S1 lists the details of the LEDs used for the custom-built LED arrays. Each array contains twelve identical LEDs, six of them connected in series. Power was supplied through an adjustable power supply with two channels (30 V, 3 A, PEAKTECH 6180, Ahrensburg, Germany).

Table 3.S1. LEDs used for the LED arrays.

λ (nm)	Power[a] (W)	Product name	Vendor	Costs[b] (€)
373	5.00	Roschwege Star-UV365-05-00-00	Conrad[c]	104.00
375	3.00	3 W High Power LED 370nm–380nm	Avonec[d]	6.05
383	3.00	3 W High Power LED 380nm–390nm	Avonec	4.65
403	3.00	Roschwege Star-UV405-03-00-00	Conrad	18.73
416	3.00	3 W High Power LED 410nm–420nm	Avonec	2.40
430	3.00	3 W High Power LED 430nm–435nm	Avonec	1.85
442	2.17	ILH-OW01-DEBL-SC211-WIR200	RS Components[e]	7.45
464	2.17	ILH-OW01-BLUE-SC211-WIR200	RS Components	6.47
495	3.00	3 W High Power LED 490nm–495nm	Avonec	2.33
504	2.24	ILH-GD01-VEGR-SC201	RS Components	7.01
518	3.00	3 W High Power LED 515nm–525nm	Avonec	1.44
522	2.17	ILH-OW01-TRGR-SC211	RS Components	7.81

a: Maximum applicable electrical power as specified by the vendor. b: Costs per LED. c: Conrad Electronic SE (Hirschau, Germany). d: Avonec (Essen, Germany). e: RS Components (Corby, UK).

A calibrated spectroradiometer PS–200 (Apogee Instruments, Logan, UT) was used to determine the current sensitivity of the irradiance for all LED arrays (Figure 3.S5–3.S16). The irradiance was quantified as the power spectral density (PSD, in µmol m^{-2} s^{-1}), which gives the amount of photons that hit the detector per unit area and time integrated over all emitted wavelengths. The template and holder to fix the detector positions were made with a 3D printer (Ultimaker 2+). The PSD values were determined for currents between 100 and 700 mA (maximum applicable current) or until the detector limit of the spectroradiometer was reached (saturation). With the low currents used for the wavelength screenings in continuous flow, detector saturation did not occur, so that deviations of >3% from the reference PSD can be excluded. With the high currents required to achieve 900% of the reference PSD for the wavelength screening in batch, detector saturation was inevitable. The PSD values for higher

currents were extrapolated from the PSD values measured at currents below the detector saturation level. The accompanying uncertainty in the extrapolated PSD values of the LED arrays was acceptable, because the batch screening served only to find appropriate conditions for selective synthesis of the intermediate.

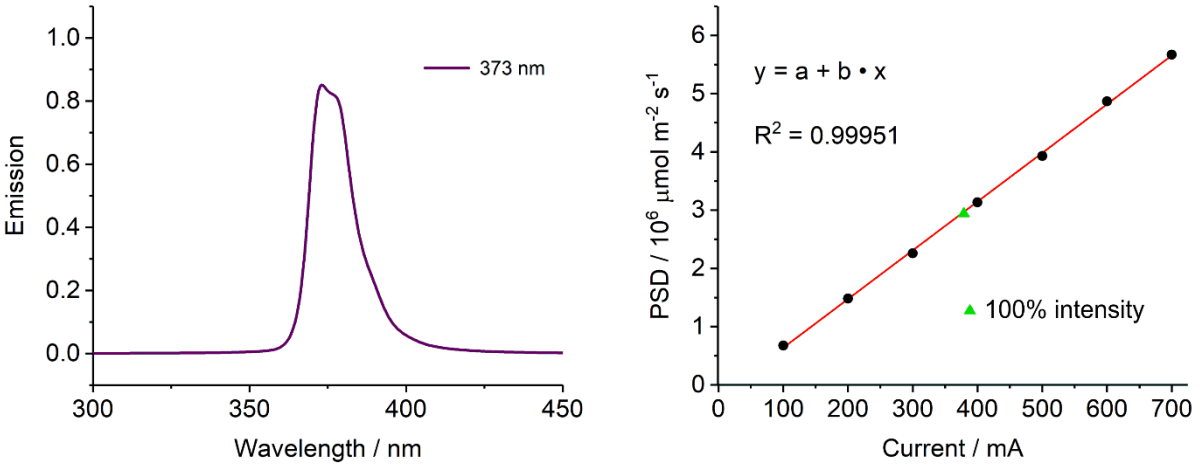

Figure 3.S5. Emission spectrum and current sensitivity curve of the LED array with λ_{max} at 373 nm.

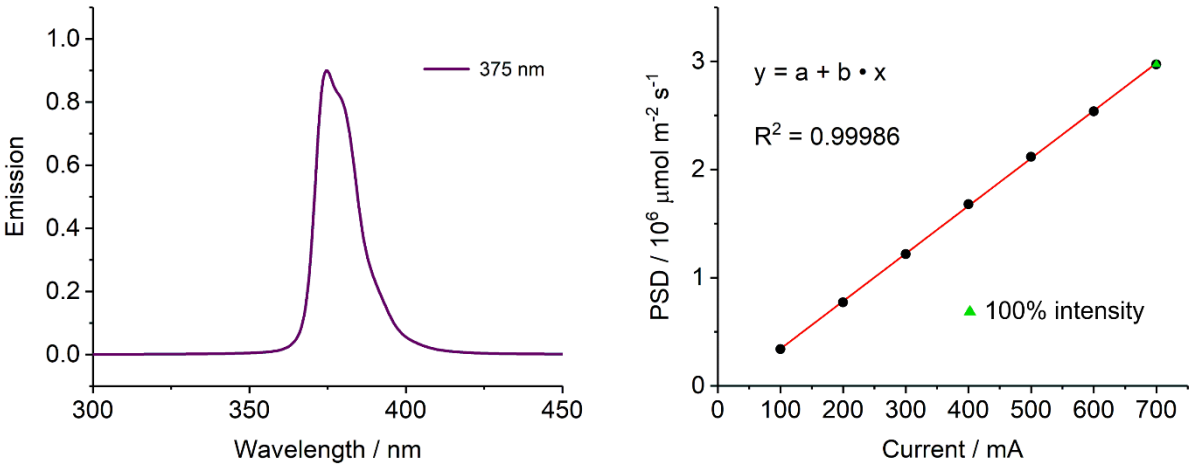

Figure 3.S6. Emission spectrum and current sensitivity curve of the LED array with λ_{max} at 375 nm.

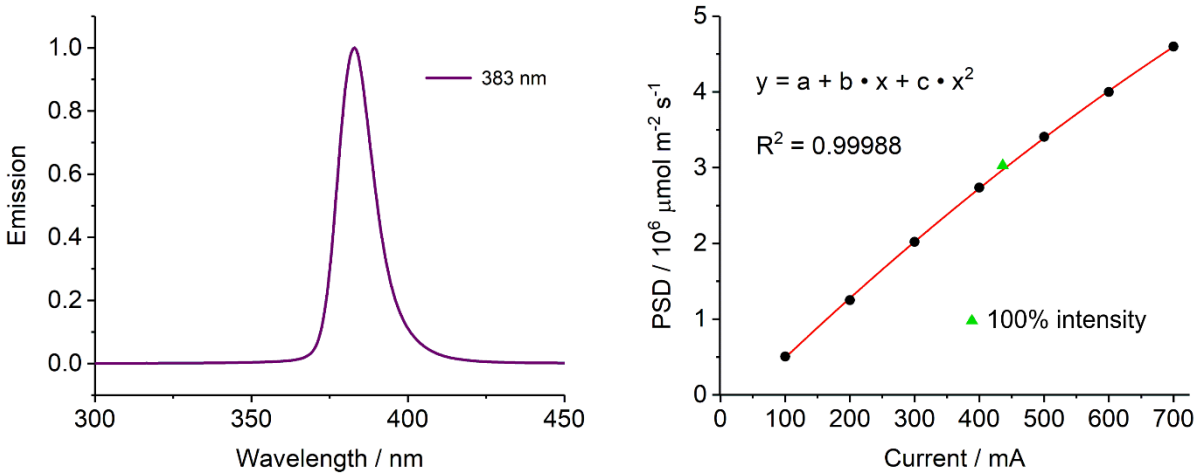

Figure 3.S7. Emission spectrum and current sensitivity curve of the LED array with λ_{max} at 383 nm.

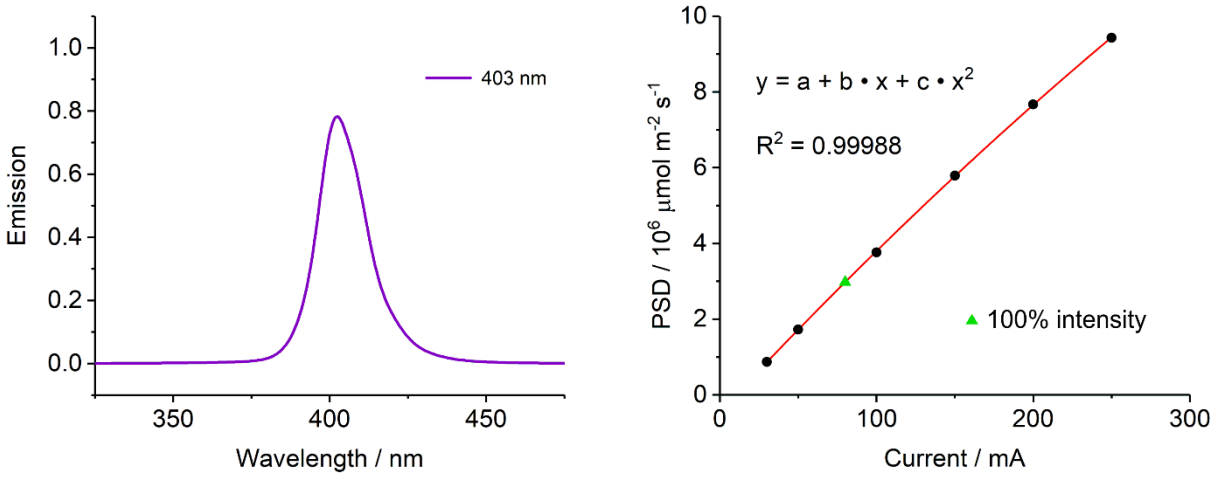

Figure 3.S8. Emission spectrum and current sensitivity curve of the LED array with λ_{max} at 403 nm.

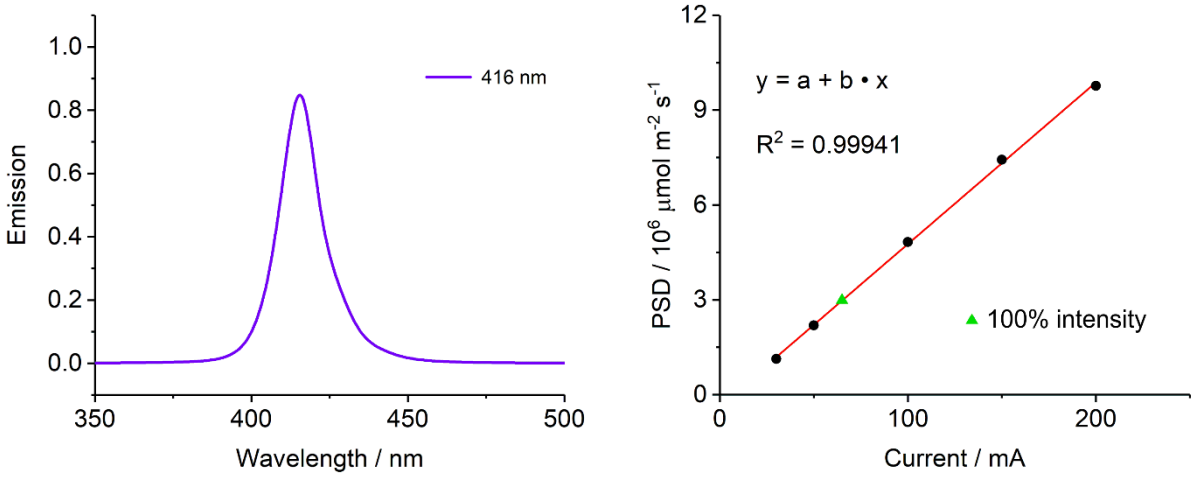

Figure 3.S9. Emission spectrum and current sensitivity curve of the LED array with λ_{max} at 416 nm.

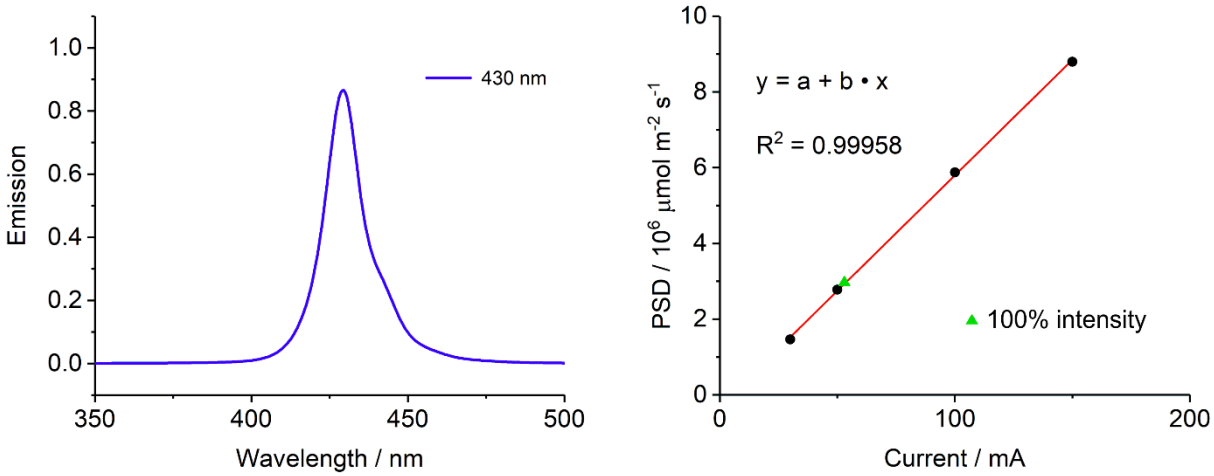

Figure 3.S10. Emission spectrum and current sensitivity curve of the LED array with λ_{max} at 430 nm.

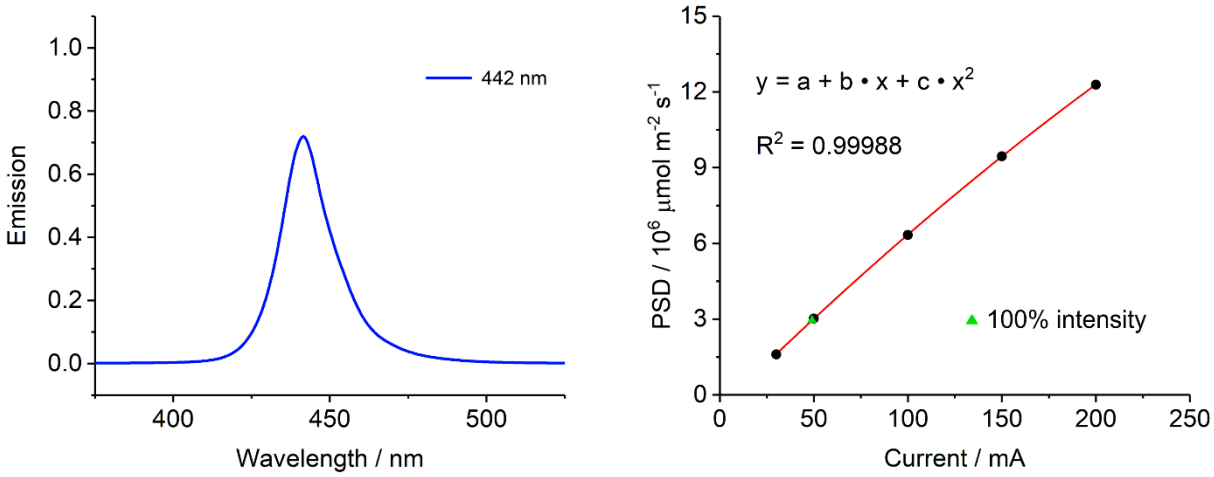

Figure 3.S11. Emission spectrum and current sensitivity curve of the LED array with λ_{max} at 442 nm.

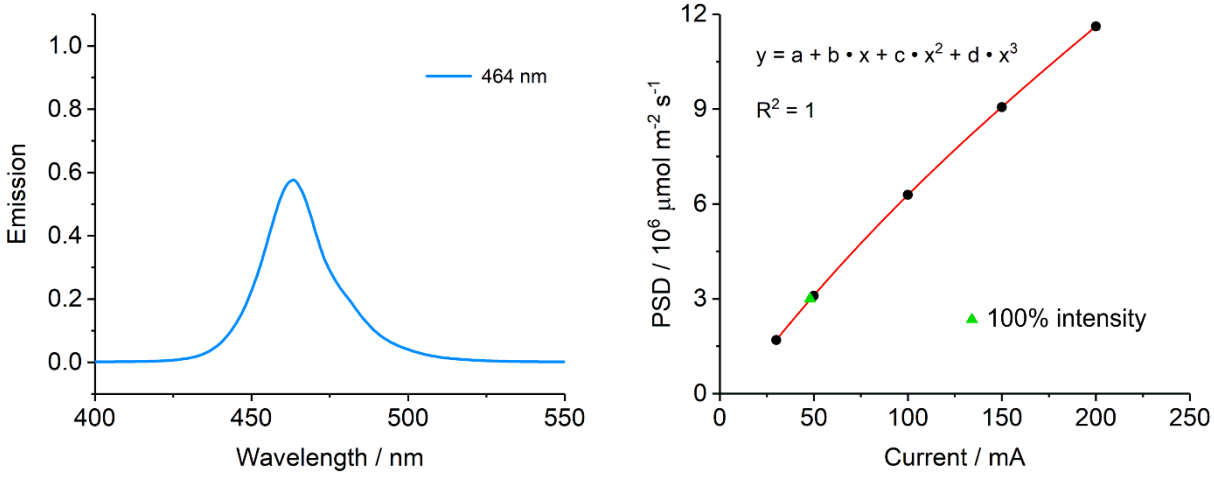

Figure 3.S12. Emission spectrum and current sensitivity curve of the LED array with λ_{max} at 464 nm.

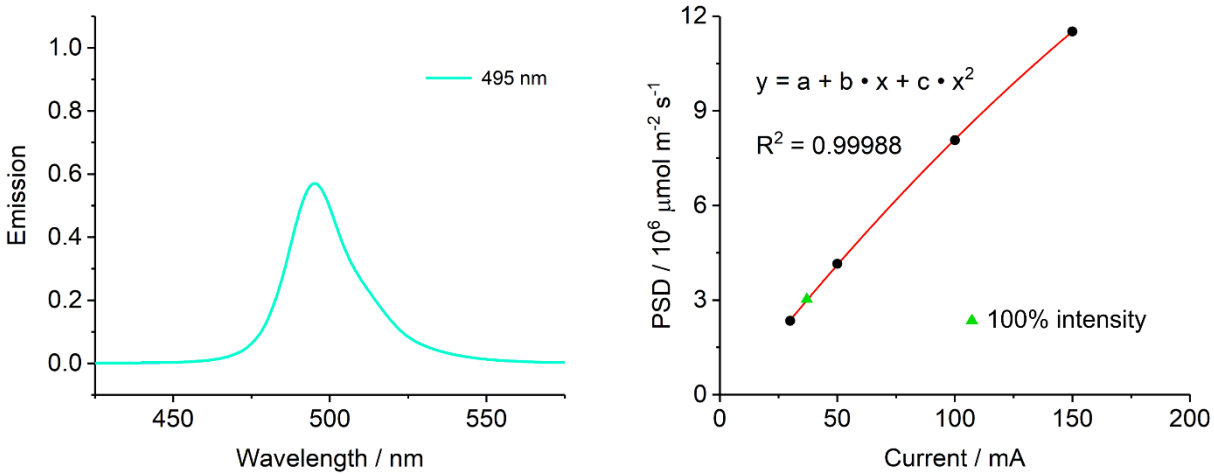

Figure 3.S13. Emission spectrum and current sensitivity curve of the LED array with λ_{max} at 495 nm.

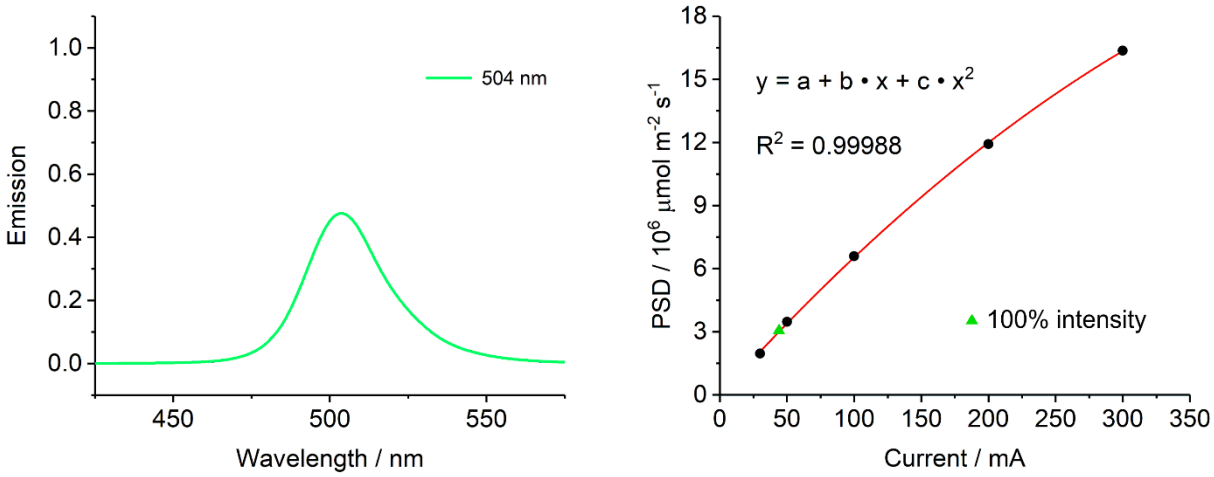

Figure 3.S14. Emission spectrum and current sensitivity curve of the LED array with λ_{max} at 504 nm.

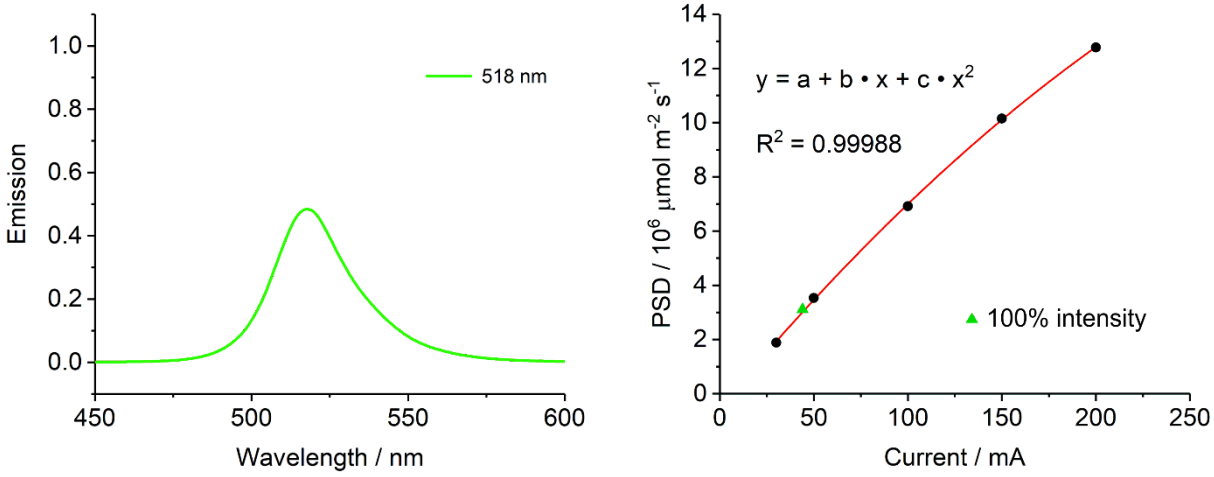

Figure 3.S15. Emission spectrum and current sensitivity curve of the LED array with λ_{max} at 518 nm.

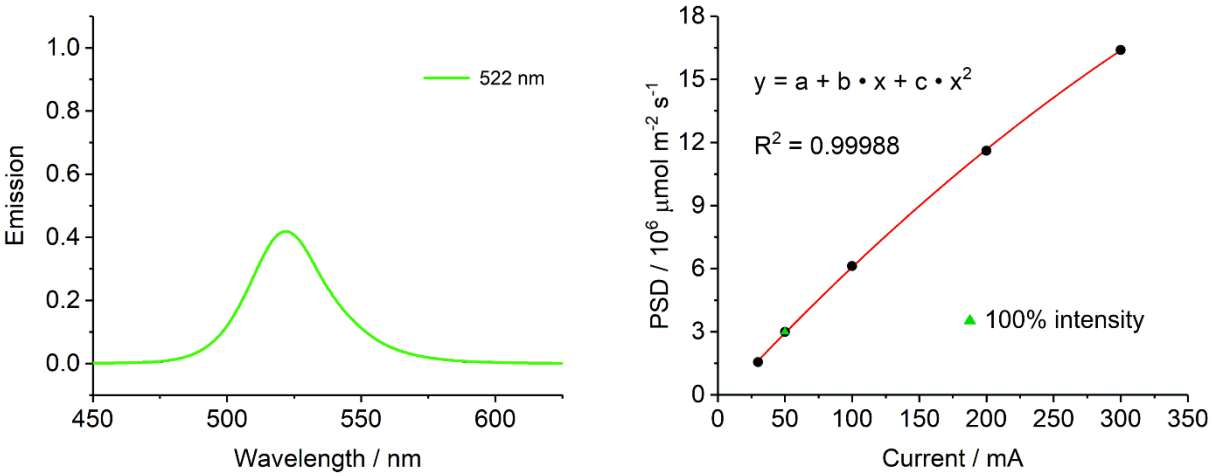

Figure 3.S16. Emission spectrum and current sensitivity curve of the LED array with λ_{max} at 522 nm.

3.5.4 LED-array automation setup

For a fully automated setup, a linear actuator (ISELGermanyAG, Eichenzell, Germany) was bought and complemented by a custom-built carriage that can accommodate up to ten LED arrays simultaneously (Figure 3.S17).

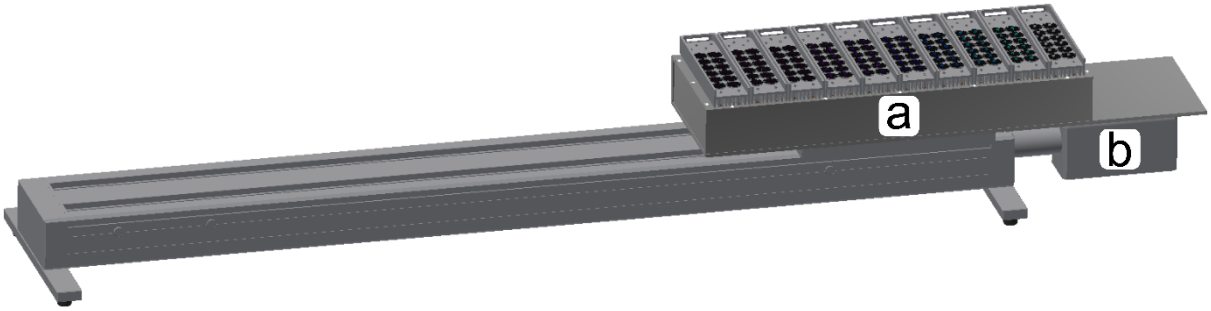

Figure 3.S17. Technical drawing of the linear actuator (b) with ten LED arrays on the carriage (a).

The photoreactor is mounted above the middle of the linear actuator. Changes of the irradiation wavelength are effected by a movement of the linear actuator that places the selected LED array below the photoreactor (Figure 3.S18).

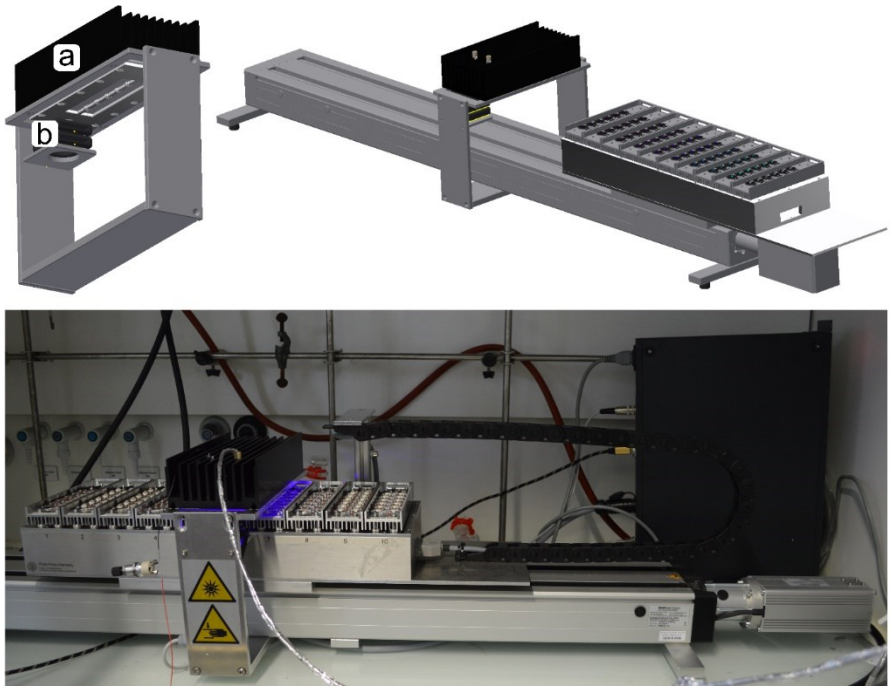

Figure 3.S18. Top: Technical drawing of the linear actuator with photo–flow reactor (a) and the radial fans (b) for active cooling of the LED array in operation. Bottom: Photograph of the complete automation setup.

The linear actuator and the LED arrays are connected to a custom-built electrical control device (Figure 3.S19).

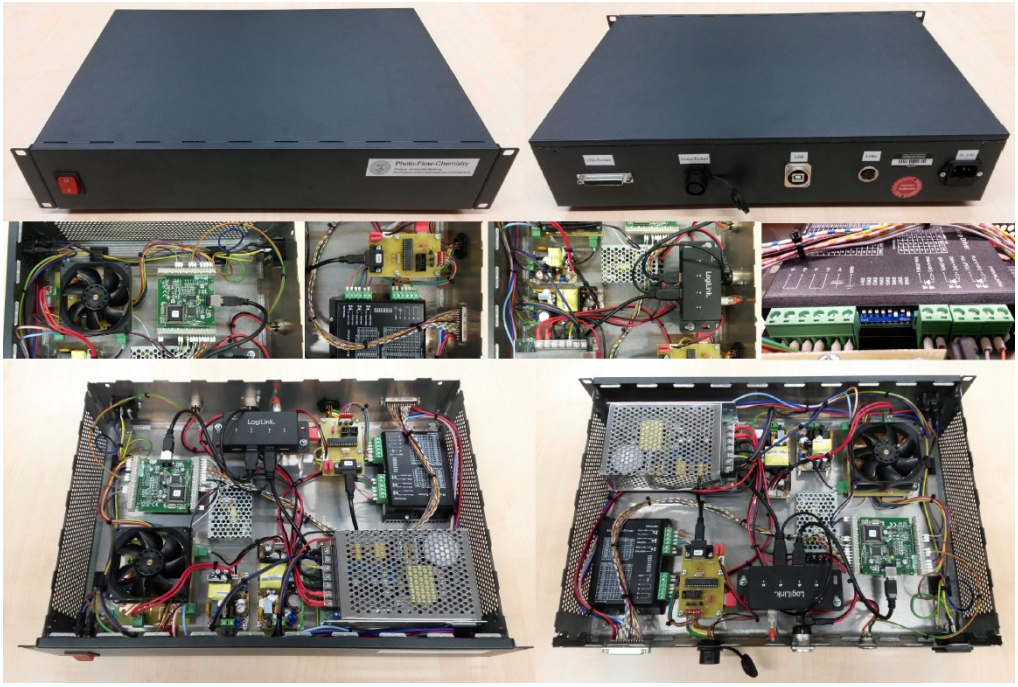

Figure 3.S19. Interior of the electrical control unit that applies the appropriate voltage and current to the LED arrays.

In-house written software is used to determine which LED array on the carriage is put into operation below the photoreactor (setting the irradiation wavelength) as well as the current applied to the operative array and the operation time (setting the irradiation intensity and time). The software was written with Free Pascal in the Lazarus development environment (www.lazarus-ide-org). Through creation of timetables a sequence of events can be programmed so that the software enables fully automated screening of the irradiation wavelength and intensity (Figure 3.S20).

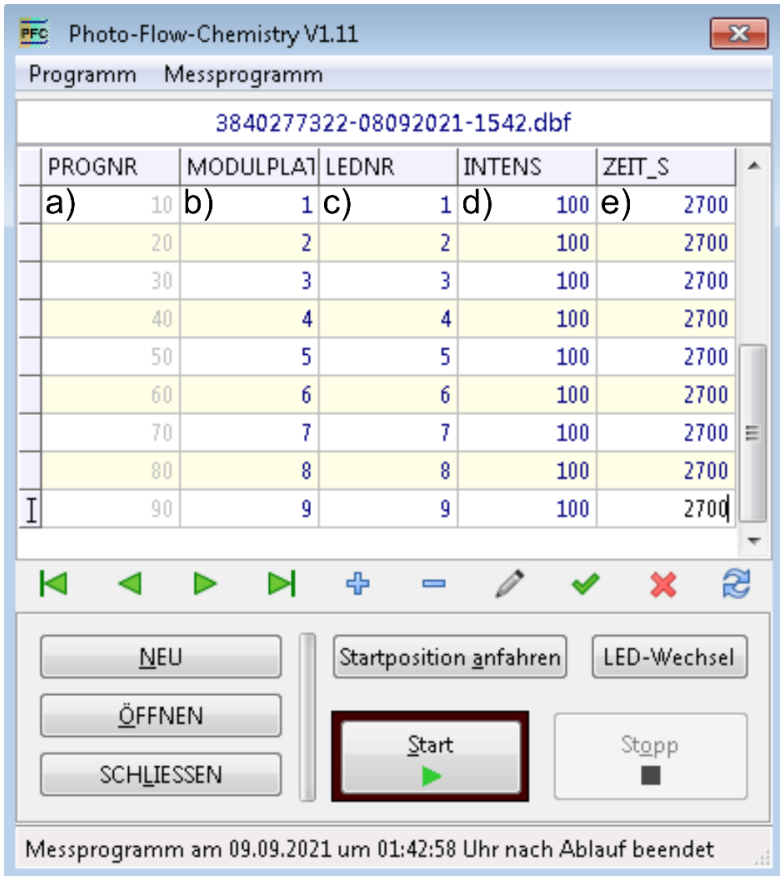

Figure 3.S20. Screenshot of the software program for creating schedules for the automation system.

The first column (a) determines the order in which the timetable entries are processed. The second column (b) indicates the slot position on the carriage tray, the third column (c) designates the LED array (LED 1, 373 nm; LED 2, 375 nm, etc.). The separation of slot position and LED array identity by the software allows high flexibility and the exchange of LED arrays on the carriage. The current sensitivity curves of all LED arrays (Figure 3.S5–3.S16) are imported into the software. This enables translation of a chosen irradiation intensity (third column, d) into the respective current that needs to be applied to a given LED array. In Figure 3.S20, the intensity is set to 100, which corresponds to the PSD of the weakest LED array at the maximum applicable current (reference PSD value). Please note that intensities above 100% are possible for any but the weakest array. The last column (e) specifies the irradiation time in seconds. The software verifies that data entries are reasonable and prevents the start of the program in case of obvious errors.

3.5.5 Two-dimensional reaction–analysis setup

The two-dimensional flow platform for parallel reaction and analysis (Figure 3.S21) was described in detail previously.[S1] The centerpiece of the first dimension is formed by a quaternary pump and a binary pump. The quaternary pump was used for screenings with atmospheric oxygen, the binary pump was used for screenings under inert gas conditions. The quaternary pump has four independent channels for precise control of the flow rate and the concentration of each reactant. A substrate solution (**1** or **7**, 12.5 mmol/L) and a dioxaborolane solution (**2**, 50 mmol/L) in acetonitrile/water 9/1 (v/v) as well as the neat binary solvent mixture were connected to the quaternary pump. The neat solvent mixture is used to dilute the substrate solution and determine suitable reactant concentrations for the screening. The binary pump is easier to connect to the inert gas flasks. A stainless-steel capillary tube was attached directly to the pump heads of the binary pump, which was connected to inert gas flasks containing the reactant solutions through a septum. The flasks remained connected to an inert gas line during the entire screening process to prevent a pressure drop due to withdrawal of solution. A backpressure regulator set to 50 bar was placed between the pumps and the photoreactor to ensure smooth operation of the HPLC pumps. Without backpressure regulator, only about 2–3 bar backpressure would be applied, for which the HPLC pumps are not actually designed. No backpressure was applied to the photoreactor.

The second dimension consists of a standard HPLC system for chromatographic separations. A 2-position/6-port valve with an injection loop of 1.3 µL volume mounted behind the reactor connects the first dimension with the second dimension. An inline diode array detector (DAD) is used to monitor the total UV absorbance of the reaction solution; constant UV absorbance indicates that the system operates in steady state. The flow path of the setup is shown in Figure 3.S21.

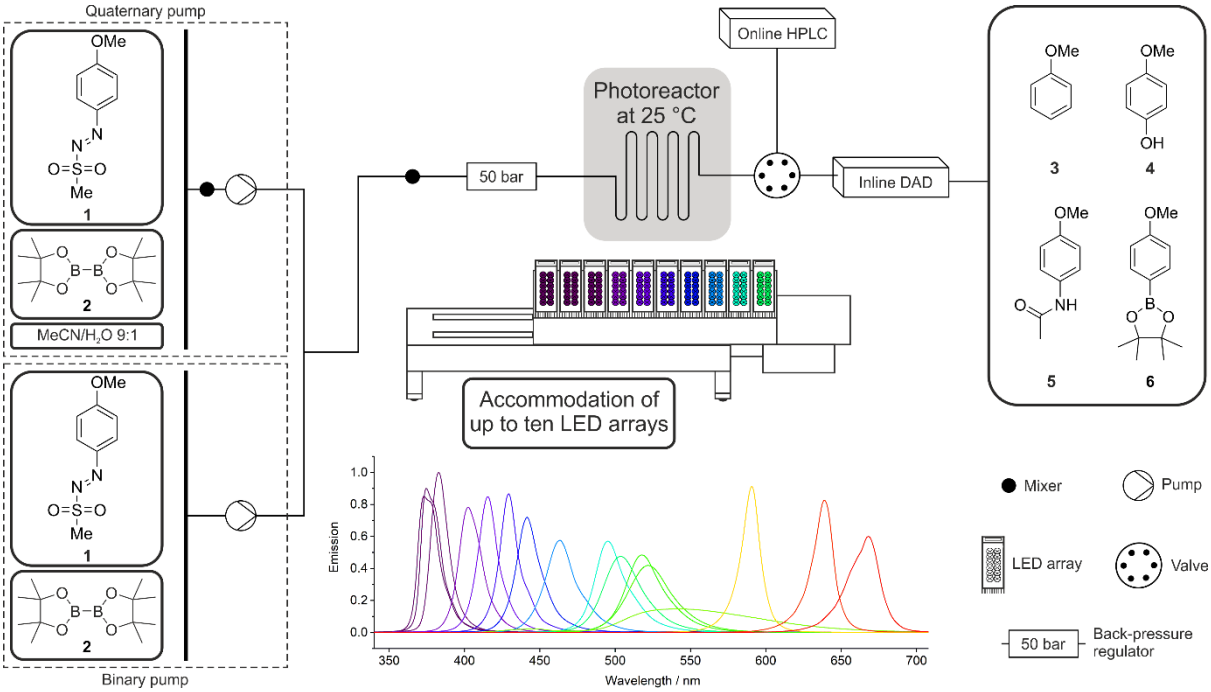

Figure 3.S21. Flow path for automated wavelength screening with up to ten LED arrays.

A photograph of the platform is shown in Figure 3.S22. The individual parts of the HPLC system were received from Agilent Technologies (Waldbronn, Germany).

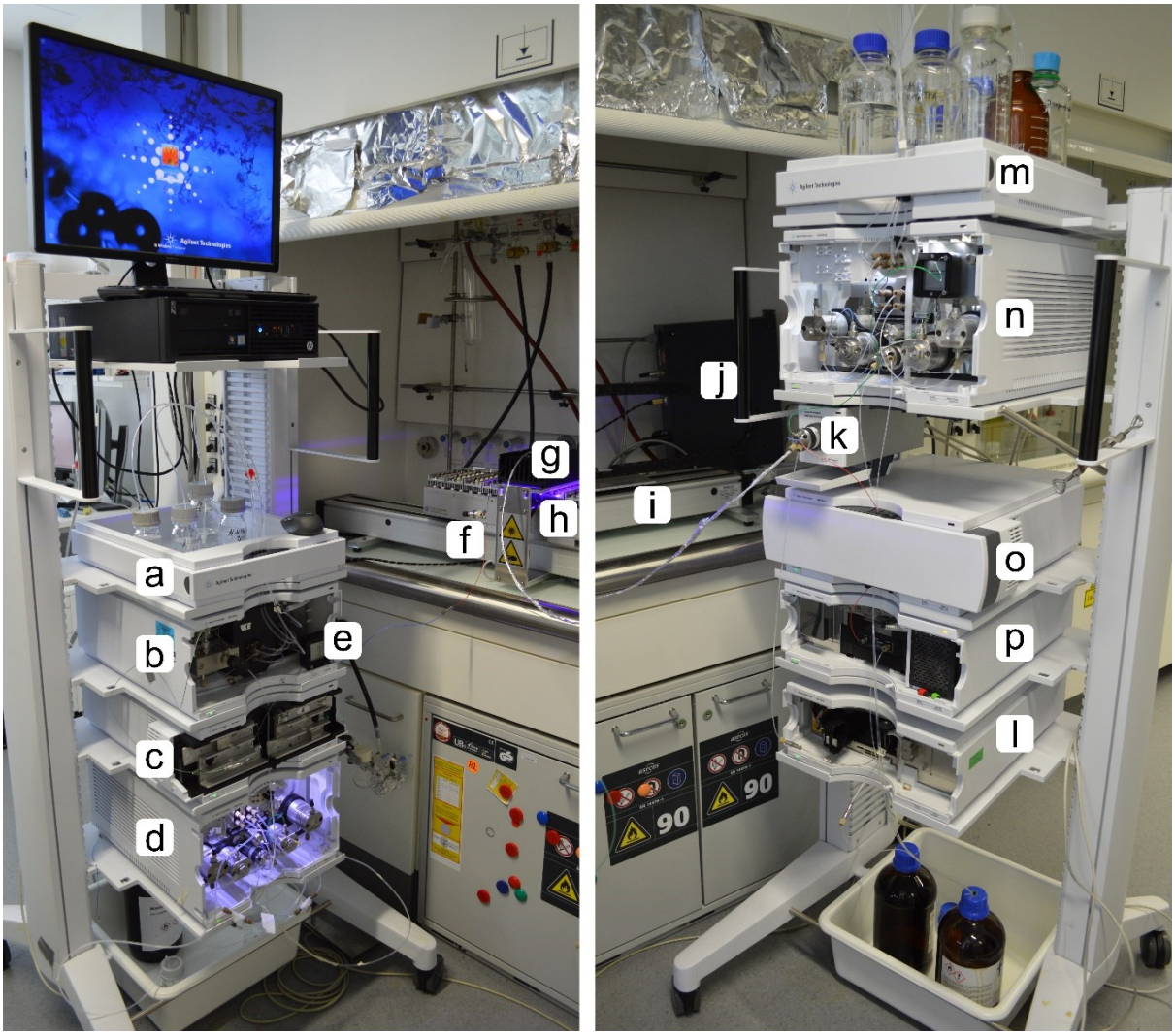

Figure 3.S22. The first dimension for reaction control is shown on the left side, the second dimension for chromatographic analysis is shown on the right side. After leaving the photoreactor (g) the reaction solution is transferred via the 2-position/6-port valve (k) to the second dimension. Reaction control: a) reactant solutions; b) quaternary pump (Agilent 1260 Infinity Series, G1311B); c) thermostatted HPLC column compartment (Agilent 1290 Infinity Series, G1316C); d) binary pump (Agilent 1290 Infinity Series, G4220A); e) Jet Weaver V35 Mixer; f) back-pressure regulator; g) photoreactor; h) LED-array rack; i) linear actuator; j) electrical control device for LED automation; k) 2-position/6-port valve (Agilent 1290 Series, G1170A); l) inline DAD (Agilent 1200 Series, G1315C). Chromatographic analysis: m) eluents; n) binary pump (Agilent 1290 Infinity Series, G4220A); o) thermostatted HPLC column compartment (Agilent 1290 Infinity Series, G1316C) with separation column (Chromolith HighResolution RP-18 endcapped, 100 x 4.6 mm, Merck KGaA, Darmstadt); p) DAD (Agilent 1290 Infinity Series, G4212A).

The separation conditions for chromatographic analysis by the online-coupled HPLC system were tuned to achieve baseline separation of all reactants, products and side products in the shortest possible analysis time (Figure 3.S23). The separation was performed at 25°C in reversed-phase mode on an endcapped C_{18} column through gradient elution with a water–acetonitrile mobile phase at a flow rate of 1 mL min^{-1}.

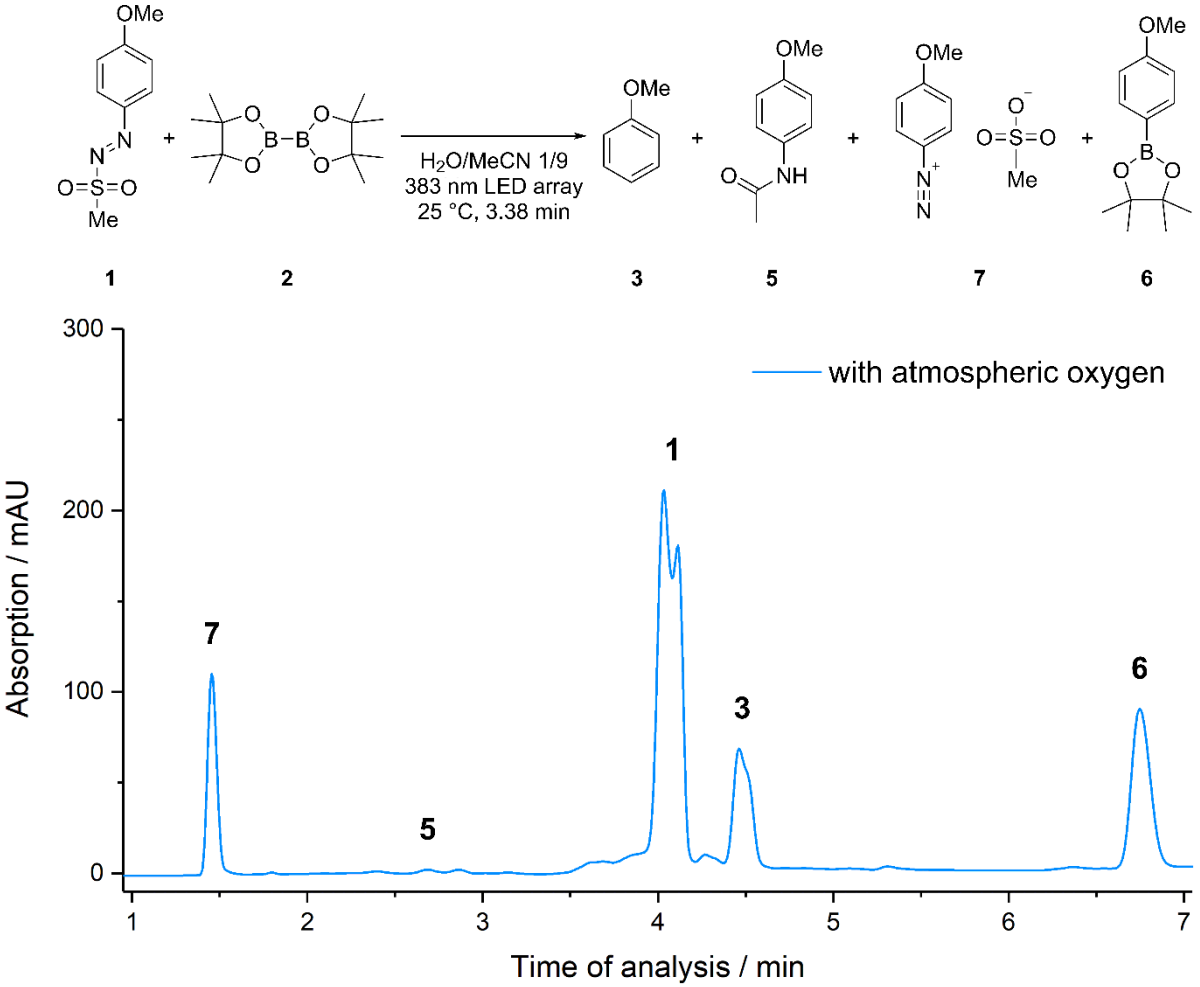

Figure 3.S23. Chromatogram from the wavelength screening of the reaction with additive. The additive **2** itself does not absorb in the wavelength range of the DAD.

For external quantification of the separated compounds from their chromatographic peaks, calibration curves were acquired (Figure 3.S24–3.S32). The quarternary pump was programmed to dilute the stock solution of a compound in acetonitrile/water 9/1 (v/v) by mixing it with the neat binary solvent mixture at various volumetric ratios to produce ten different concentrations. These solutions were sequentially fed to the chromatographic analysis system via the 2-position/6-port valve. Data points for the calibration curves were received from the area of a chromatographic peak at a specific detection wavelength and feed concentration. The determination was repeated under the gradient elution conditions of Table 3.S2 and 3.S3.

Table 3.S2. Gradient used for chromatographic analysis of the reaction without additive.

Time (min)[a]	Water (vol %)	Acetonitrile (vol %)
0.00	77	23
3.19	72	28
3.20	52	48
6.19	52	48
6.20	0	100
8.19	0	100
8.20	77	23
10.18	77	23

a: Injection at 0.08 min.

Table 3.S3. Gradient used for chromatographic analysis of the reaction with additive.

Time (min)[a]	Water (vol %)	Acetonitrile (vol %)
0.00	77	23
2.19	72	28
2.20	42	58
5.69	42	58
5.70	22	78
7.39	0	100
8.99	0	100
9.00	77	23
11.00	77	23

a: Injection at 0.08 min.

Compounds **1**, **3**, **4** and **5** showed linear behavior over the calibrated range under the gradient elution conditions of Table 3.S2 (Figure 3.S24–3.S27).

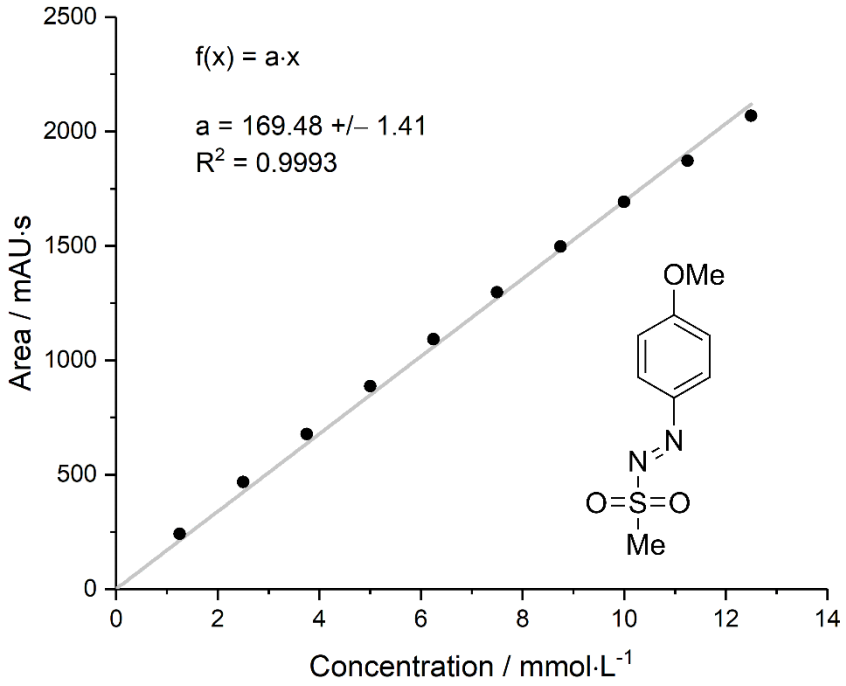

Figure 3.S24. Calibration curve of the substrate 1-(4-methoxyphenyl)-2-(methylsulfonyl)diazene (**1**) at a detection wavelength of 261 nm.

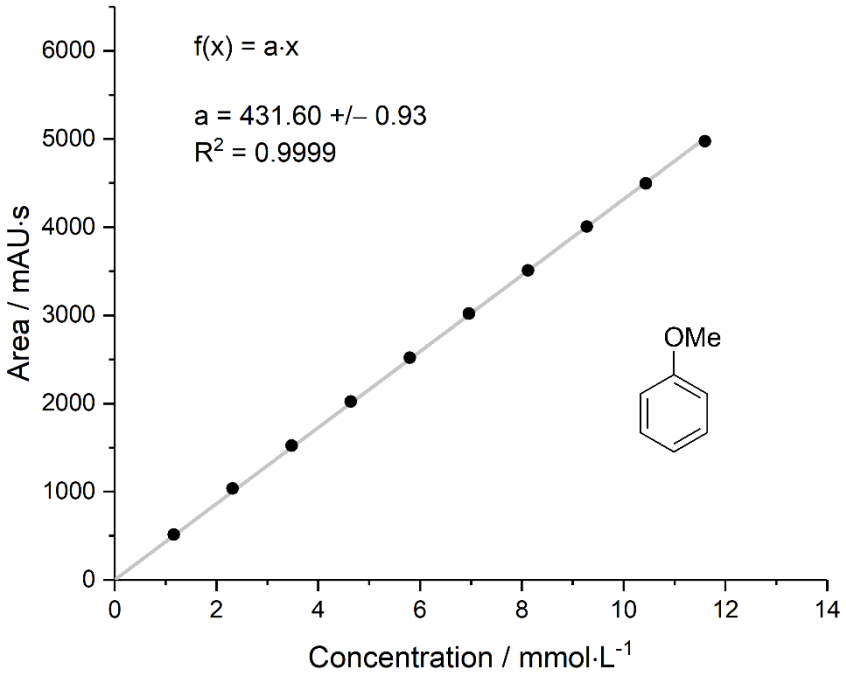

Figure 3.S25. Calibration curve of methoxybenzene (**3**) at a detection wavelength of 271 nm.

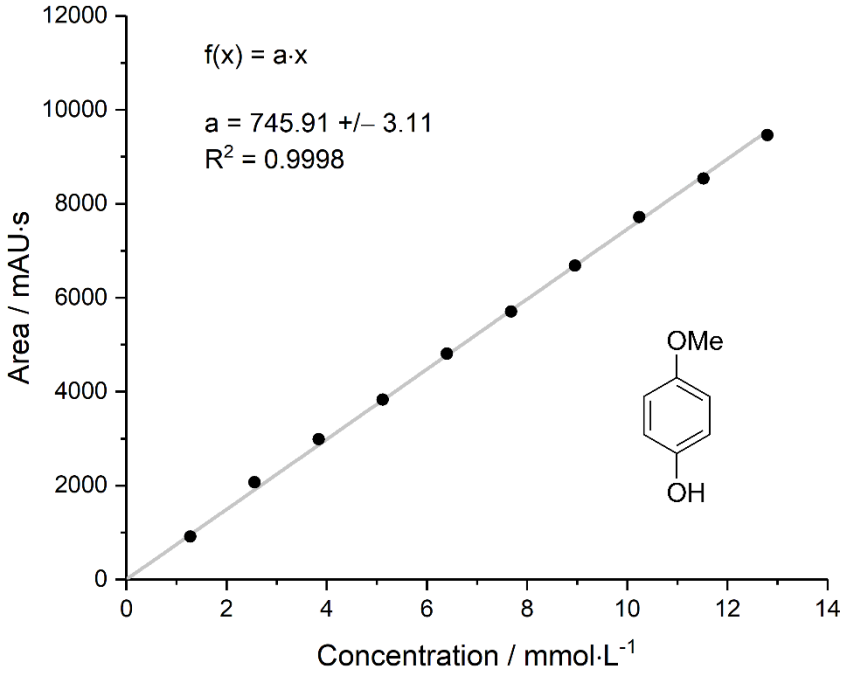

Figure 3.S26. Calibration curve of 4-methoxyphenol (**4**) at a detection wavelength of 261 nm.

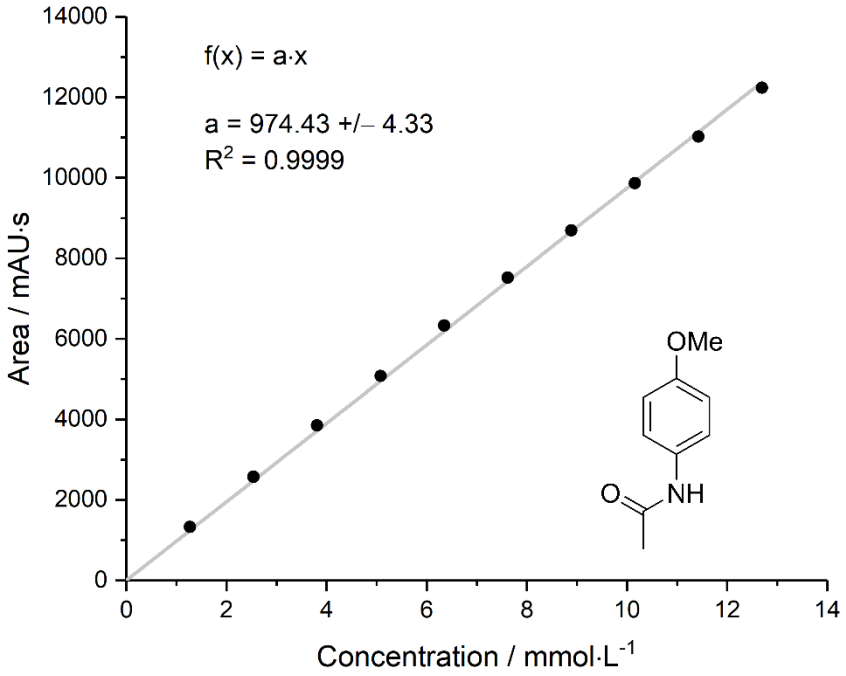

Figure 3.S27. Calibration curve of 4-methoxyacetanilide (**5**) at a detection wavelength of 271 nm.

Compounds **1**, **3**, **5** and **6** showed linear behavior over the calibrated range under the gradient elution conditions of Table 3.S3 (Figure 3.S28–3.S31).

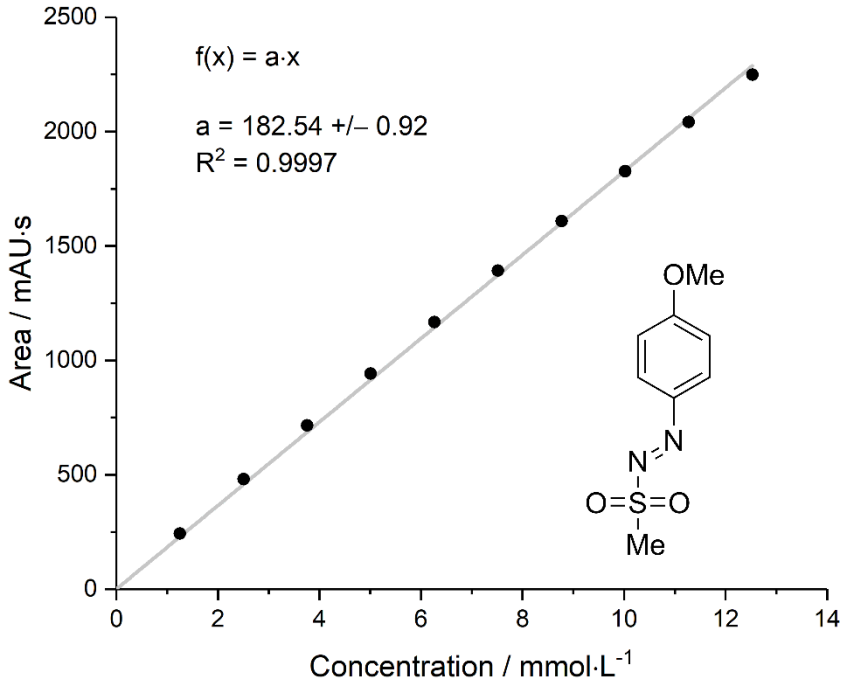

Figure 3.S28. Calibration curve of the substrate 1-(4-methoxyphenyl)-2-(methylsulfonyl)diazene (**1**) at a detection wavelength of 261 nm.

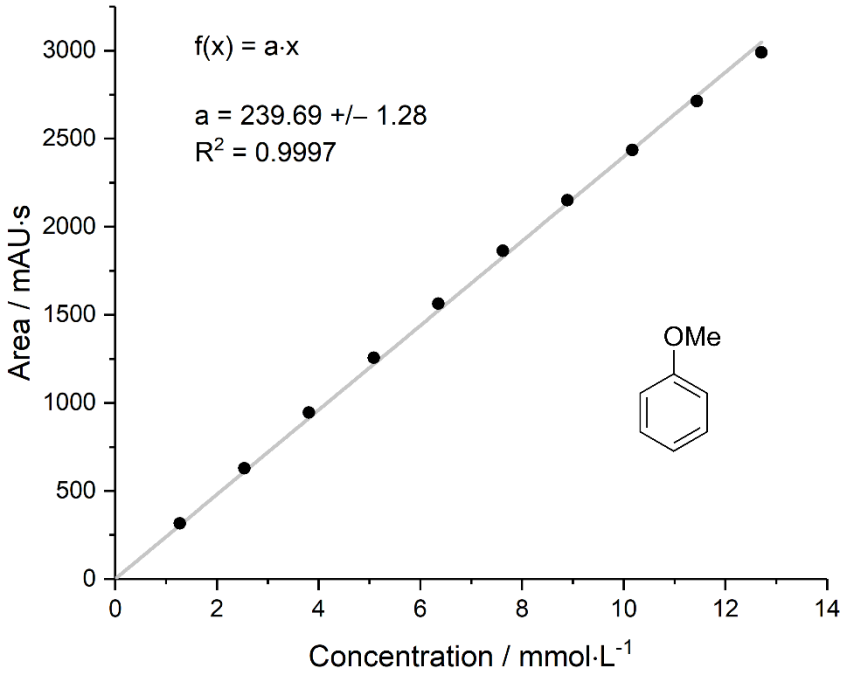

Figure 3.S29. Calibration curve of methoxybenzene (**3**) at a detection wavelength of 280 nm.

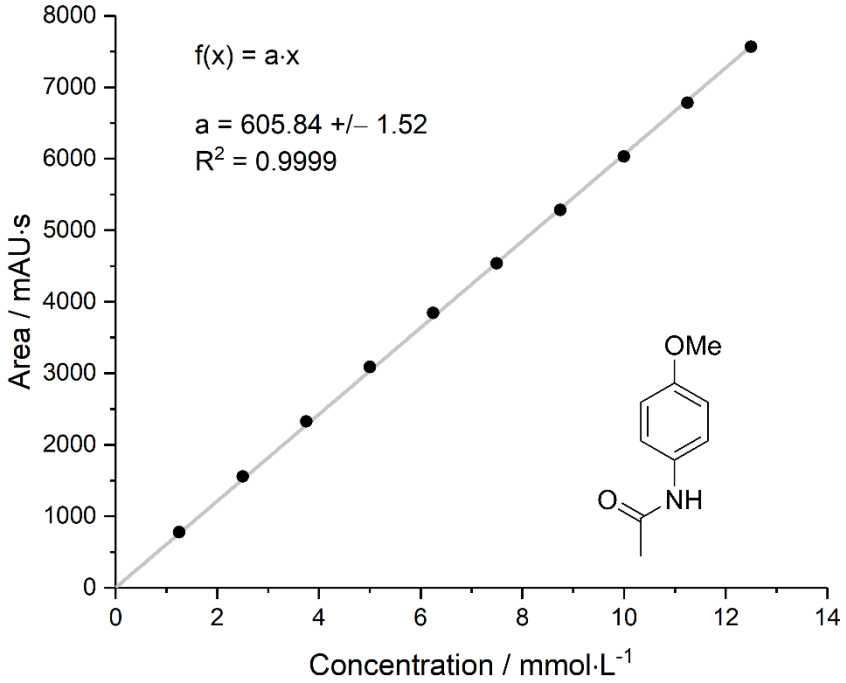

Figure 3.S30. Calibration curve of 4-methoxyacetanilide (**5**) at a detection wavelength of 280 nm.

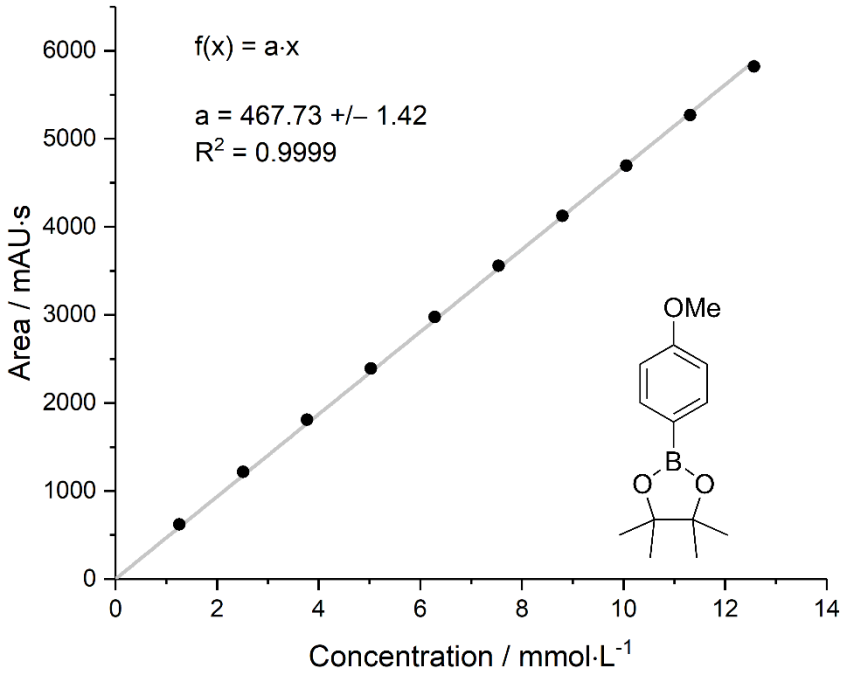

Figure 3.S31. Calibration curve of the dioxaborolane **6** at a detection wavelength of 261 nm.

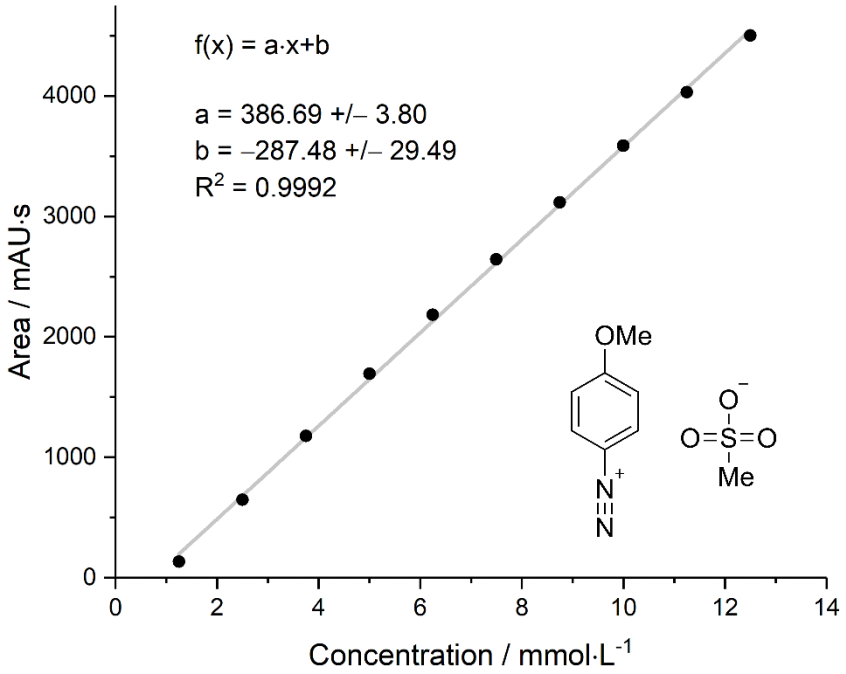

Figure 3.S32. Calibration curve of the intermediate **7** at a detection wavelength of 261 nm.

A calibration curve that passes through the origin could not be obtained for the intermediate, despite evaluating several detection wavelengths. The calibration curve of **7** is therefore only valid for concentrations between 1.25 and 12.5 mmol/L (Figure 3.S32).
Overall, the adherence to linearity observed in the calibration curves of the compounds confirms the precision and high reproducibility of data generation with our set-up.

3.5.6 Synthesis

1-(4-methoxyphenyl)-2-(methylsulfonyl)diazene (1)

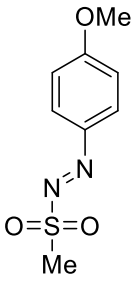

The arylazo sulfone **1** was prepared according to the literature from 4-methoxybenzenediazoniumtetrafluoroborate (**8**), prepared as described below.[S2,S3] The diazonium salt **8** (1.275 g, 5.74 mmol) was dissolved in dichloromethane (29 mL) and the solution cooled to 0 °C. After addition of sodium methanesulfinate (0.645 g, 6.31 mmol) the suspension was stirred at 0 °C for 30 minutes and then overnight at room temperature. The precipitate was filtered off and washed with dichloromethane. The filtrate was concentrated under reduced pressure. Recrystallization in *n*-hexane yielded **1** as yellow needles (1.03 g, 4.78 mmol, 83%). The NMR spectroscopic data were in accordance with those reported in the literature.[4]
^{1}H NMR (300 MHz, $CDCl_3$): δ = 8.00–7.90 (m, 2 H), 7.09–6.99 (m, 2 H), 3.94 (s, 3 H), 3.19 (s, 3 H). **— ^{13}C NMR** (75 MHz, $CDCl_3$): δ = 165.9, 143.4, 127.5, 115.1, 56.1, 35.0

2-(4-methoxyphenyl)-4,4,5,5-tetramethyl-1,3,2-dioxaborolane (6)

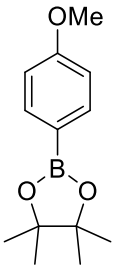

The dioxaborolane **6** was generated in the photo–flow reactor. A quaternary pump was used to supply the photoreactor with an arylazo sulfone solution (**1**, 12.5 mmol/L, 100 mL) and an 4,4,4',4',5,5,5',5'-octamethyl-2,2'-bi(1,3,2-dioxaborolane) solution (**2**, 50 mmol/L, 100 mL) in acetonitrile/water 9/1 (v/v) at a flow rate of 0.2 mL/min. The photoreactor was irradiated with the 416 nm LED array (at an applied current of 700 mA) and the reaction solution collected from the outlet for 16.7 hours. The solution was then concentrated under reduced pressure. Purification by column chromatography on silica gel with *n*-pentane/ethyl acetate 10/1 (v/v) yielded **6** as white solid (14 mg, 59.8 µmol, 2.4%). The NMR spectroscopic data were in accordance with those reported in the literature.[S4]

^{1}H NMR (300 MHz, $CDCl_3$): δ = 7.83–7.74 (m, 2 H), 6.96–6.90 (m, 2 H), 3.86 (s, 3 H), 1.37 (s, 12 H). **— ^{13}C NMR** (75 MHz, $CDCl_3$): δ = 162.3, 136.7, 113.5, 83.7, 55.2, 25.0.

4-Methoxybenzenediazonium methanesulfonate (7)

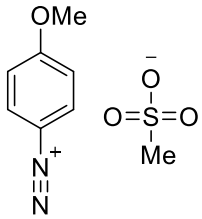

The arylazo sulfone **1** (70.0 mg, 327 µmol) was dissolved in a mixture of water (2.5 mL) and acetonitrile (22.5 mL). The solution was irradiated with the 504 nm LED array (at an applied current of 700 mA) in the presence of atmospheric oxygen for 3 h. The solution was then concentrated under reduced pressure and dried under vacuum to yield **7** (68.0 mg, 296 µmol, 91%) as a brown solid.

^{1}H NMR (300 MHz, DMSO-d_6): δ = 8.69–8.57 (m, 2 H, H2), 7.55–7.42 (m, 2 H, H3), 4.04 (s, 3 H, OMe), 2.32 (s, 3 H, SMe). **— ^{13}C NMR** (75 MHz, DMSO-d_6): δ = 168.8 (C4), 136.1 (C2), 117.2 (C3), 103.4 (C1), 57.5 (OMe), 39.7 (SMe). **— ESI (HR-MS)** calcd. for $C_7H_7N_2O^+$: 135.0553; found 135.0552, calcd. for $CH_3O_3S^-$: 94.9808; found 94.9808.

4-Methoxybenzenediazoniumtetrafluoroborate (8)

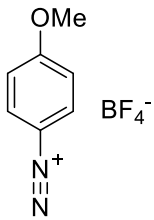

The diazonium salt **8** was prepared according to the literature.[S5] 4-Methoxyaniline (12.3 g, 100 mmol) was dissolved in water (35 mL) and an aqueous HBF_4 solution (48%, 35 mL). The mixture was cooled in an ice–salt bath to –5 °C before a pre-cooled solution of $NaNO_2$ (7.25 g, 105 mmol) in water (15 mL) was added dropwise. The drop frequency was kept so that the temperature of the reaction mixture stayed below 5 °C to prevent product loss. After complete addition of the $NaNO_2$ solution, the mixture was stirred for 30 minutes at –5 °C. Afterwards, the diazonium salt was collected by filtration and washed with cold water and diethylether. Drying in vacuo yielded **8** as a purple solid (20.805 g, 93.7 mmol, 94%). The NMR spectroscopic data were in accordance with those reported in the literature.[S6]

^{1}H NMR (300 MHz, DMSO-d_6): δ = 9.02–8.88 (m, 2 H), 7.96–7.85 (m, 2 H), 4.62 (s, 3 H). **— ^{13}C NMR** (75 MHz, DMSO-d_6): δ = 168.9, 136.2, 117.4, 103.3, 57.5.

3.5.7 NMR spectra

^{1}H NMR (300 MHz) and ^{13}C NMR (75 MHz) spectra were recorded at ambient temperature on a Bruker Avance 300 NMR spectrometer. The chemical shifts are reported in parts per million (ppm) relative to the signal of the solvents DMSO-d_6 (^{1}H NMR 2.50 ppm; ^{13}C NMR 39.52 ppm) and $CDCl_3$ (^{1}H NMR 7.26 ppm; ^{13}C NMR 77.16 ppm). Multiplicities are reported using the following abbreviations: s (singlet), m (multiplet).

1-(4-methoxyphenyl)-2-(methylsulfonyl)diazene (1)

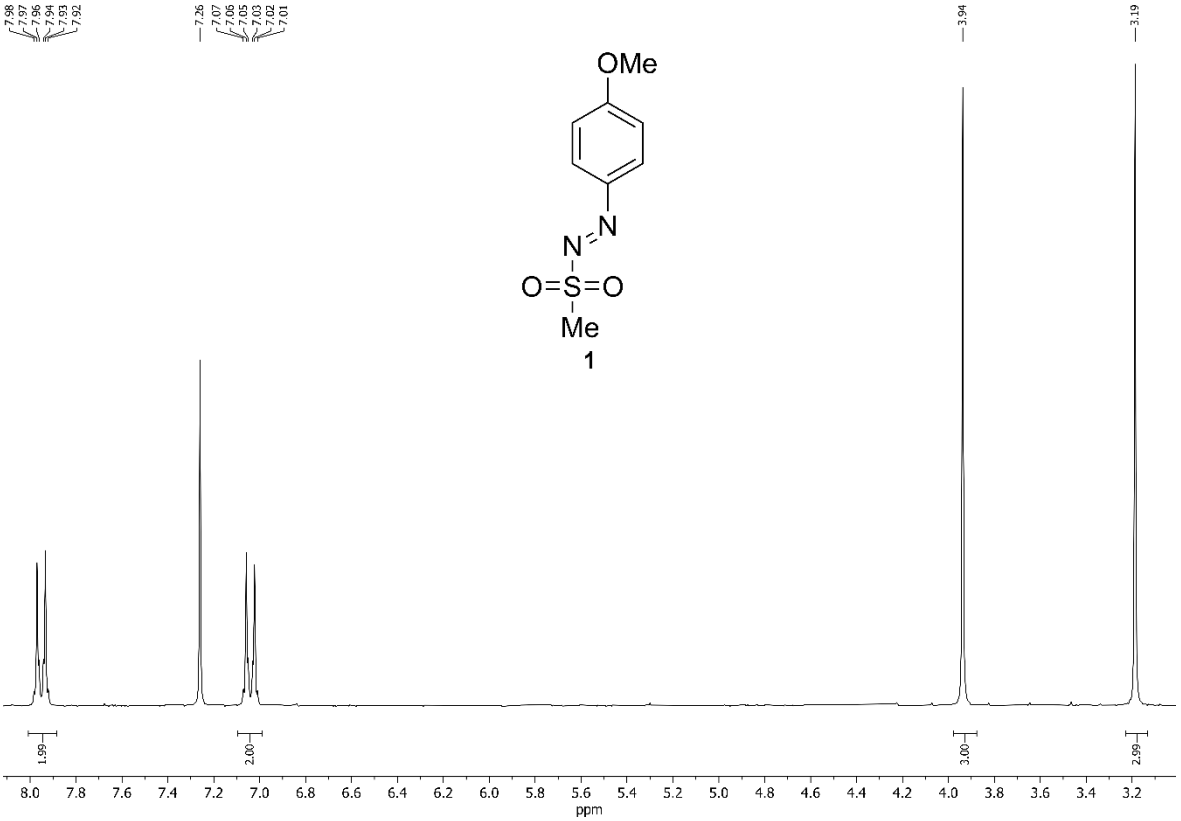

^{1}H NMR: (300 MHz, $CDCl_3$).

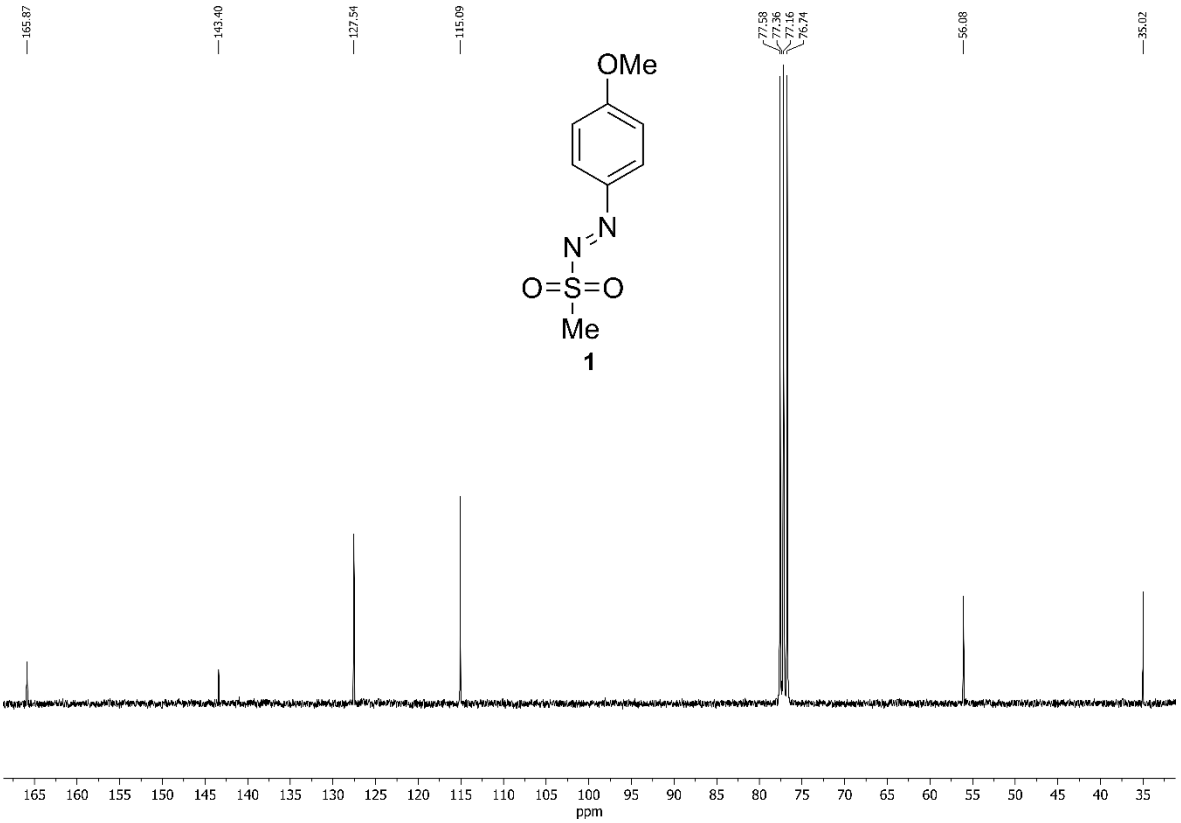

^{13}C NMR: (75 MHz, $CDCl_3$).

2-(4-methoxyphenyl)-4,4,5,5-tetramethyl-1,3,2-dioxaborolane (6)

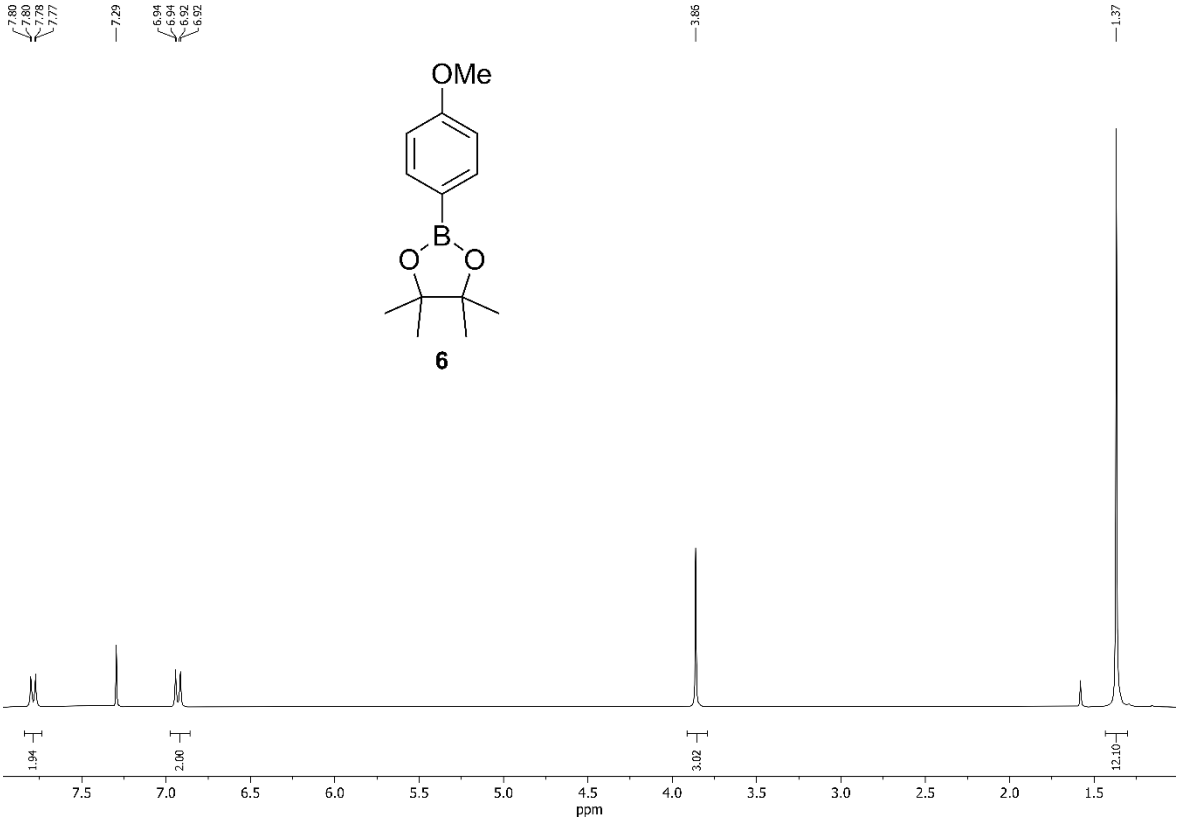

^{1}H NMR: (300 MHz, $CDCl_3$).

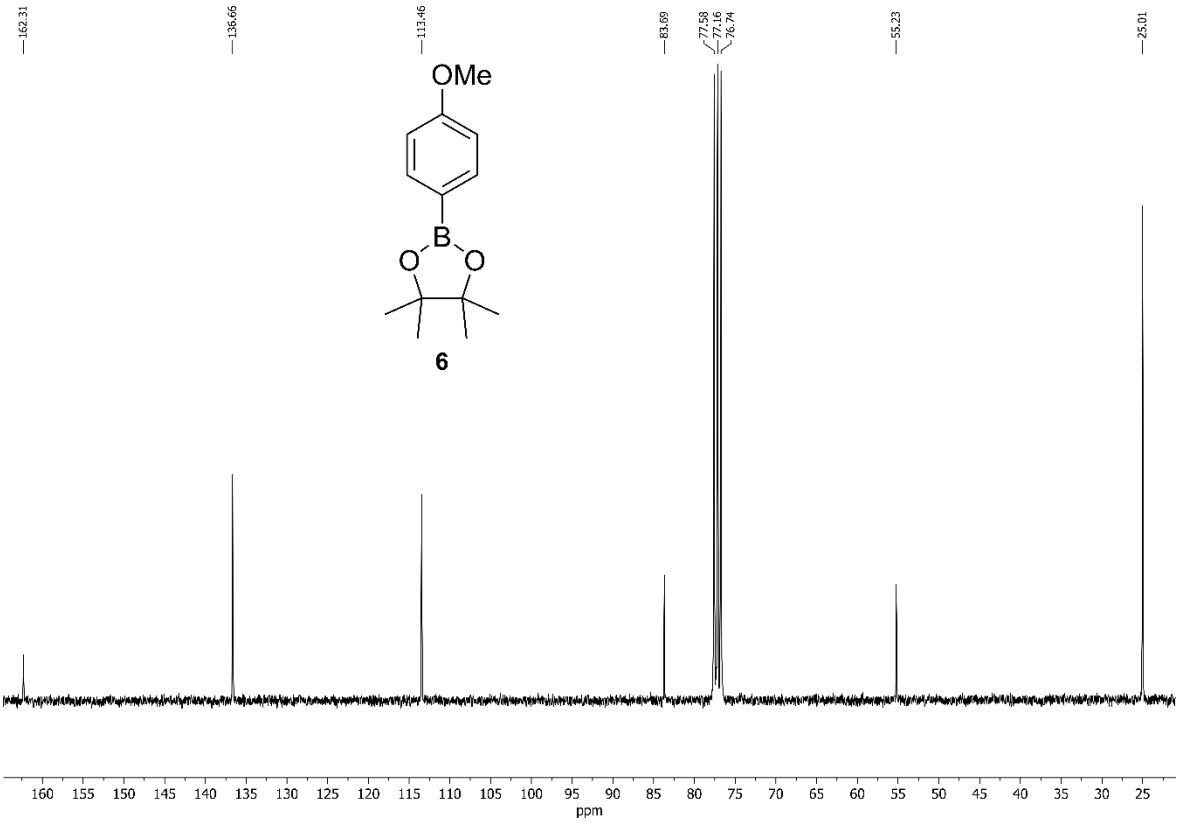

^{13}C NMR: (75 MHz, $CDCl_3$).

4-Methoxybenzenediazonium methanesulfonate (7)

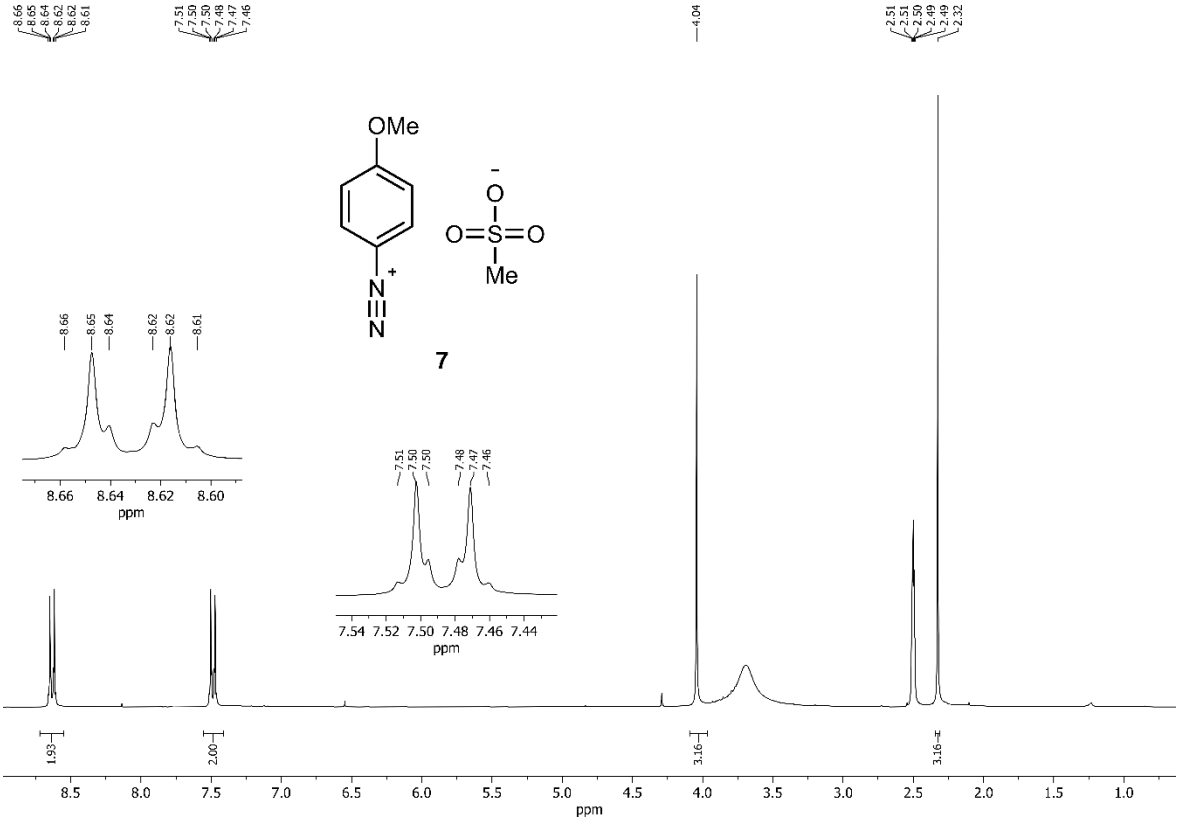

^{1}H NMR: (300 MHz, DMSO-d_6).

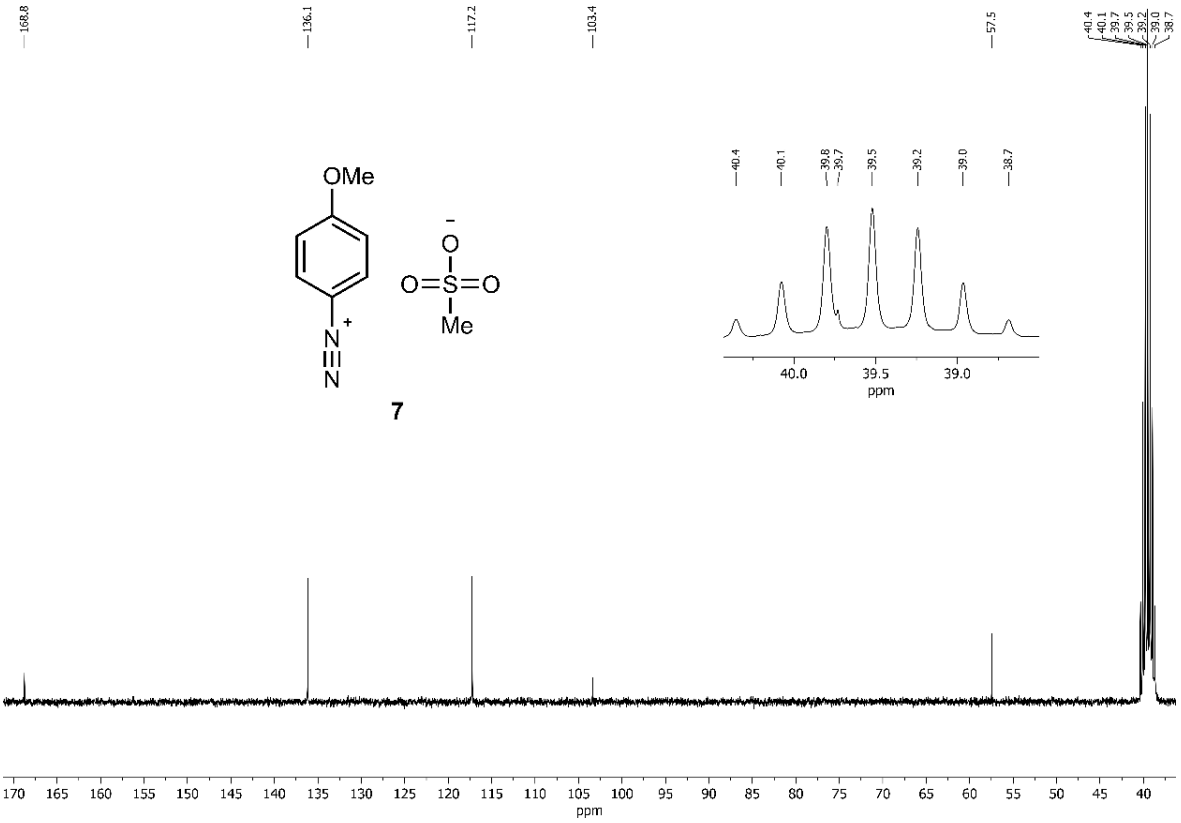

^{13}C NMR: (75 MHz, DMSO-d_6).

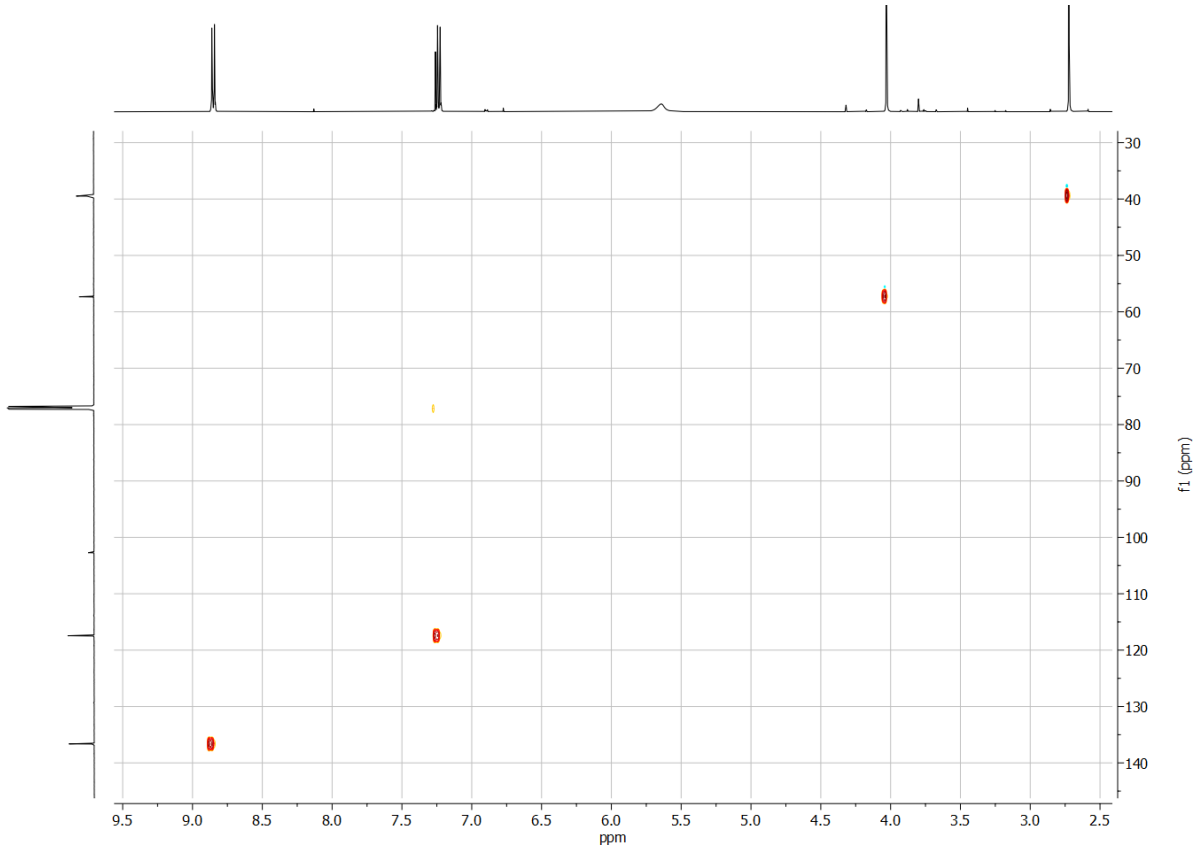

HSQC of **7**.

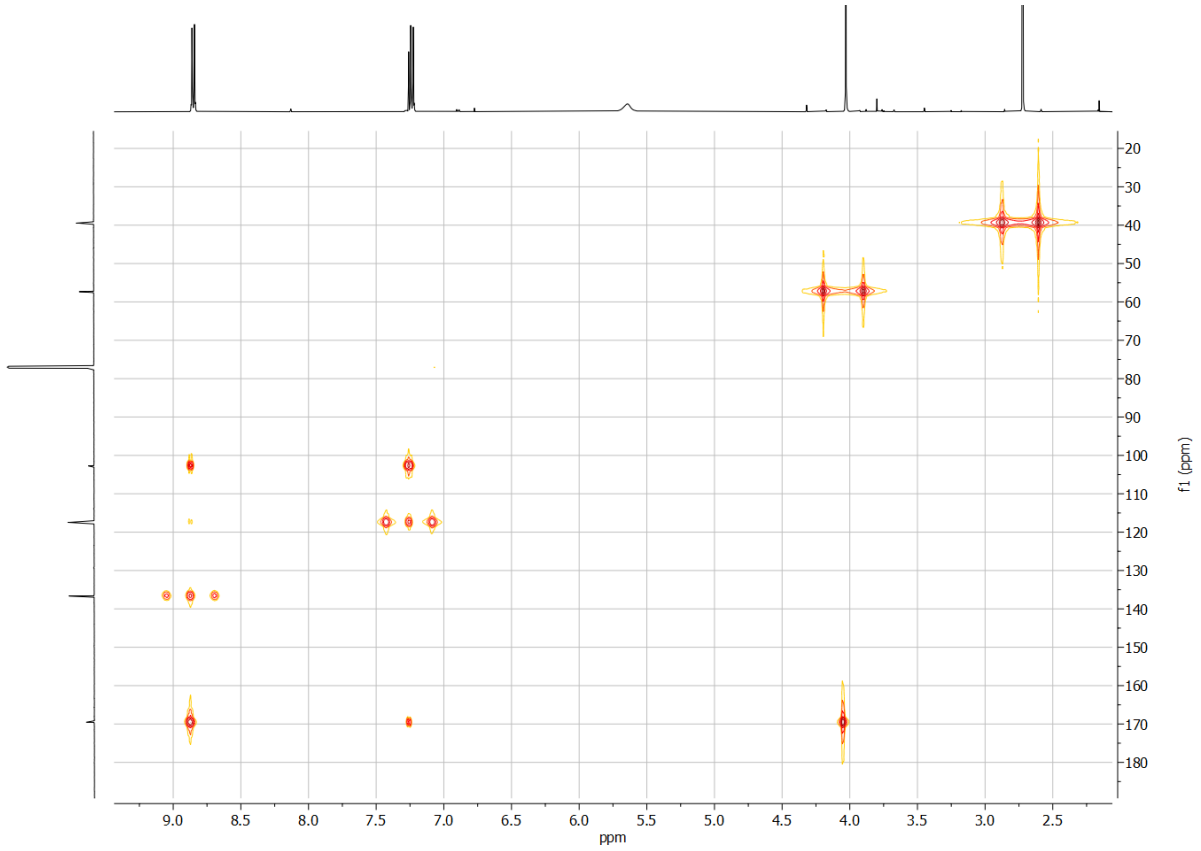

HMBC of **7**.

4-Methoxybenzenediazoniumtetrafluoroborate (8)

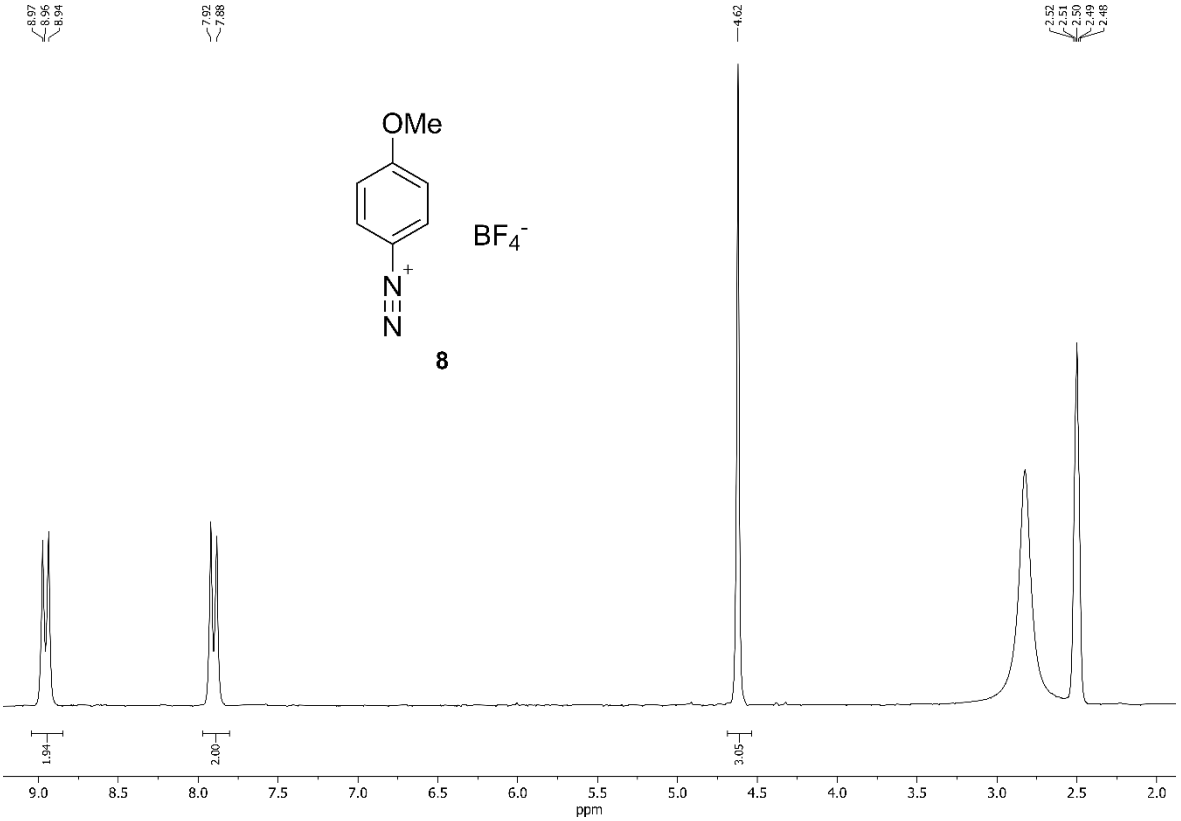

^{1}H NMR: (300 MHz, DMSO-d_6).

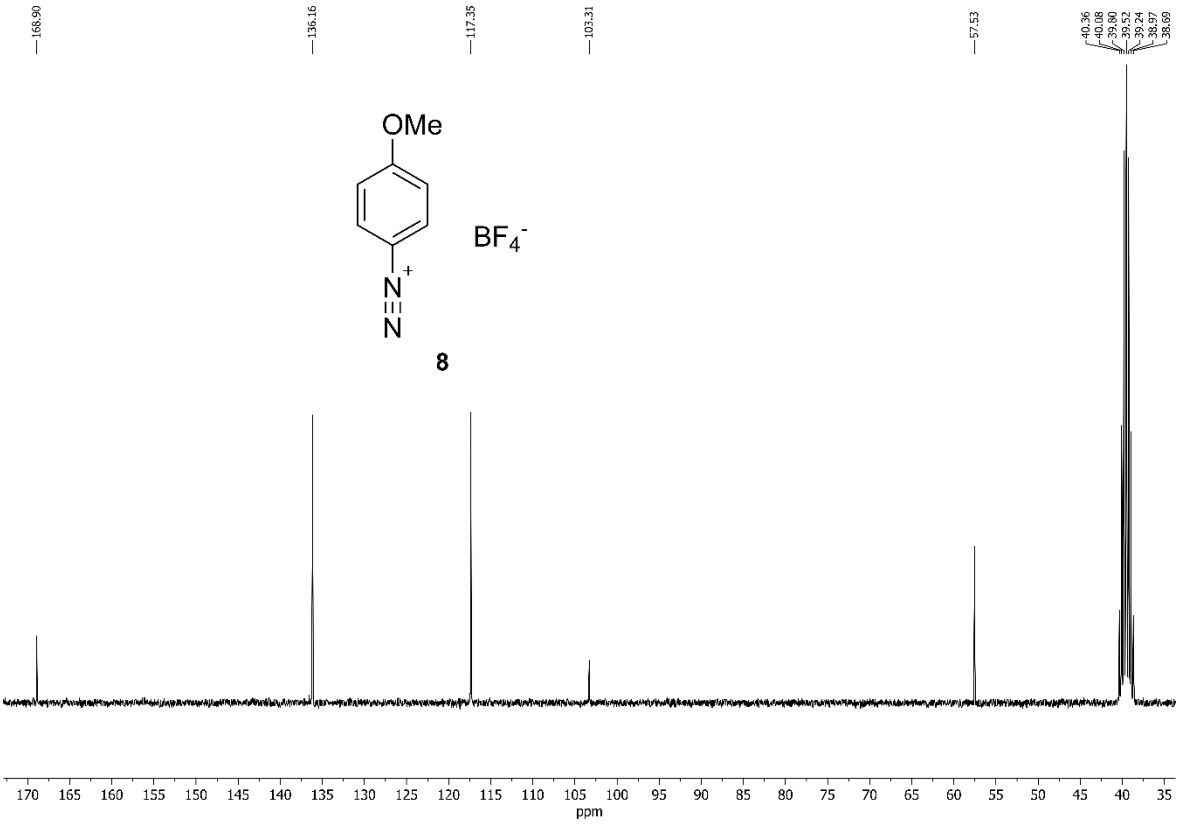

^{13}C NMR: (75 MHz, DMSO-d_6).

3.6 References

1 H. D. Roth, *Angew. Chem. Int. Ed. Engl.*, 1989, **28**, 1193–1207.
2 N. Hoffmann, *Chem. Rev.*, 2008, **108**, 1052–1103.
3 D. M. Schultz, T. P. Yoon, *Science*, 2014, **343**, 1239176.
4 J. J. Douglas, J. D. Nguyen, K. P. Cole, C. R. J. Stephenson, *Aldrichimica Acta*, 2014, **47**, 15–25.
5 T. Bach, J. P. Hehn, *Angew. Chem. Int. Ed.*, 2011, **50**, 1000–1045.
6 L. Buglioni, F. Raymenants, A. Slattery, S. D. A. Zondag, T. Noël, *Chem. Rev.*, 2022, **122**, 2752–2906.
7 M. Sender, D. Ziegenbalg, *Chem. Ing. Tech.*, 2017, **89**, 1159–1173.
8 D. Cambié, C. Bottecchia, N. J. W. Straathof, V. Hessel, T. Noël, *Chem. Rev.*, 2016, **116**, 10276–10341.
9 Y. Su, N. J. W. Straathof, V. Hessel, T. Noël, *Chem. Eur. J.*, 2014, **20**, 10562–10589.
10 A. Vasudevan, C. Villamil, J. Trumbull, J. Olson, D. Sutherland, J. Pan, S. Djuric, *Tetrahedron Lett.*, 2010, **51**, 4007–4009.
11 J. P. Knowles, L. D. Elliott, K. I. Booker-Milburn, *Beilstein J. Org. Chem.*, 2012, **8**, 2025–2052.
12 M. Oelgemöller, *Chem. Eng. Technol.*, 2012, **35**, 1144–1152.
13 D. Staveness, I. Bosque, C. R. J. Stephenson, *Acc. Chem. Res.*, 2016, **49**, 2295–2306.
14 D. Mazzarella, A. Pulcinella, L. Bovy, R. Broersma, T. Noël, *Angew. Chem. Int. Ed.*, 2021, **60**, 21277–21282.
15 A. V. Nyuchev, T. Wan, B. Cendón, C. Sambiagio, J. J. C. Struijs, M. Ho, M. Gulías, Y. Wang, T. Noël, *Beilstein J. Org. Chem.*, 2020, **16**, 1305–1312.
16 Y. Su, A. Lautenschleger, G. Chen, E. Y. Kenig, *Ind. Eng. Chem. Res.*, 2014, **53**, 390–401.
17 T. Noël, V. Hessel, *ChemSusChem*, 2013, **6**, 405–407.
18 J. Baek, P. M. Allen, M. G. Bawendi, K. F. Jensen, *Angew. Chem. Int. Ed.*, 2011, **50**, 627–630.
19 J. D. Williams, C. O. Kappe, *Curr. Opin. Green Sustain. Chem.*, 2020, **25**, 100351.
20 K. P. L. Kuijpers, M. A. H. van Dijk, Q. G. Rumeur, V. Hessel, Y. Su, T. Noël, *React. Chem. Eng.*, 2017, **2**, 109–115.
21 H. E. Bonfield, T. Knauber, F. Lévesque, E. G. Moschetta, F. Susanne, L. J. Edwards, *Nat. Commun.*, 2020, **11**, 804.
22 C. Rosso, J. D. Williams, G. Filippini, M. Prato, C. O. Kappe, *Org. Lett.*, 2019, **21**, 5341–5345.
23 Y. Chen, G. Glotz, D. Cantillo, C. O. Kappe, *Chem. Eur. J.*, 2020, **26**, 2973–2979.
24 Y. Chen, O. de Frutos, C. Mateos, J. A. Rincon, D. Cantillo, C. O. Kappe, *ChemPhotoChem*, 2018, **2**, 906–912.
25 A. Steiner, O. de Frutos, J. A. Rincón, C. Mateos, J. Williams, C. O. Kappe, *React. Chem. Eng.*, 2021, **6**, 2434–2441.
26 A. Steiner, J. D. Williams, J. A. Rincón, O. de Frutos, C. Mateos, C. O. Kappe, *Eur. J. Org. Chem.*, 2019, **33**, 5807–5811.
27 S. Crespi, S. Protti, M. Fagnoni, *J. Org. Chem.*, 2016, **81**, 9612–9619.

28 C. Raviola, C. Carrera, M. Serra, A. Palmieri, G. Lupidi, G. Maestri, S. Protti, *ChemPhotoChem*, 2021, **5**, 871–875.
29 C. P. Haas, T. Roider, R. W. Hoffmann, U. Tallarek, *React. Chem. Eng.*, 2019, **4**, 1912–1916.
30 J. P. Mcmullen, K. F. Jensen, *Annu. Rev. Anal. Chem.*, 2010, **3**, 19–42.
31 B. J. Reizman, K. F. Jensen, *Org. Process Res. Dev.*, 2012, **16**, 1770–1782.
32 K. F. Jensen, *Nature*, 2020, **579**, 346–348.
33 A. Li, Y. Li, J. Liu, J. Chen, K. Lu, D. Qiu, M. Fagnoni, S. Protti, X. Zhao, *J. Org. Chem.*, 2021, **86**, 1292–1299.
34 D. Qiu, C. Lian, J. Mao, Y. Ding, Z. Liu, L. Wei, M. Fagnoni, S. Protti, *Adv. Synth. Catal.*, 2019, **361** 5239–5244.
35 J. Liu, M. Tian, Y. Li, X. Shan, A. Li, K. Lu, M. Fagnoni, S. Protti, X. Zhao, *Eur. J. Org. Chem.*, 2020, **47**, 7358–7367.
36 A. Nitti, A. Martinelli, F. Batteux, S. Protti, M. Fagnoni, D. Pasini, *Polym. Chem.*, 2021, **6**, 5747–5751.
37 R. Wang, F. Chen, L. Jiang, W. Yi, *Adv. Synth. Catal.*, 2021, **363**, 1904–1911.
38 Q. Liu, F. Liu, H. Yue, X. Zhao, J. Li, W. Wei, *Adv. Synth. Catal.*, 2019, **361**, 5277–5282.
39 L. Blank, M. Fagnoni, S. Protti, M. Rueping, *Synthesis*, 2019, **51**, 1243–1252.
40 J. Rabani, H. Mamane, D. Pousty, J. R. Bolton, *Photochem. Photobiol.*, 2021, **97**, 873–902.
41 M. Sender, B. Wriedt, D. Ziegenbalg, *React. Chem. Eng.*, 2021, **6**, 1601–1613.
42 M. Sender, D. Ziegenbalg, *React. Chem. Eng.*, 2021, **6**, 1614–1627.
43 H. Chou, T. Yang, *J. Light & Vis. Env.*, 2016, **32**, 133–136.
S1 C. P. Haas, T. Roider, R. W. Hoffmann, U. Tallarek, *React. Chem. Eng.*, 2019, **4**, 1912–1916.
S2 I. Sapountzis, P. Knochel, *Angew. Chem. Int. Ed.*, 2004, **43**, 897–900.
S3 S. Crespi, S. Protti, M. Fagnoni, *J. Org. Chem.*, 2016, **81**, 9612–9619.
S4 K. Chen, S. Zhang, P. He, P. Li, *Chem. Sci.*, 2016, **7**, 3676–3680.
S5 M. R. Heinrich, O. Blank, D. Ullrich, M. Kirschstein, *J. Org. Chem.*, 2007, **72**, 9609–9616.
S6 M. Gruner, D. Pfeifer, H. G. O. Becker, R. Radeglia, J. Epperlein, *J. Prakt. Chem.*, 1985, **327**, 63–79.

4. Chapter 4: Olefin Ring-closing Metathesis under Spatial Confinement and Continuous Flow

Authors
F. Ziegler,[+] T. Roider,[+] M. Pyschik, C. P. Haas, D. Wang, U. Tallarek*[+] and M. R. Buchmeiser*[+]
[+]These authors contributed equally to this work.

State of publication
Published 16 February 2021 in *ChemCatChem*, Vol. 13, pp.2234–2241. DOI: 10.1002/cctc.202001993

Table of Content

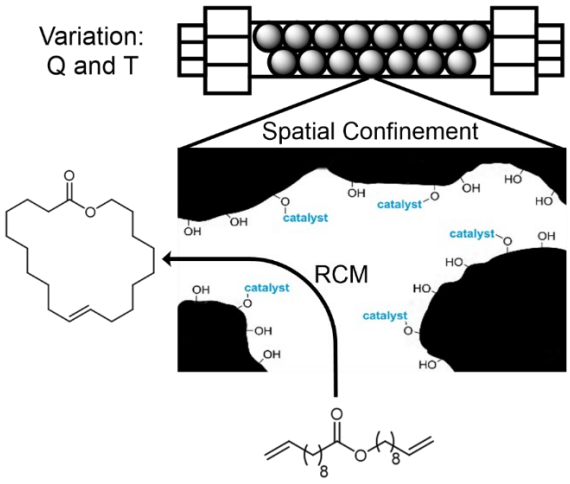

Abstract
We report on the use of a 2nd-generation Hoveyda–Grubbs-type catalyst immobilized inside mesoporous silica for the application in selective macro(mono)cyclization (MMC) of an α,ω-diene under spatially confined and continuous-flow conditions. Reactions carried out with different flow rates allow for variations in residence time; conversion and MMC selectivity can be determined for well-defined reaction times. Analysis of the reaction mixtures obtained for different reaction times and temperatures in a single flow experiment by NMR and MALDI-TOF-MS allows to address confinement effects and to determine olefin metathesis pathways. These investigations revealed that ring-chain equilibria are quickly established but substantially affected by residence time and flow, allowing for the determination of conditions under which MMC selectivity reaches a maximum. In contrast to reactions carried out in solution, in which oligomers up to the hexamer were observed, MMC under confinement predominantly proceeds via ring-closing metathesis of the monomer and backbiting from the dimer and trimer, but not from higher oligomers as their formation is suppressed. This leads to the observed high MMC selectivity, reaching 60% at a 25 mM substrate concentration.

4.1 Introduction

Olefin metathesis covers a wide spectrum of applications in organic synthesis, ranging from the production of fine chemicals (such as pharmaceuticals) to large-scale industrial processes in petrochemistry.[1] Ring-closing metathesis (RCM) refers to reactions of dienes leading to ring formation, while acyclic diene metathesis (ADMET) results in linear polymers. It is well known that RCM does not selectively proceed by cyclization of the substrate (direct RCM), but involves oligomerization followed by backbiting and concomitant RCM.[2] As a consequence, when olefin metathesis is adapted for macrocyclization, RCM and ADMET establish competing pathways, which determine macro(mono)cyclization (MMC) yields based on the ring–chain equilibrium in dependence of the substrate, substrate concentration, reaction time, and temperature.[3] In particular, if substrate dilution is insufficient, the equilibrium will favor oligomers over the desired RCM product.

One approach to improve macrocyclization yields entails the tuning of spatial confinement effects[4] during RCM combined with selective catalyst immobilization inside the pores of a support.[5] Over the past decades, many strategies have been developed for immobilization of metathesis catalysts in porous materials.[6] The primary goal of these strategies was to overcome problems associated with homogeneous catalysts like catalyst recovery, product contamination by the catalyst, and the control of contact times between catalyst and substrates. On the other hand, studies about confinement effects engendered by the pore space morphology of a support on macrocyclization selectivity, highlighting the fundamental ratio between the hydrodynamic diameter of a substrate and the mean pore size, remain scarce.[7]

While MMC formally proceeds via RCM, there exists substantial evidence that ADMET-based oligomerization followed by backbiting represents an alternative, if not the predominant pathway.[2] Conceptually, to ensure that MMC is favored over oligomerization even at high substrate concentrations, reactions under spatial confinement require the catalyst to be selectively immobilized inside the pores of a support. In addition, the pores should ideally be designed such that they allow for an unrestricted access of one or two substrate molecules to the catalyst. In this way, MMC product is either formed via direct RCM or ADMET-based dimerization followed by backbiting. At the same time, simultaneous access of further substrate molecules that might eventually lead to the formation of higher oligomers must be suppressed. Obviously, this requires tailored pores, both in terms of size and polarity. A narrow pore size distribution may be the key in this regard[6e,8] because larger pores quickly increase the risk of oligomerization (decreasing selectivity), while smaller pores impede MMC itself and also limit diffusive transport into and out of the pore network (decreasing conversion). Similar to enzymes, which create highly substrate-specific reaction sites, the concept utilizes the idea to synergistically combine a well-defined organometallic catalyst and a defined pore geometry to create chemoselective reaction sites through spatial confinement. The viability of such an approach has indeed been demonstrated recently in the RCM of various α,ω-dienes for substrate concentrations up to 25 mM using a 2nd-generation Hoveyda–Grubbs-type catalyst selectively immobilized inside the mesopores of SBA-15 silica particles,[9] a popular support for olefin metathesis catalysts.[6j] In this approach, the ratio of MMC product and undesired oligomerization products (O) due to ADMET could be increased from 0.55, corresponding to 35% MMC product obtained with the homogeneous catalyst, up to 1.49, corresponding to 60%

MMC product. A relationship between the size of a substrate and its propensity to undergo macrocyclization with the catalyst located inside silica mesopores of defined shape and size was established, identifying a narrow window for optimal macrocyclization selectivity.[9]
Here, we build on our previous experience to study olefin metathesis pathways for an α,ω-diene in the presence of spatial confinement effects and use a continuous-flow microreactor setup that allows for the precise adjustment and automated variation of both, reaction time and temperature. Only few studies have been reported on the RCM with immobilized catalysts in a continuous-flow design,[7a,7b,10] although the benefits of continuous flow *vs.* batch operation are evident.[11] They include simple product/catalyst separation and realization of a high-resolution reaction time control, which allows to translate mean residence time in the microreactor into a precisely defined reaction time.[12] Thus, systematic tuning of the residence time can be used to govern the outcome of a chemical reaction by determining reaction rates and conversion and by influencing product selectivity.[13] We show that conversion and MMC/O selectivity can be assigned to well-defined reaction times and analyze multiple reaction times and temperatures fully automated in a single flow experiment to address confinement effects and determine olefin metathesis pathways. Experiments are conducted using silica particles with different mesopore sizes. For that purpose, particles are loaded with a 2nd-generation Hoveyda–Grubbs type catalyst selectively immobilized inside their mesopores.

4.2 Results and Discussion

4.2.1 Catalyst immobilization and olefin metathesis pathways

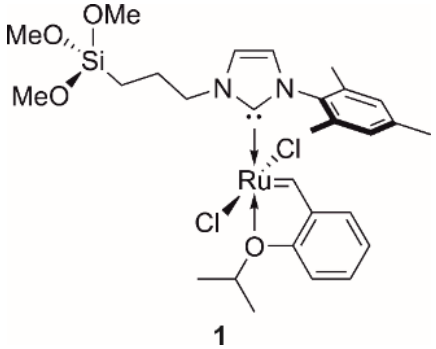

1

Figure 4.1. Structure of the 2nd-generation Hoveyda–Grubbs-type catalyst. The trimethoxysilyl tether serves for its covalent bonding to silanol groups on the inner surface of the mesoporous silica particles.

Figure 4.1 shows the homogeneous 2nd-generation Hoveyda–Grubbs-type catalyst **1**[9] carrying a trimethoxysilyl tether at the NHC used for its immobilization inside the mesopores of the silica particles. Two amorphous, mesoporous silica materials, received as spherical particles with a mean diameter of ~5 µm but different intraparticle mesopore size distributions and different (nominal) mean mesopore sizes of 60 and 100 Å, referred to as Si60 and Si100, were modified according to an established protocol to allow for the selective immobilization of **1** inside their mesopores.[9] The outcome of this selective surface modification is illustrated in Figure 4.2. As a final result, the external surface of the silica particles is rendered hydrophobic due to modification of the majority of surface silanols with trimethylsilyl groups, while the

catalyst is selectively bound to silanol groups inside the pores. The initial endcapping of silanols on the external surface by trimethylsilyl groups ensures that the catalyst only binds to unmodified silanol groups inside the mesopores. Due to its larger size, **1** is unable to access residual silanol groups on the external particle surface that could not be end capped by the smaller trimethylsilyl groups already due to steric reasons.

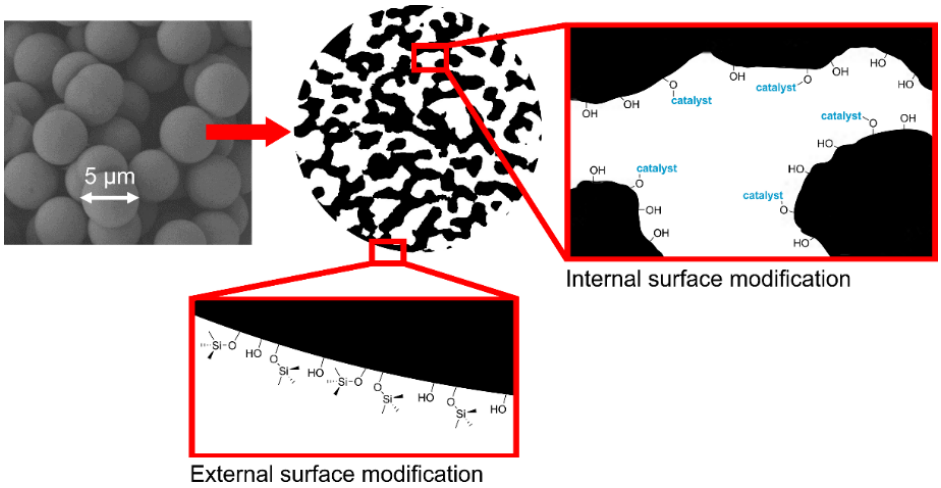

Figure 4.2. Selective immobilization of catalyst **1** inside the mesopores of the silica-based support particles. The spherical shaped particles have an average size of ~5 µm.

The mesoporous silica particles employed in this work have been characterized by nitrogen physisorption analysis; results are summarized in Figure 4.S1 and Table 4.S1 in the Supporting Information. The particles with mode pore sizes of 5.9 nm (Si60) and 13 nm (Si100) have been selected to engender different spatial confinements effects for the encountered olefin metathesis pathways. Pores smaller than in Si60 slow down intraparticle mass transfer too much, while pores larger than in Si100 essentially release the effects of spatial confinement. Intraparticle porosities ε_{intra} (i.e., the intraparticle void volume fractions) were 63% and 72% for Si60 and Si100, respectively. The higher porosity of Si100 can be rationalized with its preparation history based on pore widening of small-pore silica (hydrothermal treatment), which also leaches some of the solid. It results in wider pores and a somewhat higher porosity.
Further, the particles had specific surface areas of 793 $m^2\,g^{-1}$ (Si60) and 417 $m^2\,g^{-1}$ (Si100), respectively; intraparticle loadings with the 2nd-generation Hoveyda–Grubbs-type catalyst **1**, determined by ICP-OES, were 7.1 µmol g^{-1} for **1**@Si60 and 33.2 µmol g^{-1} for **1**@Si100 (Table 4.S2, Supporting Information). The higher loading of the Si100 particles originates in a better intraparticle transport characteristic of **1** during the immobilization step and is reflected in a larger accessible porosity and higher intraparticle diffusivity estimated by available hindrance factor expressions for mesoporous silica.[14] In the Si60 particles, transport of the bulky catalyst is more hindered, resulting in a smaller accessible porosity and intraparticle diffusivity and, consequently, in a much lower loading, even though Si60 offers almost twice the surface area of Si100. Thus, partial size-exclusion of the catalyst from the mesopore space of the particles during immobilization reduces their loadability and active surface area, an effect that is more pronounced for the Si60 than for the Si100 particles.[14c]

Next, we studied olefin metathesis pathways (highlighted in Scheme 4.1) for the α,ω-vinylic prolacton **2** at an elevated substrate concentration of 25 mM using microreactors packed with the modified silica particles. We point out the reversibility of RCM and ADMET involving ethylene due to the compact microreactor environment. As there is no volatilization of released ethylene (the olefinic coproduct), loss of ethylene is only possible via the reactor outlet, while additional ethylene is formed with fresh substrate solution entering the reactor. Consequently, regeneration of the starting α,ω-diene is an issue and the representation of equilibria in Scheme 4.1 is more accurate.[3]

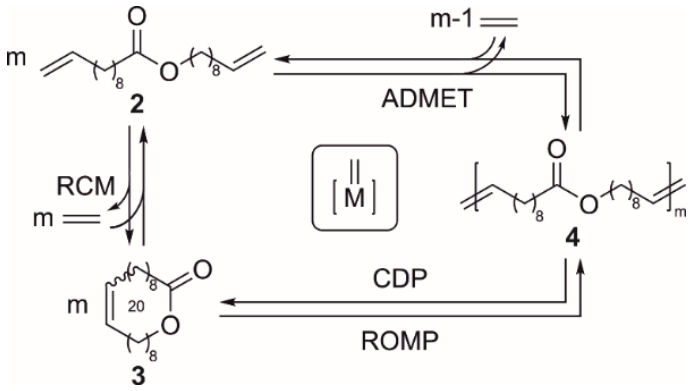

Scheme 4.1. Olefin metathesis pathways for the α,ω-vinylic prolacton **2** (substrate) to MMC product **3** and oligomer **4**, with equilibria applying to all olefinic species. RCM: ring-closing metathesis, ADMET: acyclic diene metathesis, ROMP: ring-opening metathesis polymerization, CDP: cyclodepolymerization. m denotes equivalent and M= the metal alyklidene complex.

4.2.2 Continuous-flow microreactor setup and operation

Conversion and selectivity in the RCM of substrate **2** with catalyst **1** selectively immobilized inside the mesopores of the silica particles was monitored using the setup illustrated in Figure 4.3. A commercial HPLC system was adapted as a flow-chemistry apparatus, containing a short stainless-steel column packed with the modified silica particles (4.6 mm inner diameter × 15 mm effective bed length; packed-reactor volume, $V_{reactor} \approx 0.25$ mL). To guarantee dense, stable, and homogeneous catalyst beds, which will become important for the assumption of plug-flow reactors further below, the columns were slurry-packed with the particles suspended in absolute, degassed toluene under pressures up to 75 bar using the device shown in Figure 4.S2 (Supporting Information). Slurries were prepared in a glove box and transferred to a lab packing station. Because of their different loadings with catalyst, the final particles were mixed with unloaded ones to achieve an effective catalyst loading of all reactors of about 3.5 μmol g^{-1}. The packing process and bed consolidation took ~20 minutes, after which the reactors were sealed at both ends and fixed in a thermoset column compartment. The latter guarantees an accuracy of the specified temperature of ±0.8 °C and a temperature stability of ±0.05 °C. Substrate solution (25 mM of **2** in absolute, degassed toluene) was delivered continuously by a binary pump to the reactors (flow rate accuracy, ±1%), in which olefin metathesis reactions (Scheme 4.1) took place under spatial confinement.

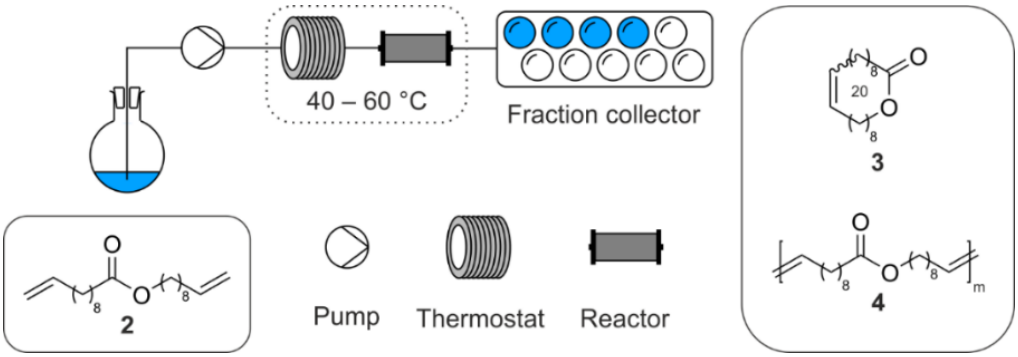

Figure 4.3. Setup of the continuous-flow microreactor used for studying the olefin metathesis pathways in Scheme 4.1 under spatial confinement. Solution of substrate **2** (25 mM in absolute toluene) is continuously flushed through the setup at a defined flow rate (reaction time on the reactor) and temperature, while conversion and selectivity are monitored on the product side, represented by MMC product **3** and oligomer **4**.

The utilization of a high-end HPLC device in the adapted configuration allows the precise control over all relevant reaction parameters in the reactor, i.e., substrate concentration, solvent composition, flow rate, and temperature. The setup also provides fully automated adjustments of flow rate and temperature over time. In addition, solvent composition and substrate type and concentration could be systematically varied, enabling the detailed and rapid screening of new catalysts and/or reactions. In our screening of the metathesis pathways illustrated in Scheme 4.1, we focused on reaction times on the order of just a few minutes, which have been revealed as most intriguing.[2,15] The programing of the flow experiments, including the precise adjustment of volumetric flow rate Q and temperature T over time, is summarized in Figure 4.4. As outlined, the flow rate (blue line) was varied between 0.07 and 0.30 mL min^{-1} (five values) at constant temperature. Then, the temperature was increased from 40 to 60 °C in steps of 5 °C (red line) and the flow rate variation repeated.

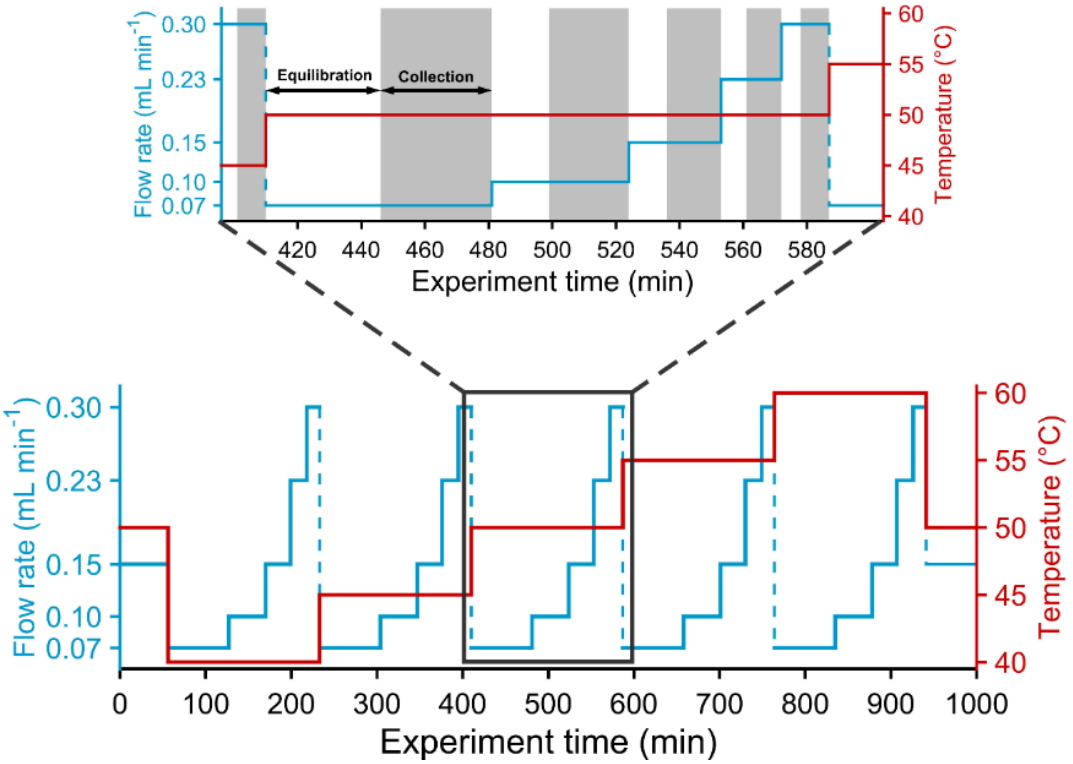

Figure 4.4. Timing of the overall flow experiment (1000 minutes) conducted with a packed microreactor, illustrating precise control and fully automated adjustment of reaction parameters in the RCM of substrate **2** (Scheme 4.1). Substrate solution (25 mM in absolute toluene) was flushed through a microreactor at five different flow rates Q from 0.07 to 0.30 mL min^{-1} (thus, reaction times) for a given temperature T (varied from 40 to 60 °C in steps of 5 °C). For each pair of the varied reaction parameters (Q, T), initial equilibration (due to a change in Q and T or only Q) is followed by sample collection, as indicated in the zoom.

The dense, uniform packings of the small (~5 µm) silica particles guarantee low back-mixing (narrow residence time distributions), supporting the assumption of plug-flow reactors.[16] This term implies that the flow pattern is uniform over the column cross-section and the associated hydrodynamic dispersion along the macroscopic flow direction remains small compared to reactor-based liquid-phase transport by the flow. Therefore, the reaction time on the reactor (t_{rct}) can be expressed by the mean residence time ($\bar{t}_{\mathrm{res}}$), calculated with the packed-reactor volume V_{reactor}, total bed porosity $\varepsilon_{\mathrm{total}}$, and volumetric flow rate Q:

$$t_{\mathrm{rct}} \equiv \bar{t}_{\mathrm{res}} = \frac{V_{\mathrm{reactor}}\,\varepsilon_{\mathrm{total}}}{Q} = \frac{\pi r_c^2\, L_{\mathrm{bed}}\,\varepsilon_{\mathrm{total}}}{Q} \qquad (1)$$

Here, L_{bed} and r_c denote packed-bed length (15 mm) and inner radius (2.3 mm) of the column, respectively.[17] The total porosity of a microreactor contains contributions from interparticle ($\varepsilon_{\mathrm{inter}}$) and intraparticle ($\varepsilon_{\mathrm{intra}}$) void volume fractions:

$$\varepsilon_{\mathrm{total}} = \varepsilon_{\mathrm{inter}} + (1 - \varepsilon_{\mathrm{inter}})\varepsilon_{\mathrm{intra}} \qquad (2)$$

Importantly, Eq. (1) refers to the mean hydrodynamic residence time, representing small, passive tracer molecules that can access the total porosity and do neither adsorb, nor react at the internal and external surface of the particles. For the studied system, however, this appears inappropriate, because substrate **2** is partially size-excluded from the particles and also retained inside the mesopores by localized adsorption with the carbonyl oxygen onto the silanol groups of the silica surface via hydrogen bonding, as revealed by molecular dynamics simulations.[9] Therefore, we prefer mean residence times directly for substrate **2**, $\bar{t}_{\mathrm{res}}(\mathbf{2})$, to express reaction times for the substrate solution in contact with the packed microreactor:

$$t_{\mathrm{rct}} \equiv \bar{t}_{\mathrm{res}}(\mathbf{2}) = \frac{\int_0^\infty tc(t)\mathrm{d}t}{\int_0^\infty c(t)\mathrm{d}t} \qquad (3)$$

For a given surface modification and solvent composition (affecting the adsorption properties of the substrate molecules), the reaction time only depends on the volumetric flow rate (cf. Eq. 1), which can be precisely controlled and adjusted; adsorption of **2** is independent of the realized flow rates and pressures. As indicated by Eq. (3), $\bar{t}_{\mathrm{res}}(\mathbf{2})$ is determined from the concentration profile $c(t)$ of **2** recorded following pulse injection onto the microreactors after the experiments, i.e., when the catalyst was mostly inactive (Figure 4.S3, Supporting Information).

The established high-resolution reaction time control allows to assign both conversion and selectivity to a well-defined reaction time and analyze multiple reaction times and temperatures fully automated in a single flow experiment (cf. Figure 4.4). Reaction times corresponding to the five flow rates in Figure 4.4 are summarized in Table 4.1 for microreactors packed with **1**@Si60 and **1**@Si100 particles. Differences in t_{rct} for microreactors at the same flow rate originate in different packing densities ($\varepsilon_{\mathrm{inter}}$-values in Eq. (2)) and surface areas of the particles available for adsorption of **2**.

Table 4.1. Reaction times for microreactors packed with **1**@Si60 and **1**@Si100.[a]

Flow rate Q (mL min^{-1})	Reaction time t_{rct} (s)	
	1@Si60	**1**@Si100
0.07	171.8 ± 2.0	263.3 ± 1.7
0.10	117.6 ± 0.6	185.8 ± 0.4
0.15	79.0 ± 0.6	124.6 ± 1.3
0.23	52.1 ± 0.3	80.3 ± 0.6
0.30	40.4 ± 0.5	61.7 ± 0.4

[a] The average time substrate molecules spend in a microreactor at a given flow rate, $\bar{t}_{\mathrm{res}}(\mathbf{2}) \equiv t_{\mathrm{rct}}$, is provided by the first moment of the residence time distribution recorded after pulse injection of **2** onto the packed column, Eq. (3), and subtracting extra-column contributions.

The zoom in Figure 4.4 for $T = 50$ °C illustrates the equilibration and sample collection periods that are associated with the five reaction times at each temperature. For sample collection, we adapted a fraction collector integrated into the setup (cf. Figure 4.3). Equilibration and collection periods were adjusted such that for each reaction time the same volumes of substrate solution were flushed through the microreactor during equilibration (0.80 mL) and sample collection by the fraction collector (2.45 mL). The extended fraction collection periods are needed to collect sufficient sample for quantitative ^{1}H NMR analysis of the reaction solutions.

4.2.3 Catalyst activity, substrate conversion, and MMC/O selectivity

Using ^{1}H NMR, we determined conversion and selectivity in the RCM of substrate **2** to MMC product **3** and oligomer **4** (cf. Scheme 4.1) according to the following integrals:

$$\text{Conversion} = \frac{I(\mathbf{3+4})}{I(\mathbf{2+3+4})} \tag{4}$$

$$\text{Selectivity} = \frac{I(\mathbf{3})}{I(\mathbf{4})} \tag{5}$$

The ^{1}H NMR based analysis of the collected reaction solutions is illustrated by Figure 4.5 and the complete ^{1}H NMR spectrum is shown in Figure 4.S4 (Supporting Information). As indicated, (*Z*)-**3** and (*E*)-**3** can be identified for the MMC product **3**, but are not distinguished further in the analysis of **2**–**4** based on the recorded ^{1}H NMR spectra.

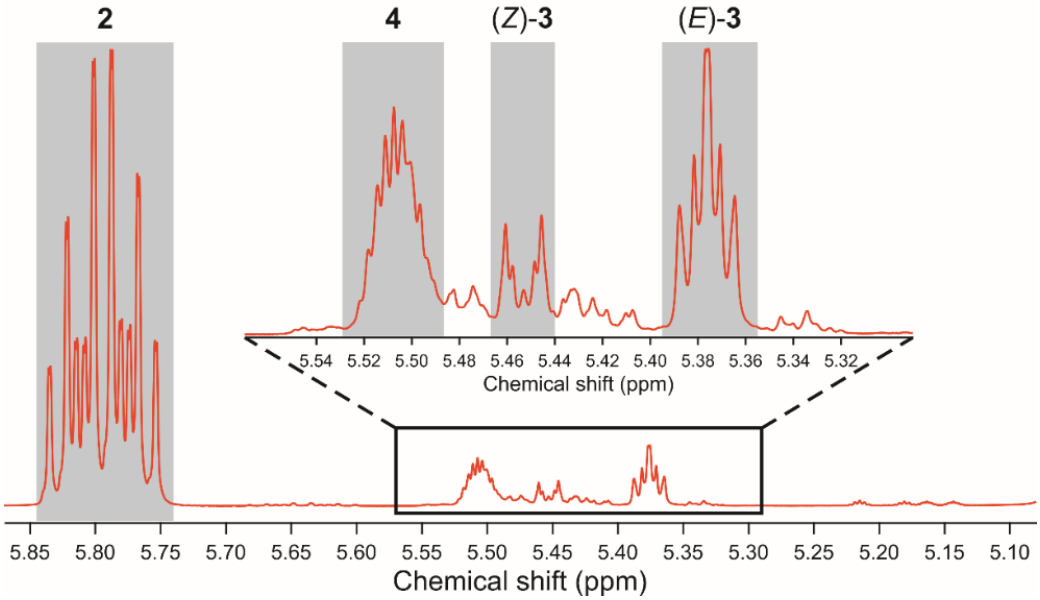

Figure 4.5. Region from the ^{1}H 500 MHz NMR spectrum of a reaction solution used for quantification of conversion and selectivity in the RCM of substrate **2** to MMC product **3** and oligomer **4** (cf. Scheme 4.1) according to Eqs. (4) and (5). The reaction solution was taken from the microreactor packed with the modified Si60 particles ($Q = 0.15$ mL min^{-1}, $T = 50$ °C).

The results of the complete flow experiment (Figure 4.4) applied to microreactors packed with **1**@Si60 and **1**@Si100 provide valuable information about the impact of the spatial confinement

on reaction mechanisms outlined in Scheme 4.1 as well as possible side reactions, e.g., the extent of isomerization. Results for the RCM of **2** with **1**@Si60 are summarized in Figure 4.6 as a plot of MMC selectivity *vs.* conversion, comparing data for different reaction temperatures. The plot reveals that the ring-chain equilibrium is reached after ~2% conversion and remains virtually independent of the reaction temperature in the studied temperature range, here 40–55 °C. We did not include the data for the highest realized temperature (60 °C) recorded at the end of the flow experiment, between approximately 750 and 950 minutes (Figure 4.4), because conversions were low and the relative amount of isomerization product high. This is further explained with Figure 4.S5 (Supporting Information), where we compare NMR spectra recorded at different times during the flow experiment (after 95.5 and 626.5 minutes), corresponding to reaction temperatures of 40 and 55 °C (see also Figure 4.4).

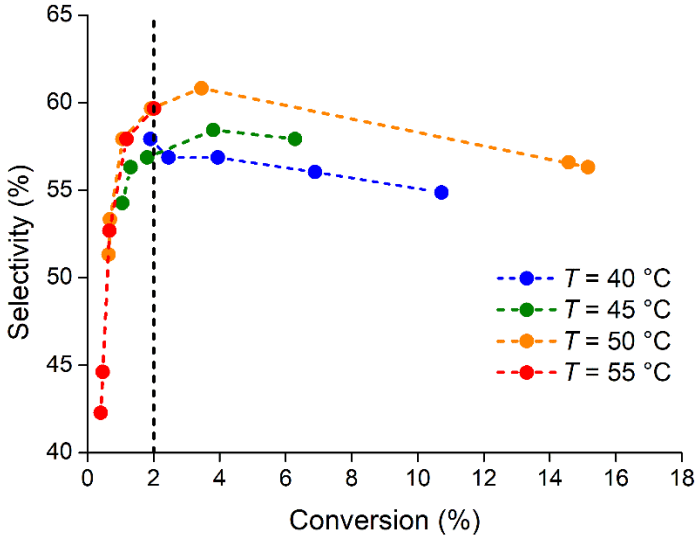

Figure 4.6. Selectivity *vs.* conversion (cf, Eqs. (4) and (5)) over ~800 minutes experiment time for the RCM of **2** with **1**@Si60 (c_0(**2**) = 25 mM), illustrating the establishment of the ring-chain equilibrium after ca. 2% conversion, independent of reaction temperature. These measurements include temperatures from 40 to 55 °C and flow rates from 0.07 to 0.30 mL min^{-1} (cf. Figure 4.4), corresponding to reaction times from 172 to 40 s (Table 4.1).

Figure 4.7 plots determined conversion (top panel) and selectivity (bottom panel) as a function of the reaction time t_{rct} specified in Table 4.1 and the reaction temperature T throughout the flow experiment, lasting for about 800 minutes (the data for T = 60 °C are not included). Clearly, the conversion decreases significantly over time, despite continuous supply with substrate solution and can be attributed to the decomposition pathways of olefin metathesis catalysts.[18] This can also be directly inferred from a look at the data for T = 50 °C at the start of the experiment (with conversions of ~15% for t_{rct} = 79 s) and after an experiment time of ca. 530 minutes when conversion has dropped to only ~1% (green data point for t_{rct} = 79 s). Interestingly, selectivity shows a maximum at a certain flow rate (i.e., residence time in the reactor and, thus, reaction time) – an observation that is made at several temperatures, although this maximum is less pronounced at the higher temperatures. In particular, for T = 50 °C and 55 °C, the selectivity increases strongly with reaction time and seems to approach a maximum beyond the longest reaction time of t_{rct} = 172 s. The plots of MMC selectivity *vs.* t_{rct} for the

individual temperatures shown in Figure 4.7 (bottom) altogether reveal the form of a concave curve. Notably, for all data points recorded at conversions ≤2%, a decrease in selectivity is observed with increasing flow rate (decreasing reaction time), while for all data points recorded at conversions >2%, a slight but reproducible increase in selectivity up to 60% is seen.
We attribute the latter observation to a shift of the ring-chain equilibrium towards the MMC product caused by a more efficient removal of the released ethylene with increasing flow rate and its reduced solubility at higher temperature. Because ethylene is much more mobile than the MMC product **3** and any oligomer **4**, it can leave the pores of the particles much faster than these compounds and is therefore removed more efficiently. By contrast, the decrease in MMC selectivity for $T \geq 45$ °C and higher flow rates is attributed to the shorter residence times of the produced oligomers. As they are intermediates in the formation of the MMC product through backbiting (Scheme 4.1), higher flow rates at ≤2% conversion result in lower MMC selectivity, because oligomers are partly removed from the microreactor. It is also worth pointing out that MMC selectivity for **2** with **1**@Si60 by far exceeds the selectivity for reaction with **1** in free solution (Supporting Information). That is, MMC selectivity for c_0(**2**) = 25 mM in free solution reached 46.6% at 40 °C within 5 min (**1**:**2** = 1:1000, mol/mol), whereas **1**@Si60 allowed for a MMC selectivity of 57% at the same temperature, reaching 60% at 50 °C (Figure 4.7).

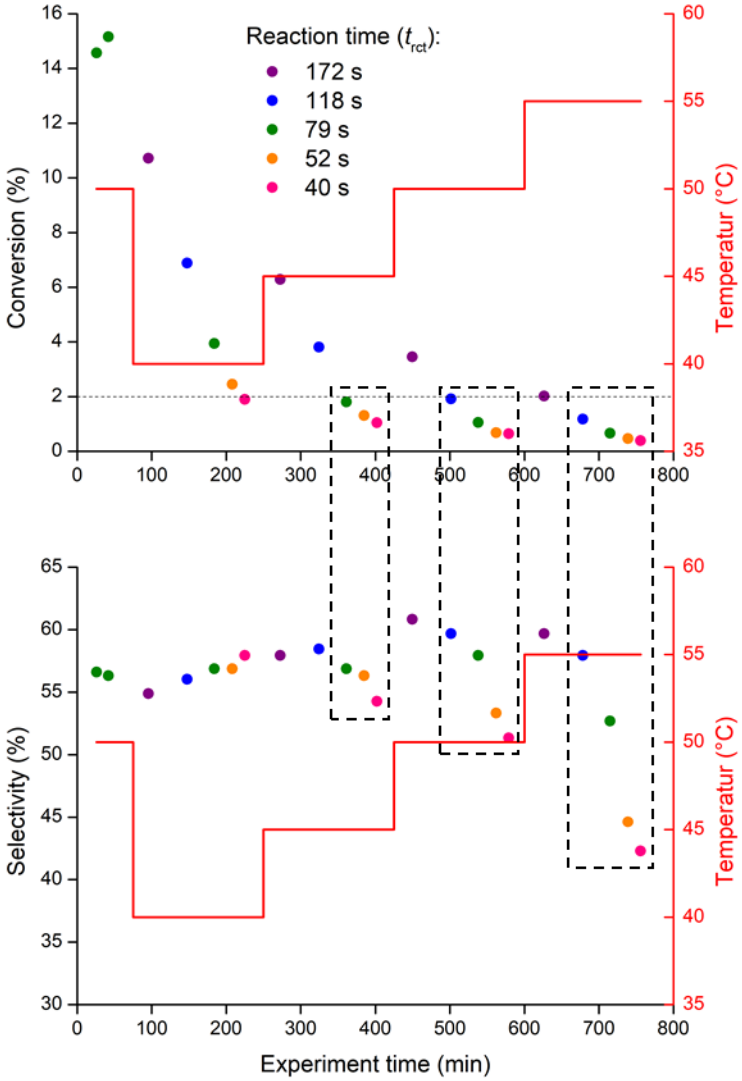

Figure 4.7. Timing of the flow experiment over ~800 minutes in the RCM of **2** with **1**@Si60, illustrating the precise control and fully automated adjustment of reaction parameters (cf. Figure 4.4). The substrate solution (25 mM **2** in absolute toluene) is flushed through the **1**@Si60-microreactor at five different flow rates Q from 0.07 to 0.30 mL min^{-1}, corresponding to reaction times (t_{rct}) between 172 and 40 s (Eq. (3) and Table 4.1) at temperatures (T) between 40 and 55 °C in steps of 5 °C. Conversion (top) and selectivity (bottom) are, in turn, determined according to Eqs. (4) and (5), respectively.

For further analysis, matrix-assisted laser desorption ionization time-of-flight (MALDI-TOF) mass spectrometric analysis of the products formed in the RCM of **2** with **1** in free solution and with **1**@Si60 was carried out. It revealed substantial differences between the homogeneous and the heterogeneous system. In line with reports by Fogg and co-workers,[2] the RCM of **2** at c_0(**2**) = 25 mM using **1** (0.1 mol-%) in free solution at 40 °C demonstrated, apart from substrate and MMC product **3**, the presence of dimer (65%), trimer (28%,) tetramer (6%), pentamer (0.7%), and hexamer (0.04%) (Table 4.S3, Supporting Information). In contrast, sampling of effluents for the RCM carried out with **1**@silica in the continuous-flow microreactor at c_0(**2**) = 25 mM

and 40 °C revealed solely the presence of substrate, **3**, dimer, and trimer – the latter two at a relative ratio of 95:5% compared to 65:28% in free solution (Table 4.S4, Supporting Information). These findings clearly support the macrocyclization mechanisms in Scheme 4.1,[2] which occur by direct RCM of **2** to **3** *and* ADMET followed by backbiting, but also illustrate the role of the spatial confinement: it suppresses formation of higher oligomers and thereby favors MMC product by shifting the ring-chain equilibrium towards **3**.
Notably, **1**@Si100 exhibited substantial isomerization (Figure 4.S6, Supporting Information), attributable to the formation of ruthenium-hydride species. Both 1st- and 2nd-generation Grubbs-type catalysts are known to produce ruthenium-hydride species in the presence of an alcohol like methanol (pK_a = 15.5) or benzylalcohol (pK_a = 15.6) and a tertiary amine that can isomerize alkenes.[19] In view of the pK_a of the surface silanol groups, reported as 4.6 on average,[20] with a pK_a of 5.6 and 8.5, respectively, for out-of-plane and in-plane silanols,[21] hydride formation may be expected to occur under confinement in the absence of a base as well. Why this occurs predominantly in Si100 is the subject of ongoing research, but it may be the result of the pore-widening process used to prepare the material. It results in a large surface area and, thus, number of silanol groups. Nonetheless, in view of the pronounced isomerization behavior, we refrained from determining MMC selectivities with this material.

4.2.4 Conclusion

In summary, the following conclusions can be drawn. First, the application of different flow rates (reaction times) and temperatures *within one single flow experiment* allows to determine a sweet spot of the macrocyclization reaction at a given substrate concentration and temperature at which MMC selectivity is highest. Second, macrocyclization carried out under confinement limits ADMET to short-chain oligomers (dimers and trimers), which in turn shifts the overall ring-chain equilibrium in favor of MMC and thus increases MMC selectivity. Third, ring-chain equilibria are reached at very low conversion (around 2%). Finally, working under continuous-flow conditions in combination with suitable analyses helps to elucidate the underlying reaction mechanisms. Here, off-line MALDI-TOF-MS revealed the role of the confinement in that it effectively suppresses the formation of higher oligomers and thus favors MMC. Ongoing research focuses on the RCM under spatial confinement using cationic group 6 metal imido/oxo alkylidene NHC complexes in combination with on-line reaction monitoring. The results of these studies will be reported in due course.

4.2.5 Experimental

Chemicals and materials: The synthesis of catalyst **1** and pore size-selective immobilization were accomplished as described previously.[9] Also, the characterization of MMC product and oligomers was carried out as described in this earlier report.

Microreactor preparation: The hardware used for preparation of packed microreactors is shown in Figure 4.S2. The 4.6 mm inner diameter × 20 mm length stainless steel columns (e) were slurry-packed with modified Si60 and Si100 particles suspended in absolute, degassed toluene under pressures up to 75 bar. Empty columns were initially terminated on one side by

a stainless-steel sieve (f) fixed in the column with a sealing ring (g), a fitting adapter (h), and the column outlet (i) with outlet fitting (j). Afterwards, this assembly was attached to the slurry/solvent reservoir (c) connected to the packing pump. Particle slurries were prepared in a glove box by suspending ca. 450 mg of the silica particles in 1.5 mL of absolute, degassed toluene. This suspension was poured into the slurry/solvent reservoir, which was completely filled with absolute, degassed toluene (~12.0 mL) and sealed with an end cap (a). Particles were then packed with absolute, degassed toluene outside the glove box using a binary HPLC pump (Agilent Technologies, Santa Clara, CA) connected to the device shown in Figure 4.S2 via the inlet (b). The packing process took ca. 30 minutes and included the following flow rate program of the pump: 0.5, 1.0, 1.5, and 2.0 mL min^{-1} (5 minutes each), then a linear increase from 2.0 to 5.0 mL min^{-1} within 5 min and holding 5 mL min^{-1} for 5 min. Afterwards, the entire packing device was removed from the pump and transferred back to the glove box, where the packed microreactor column was completed at the other side with parts (f–j), as described above.

Microreactor operation: Continuous-flow olefin metathesis experiments outlined in Figure 4.4 were performed with commercially available HPLC instrumentation (1260 and 1290 Infinity II series, Agilent Technologies). Substrate solution (25 mM of **2** in absolute, degassed toluene) and absolute, degassed toluene (both under inert gas atmosphere) were connected to the two channels of a binary pump and transferred to the pump *via* septum and metal capillary. Substrate solution was pumped at variable flow rates (Q = 0.07–0.30 mL min^{-1}) through the microreactor fixed in a tempered (T = 40–60 °C) thermostat. The effluent of the column was collected with the aid of a fraction collector. The solvent of each fraction was removed followed by offline ^{1}H NMR analysis.

Reaction monitoring: Conversion and selectivity were quantified by ^{1}H NMR. Each ^{1}H NMR spectrum was recorded at ambient temperature with 512 scans on a Bruker AVANCE III HD 500 MHz NMR spectrometer. Chemical shifts are reported in parts per million (ppm) relative to the deuterated solvent benzene-d6 (δ = 7.16 ppm).

4.3 Supporting Information

4.3.1 Equipment and Chemicals

All reactions were performed under the exclusion of air and moisture. Nitrogen physisorption measurements were carried out at 77 K on a Thermo Scientific Surfer gas adsorption porosimeter (Thermo Fisher Scientific, Waltham, MA). Prior to the experiments, the samples were evacuated for 10 h at 250 °C. Total pore volumes (V_t) were obtained with the Gurvich rule at a relative pressure of $p/p_0 = 0.95$, specific surface areas (S_{BET}) were determined by means of the Brunauer–Emmett–Teller equation in the range of $0.05 \leq p/p_0 \leq 0.3$. Pore size distributions were derived from the adsorption branches of the physisorption isotherms using the non-local density functional theory (NLDFT) method based on a cylindrical pore model.[S1]

Positive ion MALDI-TOF (matrix-assisted laser desorption ionization time-of-flight) measurements were performed on a Bruker Autoflex III with smart beam. Measurements were carried out in the reflector mode. Samples were prepared from THF solution by mixing dihydroxybenzoic acid (10 mg/mL), sample (5 mg/mL), sodium trifluoromethanesulfonate (17 mg/ml) in a ratio of 20:5:2 (wt).

ICP-OES data were recorded on a Spectro Acros 160 CCD equipped with a Cetec ASX-260 autosampler. Analysis of the samples was carried out with the Software Smart Analyzer Vision 4.02.0834.

4.3.2 Nitrogen Physisorption Analysis

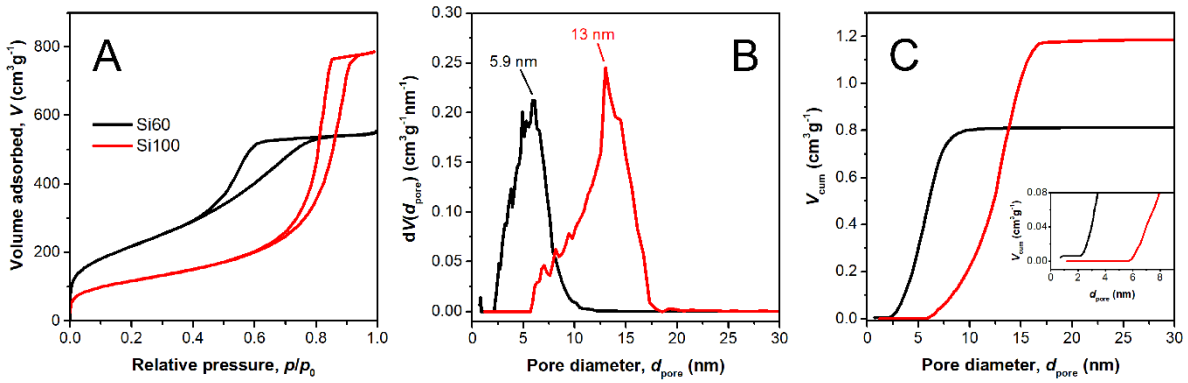

Figure 4.S1. Nitrogen physisorption isotherms (A), pore size distributions (B), and cumulative pore volumes (C) for Si60 and Si100.

Table 4.S1. Structural properties of Si60 and Si100.[a]

Material	V_t [cm^3g^{-1}]	S_{BET} [m^2g^{-1}]	S_{BET} [m^2g^{-1}]	ε_{intra} [–]
Si60	0.82	793	5.9	0.63
Si100	1.19	417	13.0	0.72

[a] Total pore volume (V_t), specific surface area (S_{BET}), and mode mesopore diameter (d_{meso}) derived from nitrogen physisorption analysis; intraparticle porosity (ε_{intra}) calculated by $\varepsilon_{intra} = V_t / (V_t + \delta_{Si}^{-1})$, were δ_{Si} denotes the density of amorphous silica (2.13 g cm^{-3}).

4.3.3 Determination of Ru-loadings via ICP-OES

The quantitative analysis of the Ru-loading of each silica sample was realized with ICP-OES.[S2] For analysis, the corresponding silica (50–70 mg) was mixed with KOH (0.38 g, 6.77 mmol) and KNO_3 (0.65 g, 6.42 mmol). The mixture was heated to 450 °C and temperature was held for 3h. After cooling to room temperature, $K_2S_2O_8$ (50.0 mg, 0.18 mmol) was added to stabilize the Ru-compounds. The colorless solid was dissolved in a minimum amount of deionized water and 1 M KOH (2 mL) was added. The suspension was filtered, transferred into a 10 mL volumetric flask and filled to the mark with deionized water. The solution was slowly added to a 25 mL volumetric flask with concentrated HCl (5 mL) and filled to the mark with deionized water. This solution was analyzed by ICP-OES for Ru. Ru was measured at λ = 240.272 nm. The background was measured at λ_1 = 240.223–240.254 nm and λ_2 = 240.295–240.340 nm. The limit of detection (LOD) was 0.0001 mg L^{-1}. For calibration, aqueous Ru-standards with a Ru concentration of 0.000, 0.100, 0.500, 1.000, 2.500, 5.000, and 10.000 mg L^{-1} were used. A reference containing the same amount of KOH, KNO_3, HCl, and deionized water was subjected to the same treatment for comparison.

Table 4.S2. Ru-content in 1@Si60 and 1@Si100 determined by ICP-OES.

Material	Mesopore size [Å]	Silica used for quantification [mg]	*c*(Ru) in diluted sample [mg L^{-1}]	µmol Ru/g silica
1@Si60	60	51	1.46	7.1
1@Si100	100	69	9.27	33.2

4.3.4 Literature Procedures

$RuCl_2$(N-mesityl-N-(3-(trimethoxysilyl)prop-1-yl)-imidazol-2-ylidene)(CH-2-(2-PrO-C_6H_4)) **1**,[S3] dec-9-en-1-yl undec-10-enoate **2**,[S4] (E)-oxacycloicos-11-en-2-one (E)-**3**,[S4] and (Z)-oxacycloicos-11-en-2-one (Z)-**3**[S4] were synthesized according to literature. The pore-selective immobilization of **1** inside the mesopores of the silica particles was carried out as described in the literature.[S3,S5]

4.3.5 Column Packing

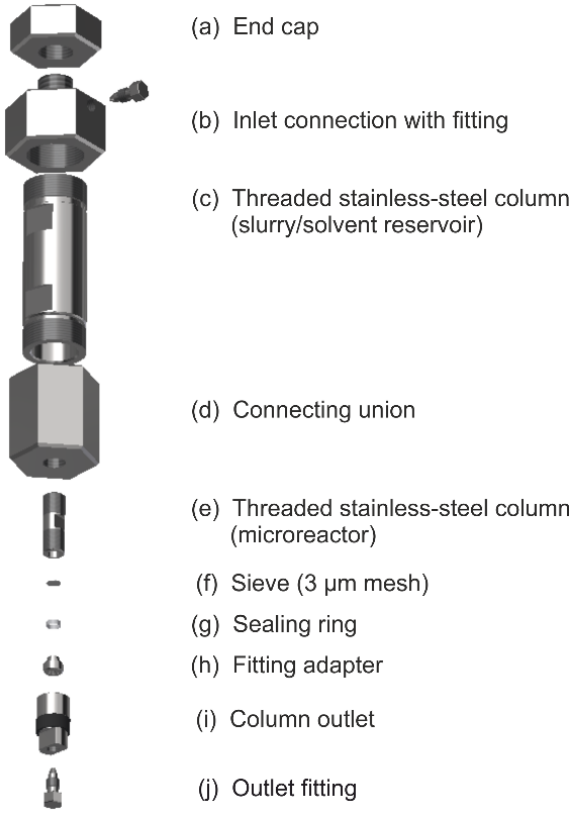

Figure 4.S2. Column packing hardware used for the preparation of densely packed microreactors. Empty microreactor column (e) dimensions: 4.6 mm inner diameter × 20 mm length. The final packed bed of particles had an effective length of only ~15 mm due to the fitting adapters (h) inserted by a few millimeters at both column ends.

4.3.6 Determination of Substrate Residence Times

As noted in the context of Eq. (3), the mean residence times $\bar{t}_{\mathrm{res}}(\mathbf{2})$ can be generally determined from concentration profiles $c(t)$ of **2**, recorded following pulse injections onto the microreactors at the employed volumetric flow rates Q. Pulse injections of **2** onto the microreactors occurred after the continuous-flow experiments, when catalyst was mostly inactive, so that $\bar{t}_{\mathrm{res}}(\mathbf{2})$ could be analyzed without interference from reaction.

This procedure is illustrated by Figure 4.S3 for $Q = 0.15$ mL min^{-1} and **1**@Si60. To account for the residence time of **2** in the system *external* to the microreactor (from injection to detection), the packed microreactor column was initially removed from the system and replaced by a ZDV (zero dead volume) union. Pulse injection of **2** then resulted in the profile shown in panel A of Figure 4.S3, providing a mean dead time in this extracolumn system of $t_{\mathrm{m}} = 37.9$ s (from the peak maximum, as indicated). The profile of **2** in the system containing the microreactor packed with **1**@Si60 (instead of the ZDV union) is shown in panel B, identifying a mean retention time in the *entire*, that is, microreactor column plus extracolumn system of $t_{\mathrm{r}} = 116.9$ s, again using the peak maximum. The mean residence time inside the microreactor for this particular experiment is therefore $\bar{t}_{\mathrm{res}}(\mathbf{2}) = t_{\mathrm{r}} - t_{\mathrm{m}} = 79.0$ s.

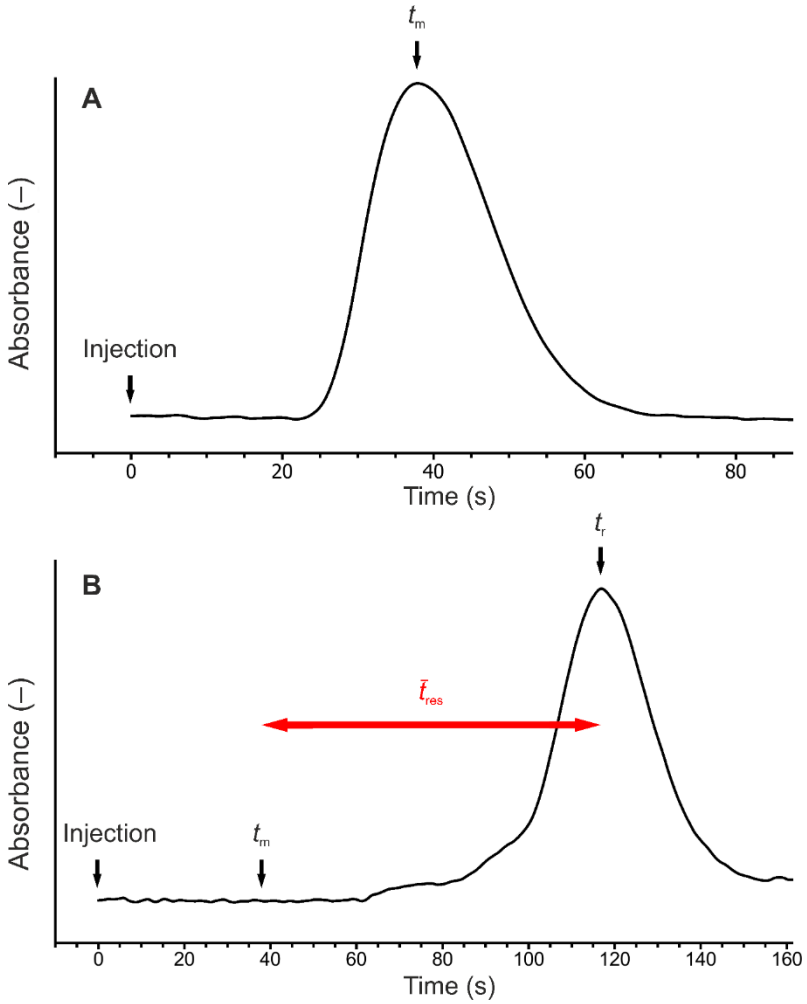

Figure 4.S3. Analysis of mean residence times $\bar{t}_{res}(\mathbf{2})$ on the packed microreactors (here, for Q = 0.15 mL min^{-1} and **1**@Si60). Profiles of **2** moving exclusively in the extracolumn system (A) and in the entire (microreactor column plus extracolumn) system (B).

4.3.7 Macrocyclization Reactions

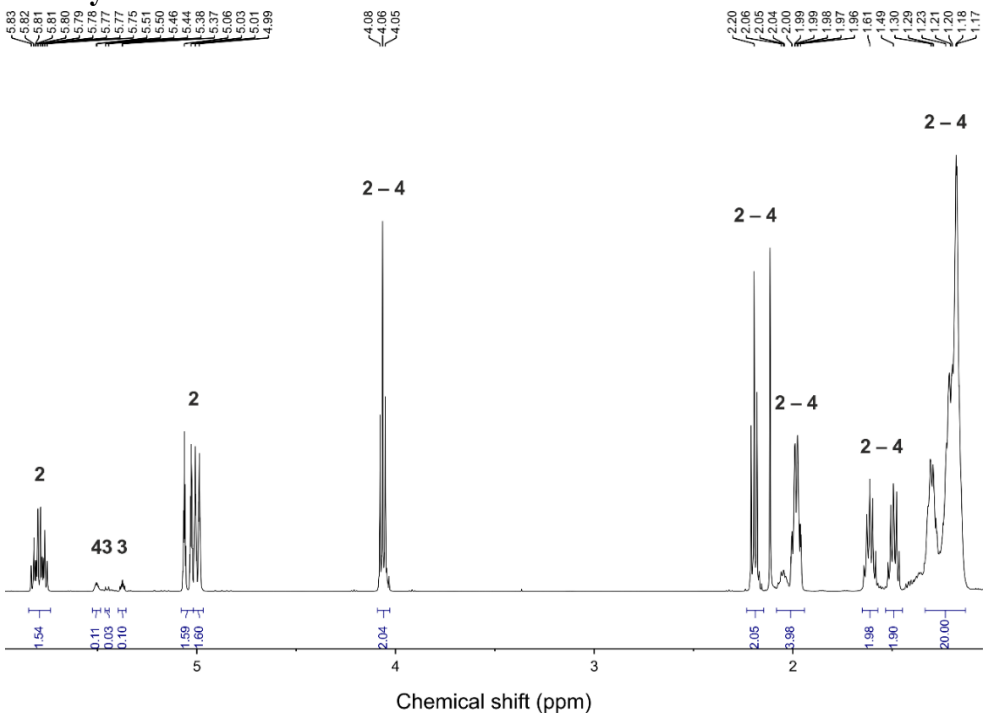

Figure 4.S4. Example ^{1}H 500 MHz NMR spectrum of a reaction solution used for quantification of conversion and selectivity in the RCM of substrate **2** to MMC product **3** and oligomer **4** (cf. Scheme 4.1) according to Eqs. (4) and (5). The reaction solution was taken from the microreactor packed with the modified Si60 particles (Q = 0.15 mL min^{-1}, T = 50 °C).

4.3.8 Macrocyclization with 1 in Solution

Substrate **2** (8.1 mg, 0.025 mmol, 1 eq.) was dissolved in toluene-d8 (0.997 mL, 25.08 mM) and a stock solution of catalyst **1** (3.3 µL, 7.5 mM, 0.1 mol-%) was added. The resulting mixture was stirred at 40 °C for 16 hours and then subjected to ^{1}H NMR analysis. Overall conversion: 62%, MMC selectivity: 45%.

In general, the isomerization of the individual components (with an exception of MMC product) increases in the course of the reaction. This is aggravated by the increasing temperature during the flow experiment (cf. Figure 4.4 in the main text). (*Z*)-**3** can no longer be accurately determined due to this isomerization (Figure 4.S5). Because the *E/Z*-ratio did not change with the conversion, the calculation of MMC selectivity was realized using the *E/Z*-ratio determined at the beginning of the reaction.
Fortunately, **1**@Si60 shows much less isomerization of substrate compared to **1**@Si100, which is illustrated in Figure 4.S6.

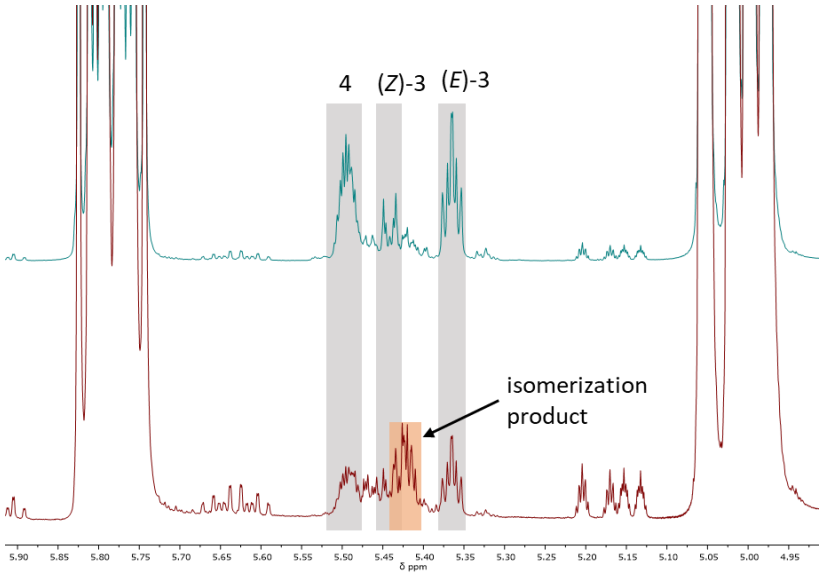

Figure 4.S5. Comparison of ^{1}H NMR spectra (500 MHz) for the RCM of **2** with **1**@Si60 at T = 40 °C (after an experiment time of t = 95.5 min; green, top) and at T = 55 °C (t = 626.5 min; red, bottom) used for calculating conversion and selectivity (Q = 0.07 mL min^{-1}).

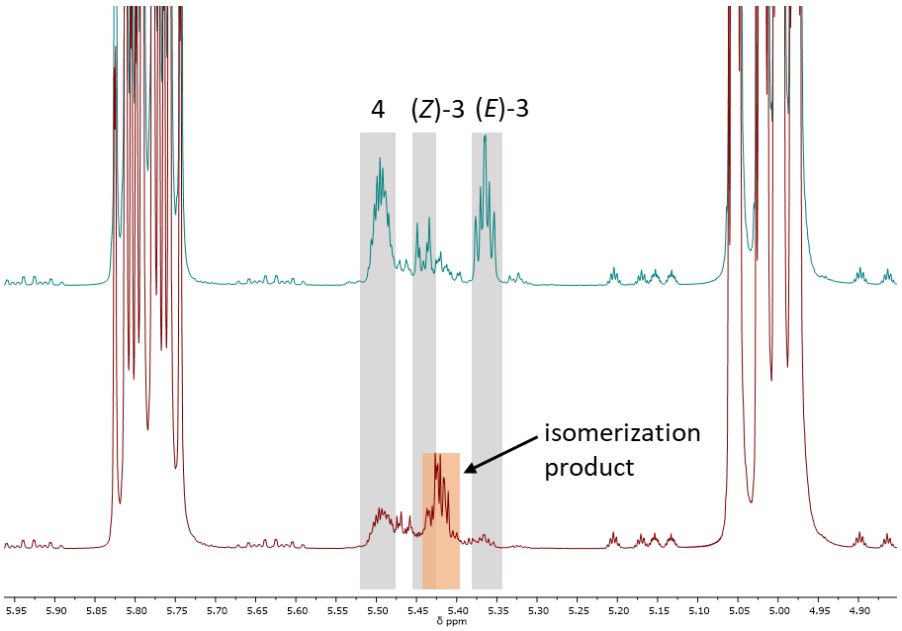

Figure 4.S6. Comparison of ^{1}H NMR spectra (500 MHz) for the RCM of **2** with **1**@Si60 (green, top) and **1**@Si100 (red, bottom) used for calculating conversion and selectivity. Q = 0.07 mL min^{-1}, T = 40 °C, experiment time: t = 95.5 min.

4.3.9 MALDI-TOF Measurements

Relative percentages of all formed oligomers (dimer, trimer, tetramer, pentamer, and hexamer) have been determined from their signal intensities. The results are summarized in Table 4.S3 and Table 4.S4.

Table 4.S3. Signal intensities and relative oligomer percentages for the RCM of **2** using **1** in solution.

	Dimer	**Trimer**	**Tetramer**	**Pentamer**	**Hexamer**
Signal Intensity	94899	40319	8543	1014	54
Relative Percentage [%]	65.52	27.84	5.90	0.70	0.04

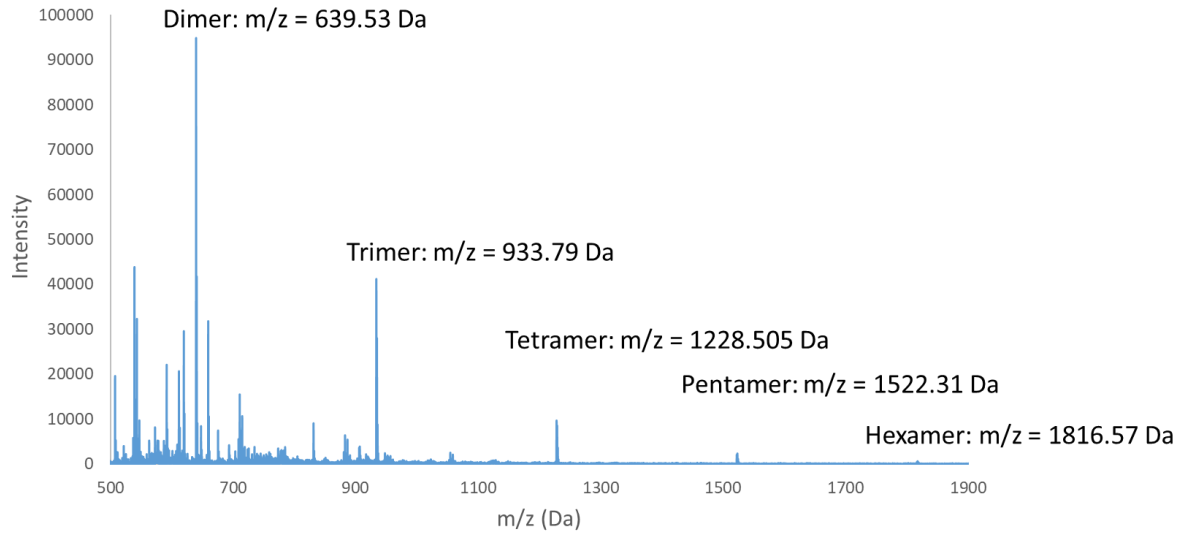

Figure 4.S7. Representative MALDI-TOF spectrum for the RCM of 2 using 1 in solution (with the corresponding *m/z*-values).

Table 4.S4. Signal intensities and relative oligomer percentages for the RCM of **2** using **1**@Si60 between 90 and 210 min experiment time.

		Dimer	**Trimer**
1	Signal Intensity	32030	1531
	Percentage [%]	95	5
2	Signal Intensity	29629	1182
	Percentage [%]	96	4
3	Signal Intensity	12567	469
	Percentage [%]	96	4
4	Signal Intensity	3642	273
	Percentage [%]	92	7
5	Signal Intensity	1254	63
	Percentage [%]	95	5

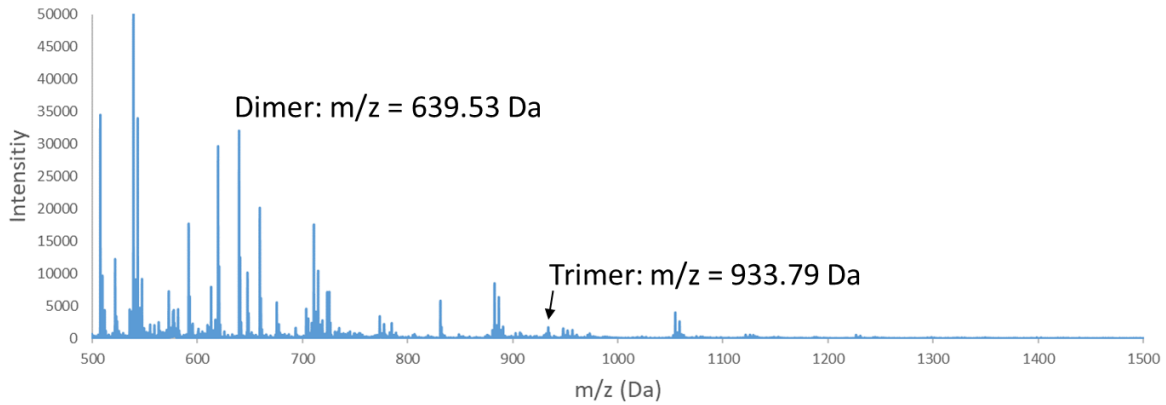

Figure 4.S8. Representative MALDI-TOF spectrum for the RCM of 2 using 1@Si60 (at Q = 0.07 mL min^{-1} and T = 40 °C) with the corresponding *m/z*-values.

4.4 References

1 a) G. C. Vougioukalakis, R. H. Grubbs, *Chem. Rev.* **2010**, *110*, 1746–1787; b) *Olefin Metathesis: Theory and Practice* (Ed.: K. Grela), John Wiley & Sons, Hoboken, NJ, **2014**; c) *Handbook of Metathesis* (Ed.: R. H. Grubbs, A. G. Wenzel, D. J. O'Leary, E. Khosravi), Wiley-VCH, Weinheim, **2015.**

2 J. C. Conrad, M. D. Eelman, J. A. Duarte Silva, S. Monfette, H. H. Parnas, J. L. Snelgrove, D. E. Fogg, *J. Am. Chem. Soc.* **2007**, *129*, 1024–1025.

3 S. Monfette, D. E. Fogg, *Chem. Rev.* **2009**, *109*, 3783–3816.

4 a) E. G. Derouane, *J. Catal.* **1986**, *100*, 541–544; b) Special issue on confinements effects, *J. Mol. Catal. A: Chem.* **2009**, *305*, 1–190.

5 S. Polarz, B. Völker, F. Jeremias, *Dalton Trans.* **2010**, *39*, 577–584.

6 a) C. Copéret, J.-M. Basset, *Adv. Synth. Catal.* **2007**, *349*, 78–92; b) M. R. Buchmeiser, *Chem. Rev.* **2009**, *109*, 303–321; c) M. R. Buchmeiser, *New J. Chem.* **2004**, *28*, 549–557; d) M. R. Buchmeiser, *Immobilization of Metathesis Catalysts*, in: "Olefin Metathesis – Theory and Praxis" (Ed.: K. Grela), John Wiley & Sons, Hoboken, NJ, **2014**; e) H. Balcar, J. Čejka, *Coord. Chem. Rev.* **2013**, *257*, 3107–3124; f) A. Dewaele, F. Verpoort, B. Sels, *ChemCatChem* **2016**, *8*, 3010–2030; g) R. Zhong, A. C. Lindhorst, F. J. Groche, F. E. Kühn, *Chem. Rev.* **2017**, *117*, 1970–2058; h) W. Wang, L. Cui, P. Sun, L. Shi, C. Yue, F. Li, *Chem. Rev.* **2018**, *118*, 9843–9929; i) C. Copeŕet, F. Allouche, K. W. Chan, M. P. Conley, M. F. Delley, A. Fedorov, I. B. Moroz, V. Mougel, M. Pucino, K. Searles, K. Yamamoto, P. A. Zhizhko, *Angew. Chem. Int. Ed.* **2018**, *57*, 6398–6440; j) H. Balcar, J. Čejka, *Catalysts* **2013**, *9*, 743.

7 a) M. Bru, R. Dehn, J. H. Teles, S. Deuerlein, M. Danz, I. B. Müller, M. Limbach, *Chem. Eur. J.* **2013**, *19*, 11661–11671; b) A. Dewaele, B. Van Berlo, J. Dijkmans, P. A. Jacobs, B. F. Sels, *Catal. Sci. Technol.* **2016**, *6*, 2580–2597; c) E. Pump, Z. Cao, M. K. Samataray, A. Bendjeriou-Sedjerari, L. Cavallo, J. M. Basset, *ACS Catal.* **2017**, *7*, 6581–6586.

8 N. A. Grooso-Giordano, S. I. Zones, A. Katz, *Catal. Commun.* **2019**, *31*, 72–126.

9 F. Ziegler, J. Teske, I. Elser, M. Dyballa, W. Frey, H. Kraus, N. Hansen, J. Rybka, U. Tallarek, M. R. Buchmeiser, *J. Am. Chem. Soc.* **2019**, *141*, 19014–19022.

10 a) J. O. Krause, S. Lubbad, O. Nuyken, M. R. Buchmeiser, *Adv. Synth. Catal.* **2003**, *345*, 996–1004; b) B. Van Berlo, K. Houthoofd, B. F. Sels, P. A. Jacobs, *Adv. Synth. Catal.* **2008**, *350*, 1949–1953; c) K. H. Park, S. Kim, Y. K. Chung, *Bull. Korean Chem. Soc.* **2008**, *29*, 2057–2060; d) J. Lim, S. S. Lee, J. Y. Ying, *Chem. Commun.* **2010**, 806–808; e) J. Cabrera, R. Padilla, M. Bru, R. Lindner, T. Kageyama, K. Wilckens, S. L. Balof, H.-J. Schanz, R. Dehn, J. H. Teles, S. Deuerlein, K. Müller, F. Rominger, M. Limbach, *Chem. Eur. J.* **2012**, *18*, 14714–14724; f) E. Borré, M. Rouen, I. Laurent, M. Magrez, F. Caijo, C. Crévisy, W. Solodenko, L. Toupet, R. Frankfurter, C. Vogt, A. Kirschning, M. Maudit, *Chem . Eur. J.* **2012**, *18*, 16369–16382; g) K. Skowerski, S. J. Czarnocki, P. Knapkiewicz, *Chem. Sus. Chem.* **2014**, *7*, 536–542; h) A. Chołuj, A. Zielinski, K. Grela, M. J. Chmielewski, *ACS Catal.* **2016**, *6*, 6343–6349; i) K. Skowerski, J. Pastva, S. J. Czarnocki, J. Janascova, *Org. Proc. Res. Dev.* **2015**, *19*, 872–877.

11 C. G. Frost, L. Mutton, *Green Chem.* **2010**, *12*, 1687–1703.

12 a) J. Yoshida, *Chem. Rec.* **2010**, *10*, 332–341; b) J. Yoshida, Y. Takahashi, A. Nagaki, *Chem. Commun.* **2013**, *49*, 9896–9904.

13 I. M. Mandity, S. B. Ötvös, F. Fülöp, *ChemistryOpen* **2015**, *4*, 212–223.

14 a) S.-J. Reich, A. Svidrytski, D. Hlushkou, D. Stoeckel, C. Kübel, A. Höltzel, U. Tallarek, *Ind. Eng. Chem. Res.* **2018**, *57*, 3031–3042; b) S.-J. Reich, A. Svidrytski, A. Höltzel, W. Wang, C. Kübel, D. Hlushkou, U. Tallarek, *Microporous Mesoporous Mater.* **2019**, *282*, 188–196; c) U. Tallarek, J. Hochstrasser, F. Ziegler, X. Huang, C. Kübel, M. R. Buchmeiser, *ChemCatChem* **2021**, *13*, 281–292.

15 a) S. Monfette, M. Eyholzer, D. M. Roberge, D. E. Fogg, *Chem. Eur. J.* **2010**, *16*, 11720–11725; b) P. Plouffe, A. Macchi, D. M. Roberge, *Org. Proc. Res. Dev.* **2014**, *18*, 1286–1294.

16 a) H. S. Fogler, *Elements of Chemical Reaction Engineering*, 4th ed., Prentice Hall, Upper Saddle River, NJ, **2006**, Chapter 14.4.1; b) R. L. Hartman, J. P. McMullen, K. F. Jensen, *Angew. Chem. Int. Ed.* **2011**, *50*, 7502–7519.

17 C. P. Haas, T. Müllner, R. Kohns, D. Enke, U. Tallarek, *React. Chem. Eng.* **2017**, *2*, 498–511.

18 a) S. H. Hong, M. W. Day, R. H. Grubbs, *J. Am. Chem. Soc.* **2004**, *126*, 7414–7415 ; b) S. H. Hong, A. G. Wenzel, T. T. Salguero, M. W. Day, R. H. Grubbs, *J. Am. Chem. Soc.* **2007**, *129*, 7961–7968.

19 a) M. B. Dinger, J. C. Mol, *Organometallics* **2003**, *22*, 1089–1095; b) M. B. Dinger, J. C. Mol, *Eur. J. Inorg. Chem.* **2003**, 2827–2833.

20 K. Leung, I. M. B. Nielsen, L. J. Criscenti, *J. Am. Chem. Soc.* **2009**, *131*, 18358–18365.

21 M. Sulpizi, M. P. Gaigeot, M. Sprik, *J. Chem. Theory Comput.* **2012**, *8*, 1037–1047.

S1 K. A. Cychosz, R. Guillet-Nicolas, J. García-Martínez, M. Thommes, *Chem. Soc. Rev.* **2017**, *46*, 389–414.

S2 T. Suoranta, M. Niemelä, P. Perämäki, *Talanta* **2014**, *119*, 425–429.

S3 F. Ziegler, J. Teske, I. Elser, M. Dyballa, W. Frey, H. Kraus, N. Hansen, J. Rybka, U. Tallarek, M. R. Buchmeiser, *J. Am. Chem. Soc.* **2019**, *141*, 19014–19022.

S4 V. M. Marx, M. B. Herbert, B. K. Keitz, R. H. Grubbs, *J. Am. Chem. Soc.* **2013**, *135*, 94–97.

S5 J. D. Webb, T. Seki, J. F. Goldston, M. Pruski, C. M. Crudden, *Microporous Mesoporous Mater.* **2015**, *203*, 123–131.

5. Chapter 5: Olefin metathesis under spatial confinement and continuous flow: Investigation of isomeric side reactions with a Grubbs–Hoveyda catalyst

Authors
A. Böth,[+] T. Roider,[+] F. Ziegler, X. Xie, M. R. Buchmeiser and U. Tallarek*
[+]These authors contributed equally to this work.

State of publication
Submitted 20 October 2022 to *ChemCatChem*, *under review.*

Table of Content

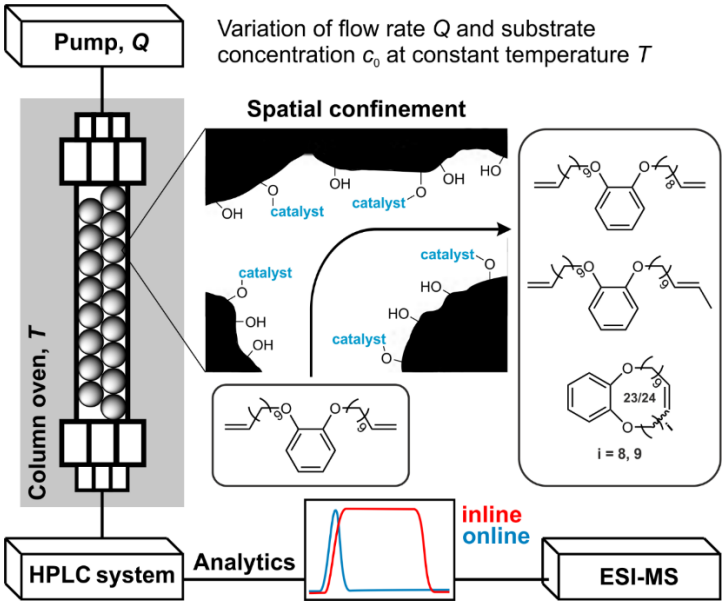

Abstract
A second-generation Grubbs–Hoveyda catalyst was immobilized inside mesoporous silica and used in the ring-closing metathesis (RCM) of an α,ω-diene to a medium-sized macro(mono)cycle to investigate the relationship between substrate concentration, reaction time and the overall experiment time on the rate of isomerization under spatial confinement and continuous flow. RCM reactions are commonly monitored by ^{1}H NMR analysis, however, elucidation of reaction mixtures yielding medium-sized rings with a difference of only a single carbon atom remains difficult, because the NMR signals are closely intertwined and sometimes indistinguishable. By the utilization of a two-dimensional continuous-flow platform enabling the on-line coupling of reaction and separation/analysis, the identification as well as quantification of every compound became possible despite chemical similarity. The derived kinetic data revealed that the isomerization increases with higher substrate concentrations and longer reaction times but shows a distinct decline with prolonged experiment times.

5.1 Introduction

Ruthenium-based olefin metathesis catalysts are compelling tools to generate new carbon-carbon double bonds.[1-4] However, the 2nd-generation Grubbs catalyst[5] and its phosphine-free analogue, i.e., the 2nd-generation Grubbs–Hoveyda catalyst,[6] known for their outstanding versatility, are prone to ruthenium-hydride formation and thus to double-bond isomerization.[7] As a result, a wider range of side products and macro(mono)cycles (MMCs) of different ring sizes can be observed, which negatively impacts the selectivity and product yield. Furthermore, it has been proposed that intrinsic catalyst deactivation and the formation of isomeric species are connected.[8] Therefore, a combined identification and quantification of the isomeric compounds provides deeper insight into the relationship between double-bond isomerization and catalyst deactivation. The separation of such complex mixtures is often not feasible by standard purification techniques.[9] Thus, it is common to study reaction mixtures by ^{1}H NMR and to determine conversions as well as selectivities from NMR data. However, interpretation of reaction mixtures with a medium-sized α,ω-diene as starting material remains challenging, because the signals of the product and side products as well as the α,ω-diene are often indistinguishable.[10] Alternatively, gas chromatographic methods have been established to determine the progress of RCM reactions.[11] Still, involatile compounds such as oligomers complicate their quantification and require indirect measurement based on calibration to show the conversion of the substrate and formation of RCM products.

In our previous work, we investigated the macro(mono)cyclization of an α,ω-diene under the conditions of spatial confinement and continuous-flow reactor operation.[12] To meet these conditions, the 2nd-generation Grubbs–Hoveyda catalyst was selectively immobilized inside mesoporous silica particles and continuous-flow operation was realized by implementing a high-end HPLC configuration equipped with a packed microreactor containing the modified silica particles. This setup allowed fully automatic, highly precise adjustments of temperatures and flow rates, in contrast to the often used syringe-pump design. With a fraction collector, the effluent of the column was collected, the solvent removed under reduced pressure and the residue analyzed via offline ^{1}H NMR. In this work, we further improved this setup by coupling a second dimension on-line, covering a chromatographic column (for high-resolution separations), a diode-array detector (DAD) and electrospray ionization-mass spectrometry (ESI-MS). The combination of the first (microreactor) dimension with the second (separation–analysis) dimension enabled the real-time reaction control (monitoring) and simultaneous quantification of all compounds. In this regard, ESI-MS is of importance to receive an overview of the formed by-products. The 2D-LC/MS setup is particularly suited for complex reaction mixtures, e.g., from RCM reactions that yield medium-sized rings, where target molecules are nearly identical and, as a result, need to be separated prior to analysis to reliably determine conversion and selectivity. In addition, by scaling up to a semi-preparative column and exchanging the ESI-MS with a fraction collector, offline analysis became possible, which we used to investigate the dependence of the isomerization rate on substrate concentration and experiment time.

Figure 5.1 presents an overview of the investigated reaction (Figure 5.1a), common by-products from isomerization (Figure 5.1b) and the used catalyst (Figure 5.1c). Problems that arise in the determination of conversion and selectivity for the reaction mixture via ^{1}H NMR analysis from

overlapping signals are illustrated in the Supporting Information (Section 5.3.4) for this particular example.

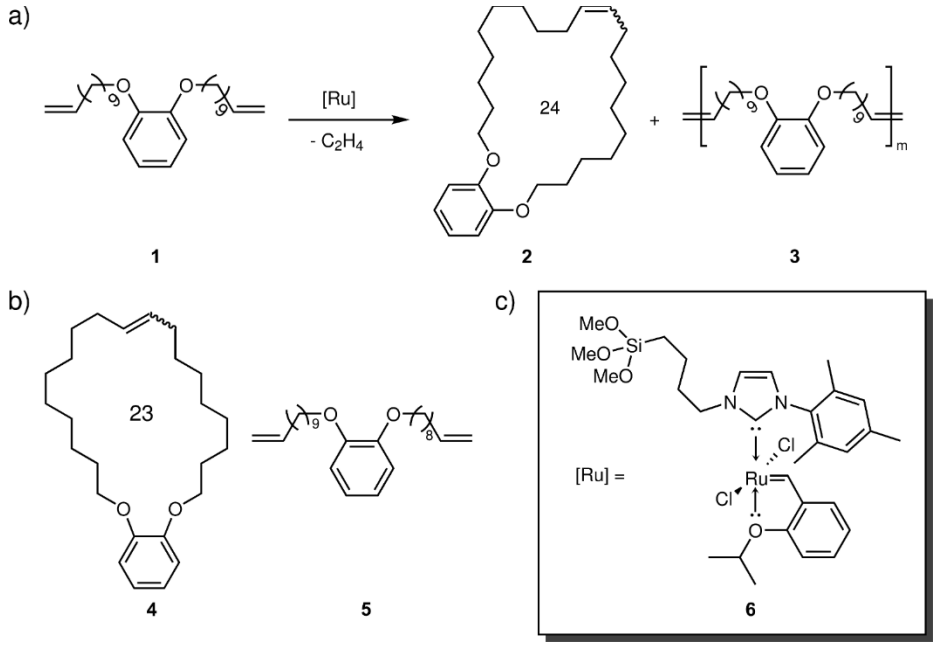

Figure 5.1. a) Investigated RCM reaction. b) Species formed from isomers. c) Structure of the 2nd-generation Grubbs–Hoveyda type catalyst. The trimethoxysilyl tether at the NHC serves for the covalent attachment to the internal surface of the mesoporous silica particles.

5.2 Results and Discussion

5.2.1 Catalyst immobilization

As in our previous work, we used spherical-shaped, mesoporous amorphous silica particles with a particle diameter of about 5 µm (mode) and a mean mesopore size of 5.9 nm.[12] Immobilization of the 2nd-generation Grubbs–Hoveyda type catalyst **6** (Figure 5.1c) selectively inside the mesoporous silica particles was carried out following an established protocol.[13] The particles had a specific surface area of 793 $m^2\ g^{-1}$ (nitrogen physisorption) and showed a loading with **6** of 7.2 µmol g^{-1} (ICP-OES).[12]

The modified silica particles are well suited for the study of spatial confinement effects on selectivity in the olefin metathesis with the chosen substrate and expected (side) products (cf. Figure 5.1). This is demonstrated by their diffusive hindrance factor characteristics, which were derived from pore-scale simulations of hindered diffusion in physical (electron tomography-based) reconstructions of the material.[14]

5.2.2 Olefin metathesis pathways

We investigated olefin metathesis pathways with the α,ω-diene **1** to the MMC product **2** and oligomer **3** (Scheme 5.1, cycle A), where we focused on individual routes resulting from isomerization of **1** followed by cross-metathesis (Scheme 5.1, cycle B). Because the microreactor is constantly supplied with fresh substrate solution, new ethylene is also

permanently formed and affects the reaction equilibria. Also, it can be assumed that all reaction pathways including ethylene are in principle reversible.[15]

It has been proposed that ethylene decomposes the ruthenium catalyst to ruthenium hydrides, which promote isomerization.[16] A higher substrate concentration will cause a higher local ethylene concentration. Consequently, more ruthenium hydrides should be formed inside the mesoporous material and the concentration of isomers should increase. Because the focus of this work is on the formation of isomers, rather high concentrations between 25 and 250 mM were chosen for the substrate solutions. Isomerization of **1** yields **8**, whose RCM is impeded by the presence of an internal olefin (Scheme 5.1). After cross-metathesis of **8** to a smaller substrate **5**, however, olefin metathesis is facilitated (cycle B). Diene **5** can react with **1** or with itself by acyclic diene metathesis to form oligomer **9**, where the individual dienes of the oligomer have different chain lengths (i = 8 or 9). Backbiting of these oligomers yields either the RCM product **2** of cycle A or the RCM product **4** of substrate **5** (cycle B). Cross-metathesis of substrate **1** also leads to a non-terminal alkene **7**.

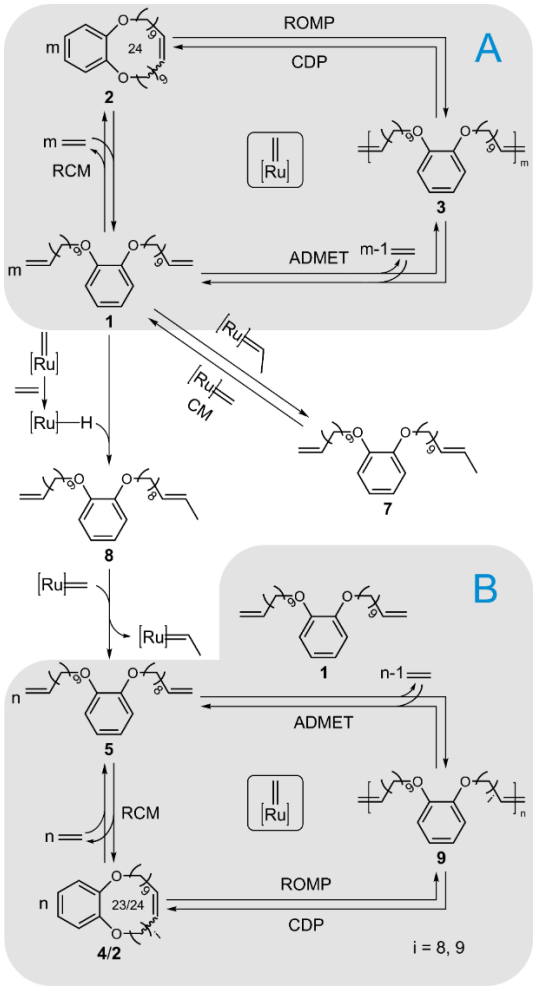

Scheme 5.1. Olefin metathesis pathways of the α,ω-diene **1** to the MMC **2** and oligomer **3**. Isomerization of **1** leads to a smaller substrate **5**, which is also susceptible to olefin metathesis. RCM: ring-closing metathesis, ADMET: acyclic diene metathesis, ROMP: ring-opening metathesis polymerization, CDP: cyclodepolymerization, CM: cross-metathesis. n denotes substrate equivalents and i the number of methylene groups, [Ru=] represents the metal alkylidene complex.

5.2.3 Experimental configuration and 2D-LC/MS setup

Olefin metathesis of substrate **1** with the immobilized catalyst **6** under continuous-flow was realized by adapting the 2D-LC/MS configuration illustrated in Figure 5.2. In the first dimension of that setup, a binary pump (4) was used to feed reactant solution into a microreactor column packed with the modified silica particles (4.6 mm inner diameter × 15 mm effective packed-bed length; packed-reactor volume, $V_{reactor} \approx 0.18$ mL) at a precise and constant flow rate. The residence time of the substrate solution on the packed microreactor (and thus, the reaction time) was controlled by the pump flow rate and depended on the volume in the microreactor available to the pumped solution. The microreactor was located in a temperature-controlled column oven compartment (9), which also allowed the reaction temperature to be adjusted within the system. After the reactor, there was an injection valve (5) connecting the first with the second dimension that allowed to analyze the reaction solution (effluent). In the second (analytical) dimension, the injected sample was then purified by a chromatographic column (8) and the separated compounds were detected with an on-line DAD (7) and an ESI-MS (12). Through the replacement of the analytical-scale chromatographic column by a semi-preparative column and the ESI-MS by a fraction collector (11), additional offline analysis was possible. A more detailed description of all individual components of the 2D-LC/MS setup can be found in the Supporting Information (Section 5.3.2, Figure 5.S1).

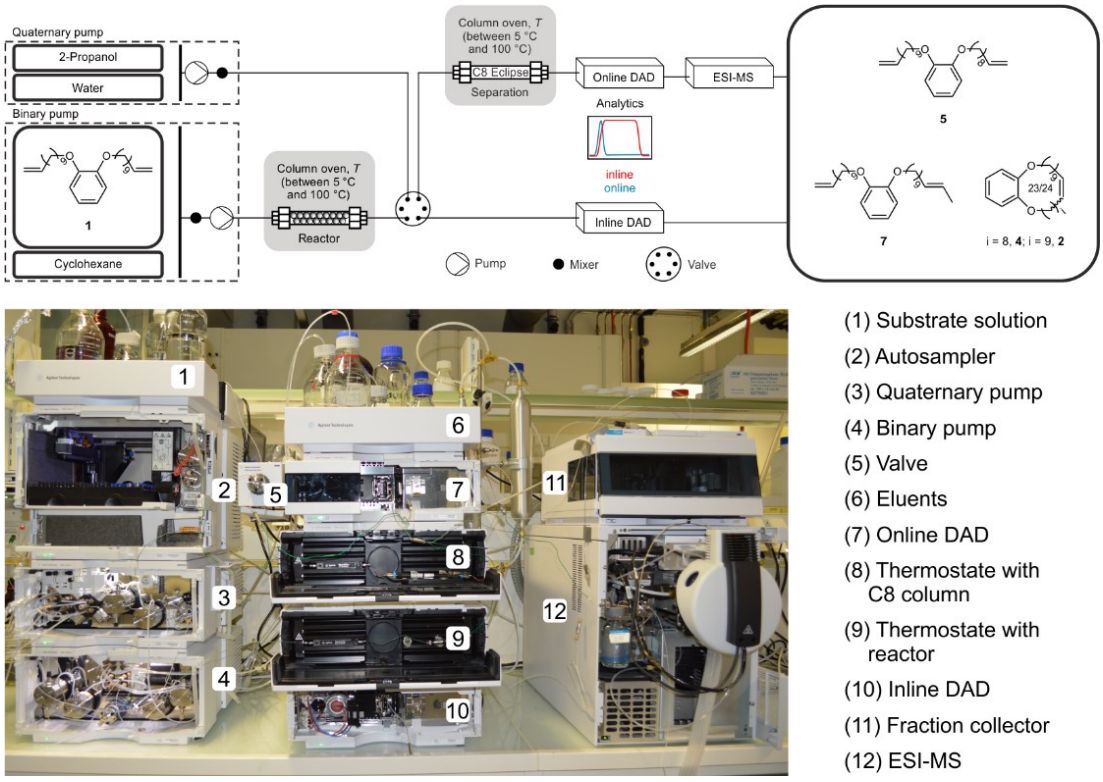

Figure 5.2. Photograph illustrating the two-dimensional continuous-flow platform adapted for the screening of olefin metathesis under spatial confinement using substrate **1** (25, 50, 100 and 250 mM in absolute cyclohexane, (1)). An injection valve (5), located after the microreactor compartment (9), connects the first (reaction) dimension with the second (analytical) dimension that enables the high-resolution chromatographic separation of the reaction mixture (8) and on-line analysis of the separated compounds using a DAD (7) and an ESI-MS (12). Steady-state operation of the microreactor was confirmed by an in-line DAD (10).

To identify all reactants, products and side products and to quantify their concentrations with the 2D-LC/MS system, it is necessary to identify conditions for which all compounds were baseline-separated by the chromatographic column of the second dimension (8). For that purpose, a batch reaction of **1** with the modified silica material was carried out to generate a sample that was subsequently used to determine the optimal separation conditions. Figure 5.3 shows an example chromatogram, in which the dienes as well as the MMCs and oligomers are apparent.

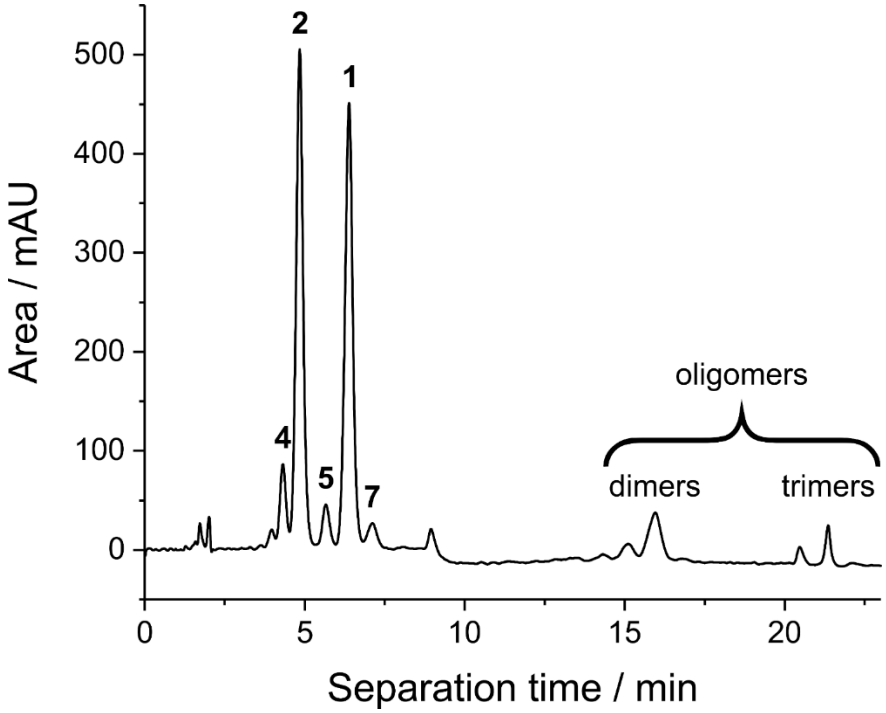

Figure 5.3. Separation of a RCM reaction sample of substrate **1** by reversed-phase liquid chromatography on an analytical-scale HPLC column packed with 5 µm-sized, C8-modified silica particles (detection at 208 nm).

Because the HPLC separation had to be completely finished after each injection of sample onto the chromatographic column before the next injection can take place, it was necessary to keep the time for the analysis cycle as short as possible. Especially when the lifetime of the microreactor is limited due to catalyst deactivation, a short analysis time is essential to be able to generate a sufficient number of data points for, e.g., different substrate concentrations, reaction times, and temperatures with each microreactor.

The α,ω-diene **1**, RCM products **2** and **4** as well as the isomeric species **5** and **7** (Scheme 5.1) could be eluted from the column and separated under isocratic conditions, that is, with a constant composition of the eluent, in less than eight minutes (Figure 5.3). For the oligomers, however, it was necessary to run a gradient in the eluent composition to elute them in a timely manner, which resulted in an overall duration of the chromatographic separation of about 23 minutes. Moreover, after applying the mobile phase gradient, equilibration of the separation column was needed before the next injection, which added another ~3 minutes. Due to these circumstances, we did not further investigate the oligomers, which allowed us to shorten the separation time and focus exclusively on the isomeric compounds. Details of the separation

conditions used for the screenings and further information on the calibration of relevant compounds can be found in the Supporting Information (Section 5.3.2 and 5.3.3, Figure 5.S2–5.S6).

The process adapted for the slurry-packing of the stainless-steel microreactor columns with the selectively modified silica particles has been described in detail before.[12] The packing station for the microreactors illustrated in Figure 5.4 guaranteed the preparation of dense and stable as well as homogeneous beds of these fine (~5 µm-sized) catalyst particles. This also ensured that relatively little solute dispersion occurs during hydrodynamic flow and transport of substrate solution in a continuous-flow experiment[17] and that plug-flow conditions were realized on the microreactors.[18] These conditions allow the transformation of flow rate through a reactor (and mean residence time on a reactor) into a sharp reaction time of the transported substrate molecules.[19] Consequently, a high-resolution reaction time control and discrete variation of reaction times was realized by straightforward adjustment and programming of the volumetric flow rate delivered by the high-precision, high-pressure pumps.[20]

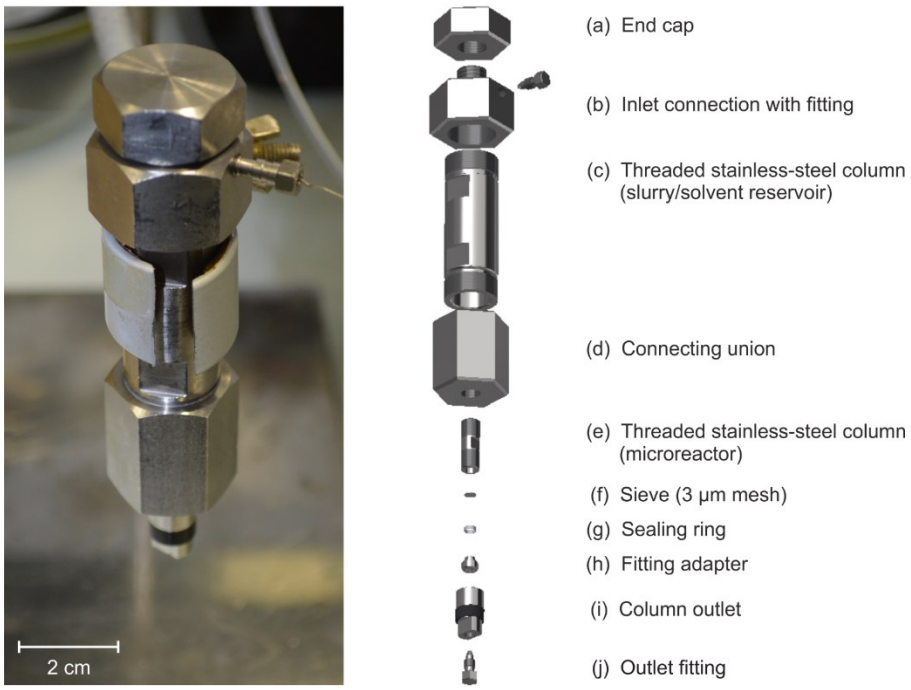

Figure 5.4. Setup used for the slurry-packing of microreactor columns (left) and its individual components (right). The packing station was connected via inlet (b) to a binary pump of the HPLC equipment.

For olefin metathesis under continuous-flow conditions substrate solution was continuously flushed through the microreactor at a set volumetric flow rate Q using a binary pump. Additionally, the temperature was set to T = 50°C and held constant by the column oven. Translating flow rate into reaction time on the reactor was accomplished by measuring the mean residence time ($\bar{t}_{res}$) of the substrate on a catalytically inactive microreactor.[12] Because **1** was partially size-excluded from the mesopores of the particles[14] and was also retained on the column through adsorption with the carbonyl oxygen onto the residual silanol groups of the silica surface,[13] we recorded mean residence times of **1** (which represent the effects of size-

exclusion and adsorption) to express reaction times for the substrate solutions in contact with a packed microreactor. These $\bar{t}_{res}$(**1**) were determined through concentration profiles of **1** recorded from pulse injections onto the microreactor after the experiments, when the catalyst was mostly inactive. The flow rates used in the experiments and corresponding reaction times are summarized in Table 5.1.

Table 5.1. Reaction times of substrate **1** on microreactors packed with the silica particles containing the 2nd-generation Grubbs–Hoveyda type catalyst **6**.

Flow rate Q [mL min^{-1}]	Reaction time t_{rct} [min]
0.01	18.6
0.02	9.3
0.04	4.4
0.06	3.1
0.1	1.9
0.14	1.2

5.2.4 Conversion and selectivity

Conversion and selectivity for the MMC product and the isomers were determined as follows:

$$\text{Conversion (MMC)} = \frac{n(\text{MMC})}{n_0(\text{Substrate})} \quad (1)$$

$$\text{Conversion (Isomers)} = \frac{n(\text{Isomers})}{n_0(\text{Substrate})} \quad (2)$$

$$\text{Selectivity} = \frac{n(\text{MMC})}{n(\text{MMC}) + n(\text{Isomers})} \quad (3)$$

We first investigated how different reaction times affect reaction and isomerization. For this purpose, a substrate concentration of 25 mM was selected and flow rates were varied from 0.02 to 0.14 mL min^{-1}, starting with the lowest flow rate (Table 5.1). The results of this screening are shown in Figure 5.5.

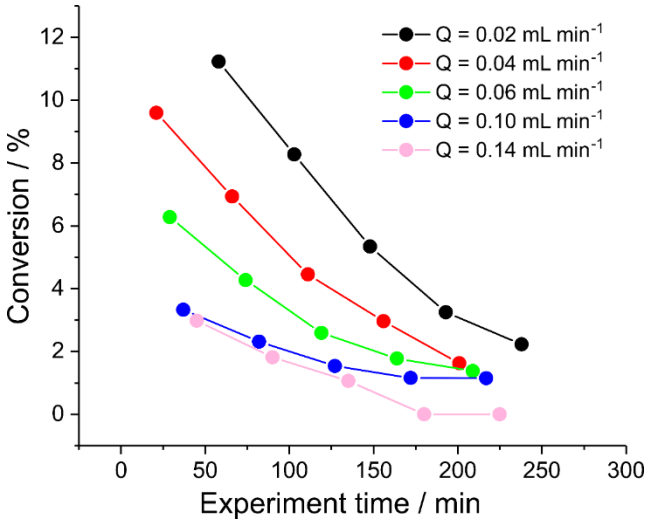

Figure 5.5. Reaction of substrate **1** with the immobilized 2nd-generation Grubbs–Hoveyda catalyst **6**. **1** was supplied at different flow rates (Q = 0.02–0.14 mL min^{-1} varied automatically from low to high), corresponding to the reaction times listed in Table 1 (substrate concentration: 25 mM, T = 50°C). Conversion of substrate to the MMC **2** was calculated according to Eq. (1).

During the overall experiment time of ~250 minutes, no isomeric compounds could be detected. For the isomerization process to occur, the active catalyst needs to react with ethylene to form the ruthenium hydride species.[16] For the selected reaction conditions it can be assumed that the conversion (and the resulting ethylene concentration) was insufficient to produce a significant amount of ruthenium hydrides. In addition, using higher flow rates ensures that produced ethylene can be removed more efficiently from the microreactor, hindering the isomerization process. The general decrease in conversion with increasing experiment time in Figure 5.5 is attributed to catalyst deactivation.[16]

As a consequence, for the subsequent experiments we selected the lowest possible flow rate (0.01 mL min^{-1}, limited by the pump), translating to the longest reaction time (Table 1), to favor isomer formation but increased the substrate concentration substantially (up to 250 mM) to push ethylene production in the microreactor and favor isomerization further. The results of these experiments are summarized in Figure 5.6.

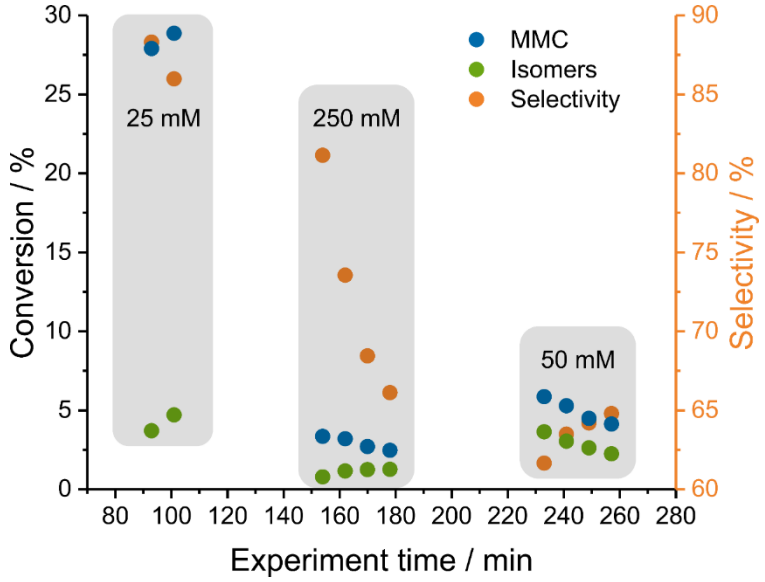

Figure 5.6. Conversion and selectivity in the RCM of substrate **1** to MMC **2** and isomers **5** and **7** calculated according to Eqs. (1)–(3). **1** was supplied at different concentrations (indicated in the figure), but with a constant flow rate Q of 0.01 mL min^{-1}, corresponding to a reaction time of 18.6 minutes (T = 50°C).

The grey-shaded areas in Figure 5.6 indicate the different substrate concentrations used for that screening (25 mM → 250 mM → 50 mM). Times between these areas were needed for the reactor to equilibrate at the new concentrations. During these times, catalyst deactivation nevertheless progressed. Already with the substrate concentration of 25 mM, isomeric compounds started to form (i.e., between 80 and 110 minutes in Figure 5.6). This can be attributed to the relatively high conversion (~30%) compared to the previous reactor and the generation of a sufficient amount of ethylene to form the ruthenium hydride species. With a concentration of 250 mM the amount of isomers increased even further and a sudden drop of selectivity (until a minimum of ~65%) could be measured. Interestingly, with a concentration of 50 mM, the selectivity started to increase again. We assume that the reason for this increase in selectivity is more likely the prolonged experiment time (~240 min) than the change in concentration.

To verify this assumption, we conducted a flow experiment at the same flow rate of 0.01 mL min^{-1} (as before, Figure 5.6), but without changing the initial substrate concentration, which was now set to 100 mM. The results of this control experiment are summarized in Figure 5.7. Microreactor performance showed the same pattern as for the previous reactor (Figure 5.6), but with a lesser decrease in selectivity. This time, a plateau from about 100 to 140 min could be observed, followed by a sudden increase in selectivity, which reinforces the assumption that the selectivity increase (noticed in Figure 5.6) is based on the experiment time rather than substrate concentration.

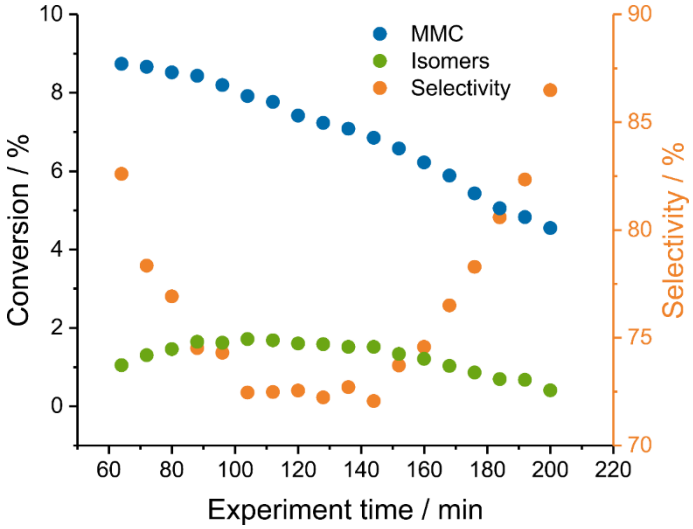

Figure 5.7. Conversion and selectivity in the RCM of substrate **1** to MMC **2** and the isomers **4**, **5** and **7** calculated using Eqs. (1)–(3). **1** was supplied at a constant flow rate Q of 0.01 mL min^{-1}, corresponding to a reaction time of 18.6 minutes (substrate concentration: 100 mM, T = 50°C).

In order for the isomerization products to be formed, ruthenium hydride species must first be generated, for which ethylene is required. Three different stages of microreactor performance can be distinguished. In the first stage (up to 100 minutes), a higher conversion is present, as the catalyst is still mostly active, which also leads to the formation of a large amount of ethylene. Because of the high local ethylene concentration, the ruthenium hydride species can also form very well. Therefore, more and more isomers are generated during this stage and the selectivity decreases until it reaches a plateau at about 100 minutes. At this point, the second stage from 100 to 145 minutes begins, in which enough ethylene is formed to allow formation of new ruthenium hydride species and selectivity therefore does not change over a longer period of time. The observed plateau can be described as a steady-state between the formation and decomposition of the ruthenium hydride species. After the plateau, the third stage (140 to 200 minutes) of microreactor performance begins. In this third stage, the deactivation of the catalyst has progressed, whereby conversion has decreased and thus the local concentration of ethylene is also significantly lower. As a result, the formation of additional ruthenium hydride species becomes slower than their decomposition and the selectivity begins to increase again.
The employed 2D-LC/MS setup allows to display these stages with high resolution, which on the other hand would not have been possible using ^{1}H NMR due to the overlapping signals. In addition, the combination of continuous-flow chemistry with the automated analysis of all compounds allows these measurement points to be recorded in a very short time. By contrast, in an overnight batch experiment, the presence of these different stages of microreactor performance would have been obscured, and it would be much more time-consuming to generate all points individually via batch operation. In addition, it has to be ensured that the solutions can be well quenched at different points in order to assign reaction times sufficiently discrete.

5.2.5 Conclusion

We were able to show that the 2D-LC/MS setup used in this work is an excellent analytical tool for elucidating reaction mechanisms of complex systems for which conventional approaches based on, e.g., ^{1}H NMR analysis would be insufficient. The 2D-LC/MS setup made it possible to study reaction mechanisms of isomerization in olefin metathesis and to show which by-products are formed (and also, under which conditions they are formed preferentially). In addition, several distinct performance stages of a microreactor operating with the 2nd-generation Grubbs–Hoveyda catalyst immobilized inside mesoporous silica particles were resolved and shown to produce different selectivities with respect to RCM and isomerization. We demonstrated that deactivation of the catalyst has a strong influence not only on conversion, but also on the selectivity of olefin metathesis and that more attention should be devoted to the deactivation of the catalyst.

5.2.6 Experimental

Chemicals and materials: The synthesis and immobilization of the 2nd-generation Grubbs–Hoveyda catalyst were accomplished as described in our previous work.[12] Detailed information on chemicals used and the produced compounds can be found in the Supporting Information (Section 5.3.1 and 5.3.5).

Microreactor preparation: Packing of the microreactor (Figure 5.4) was conducted in the same manner as described previously.[12]

Microreactor operation: RCM reactions under continuous flow were performed by implementing commercially available HPLC instrumentation (1260 and 1290 Infinity II series, Agilent Technologies) as depicted in Figure 5.2. Substrate solution (25, 50, 100 and 250 mM of **1** in degassed, absolute cyclohexane) and degassed, absolute cyclohexane (both under nitrogen gas atmosphere) were connected to a binary pump (Figure 5.2, (4)) via a septum and metal capillary. Substrate solution was pumped at various flow rates (0.01–0.14 mL min^{-1}) through the microreactor placed in a thermostatted compartment (T = 50°C, Figure 5.2, (9)). The reaction solution from the microreactor passed an in-line DAD (Figure 5.2, (10)) and was transferred by a valve (Figure 5.2, (5)) to the second (analytical) dimension. There, the reaction mixture was separated on a reversed-phase liquid chromatography column (Figure 5.2, (8)) and analyzed with an on-line DAD (Figure 5.2, (7)) and ESI-MS (Figure 5.2, (12)).

Reaction monitoring: Conversion and selectivity were quantified through external calibration. For offline analysis, the effluent was collected by a fraction collector and the solvent was removed. Further information on the experimental setup and calibration is provided in the Supporting Information (Section 5.3.2 and 5.3.3).

Structure elucidation: For relevant compounds (diene **1**, isomers **5** and **7**, and MMCs **2** and **4**), ^{1}H and ^{13}C NMR spectra as well as 2D spectra (^{1}H-^{13}C HSQC and ^{1}H-^{1}H DQF-COSY) were recorded. These spectra as well as an exact assignment of the signals are summarized in the Supporting Information (Section 5.3.6).

5.3 Supporting Information

5.3.1 Materials

11-Bromo-1-undecene was received from Sigma–Aldrich (St. Louis, MO) with a purity of 95%. *N*,*N*-Dimethylformmide (DMF) was received from Sigma–Aldrich (St. Louis, MO) with a purity of 99.8 %. Cyclohexane (absolute) was received from Alfa Aesar (Kandel, Deutschland). Acetone (for HPLC) was received from VWR Chemicals (Darmstadt, Germany). All other chemicals were received from Sigma–Aldrich (St. Louis, MO) with a purity of >99%. All chemicals were used as received, without further purification. Isopropanol and water were used for the HPLC Separations. Isopropanol (for HPLC) was received from Sigma-Aldrich (St. Louis, MO). Water was obtained from a Milli–Q gradient purification system (Millipore, Bedford, MA).

5.3.2 Reaction setup

An HPLC system from Agilent Technologies (Santa Clara, CA) was used both for reaction control and analysis. Figure 5.S1 repeats Figure 5.2 for easy reference of the description below.

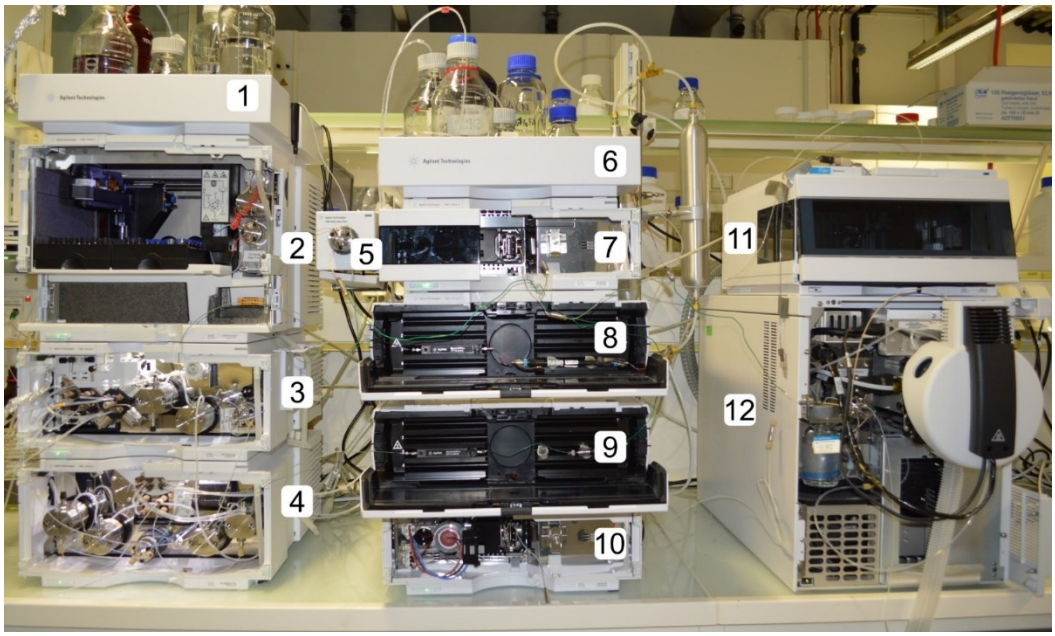

Figure 5.S1.
Two-dimensional continuous-flow platform for coupled reaction–separation/analysis.
Hardware components used for the reaction: 1) Substrate solutions; 4) binary pump for reaction control (Agilent 1290 Infinity II Series, G7120A); 5) 2-position/6-port valve (Agilent 1290 Infinity Series, G1170A); 9) thermostatted HPLC column compartment with reactor (Agilent 1290 Infinity II Series, G7116B); 10) inline DAD (Agilent 1260 Infinity II Series, G7115A).
Hardware components used for analysis: 2) autosampler (Agilent 1290 Infinity II Series, G7129B); 3) quaternary pump for analytics (Agilent 1290 Infinity II Series, G7104A); 6) eluents; 7) online DAD (Agilent 1260 Infinity II Series, G7115A); 8) thermostatted HPLC column compartment with C-8-column (Agilent 1290 Infinity II Series, G7116B); 11) fraction collector (Agilent 1260 Infinity II Series, G1364E); 12) ESI-MS (Agilent 6150 Quadrupole LC/MS, G6150B).

The HPLC pumps allow a precise control of the volumetric flow rate and, thus, of the residence and reaction times. In addition, the substrate solution can be diluted with another cyclohexane solution by the pumps to adjust the starting concentration of the substrate in the reactor. The thermostatted HPLC column compartment (Figure 5.S1, (8)) was used to precisely set and hold the temperature of the reactor. Furthermore, the product solutions can be analyzed and yields as well as selectivities determined online. To make this possible, the chromatographic separation procedure of the online-coupled analytical HPLC system had been optimized so that all reactants, additives, products and by-products became baseline separated in the shortest possible analysis time. All separations carried out for the determination of yields and selectivities were performed at 25°C on a reversed-phase separation column (Eclipse Plus C8; 5 µm-sized particles, 4.6 mm i.d. x 100 mm length) from Agilent Technologies (Santa Clara, CA) through isocratic elution using a mixture of water (+0.1% trifluoroacetic acid, 30 vol %) and isopropanol (70 vol %) as the eluents.

The online separation of the reaction solution was performed with very small amounts of the compounds, sufficient for quantification with the diode-array detector (DAD, Figure 5.S1, (7)). However, these small amounts are not sufficient to clearly identify all the different compounds in NMR experiments. For this purpose, separate experiments were carried out in batch to specifically produce the respective isomers. More detailed information on the reaction procedure can be found in Section 5.3.5. To allow the injection of a larger volume (from 2.57 to 450 µL), the loop attached to the 2-position/6-port valve (Figure 5.S1, (5)) was replaced. In addition, the analytical separation column was exchanged by a semi-preparative separation column (ZORBAX C8, 5 µm-sized particles, 9.4 mm i.d. x 250 mm length). Pulse injection was not possible with the semi-preparative column, because 450 µL were injected and high flow rates could not be realized due to the high backpressure. To avoid extreme band broadening, a high water content of the eluent (90 vol %) was selected at the beginning of the separation to concentrate the analytes at the top of the column during injection. Subsequently, the fraction of isopropanol was increased to 75 vol % to allow a separation within 90 minutes. Table 5.S1 summarizes the gradient developed for the separation with the semi-preparative column.

Table 5.S1. Elution gradient used for the separation of the reaction mixture with the semi-preparative column (flow rate: 1.2 mL min^{-1}).

Time (min)	Water (vol %)	Isopropanol (vol %)
0.00*	90	10
2.50	90	10
2.51	25	75
90.00	25	75

*Point of injection.

The separation was repeated several times and the analytes were collected using a fraction collector until enough substance for identification by NMR was available.

5.3.3 Calibration

Calibration curves were needed for quantification of the respective compounds based on their chromatographic peaks (Figure 5.S2–5.S6). For the calibration solutions, the compounds obtained by separation on the semi-preparative column were used. In order to keep the amount of substance required for calibration as low as possible, the calibration was carried out using an autosampler. For this purpose, a 1 mL solution of each substance was prepared in cyclohexane. The sample volume to be injected with the autosampler was then varied and the amount of substance related to the volume of the loop (2.57 µL) to cover the different possible amounts of substances during the reactor screening.

The separation conditions for the HPLC system of the calibration corresponded to the isocratic separation condition in the reactor screening. Double-determinations were performed for each point. Data points for the calibration curves were taken from the area of a chromatographic peak at a given detection wavelength and a given injection volume of the autosampler. All compounds demonstrated a linear behavior over the calibrated range.

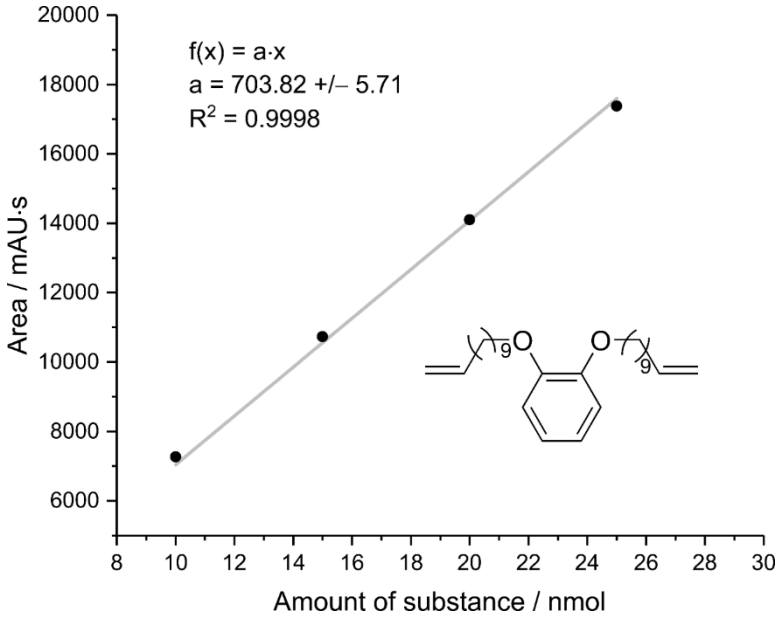

Figure 5.S2. Calibration curve of the substrate 1,2-bis(undec-10-enyloxy)benzene **1** at a detection wavelength of 208 nm.

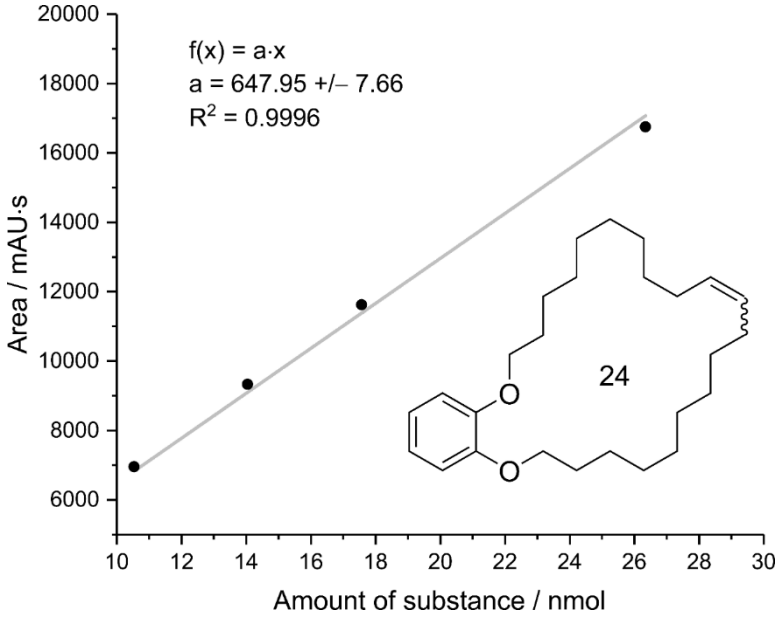

Figure 5.S3. Calibration curve of the monomacrocycle **2** at a detection wavelength of 208 nm.

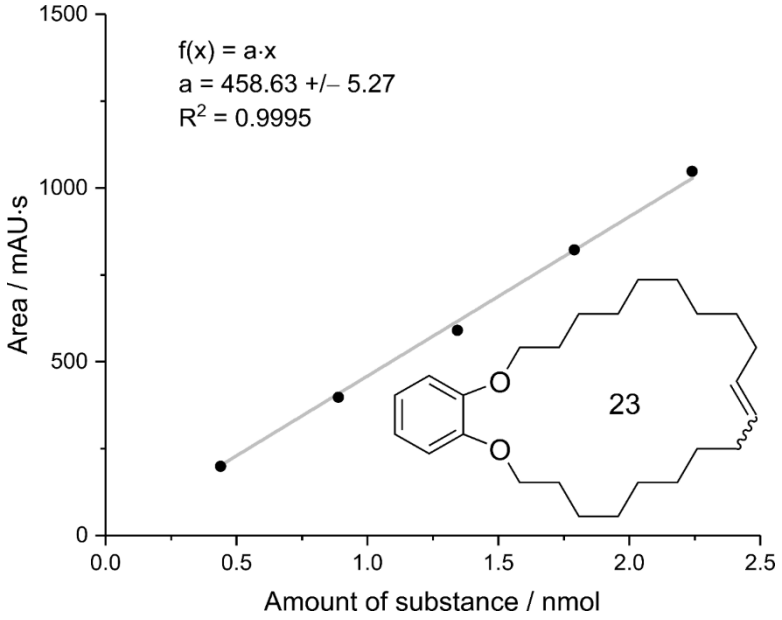

Figure 5.S4. Calibration curve of the monomacrocycle **4** at a detection wavelength of 208 nm.

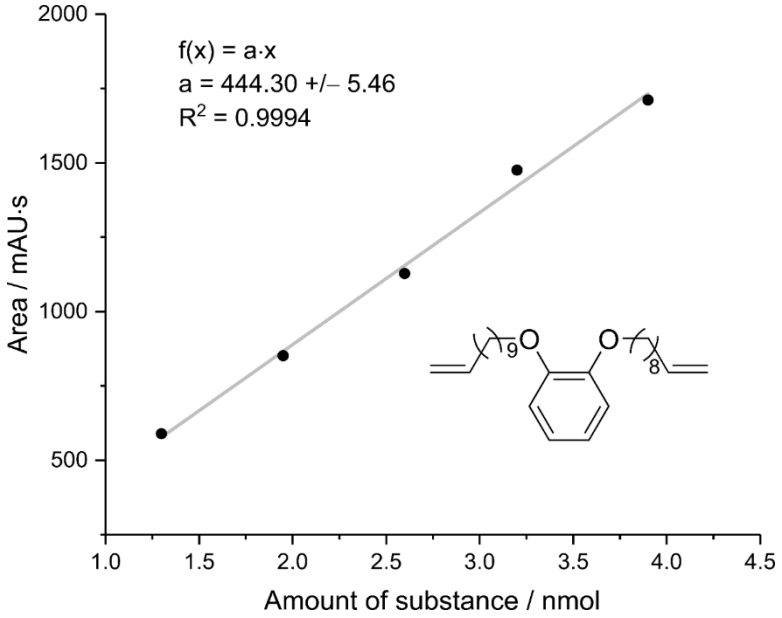

Figure 5.S5. Calibration curve of the diene **5** at a detection wavelength of 208 nm.

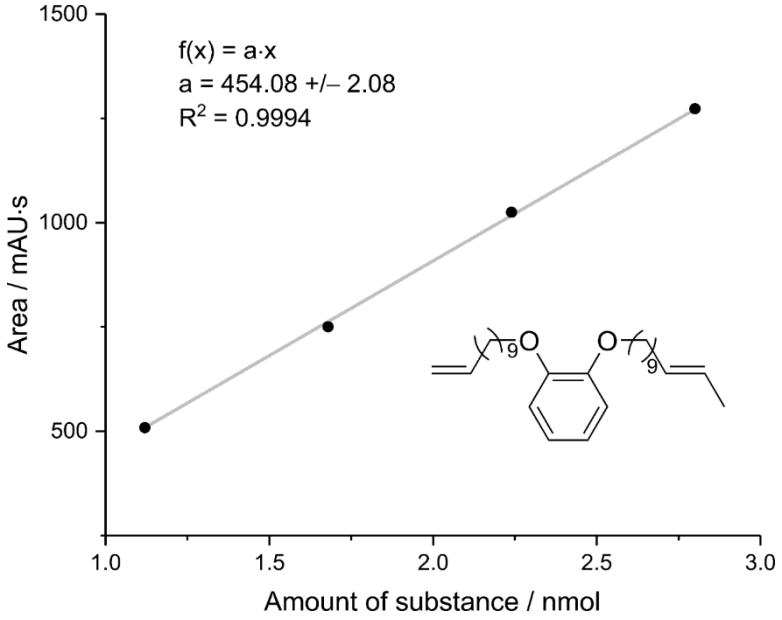

Figure 5.S6. Calibration curve of the diene **7** at a detection wavelength of 208 nm.

5.3.4 Problems with the determination of conversion and selectivity by ^{1}H NMR

It is common practice to determine conversion and selectivity in olefin metathesis through ^{1}H NMR analysis. However, problems often occur because the signals of the products overlap with the signals of typical by-products and thus their ratio cannot be determined exactly. This is illustrated by Figure 5.S7. In order to determine the conversion of a reaction or selectivities of several compounds among each other by ^{1}H NMR, at least one signal of each compound is needed that does not overlap with any other compound.

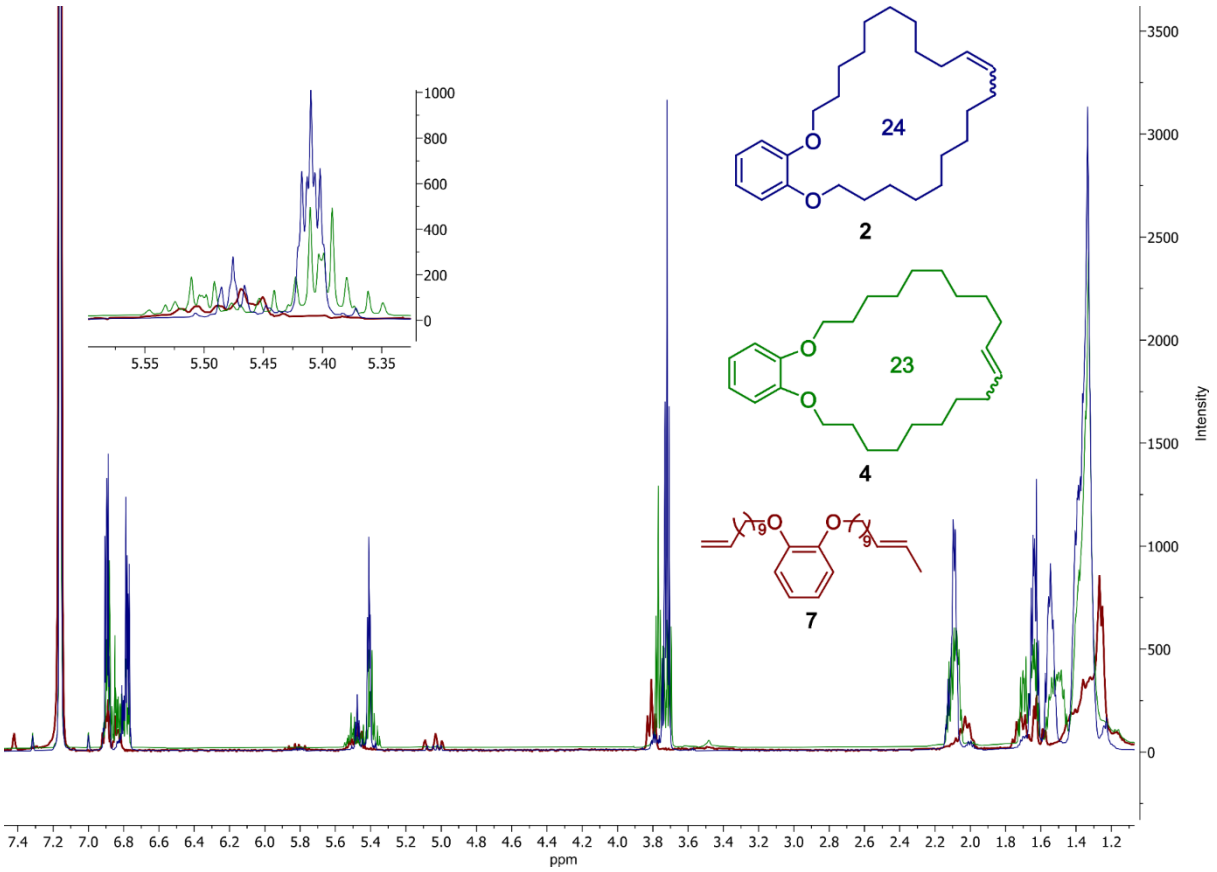

Figure 5.S7. Superimposed ^{1}H NMR spectra of the monomacrocycle **2** and by-products **4** and **7**.

However, there is often no signal available that does not overlap with the signal of a side compound, because the compounds are quite similar. In this case, clean signals are only present for the diene **7** (in the range 5.9–5.7 ppm and 5.2–4.9 ppm). However, for the desired product **4**, neither conversion nor selectivities would be determined accurately. The method presented in the paper using a HPLC system and external calibration is therefore much more suitable for this purpose.

Figure 5.S8 shows a reaction mixture from olefin metathesis.

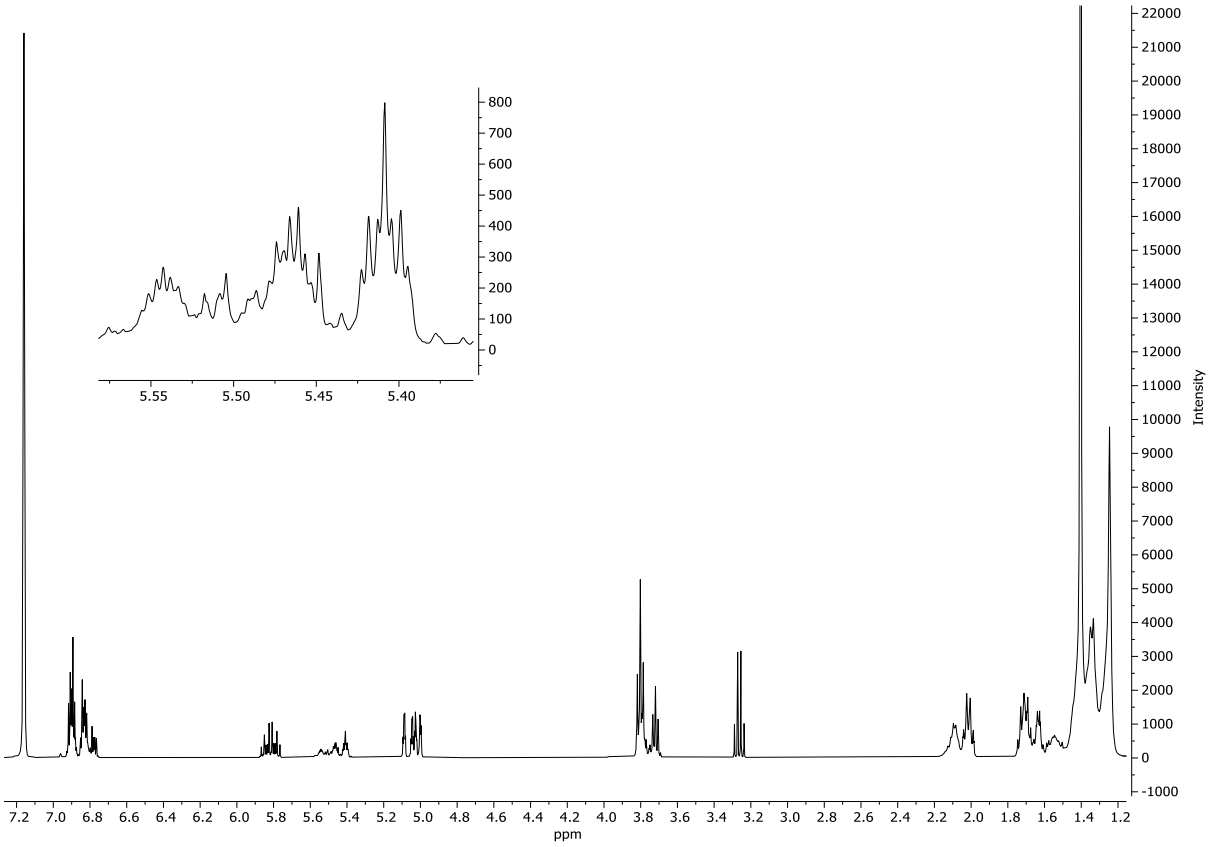

Figure 5.S8. ^{1}H NMR spectrum of a reaction mixture from olefin metathesis conducted under spatial confinement within the modified silica particles at 50°C.

Here, it becomes evident that only the *E*-isomer of the product can be cleanly identified in the range 5.43–5.37 ppm, although it also overlaps with by-product **4**. For the determination of conversion or selectivities, however, the signal of the *Z*-isomer is also necessary. The signal is expected in the range between 5.49 and 5.44 ppm, but cannot be detected due to the by-products. Therefore, quantification by ^{1}H NMR is not suitable and quantification with the implemented HPLC system shows distinct advantages.

5.3.5 Synthesis

General procedure for the synthesis of the isomers (GP 1)

1: The substrate (**1**, 25 µmol) was dissolved in acetone (1 mL) and the solution was heated to 50 °C. The Grubbs-Hoveyda catalyst (**6**, 1.1 mg, 5 mol%) was added and the reaction solution stirred for 18 hours at 50 °C. Afterwards, the same amount of Grubbs-Hoveyda catalyst (**6**, 1.1 mg, 5 mol%) was added and the solution stirred for another 3 hours. Grubbs-Hoveyda catalyst (**6**, 1.1 mg, 5 mol%) was added for a third time and the solution was stirred for another 18 h. The reaction solution was then allowed to cool to room temperature and filtered using a syringe filter (Sartorius RC 0.20 µm), before being injected onto the semi-preparative chromatographic separation column. The separation was performed using the gradient from Table 5.S1. Achieved baseline separation of the compounds is shown in Figure 5.S9.

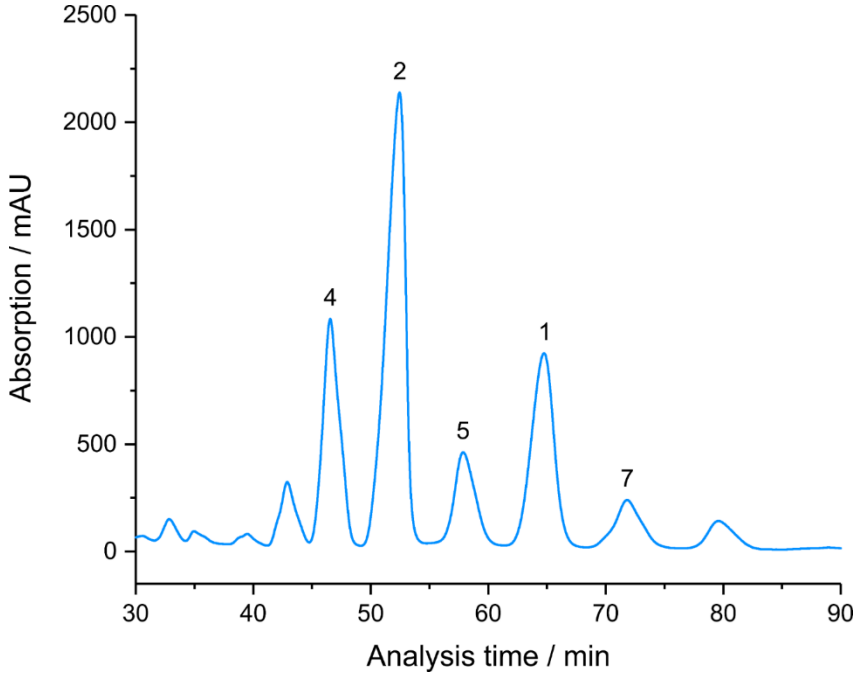

Figure 5.S9. Compounds elute in the following order: monomacrocycle **4** (46.6 min), monomacrocycle **2** (52.5 min), diene **5** (57.9 min), diene **1** (64.7 min), and diene **7** (71.8 min). The detection wavelength of the DAD was 208 nm.

Synthesis of 1,2-bis(undec-10-enyloxy)benzene (1)

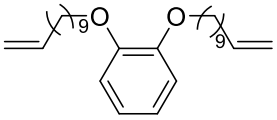

1 was prepared according to the literature.[S1] 1,2-Benzenediol (2.0 g, 18.2 mmol) was dissolved in DMF (100 mL) and NaOH (3.0 g, 75.0 mmol) as well as 11-bromo-1-undecene (12.0 g, 51.5 mmol) were added. The solution was stirred at 40 °C for 16 hours. Afterwards, H_2O (100 mL) and diethyl ether (100 mL) were added and the aqueous and organic phases were separated. The aqueous layer was extracted with diethyl ether (200 mL) and the combined organic layers were washed with brine, dried over magnesium sulfate and concentrated under reduced pressure. Purification by column liquid chromatography over silica gel (*n*-pentane/diethylether 20:1) yielded **1** as colorless solid (6.0 g, 14.6 mmol, 80%). The NMR spectroscopic data were in accordance with those reported in the literature.[S1] **1H NMR** (500 MHz, benzene-d_6) δ = 6.92–6.89 (m, 2H), 6.85–6.81 (m, 2H), 5.82 (ddt, J = 17.1, 10.3, 6.7 Hz, 2H), 5.07 (dq, J = 17.5, 1.6 Hz) and 5.01 (ddt, J = 10.2, 2.2, 1.1 Hz, 4H), 3.80 (t, J = 6.4 Hz, 4H), 2.01 (qt, J = 7.2 1.4 Hz, 4H), 1.70 (qu, J = 7.0 Hz, 4H), 1.43 (qu, J =7.2 Hz, 4H), 1.35 (qu, J = 6.6 Hz, 4H), 1.28–1.24 (m, 16H). **^{13}C NMR** (126 MHz, benzene-d_6) δ = 150.20 (2C), 139.28 (2C), 121.32 (2C), 114.55 (2C), 114.48 (2C), 69.14 (2C), 34.27 (2C), 30.03 (2C), 29.93 (2C), 29.90 (2C), 29.84 (2C), 29.57 (2C), 29.39 (2C), 26.56 (2C). **APCI (HR-MS)** calcd. for $C_{28}H_{47}O_2$: 415.3571; found 415.3565.

Synthesis of 2,3,4,5,6,7,8,9,10,13,14,15,16,17,18,19,20,21-octadecahydrobenzo[*b*][1,4]dioxacyclotetracosine (2)

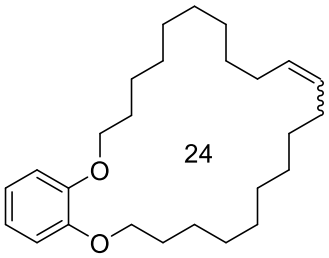

Compound **2** was prepared according to GP 1. Purification by column liquid chromatography (ZORBAX C8, 5 µm, 9.4 x 250 mm) yielded **2** as colorless oil (retention time: 52.5 min). The yield was determined through HPLC analysis, using the peak area measured by the DAD at an absorbance wavelength of 208 nm. The NMR spectroscopic data were in accordance with those reported in the literature.[S1] **^{1}H NMR** (79:21 *E*/*Z*-ratio, 500 MHz, benzene-d_6) The signal marked with * belong to the (*E*)-isomer exclusively. δ = 6.93–6.87 (m, 2H), 6.82–6.75 (m, 2H), 5.47 (td, *J* = 4.7, 2.3 Hz, 0.37H), 5.41* (td, *J* = 3.9, 2.0 Hz, 1.43H), 3.72 (t, *J* = 5.8 Hz, 4H), 2.17–2.03 (m, 4H), 1.73–1.59 (m, 4H), 1.59–1.48 (m, 4H), 1.47–1.17 (m, 20H). **^{13}C NMR** (126 MHz, benzene-d_6) Signals marked with * belong to the (*E*)-isomer exclusively. δ = 150.34 (2C), 150.15* (2C), 131.30* (2C), 130.54 (2C), 121.37 (2C), 121.11* (2C), 114.58 (2C), 113.83* (2C), 69.26 (2C), 68.84* (2C), 32.61* (2C), 30.60* (2C), 30.56 (2C), 30.26 (2C), 30.22* (2C), 30.16* (2C), 30.14 (2C), 30.12 (2C), 30.10* (2C), 29.82 (2C), 29.51 (2C), 29.48* (2C), 28.86* (2C), 27.39 (2C), 27.23 (2C), 27.13* (2C). **APCI (HR-MS)** calcd. for $C_{26}H_{43}O_2$: 387.3258; found 387.3251.

Synthesis of 3,4,5,6,7,8,9,10,13,14,15,16,17,18,19,20-hexadecahydro-2*H*-benzo[*b*][1,4]dioxacyclotricosine (4)

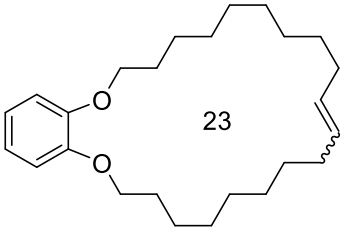

Compound 4 was prepared according to GP 1. Purification by column liquid chromatography (ZORBAX C8, 5 µm, 9.4 x 250 mm) yielded **4** as colorless oil (retention time: 46.6 min). The yield was determined through HPLC analysis, using the peak area measured by the DAD at an absorbance wavelength of 208 nm. **^{1}H NMR** (73:27 *E*/*Z*-ratio, 500 MHz, benzene-d_6) The signal marked with * belong to the (*E*)-isomer exclusively. δ = 6.92–6.75 (m, 4H), 5.55–5.46 (m, 0.51H), 5.46–5.34 (m, 1.33 H), 3.77 (t, *J* = 6.2 Hz, 2H), 3.71 (t, *J* = 5.8 Hz, 2H), 2.15–2.03 (m, 4H), 1.74–1.59 (m, 4H), 1.58–1.44 (m, 4H), 1.41–1.29 (m, 18H). **^{13}C NMR** (126 MHz, benzene-d_6) Signals marked with * belong to the (*E*)-isomer exclusively. δ = 150.66*, 150.42, 150.36, 150.35*, 131.46*, 131.10*, 130.61, 130.29, 121.68*, 121.47, 121.43, 121.31*, 115.65*, 114.89, 114.73, 114.36*, 69.83*, 69.30, 69.28, 69.01*, 32.56*, 32.40*, 30.43*, 30.31*, 30.29, 30.22*, 30.15*, 30.11, 30.07*, 30.04*, 30.02, 29.92*, 29.88, 29.60*, 29.44, 29.40, 29.31, 29.08, 28.94*, 28.60*, 28.40*, 27.20, 27.11, 27.03, 26.99*, 26.79, 26.64*. Three signals from the lower concentrated (*E*)-isomer could not be clearly resolved, but are expected in the range of 30.5 to 28.3. **ESI (HR-MS)** calcd. for $C_{25}H_{41}O_2$: 373.3101; found 373.3093.

Synthesis of 1-(dec-9-en-1-yloxy)-2-(undec-10-en-1yloxy)benzene (5)

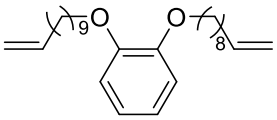

Compound **5** was prepared according to GP 1. Purification by column liquid chromatography (ZORBAX C8, 5 µm, 9.4 x 250 mm) yielded **5** as a colorless oil (Retention time: 57.9 min). The yield was determined through HPLC analysis, using the peak area measured by the DAD at an absorbance wavelength of 208 nm. **^{1}H NMR** (300 MHz, benzene-d_6) δ = 6.96–6.77 (m, 4H), 5.82 (ddt, J = 17.0, 10.2, 6.7 Hz, 1H), 5.81 (ddt, J = 17.0, 10.2, 6.7 Hz, 1H), 5.07 (dq, J = 17.5, 1.6 Hz) and 5.02 (dt, J = 10.2, 1.1 Hz, 2H), 5.06 (dq, J = 17.5, 1.6 Hz) and 5.01 (dt, J = 10.1, 1.0 Hz, 2H), 3.80 (t, J = 6.4 Hz, 2H), 3.79 (t, J = 6.4 Hz, 2H), 2.16–1.91 (m, 4H), 1.78–1.59 (m, 4H), 1.46–1.39 (m, 4H), 1.37–1.31 (m, 4H), 1.27–1.08 (m, 14 H). **^{13}C NMR** (126 MHz, benzene-d_6) δ = 150.20 (2C), 139.28 (2C), 121.32 (2C), 114.55 (2C), 114.49 (2C), 69.14 (2C), 34.26 (2C), 30.03, 29.93, 29.91, 29.90 (2C), 29.84, 29.78, 29.57, 29.50, 29.39, 29.37, 26.56, 26.54. **ESI (HR-MS)** calcd. for $C_{27}H_{44}O_2Na_1$: 423.3234; found 423.3225.

Synthesis of 1-(dodec-10-en-1-yloxy)-2-(undec-10-en-1-yloxy)benzene (7)

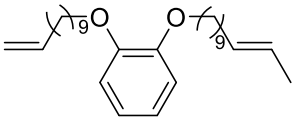

Compound **7** was prepared according to GP 1. Purification by column liquid chromatography (ZORBAX C8, 5 µm, 9.4 x 250 mm) yielded **7** as a colorless oil (retention time: 71.8 min). The yield was determined through HPLC analysis, using the peak area measured by the DAD at an absorbance wavelength of 208 nm. **^{1}H NMR** (500 MHz, DMSO-d_6) δ = 6.92–6.89 (m, 2H), 6.85–6.82 (m, 2H), 5.82 (ddt, J = 17.1, 10.2, 6.8 Hz, 1H), 5.54–5.45 (m, 1H), 5.48–5.40 (m, 1H), 5.07 (dq, J = 17.1, 1.8 Hz) and 5.01 (ddt, 10.2, 2.2, 1.1 Hz, 1H), 3.80 (t, J = 6.5 Hz, 4H), 2.06–2.00 (m, 4H), 1.74–1.67 (m, 4H), 1.63 (d, J = 4.8 Hz, 3H), 1.47–1.39 (m, 4H), 1.39–1.31 (m, 4H), 1.29–1.22 (m, 16H). **^{13}C NMR** (126 MHz, DMSO-d_6) δ = 150.21 (2C), 139.28, 132.00, 124.89, 121.32 (2C), 114.55, 114.50 (2C), 69.15 (2C), 34.27, 33.17, 30.23 (2C), 30.12–29.84 (8C overlap), 29.90 (2C), 26.57, 19.17. **ESI (HR-MS)** calcd. for $C_{29}H_{48}O_2Na_1$: 451.3547; found 451.3543.

5.3.6 NMR spectra

As some compounds (**4**, **5**, **7**) were only generated in small amounts, no more than 1–3 mg of these compounds could be isolated. In order to obtain reliable NMR signals, the isomeric compounds **4**, **5** and **7** were dissolved in 200 µL benzene-d_6 and filled in Wilmad 3 mm tubes (Rototec-Spintec, Bad Wildbad, Germany). Due to the smaller diameter of the NMR tube, it is possible to use less solvent, which means that the concentration of the respective compound is higher and more distinct signals are obtained. The ^{1}H, ^{13}C, ^{1}H-^{1}H DQF-COSY, and ^{1}H-^{13}C HSQC spectra were obtained on a Bruker AVIII 500 spectrometer equipped with a 5 mm cryo BBO probe Prodigy at room temperature (RT). The two-dimensional and the ^{13}C spectra were recorded with 32 to 128 and 64 000 transients, respectively. All spectra were processed using the Bruker program package Topspin 4.0. Chemical shifts are reported in parts per million (ppm) relative to the solvent benzene-d_6 (^{1}H NMR 7.16 ppm; ^{13}C NMR 128.06 ppm). Multiplicities are reported with the following abbreviations: d (doublet), t (triplet), dt (doublet of triplets), ddt (doublet of doublets of triplets), td (triplet of doublets), dq (doublet of quartets), qt (quartet of triplets), qu (quintet), and m (multiplet).

The ^{1}H and ^{13}C NMR signals of the macrocyclic compounds **2** and **4** each showed two sets of resonance peaks, which were assigned to isomers with *E* and *Z* configuration, respectively. Although the ^{1}H signals of the two isomers showed severe overlap, the ^{13}C signals of carbons at position b appeared well separated. Information of the ^{13}C chemical shift of C_b can therefore be used to assign the *E*/*Z* configuration. Because of a stronger steric repulsion in the *Z* configuration, its C_b resonance shows usually a high-field shift.[S2] Therefore, for the monomacrocycle **2**, the two ^{13}C signals observed at 32.61 and 27.39 ppm were assigned to C_b of the *E*- and *Z*-isomer, respectively. Accordingly, in the monomacrocycle **4**, the two signals from the ^{13}C NMR observed at 32.56/32.40 and 27.20/27.11 ppm were assigned to the $C_b/C_{b'}$ of the *E*- and *Z*-isomer, respectively.

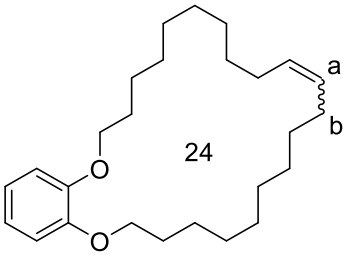

2

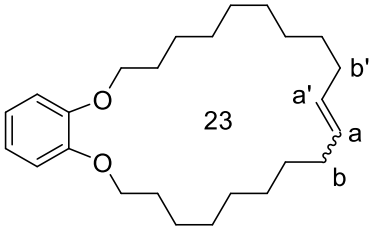

4

Table 5.S2. NMR spectroscopic data (500 MHz, benzene-d_6, RT) of diene **1**.

Position	δ_C	δ_H (*J* in Hz)	COSY
a	114.55	5.07, dq (17.5, 1.6) 5.01, ddt (10.2, 2.2, 1.1)	b
b	139.27	5.82, ddt (17.1, 10.3, 6.7)	a, c
c	34.27	2.01, qt (7.2, 1.4)	b, c1
c1	29.39	1.35, qu (6.6)	c, d
d*	30.03, 29.90 29.84, 29.57	1.28 – 1.24, m	c1, e1
e	29.93	1.70, qu (7.0 Hz)	e1, f
e1	26.56	1.43, qu (7.2)	d, e
f	69.14	3.80, t (6.4)	e
f1	150.20	-	-
g	114.48	6.85 – 6.81, m	h
h	121.32	6.92 – 6.89, m	g

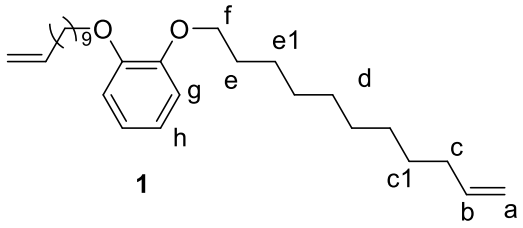

1

*d denotes the central CH_2-groups, which were not well resolved and therefore not fully assigned.

Table 5.S3. NMR spectroscopic data (500 MHz, benzene-d_6, RT) of monomacrocycle **2**. Signals shown in the table belong to the main isomer (*E*)-**2**.

Position	δ_C	δ_H (*J* in Hz)	COSY
a	131.30	5.41, td (3.9, 2.0)	b
b	32.61	2.17 – 2.03, m	a, c
c*	30.60, 30.22, 30.16, 30.10, 28.86	1.47 – 1.17, m	b, e1
e	29.48	1.73 – 1.59, m	e1, f
e1	27.13	1.59 – 1.48, m	c, e
f	68.84	3.72, t (5.8)	e
f1	150.15	-	-
g	113.83	6.82 – 6.75, m	h
h	121.11	6.93 – 6.87, m	g

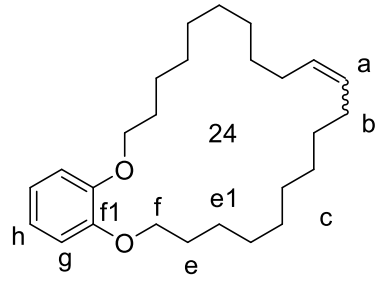

2

*c denotes the central CH_2-groups, which were not well resolved and therefore not fully assigned.

Table 5.S4. NMR spectroscopic data (500 MHz, benzene-d_6, RT) of monomacrocycle **4**. Signals shown in the table belong to the main isomer (*E*)-**4**.

Position	δ_C	δ_H (*J* in Hz)	COSY
a/a'	131.46	5. 46 – 5.34, m	b, b'
a/a'	131.10	5. 46 – 5.34, m	b, b'
b/b'	32.56	2.15 – 2.03, m	a, a', c, c'
b/b'	32.40	2.15 – 2.03, m	a, a', c, c'
c/c'*	30.43, 30.22, 30.15, 30.04, 29.92, 29.60, 28.94, 28.60, 28.40	1.41 – 1.29, m	b, b', e1, e1'
e/e'	30.31	1.74 – 1.59, m	e1, e1', f, f'
e/e'	30.07	1.74 – 1.59, m	e1, e1', f, f'
e1/e1'	26.99	1.58 – 1.44, m	c, c', e, e'
e1/e1'	26.64	1.58 – 1.44, m	c, c', e, e'
f/f'	69.83	3.77, t (6.2)	e, e'
f/f'	69.01	3.71, t (5.8)	e, e'
f1/f1'	150.66	-	-
f1/f1'	150.35	-	-
g/g'	115.65	6.86 – 6.75, m	h, h'
g/g'	114.36	6.86 – 6.75, m	h, h'
h/h'	121.68	6.92 – 6.86, m	g, g'
h/h'	121.31	6.92 – 6.86, m	g, g'

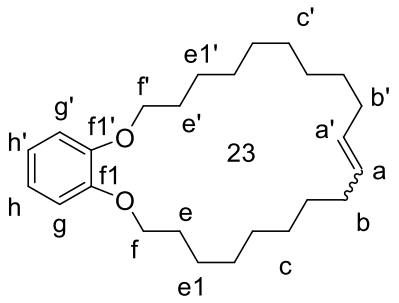

4

*c/c' denotes the central CH_2-groups, which were not well resolved and therefore not fully assigned.

Table 5.S5. NMR spectroscopic data (500 MHz, benzene-d_6, RT) of diene 5.

Position	δ_C	δ_H (J in Hz)	COSY
a/a'	114.55	5.07, dq (17.5, 1.6) 5.02, dt (10.2, 1.1)	b/b'
a/a'	114.55	5.06, dq (17.5, 1.6) 5.01, dt (10.1, 1.0)	b/b'
b/b'	139.28	5.82, ddt (17.0, 10.2, 6.7)	a/a', c
b/b'	139.28	5.81, ddt (17.0, 10.2, 6.7)	a/a', c
c	34.26	2.16 – 1.91, m	a/a', c1
c1/c1'	29.39	1.37 – 1.31, m	c, d
c1/c1'	29.37	1.37 – 1.31, m	c, d
d/d'*	30.03, 29.93 29.91, 29.84 29.78, 29.57 29.50	1.27 – 1.08, m	c1, e1
e	29.90	1.78 – 1.59, m	e1, f/f'
e1/e1'	26.54	1.46 – 1.39, m	d, e
e1/e1'	26.56	1.46 – 1.39, m	d, e
f/f'	69.14	3.80, t (6.4)	e
f/f'	69.14	3.79, t (6.4)	e
f1	150.20	-	-
g	114.49	6.82 – 6.77, m	h
h	121.32	6.96 – 6.89, m	g

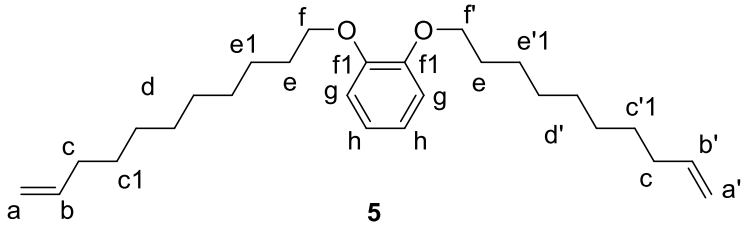

5

*d/d' denotes the central CH_2-groups, which were not well resolved and therefore not fully assigned.

Table 5.S6. NMR spectroscopic data (500 MHz, benzene-d_6, RT) of diene 7.

Position	δ_C	δ_H (*J* in Hz)	COSY
a1	18.17	1.63, d (4.8)	a
a	124.89	5.48 – 5.40 (m)	a1
a'	114.55	5.07, dq (17.1, 1.8) 5.01, ddt (10.2, 2.2, 1.1)	b'
b	132.00	5.54 – 5.45 (m)	c
b'	139.28	5.82, ddt (17.1, 10.2, 6.8)	a'
c	33.17	2.06 – 2.00, m	b, c1
c'	34.27	2.04 – 1.99, m	b', c'1
c1/c1'	30.23	1.39 – 1.31, m	c, d
d/d'*	30.12 – 29.84 (overlap)	1.29 – 1.22, m	c1, e1
e	29.90	1.74 – 1.67, m	e1, f/f'
e1	26.57	1.47 – 1.39, m	d, e
f	69.15	3.80, t (6.5)	e
f1	150.21	-	-
g	114.50	6.85 – 6.82, m	h
h	121.32	6.92 – 6.89, m	g

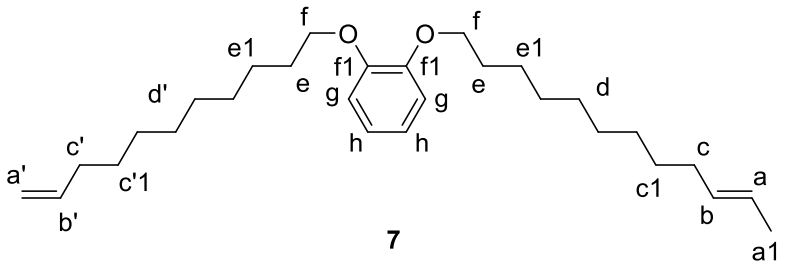

7

*d/d' denotes the central CH_2-groups, which were not well resolved and therefore not fully assigned.

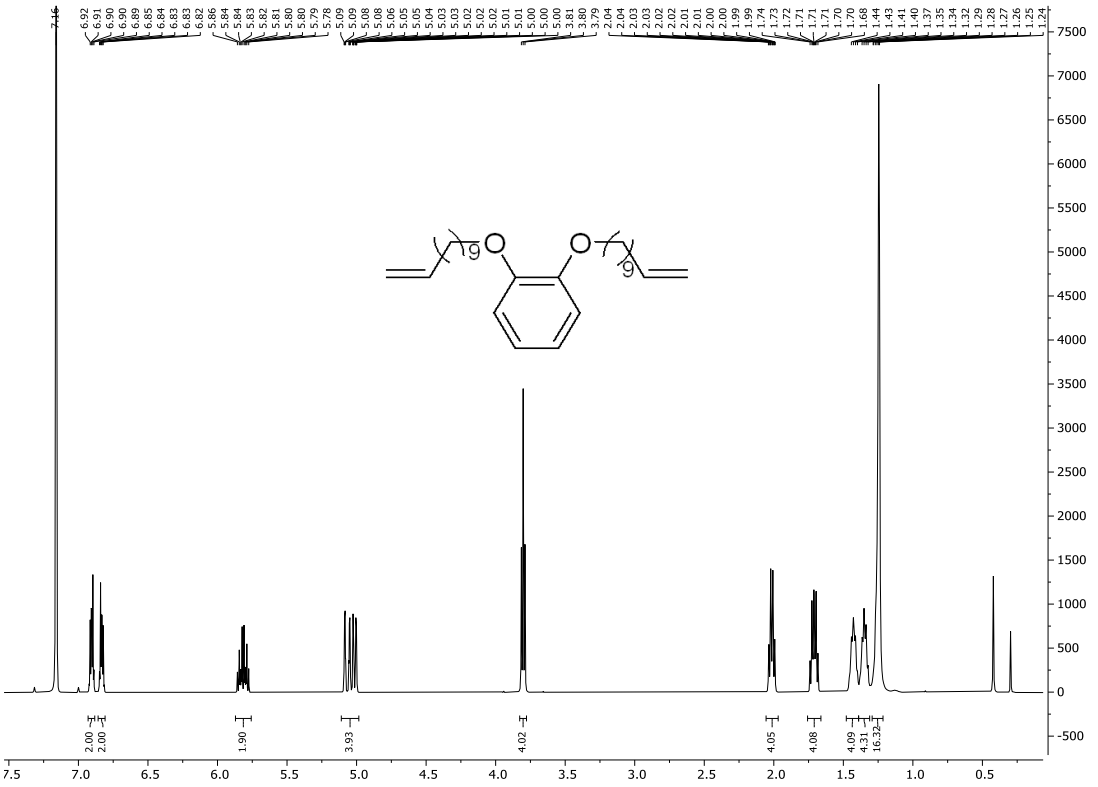

Figure 5.S10. ^{1}H NMR spectrum of **1** in benzene-d_6 at RT (500 MHz).

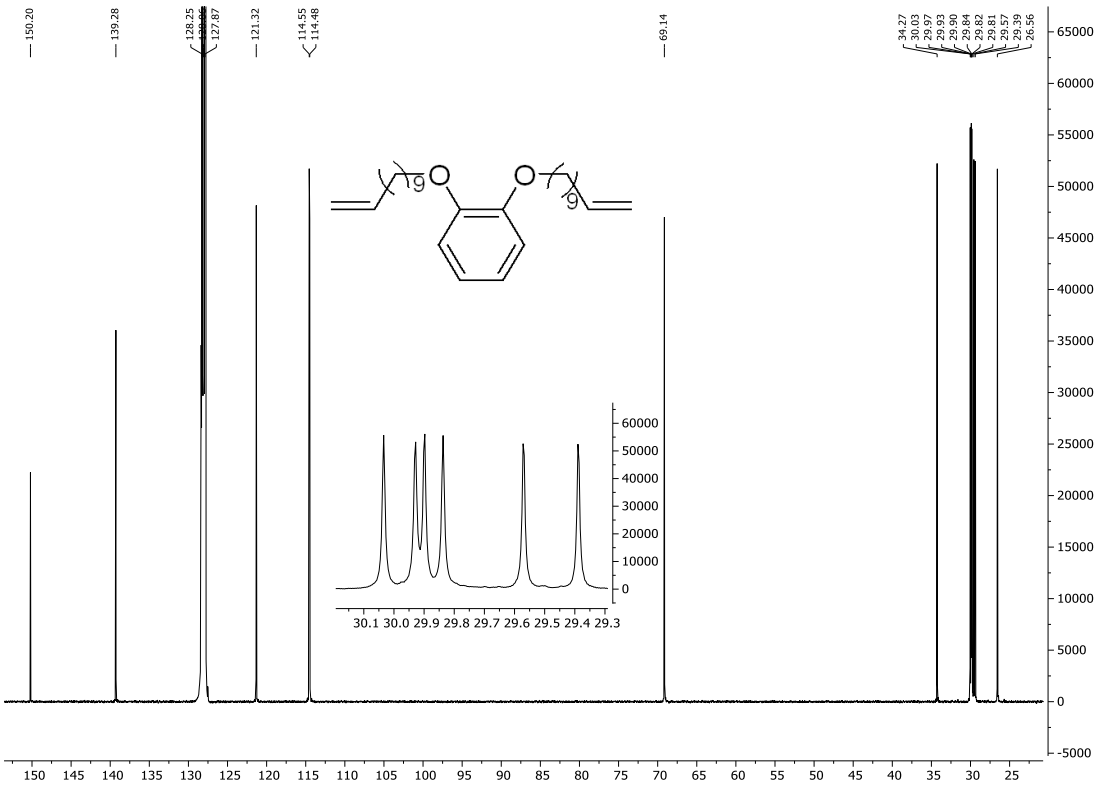

Figure 5.S11. ^{13}C NMR spectrum of **1** in benzene-d_6 at RT (126 MHz).

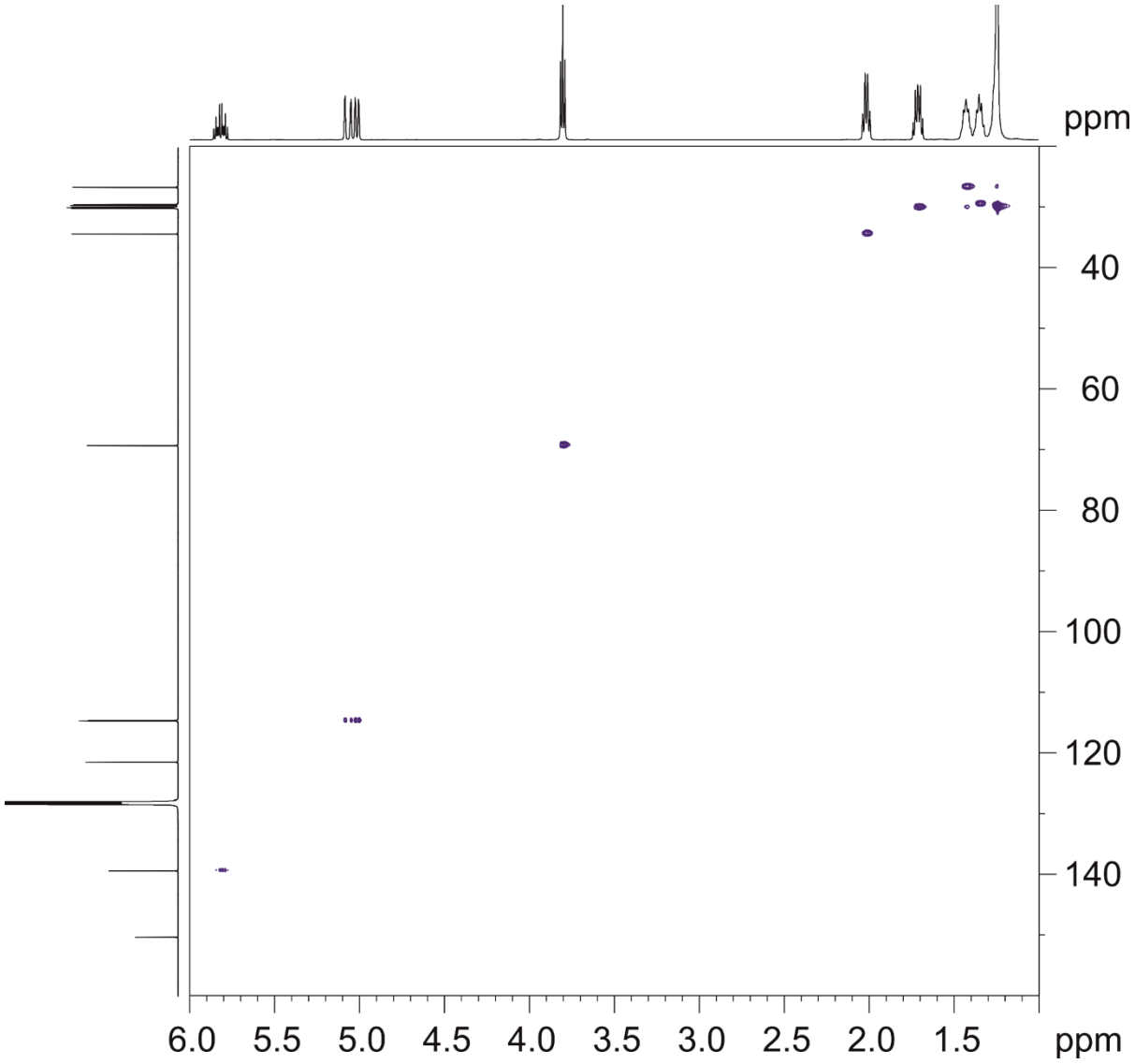

Figure 5.S12. ^{1}H-^{13}C HSQC spectrum of **1** in benzene-d_6 at RT.

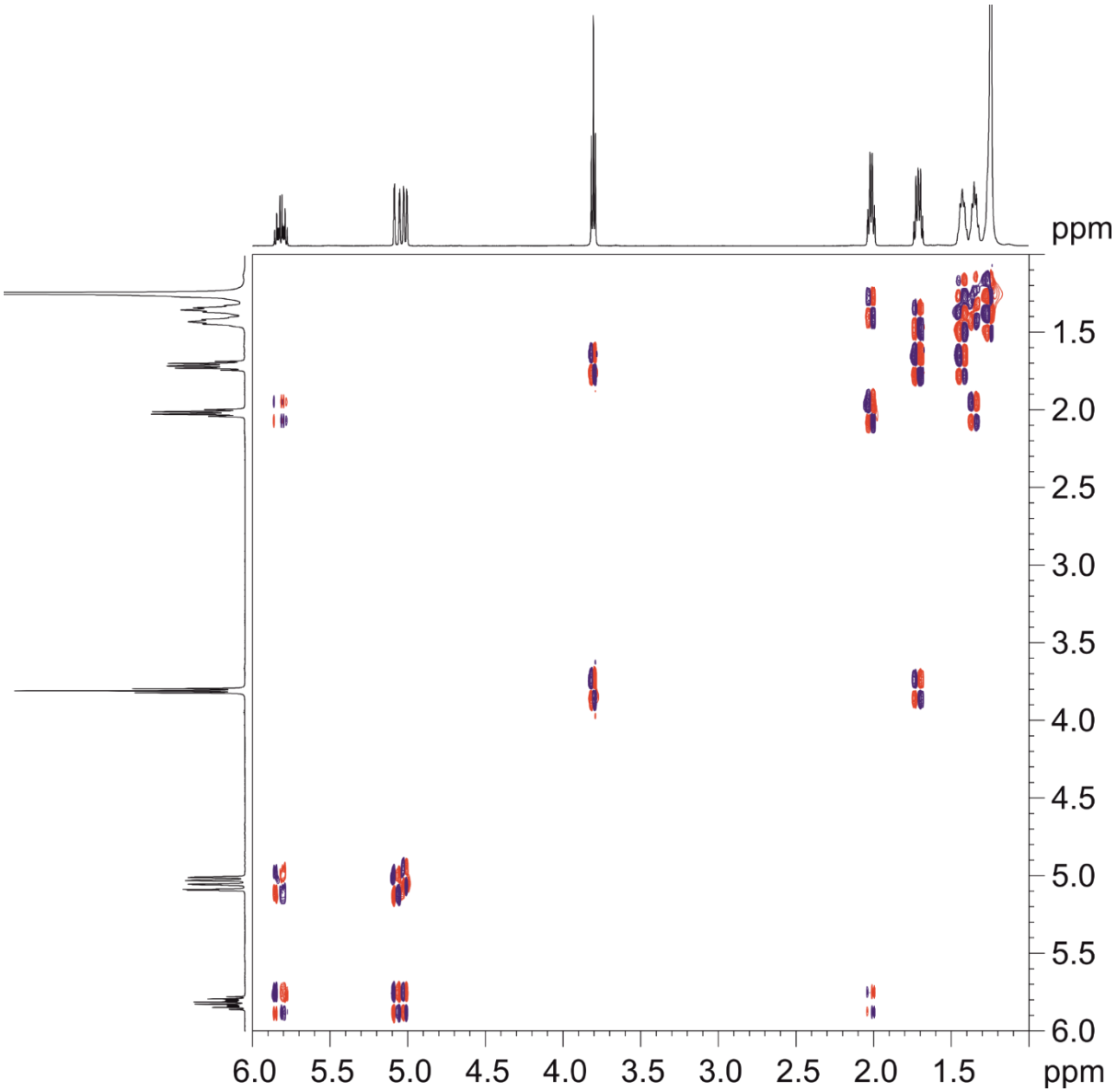

Figure 5.S13. ^{1}H-^{1}H DQF-COSY spectrum of **1** in benzene-d_6 at RT (500 MHz).

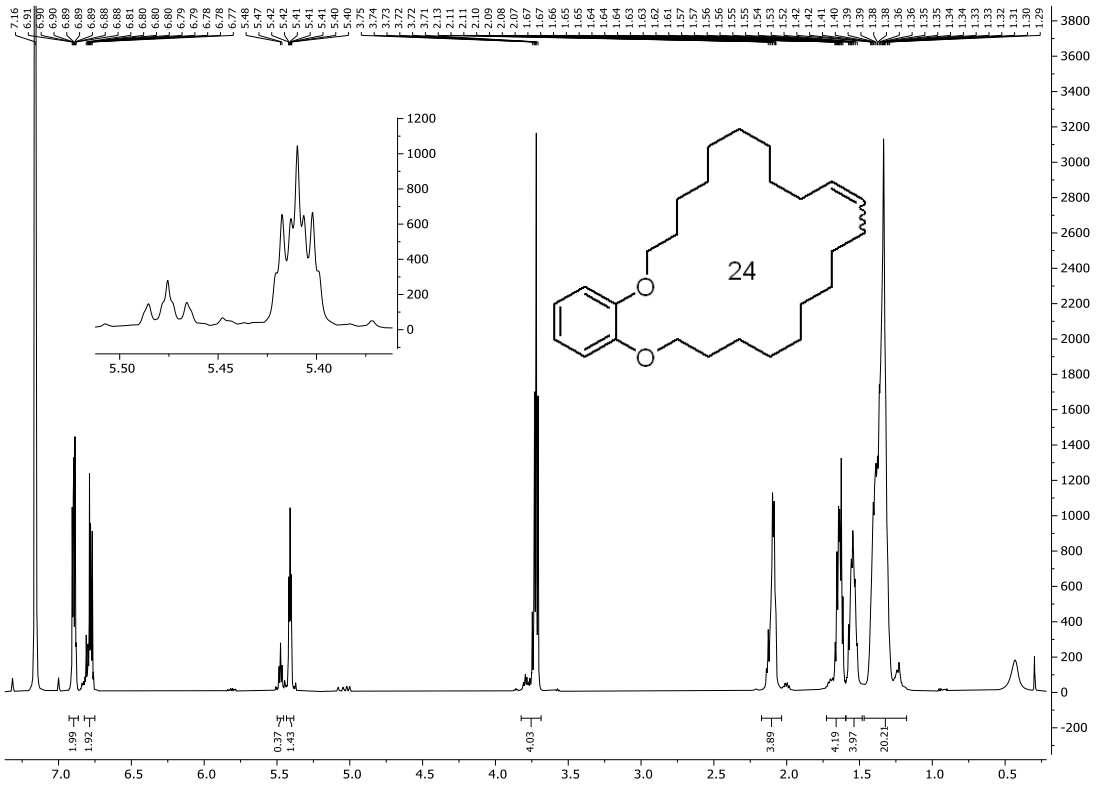

Figure 5.S14. ^{1}H NMR spectrum of **2** in benzene-d_6 at RT (500 MHz).

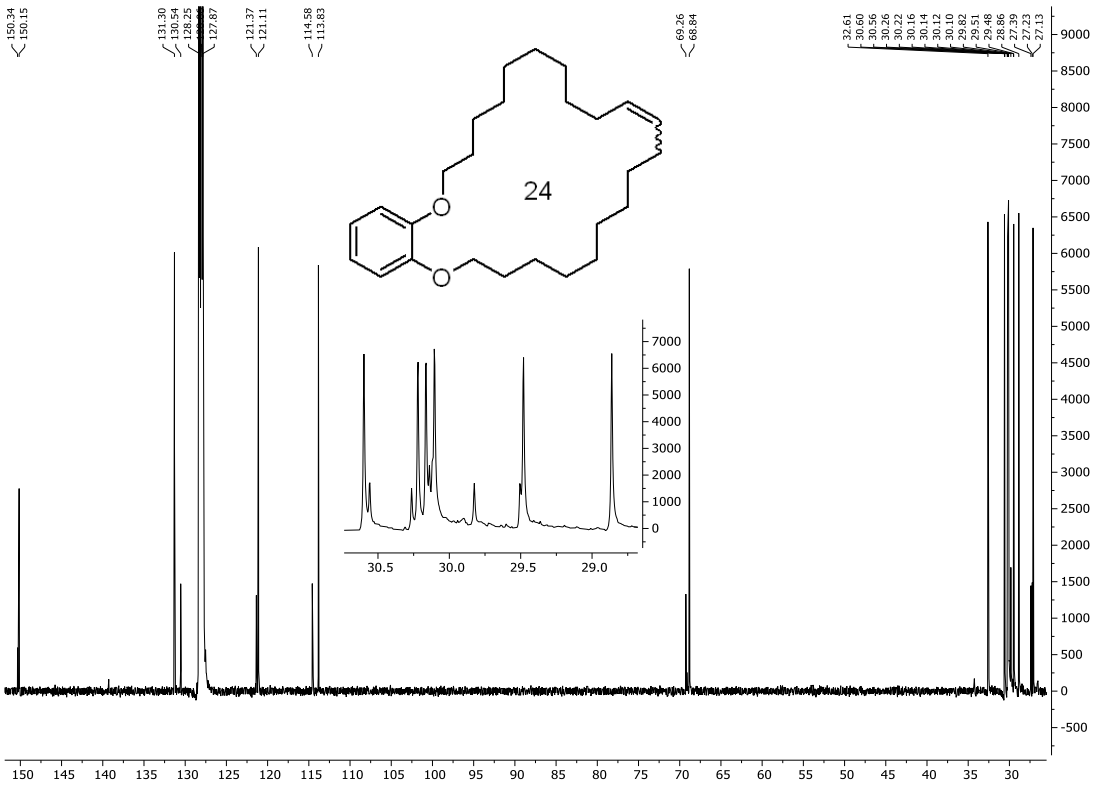

Figure 5.S15. ^{13}C NMR spectrum of **2** in benzene-d_6 at RT (126 MHz).

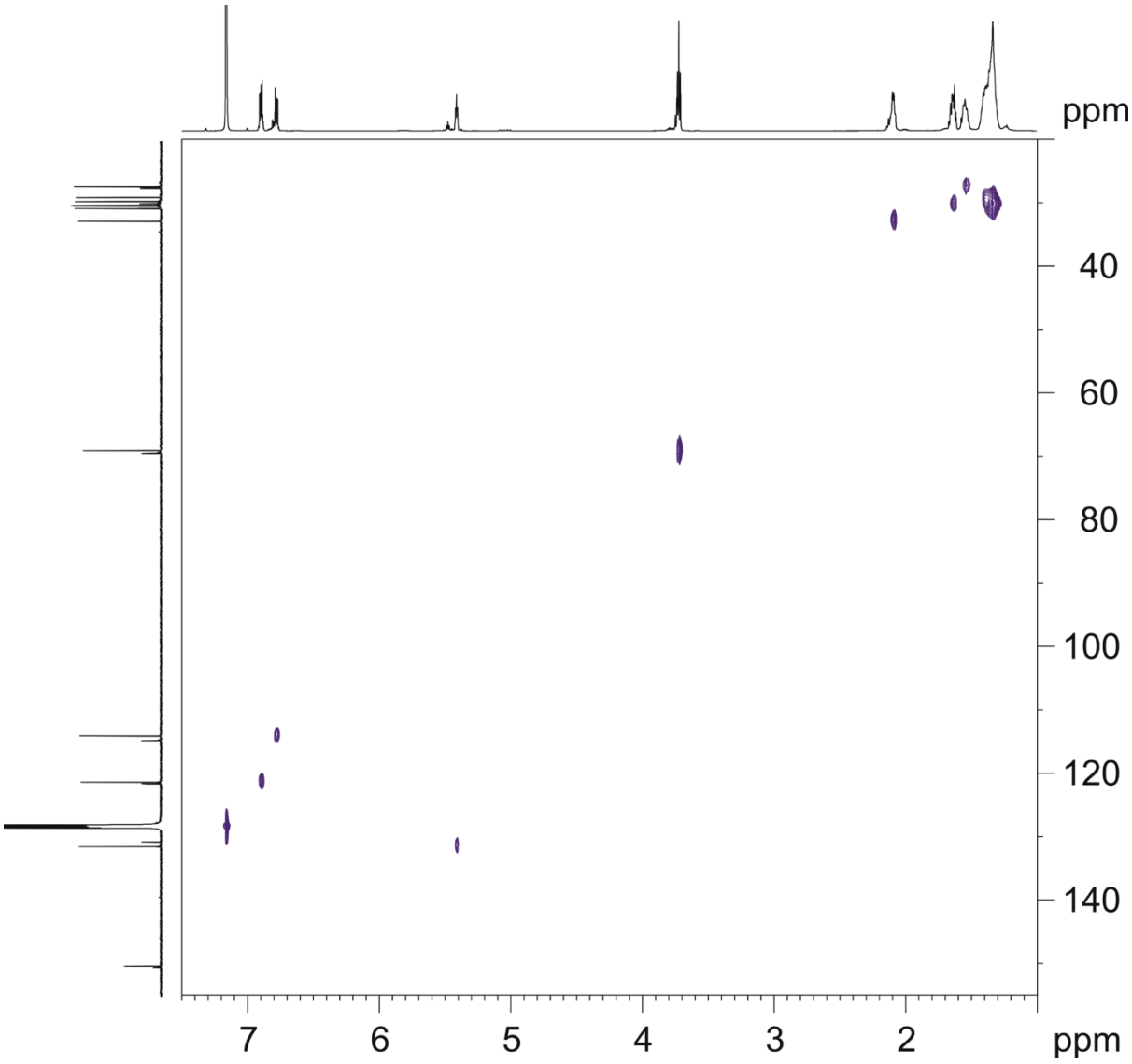

Figure 5.S16. ^{1}H-^{13}C HSQC spectrum of **2** in benzene-d_6 at RT.

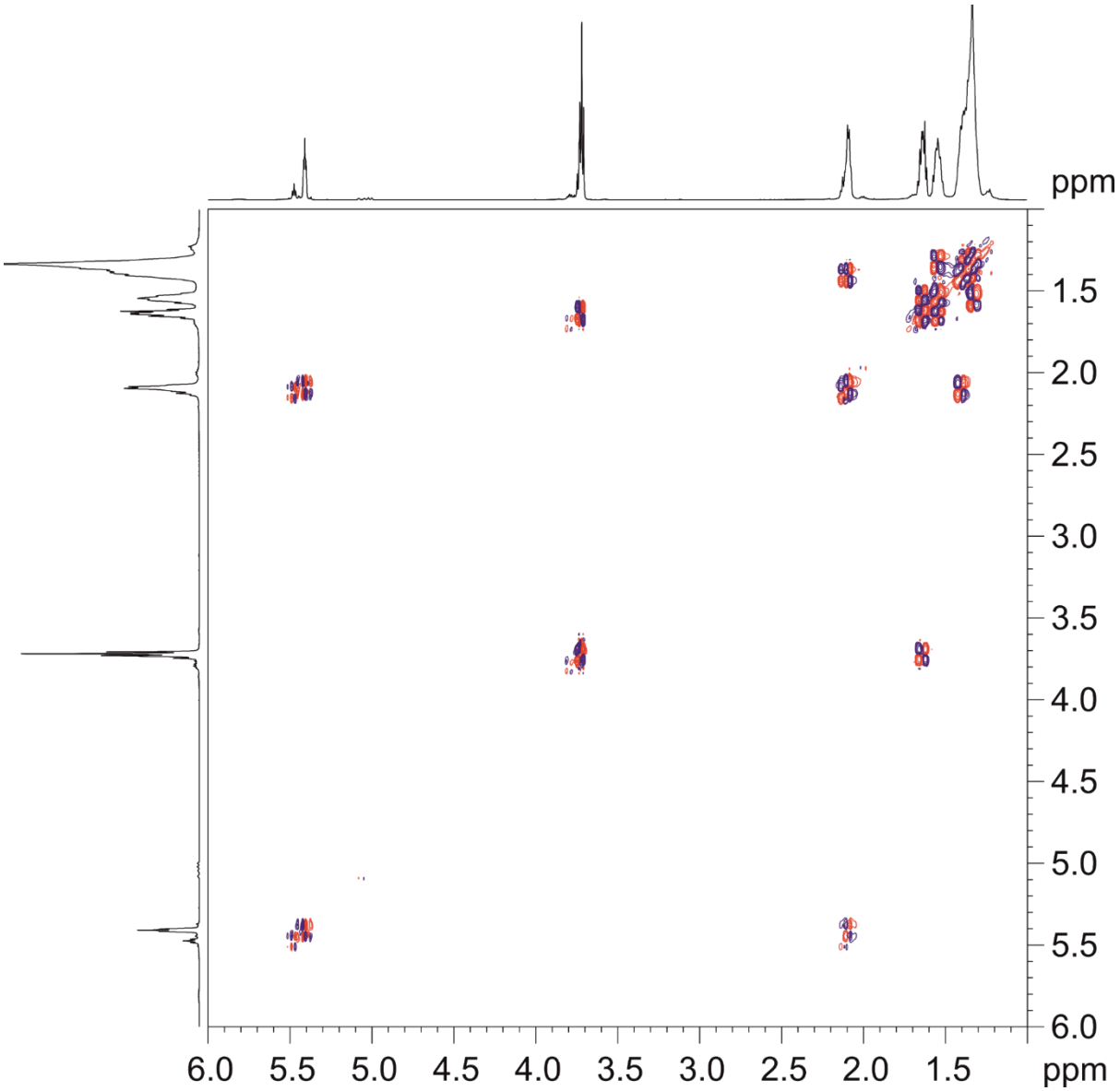

Figure 5.S17. ^{1}H-^{1}H DQF-COSY spectrum of **2** in benzene-d_6 at RT (500 MHz).

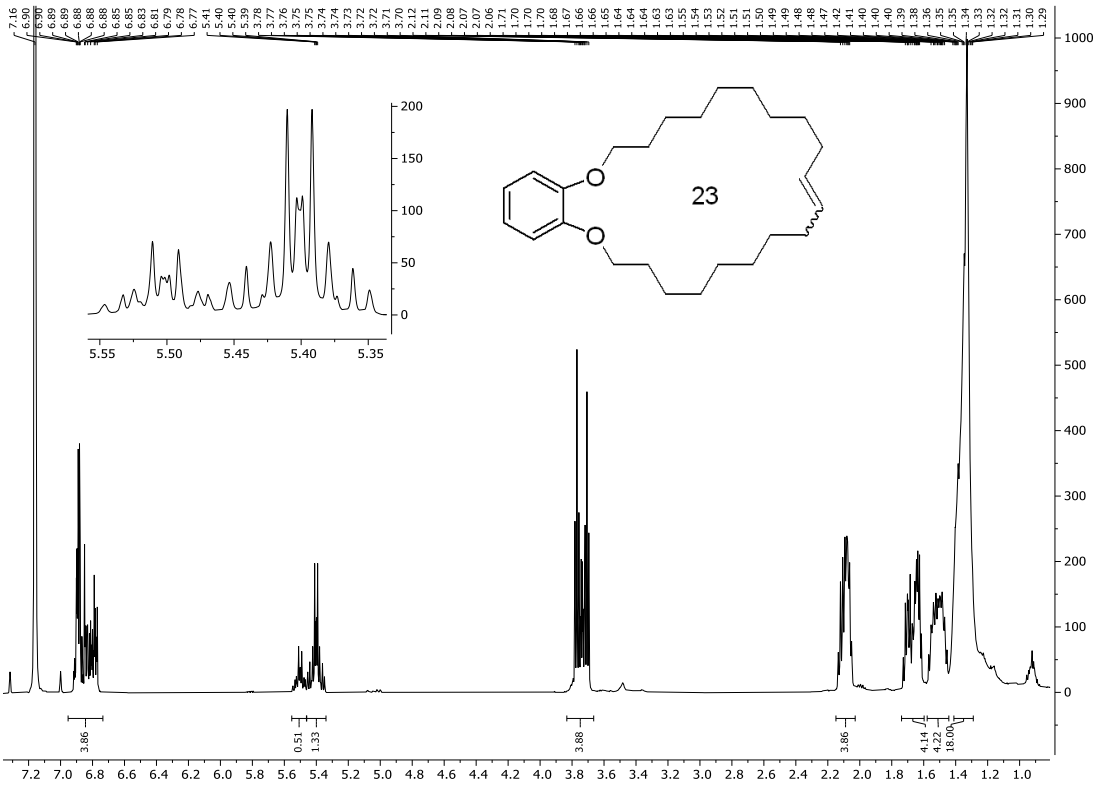

Figure 5.S18. ^{1}H NMR spectrum of **4** in benzene-d_6 at RT (500 MHz).

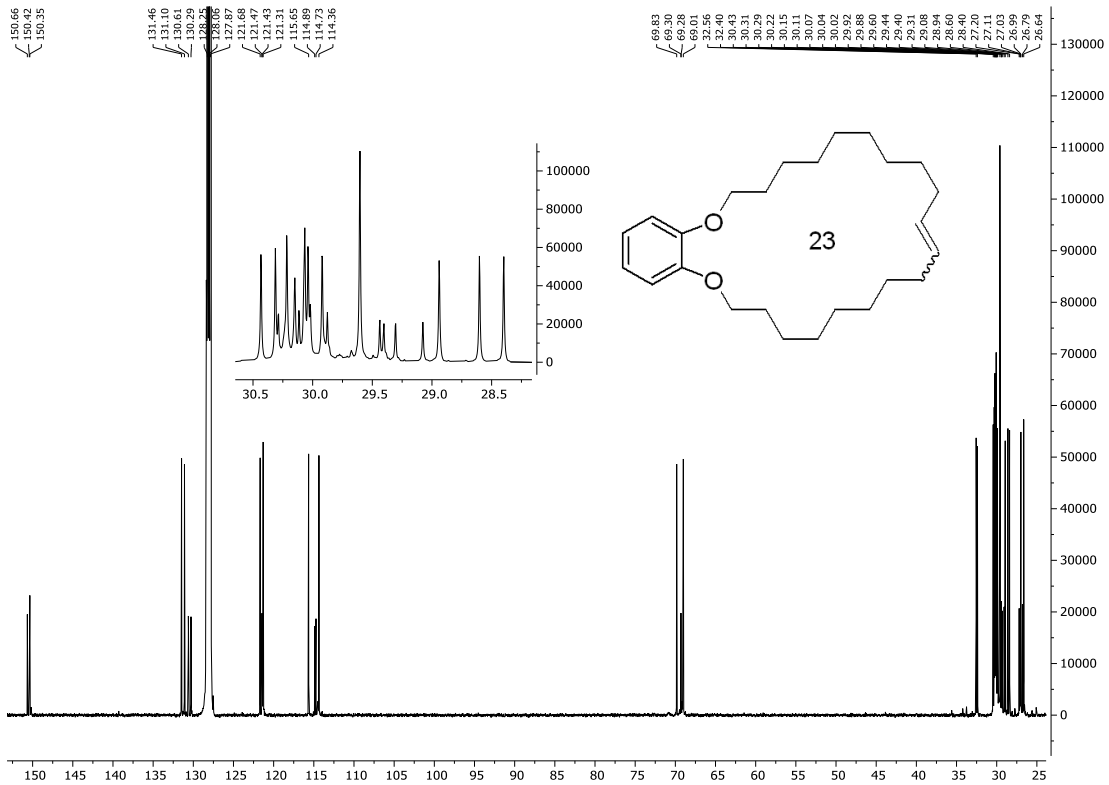

Figure 5.S19. ^{13}C NMR spectrum of **4** in benzene-d_6 at RT (126 MHz).

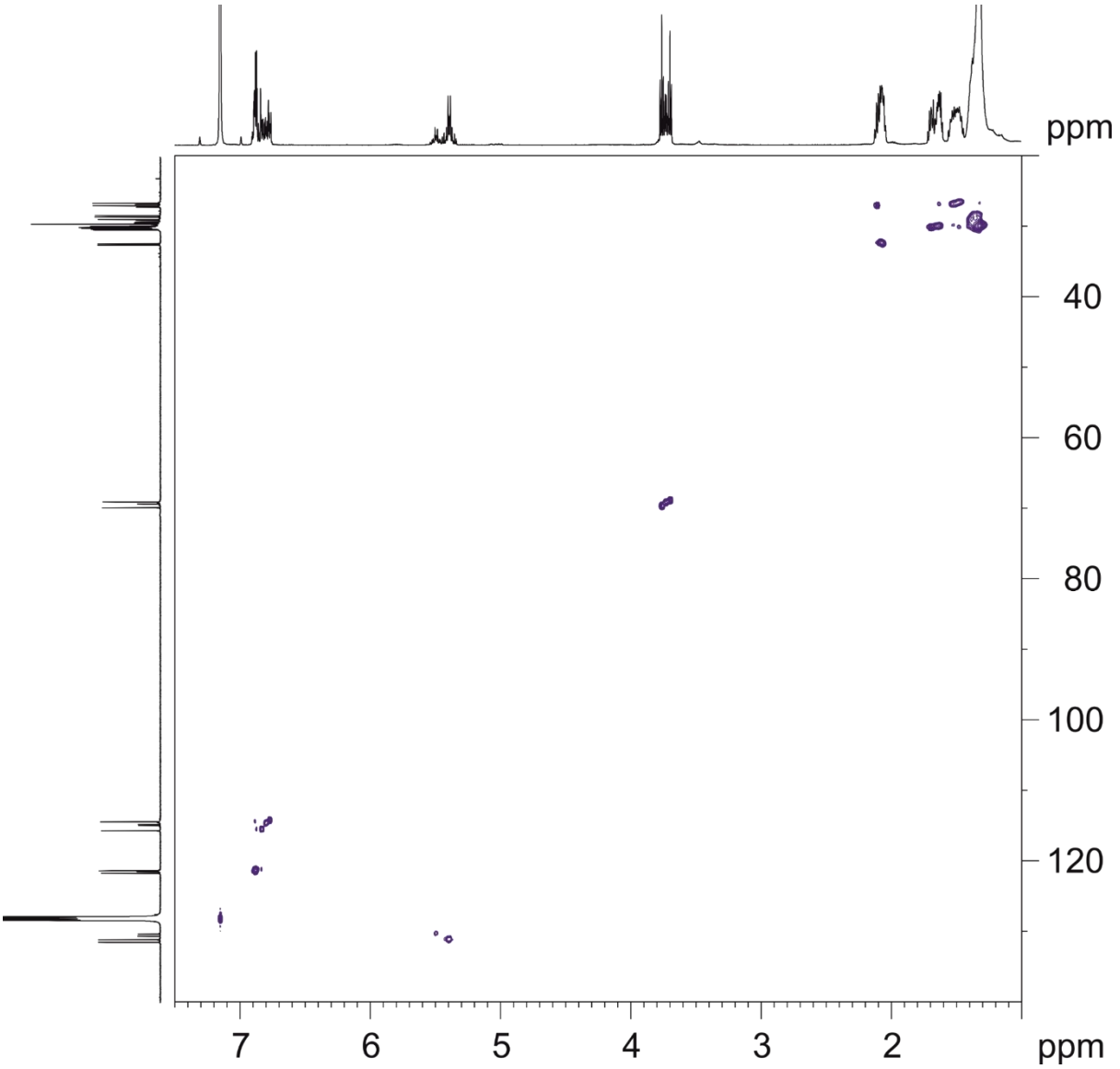

Figure 5.S20. ^{1}H-^{13}C HSQC spectrum of **4** in benzene-d_6 at RT.

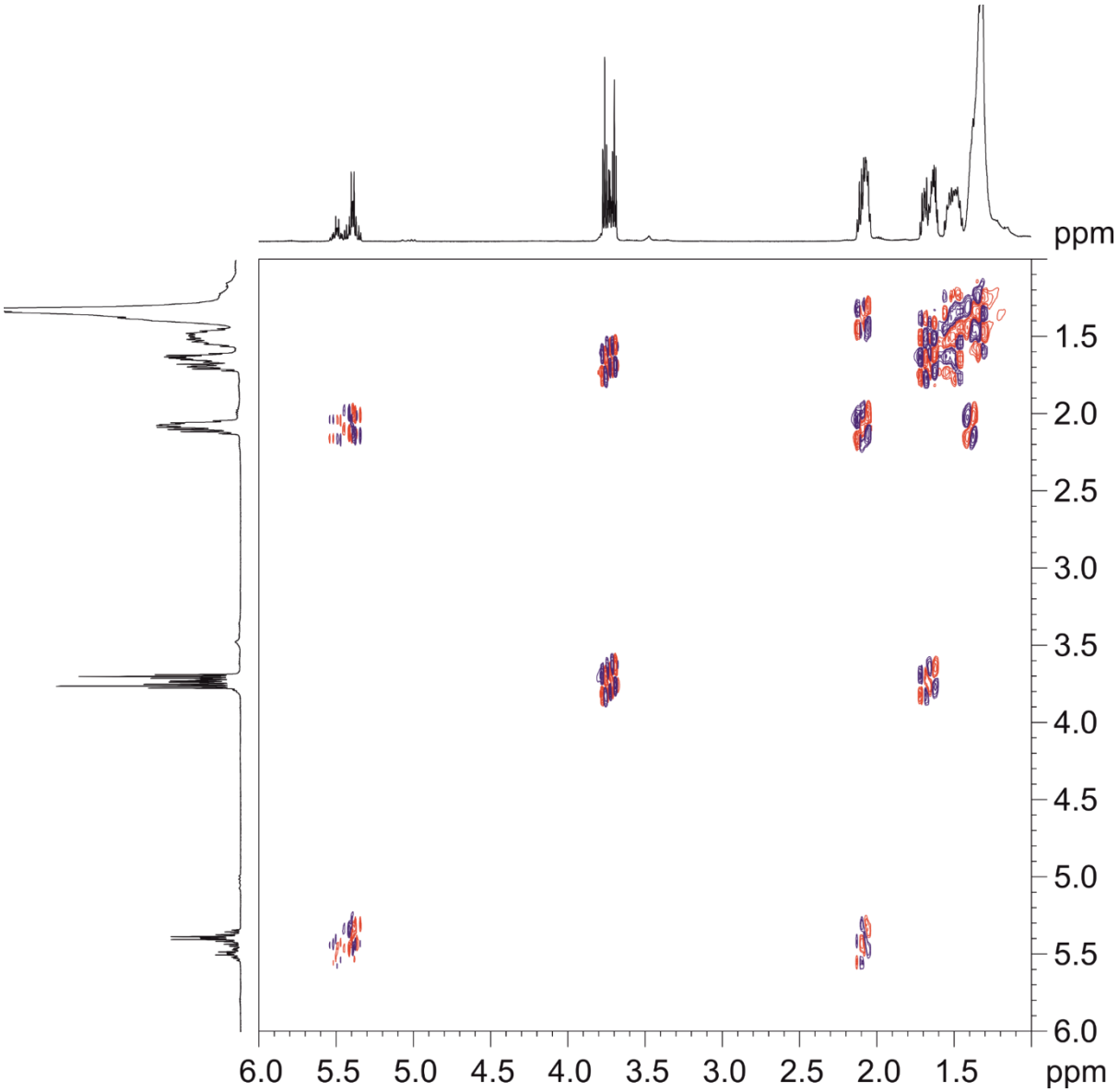

Figure 5.S21. ^{1}H-^{1}H DQF-COSY spectrum of **4** in benzene-d_6 at RT (500 MHz).

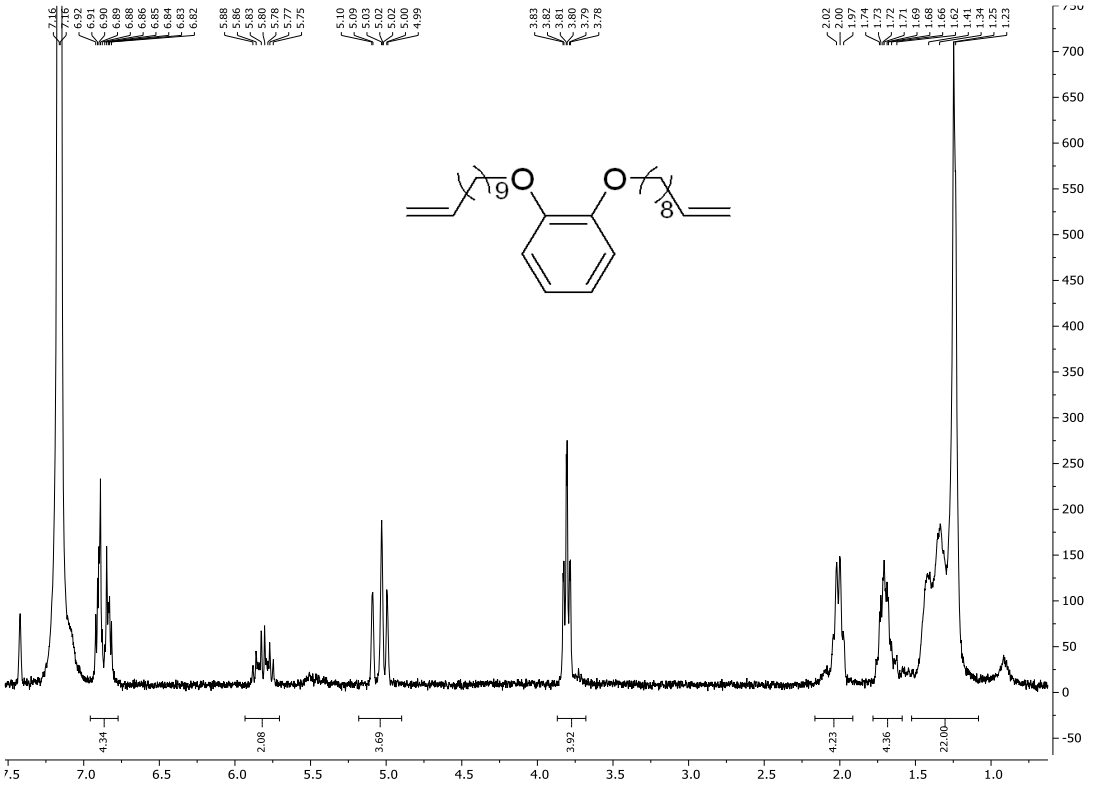

Figure 5.S22. ^{1}H NMR spectrum of **5** in benzene-d_6 at RT (500 MHz).

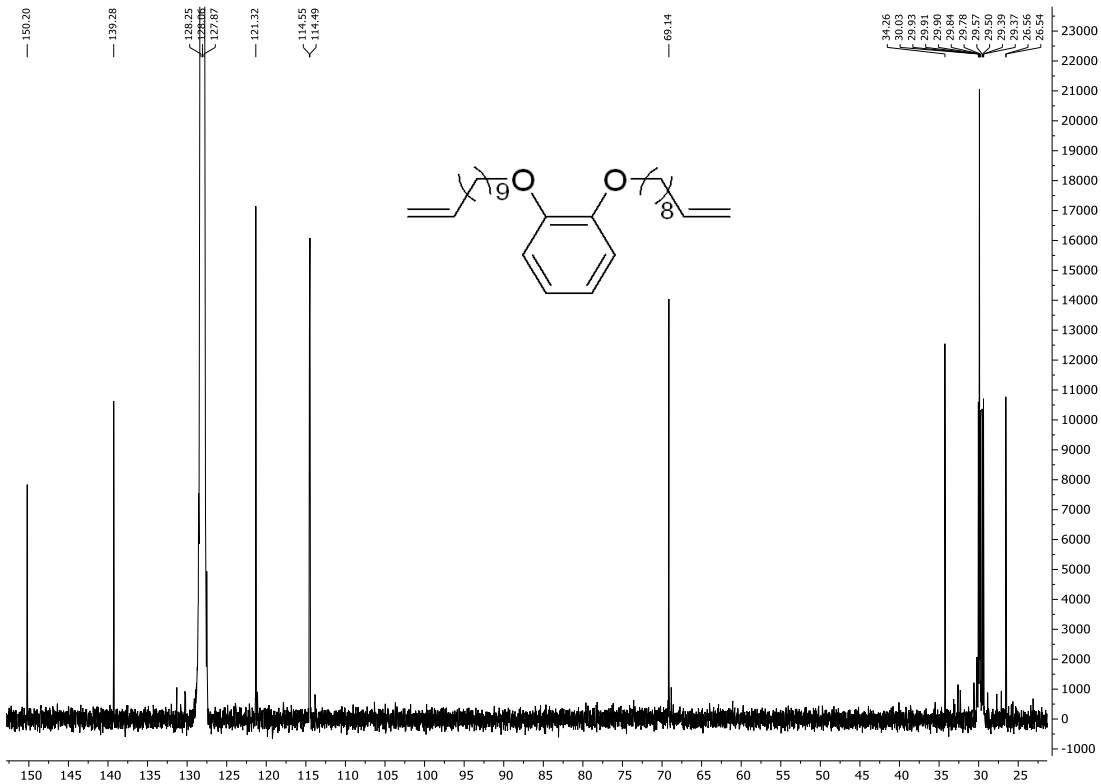

Figure 5.S23. ^{13}C NMR spectrum of **5** in benzene-d_6 at RT (126 MHz).

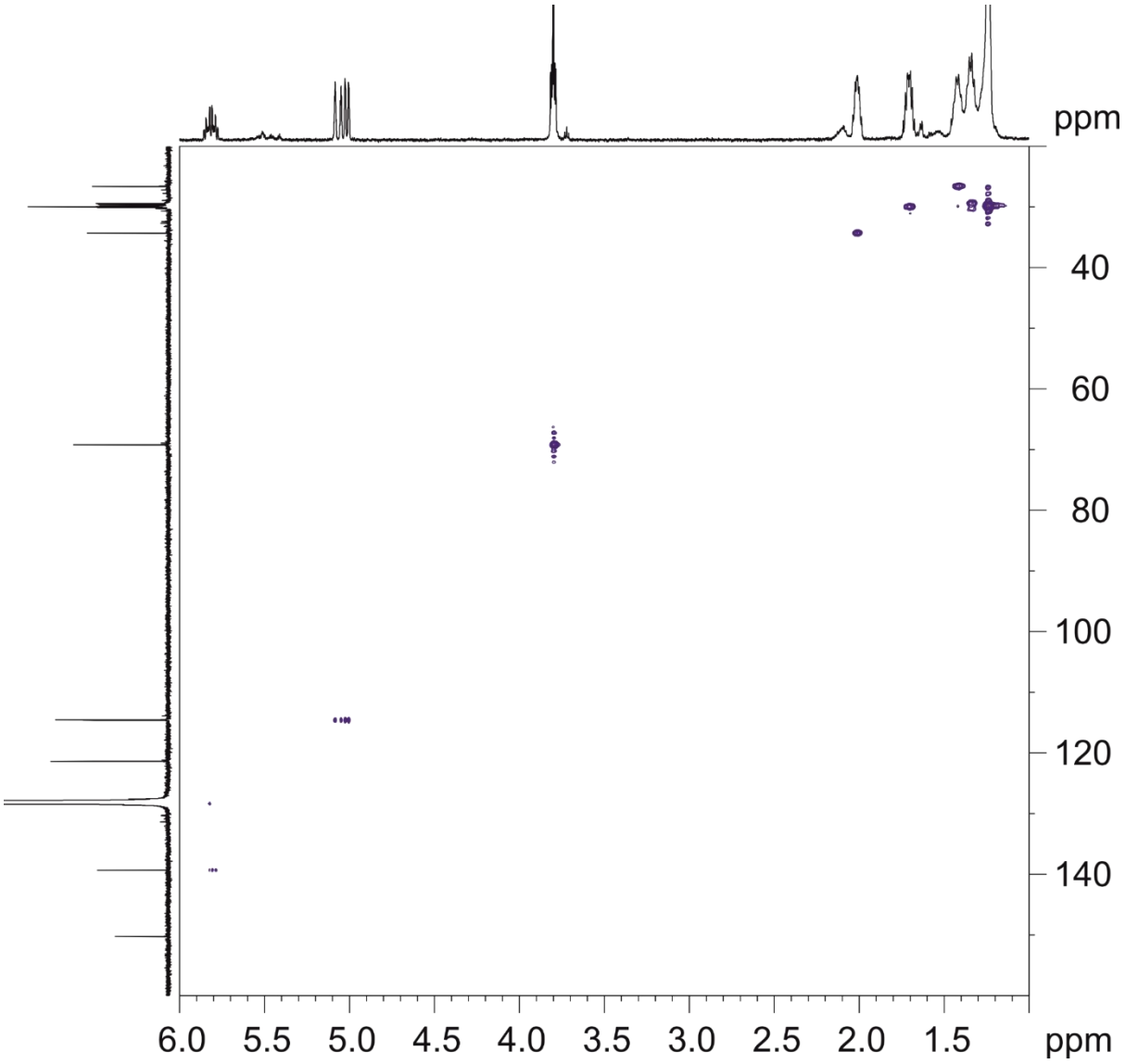

Figure 5.S24. Section of the ^{1}H-^{13}C HSQC spectrum of **5** in benzene-d_6 at RT.

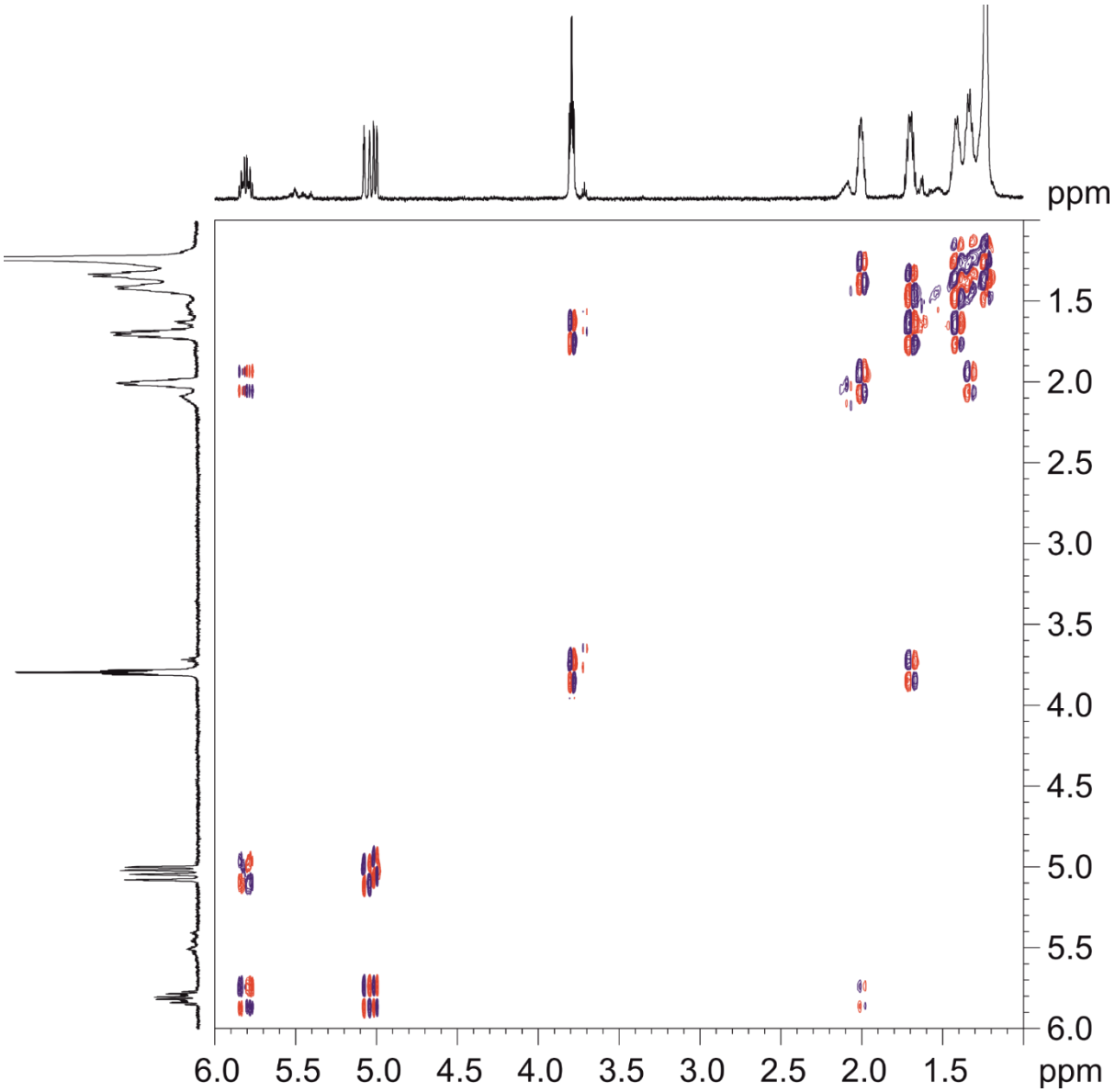

Figure 5.S25. Section of the ^{1}H-^{1}H DQF-COSY spectrum of **5** in benzene-d_6 at RT (500 MHz).

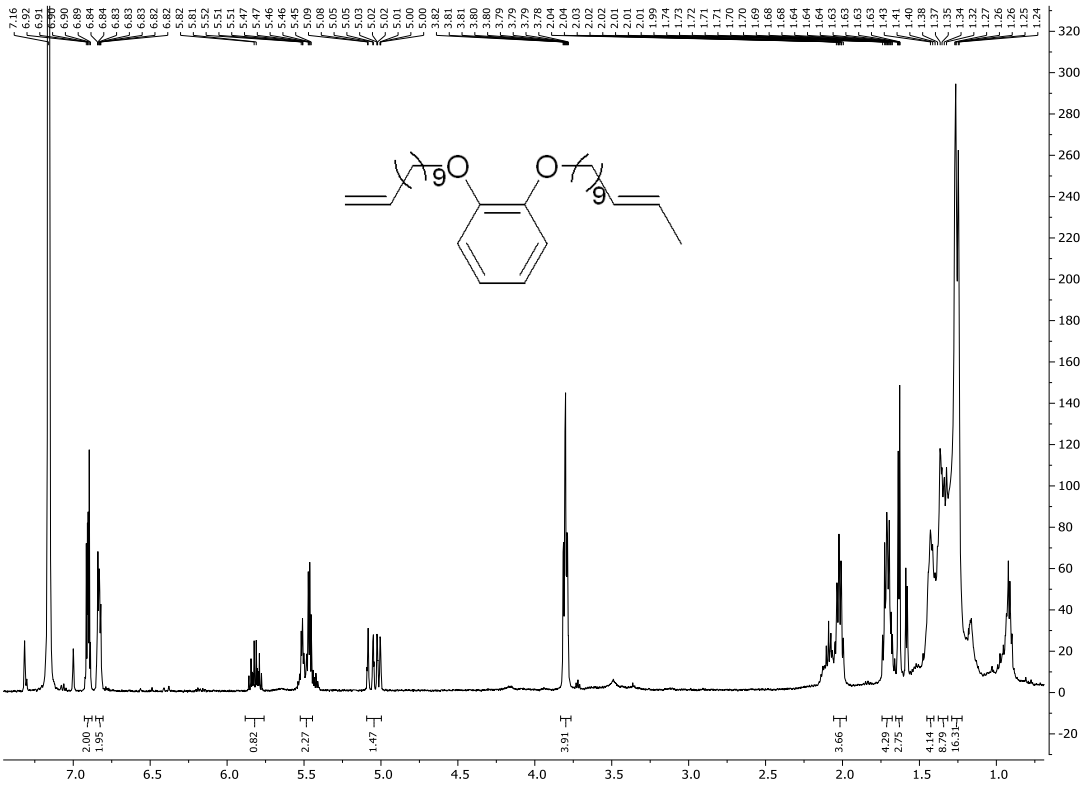

Figure 5.S26. ^{1}H NMR spectrum of **7** in benzene-d_6 at RT (500 MHz).

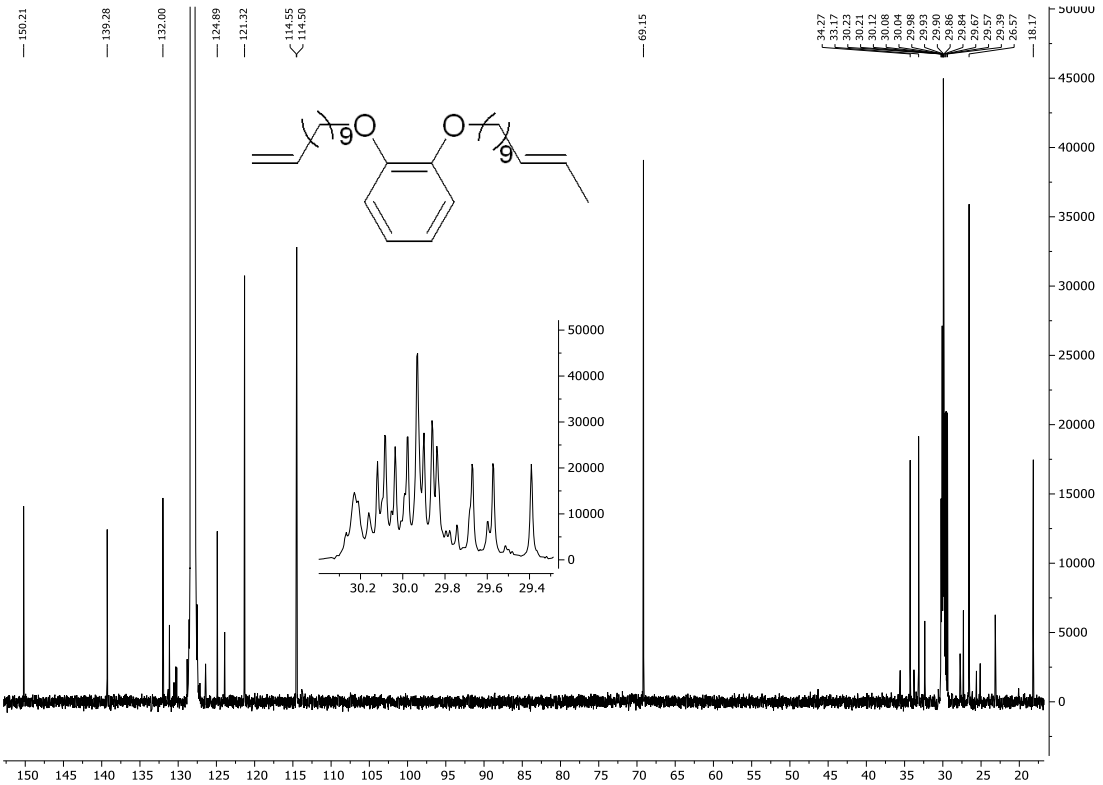

Figure 5.S27. ^{13}C NMR spectrum of **7** in benzene-d_6 at RT (126 MHz).

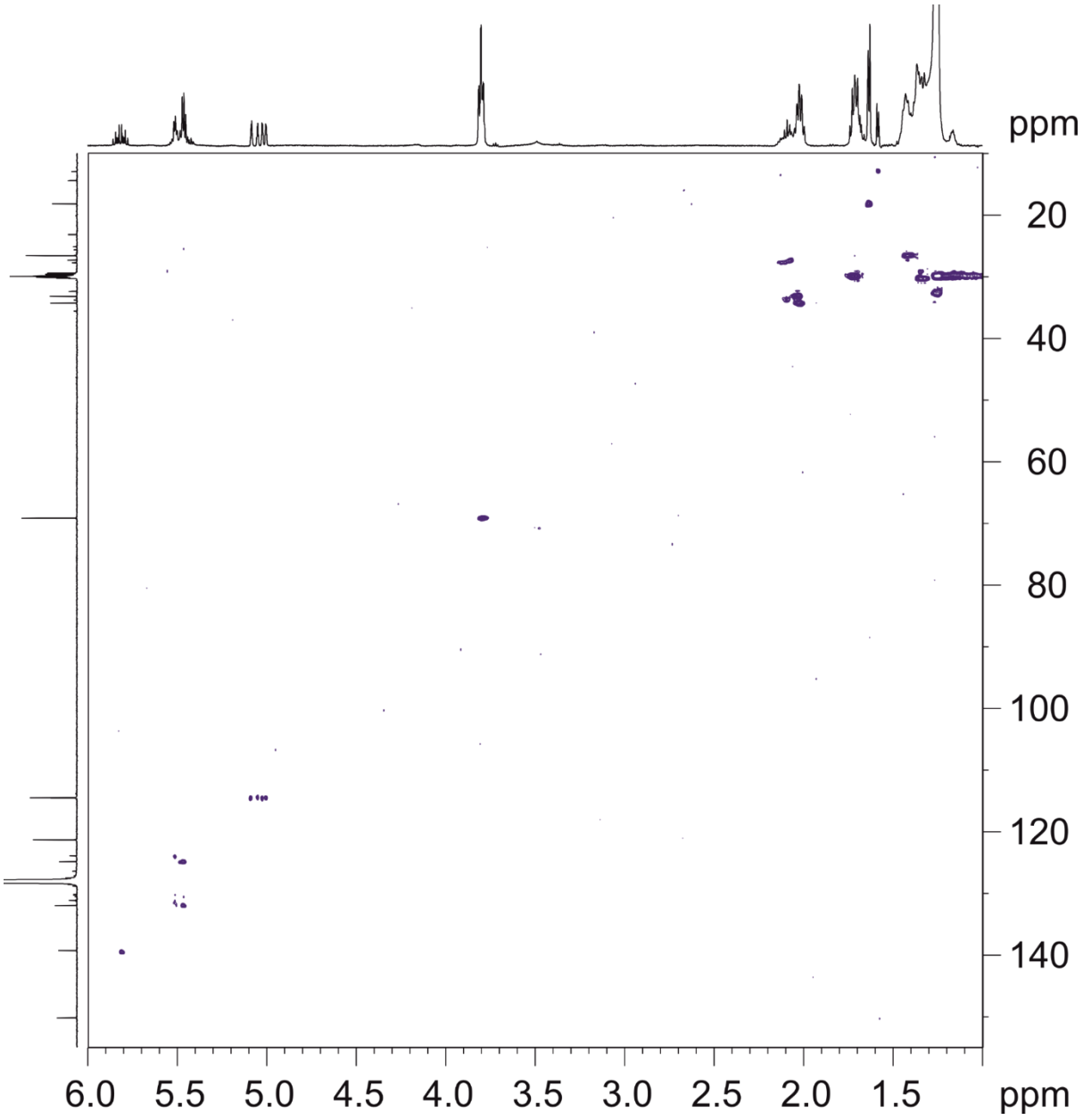

Figure 5.S28. ^{1}H-^{13}C HSQC spectrum of **7** in benzene-d_6 at RT.

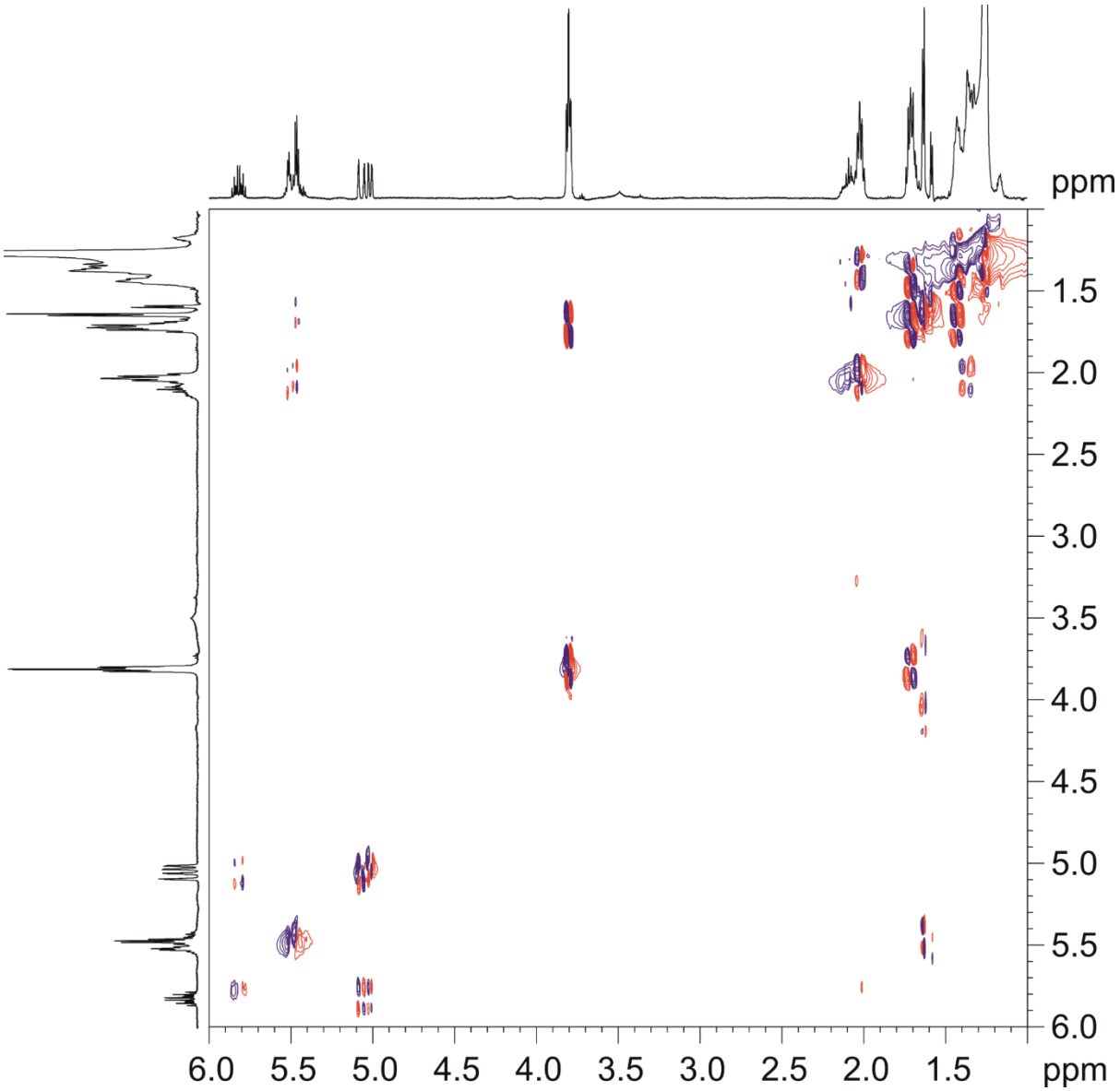

Figure 5.S29. ^{1}H-^{1}H DQF-COSY spectrum of **7** in benzene-d_6 at RT (500 MHz).

5.4 References

1 R. H. Grubbs, S. Chang, *Tetrahedron* **1998**, *54*, 4413–4450.

2 K. C Nicolaou, P. G. Bulger, D. Sarlah, *Angew. Chem. Int. Ed.* **2005**, *44*, 4490–4527.

3 C. Lecourt, S. Dhambri, L. Allievi, Y. Sanogo, N. Zeghbib, R. Ben Othman, M. I. Lannou, G. Sorin, J. Ardisson, *Nat. Prod. Rep*. **2018**, *35*, 105–124.

4 R. Garcia-Fandino, M. J. Aldegunde, E. M. Codesido, L. Castedo, J. R. Granja, *J. Org. Chem*. **2005**, *70*, 8281–8290.

5 M. Scholl, S. Ding, C. W. Lee, R. H. Grubbs, *Org. Lett*. **1999**, *1*, 953–956.

6 a) S. Gessler, S. Randl, S. Blechert, *Tetrahedron Lett*. **2000**, *41*, 9973–9976; b) S. B. Garber, J. S. Kingsbury, B. L. Gray, A. H. Hoveyda, *J. Am. Chem. Soc.* **2000**, *122*, 8168–8179.

7 Selected examples: a) V. I. Petkovska, T. E. Hopkins, D. H. Powell, K. B. Wagner, *Macromolecules* **2005**, *38*, 5878–5885; b) R. Ahuja, S. Kundu, A. S. Goldman, M. Brookhart, B. C. Vicente, S. L. Scott, *Chem. Commun*. **2008**, *2*, 253–255; c) A. Fürstner, O. R. Thiel, L. Ackermann, H.-J. Schanz, S. P. Nolan, *J. Org. Chem*. **2000**, *65*, 2204–2207; d) P. C. M. van Gerven, J. A. A. W. Elemans, J. W. Gerritsen, S. Speller, R. J. M. Nolte, A. E. Rowan, *Chem. Commun*. **2005**, *28*, 3535–3537; e) M. Martinez-Amezaga, C. M. L. Delpiccolo, L. Méndez, I. Dragutan, V. Dragutan, E. G. Mata, *Catalysts* **2017**, *7*, 111.

8 J. Engel, W. Smit, M. Foscato, G. Occhipinti, K. W. Törnroos, V. R. Jensen, *J. Am. Chem. Soc*. **2017**, *139*, 16609–16619.

9 K. C. Nicolaou, P. G. Bulger, D. Sarlah, *J. Am. Chem. Soc.* **2005**, *127*, 17160–17161.

10 S. Monfette, A. K. Crane, J. A. Duarte Silva, G. A. Facey, E. N. dos Santos, M. H. Araujo, D. E. Fogg, *Inorg. Chim. Acta* **2010**, *363*, 481–486.

11 Selected examples: a) S. Monfette, M. Eyholzer, D. M. Roberge, D. E. Fogg, *Chem. Eur. J*. **2010**, *16*, 11720–11725; b) A. Fürstner, O. R. Thiel, L. Ackermann, *Org. Lett*. **2001**, *3*, 449–451; c) E. Tzur, A. Ben-Asuly, C. E. Diesendruck, I. Goldberg, N. G. Lemcoff, *Angew. Chem. Int. Ed*. **2008**, *47*, 6422–6425.

12 F. Ziegler, T. Roider, M. Pyschik, C. P. Haas, D. Wang, U. Tallarek, M. R. Buchmeiser, *ChemCatChem* **2021**, *13*, 2234–2241.

13 F. Ziegler, J. Teske, I. Elser, M. Dyballa, W. Frey, H. Kraus, N. Hansen, J. Rybka, U. Tallarek, M. R. Buchmeiser, *J. Am. Chem. Soc*. **2019**, *141*, 19014–19022.

14 U. Tallarek, J. Hochstrasser, F. Ziegler, X. Huang, C. Kübel, M. R. Buchmeiser, *ChemCatChem* **2021**, *13*, 281–292.

15 a) S. Monfette, D. E. Fogg, *Chem. Rev*. **2009**, *109*, 3783–3816; b) A. H. Hoveyda, Z. Liu, C. Qin, T. Koengeter, Y. Mu, *Angew. Chem. Int. Ed.* **2020**, *59*, 22324–22348.

16 S. H. Hong, A. G. Wenzel, T. T. Salguero, M. W. Day, R. H. Grubbs, *J. Am. Chem. Soc.* **2007**, *129*, 7961–7968.

17 D. Enke, R. Gläser, U. Tallarek, *Chem. Ing. Tech.* **2016**, *88*, 1561–1585.

18 a) H. S. Fogler, *Elements of Chemical Reaction Engineering*, 4th ed., Prentice Hall, Upper Saddle River, N.J., **2006**, Chapter 14.4.1; b) R. L. Hartman, J. P. McMullen, K. F. Jensen, *Angew. Chem. Int. Ed.* **2011**, *50*, 7502–7519.

19 a) J. Yoshida, *Chem. Rec.* **2010**, *10*, 332–341; b) J. Yoshida, Y. Takahashi, A. Nagaki, *Chem. Commun.* **2013**, *49*, 9896–9904.

20 C. P. Haas, T. Müllner, R. Kohns, D. Enke, U. Tallarek, *React. Chem. Eng.* **2017**, *2*, 498–511.

S1 S. F. Song, Y. T. Guo, R. Y. Wang, Z. S. Fu, J. T. Xu, Z. Q. Fan, *Macromolecules* **2016**, *49*, 6001–6011.

S2 H.-O. Kalinowski, S. Berger, and S. Braun, in *^{13}C-NMR-Spektroskopie*; Georg Thieme Verlag: Stuttgart, **1984**; Chapter 3.

IV Conclusions and Perspective

IV.1 Conclusion

This thesis deals with the investigation of reactions in continuous-flow, and can be divided thematically into two areas. The first area deals with the study of photochemical reactions and how they can be influenced by irradiation of light with different wavelengths. The second area deals with the influence of spatial confinement on olefin metathesis reactions using a Grubbs–Hoveyda catalyst.

In the first chapter, the influence of the wavelength of the light used on the perfluoroalkylation of 2-methylindole was shown. Different reaction pathways were accessed by the choice of the light source as well as the reactant composition. In the wavelength range between 430 and 550 nm in which the catalyst Eosin Y absorbs, the reaction occurred via photoredox catalysis. However, through the wavelength investigation, a second range between 365 and 400 nm was observed in which the reaction takes place even though the catalyst shows no absorption in this wavelength range. This revealed another reaction pathway via an EDA complex between the substrate and the base, which was used as an additive. However, even without the base, the reaction can still occur via an EDA complex between the two substrates 2-methylindole and nonafluoroiodobutane. As a result, the wavelength study provided further insight into the mechanism and additionally optimized the reaction to use as few substances as possible, making the reaction more cost-effective and eliminating purification steps. In the second chapter, a method was presented that allows selective activation of the α-CF_2-group in $C_{(3)}$ position of a perfluorinated side chain of 1*H*-Indoles without a catalyst. Thus, it was possible to introduce a nucleophile into the perfluorinated side chain under mild reaction conditions, providing a cost-effective synthetic route for 2-phenyl-1*H*-indoles with modified perfluorinated side chain, which are used as promising building blocks for medicinal chemistry. Due to the effective interaction between reaction control and instrumental analysis of the HPLC systems, the reaction could already be observed as a side reaction in chapter 1, which made this follow-up project possible. In the third chapter, the setup for the study of photochemical reactions on the dependence of the wavelength of the light used was completed. Thereby, it is now possible to investigate photochemical reactions in a fully automated way with respect to the dependence of the irradiated wavelength and the intensity of the used light source. In this chapter, it was shown that even a small difference in the operating wavelength can lead to the generation of a different product and thus to a different reaction pathway. Therefore, it is absolutely necessary to specify

the emission spectrum of the light source used in photochemical investigations to enable the reactions to be reproduced.
In the fourth chapter, the field of photochemical studies was left and the field of heterogeneous catalysis was entered. It was shown that spatial confinement has a positive effect on the ratio between formed product from ring closing metathesis and formed oligomers in olefin metathesis using a Grubbs catalyst. Thus, the range of generated oligomers from the dimer to the hexamer with the free catalyst was narrowed down to the dimer and the trimer in spatial confinement. In addition, selectivities of up to 57% were obtained under spatial confinement instead of up to 47% with the free catalyst. Furthermore, it was possible to gain insight into the impact of the generated ethene on the equilibrium of the reaction. Therefore, it was shown that the spatial confinement can lead to the formation of high ethene concentrations, which have a negative effect on the selectivity of the reaction. In the fifth chapter, insights into the isomerization reactions of the Grubbs catalyst were gained. Different isomerization products were identified and quantified, and conditions were found in which a higher amount of isomerization products is formed. In addition, it could be shown that the 2D-LC/MS system consisting of reaction control (first dimension) coupled with the separation and quantification of the product mixture (second dimension) is very well suited for complex reaction mixtures and that the quantification of products from reaction mixtures in olefin metathesis using NMR analysis can be very error-prone. Overall, it could be shown that catalyst poisoning should be given more attention, since it is responsible for the isomerization reactions and catalyst poisoning thus affects not only the conversion but also the selectivity of the reaction.

Overall, it was shown how much potential there is to include the wavelength as in input parameter in photochemical reactions and to pay more attention to this parameter. In addition, it was shown how efficiently the interaction between two HPLC systems for reaction control and analysis of the reaction mixture can operate and that therefore not much time is needed to carry out systematic comprehensive investigations. Especially in the field of heterogeneous catalysis, where the effects of catalyst poisoning were worked out based on an olefin metathesis reaction with a Grubbs catalyst, it is very advantageous because ideally as many measuring points as possible can be recorded before catalyst poisoning can have a serious impact on the reaction system. The high temporal resolution of the measurements also makes it possible to gain further insights into reaction mechanisms. The next section provides concrete ideas on how the setup can be further optimized.

IV.2 Perspective

In the field of photochemical investigations, the setup is ahead of its time. In the next years, there will be more and more reactions in which the result of the reaction changes due to the use of light of a different wavelength, which is a good indication that there is more to it than meets the eye. Usually, however, these investigations are not carried out as systematically as it is possible with the setup presented in this work. In this respect, the reactions can be picked up and checked to what extend the wavelength really influences the reaction. In addition, it is of course also possible to search for reactions oneself where an influence of the used wavelength can be expected. A promising reaction system for this purpose are photochemical reactions with decatungstate.[1–3]

The setup can also be expanded very well with newly developed reactors. As long as the reactor can be connected to the mounting bracket of the automation unit and the irradiated area corresponds to the irradiated area of the already established reactor, it can be exchanged at will and all functions of the system can be used. However, it should be borne in mind that he LED arrays need to be calibrated again, as the LEDs age and the emission spectrum and intensity of the emitted light can shift slightly as a result. A disadvantage of the currently used reactor is that it does not tolerate high backpressure and the temperature of the reactions cannot be varied. This could be improved with a newly developed reactor. In addition, a reactor could also be designed to enable the study of photochemical reactions in the field of heterogeneous catalysis.

In the field of olefin metathesis, two problems stand out clearly. One problem lies in the nature of the Grubbs catalyst used for the studies, which tends to perform isomerization reactions. This problem can be easily solved. Comparable reactions have already been investigated with molybdenum catalysts, where similar results were obtained, but without any isomerization reactions.[4–5] In this respect, the corresponding molybdenum catalyst should be used in future projects. The second problem lies in the catalyst poisoning. This problem cannot be completely eliminated, but there are a few ways to limit the effect of the catalyst poisoning. Since the molybdenum catalyst is much more susceptible to oxygen and moisture from the air, it is important to protect it from the air atmosphere. The proportion of air and moisture in the HPLC system is very low, but cannot be avoided completely, as air can diffuse through the tubes and the pump heads also draw in some of the air. However, this can be avoided by transferring a part of the HPLC system into a glovebox. For this purpose, it is sufficient to place a pump and

a column oven in the glovebox and to operate the rest of the system outside the glovebox. A connection can be established via a capillary embedded in epoxy resin, which is placed in the wall of the glovebox. A glovebox that is ideally suited for this task has already been selected and customized as part of the thesis. However, due to the long delivery time, initial results have not yet been achieved.

Another way to minimize the influence of catalyst poisoning is to perform more measurements in a shorter time. This makes it more likely to identify sections where the catalyst gives nearly constant results, in order to record kinetics of reactions, for example. There are two approaches to deal with this issue. One approach is to reduce the analysis time. The olefin metathesis reactions were investigated in cyclohexane in this work. However, cyclohexane has the disadvantage that it is immiscible with many common eluents that are very well suited for reversed phase separation (such as water or acetonitrile). Therefore, the separations had to be carried out in an isopropanol/water mixture, which, however, reduced the separation performance and increased the analysis time. Since the beginning of the year, Agilent has been offering a multisampler that is suitable for drawing a defined volume from the reaction solution and injecting it onto the column using a special technique (feed injection), whereby the injection does not take place as a plug but is injected into the running eluent in a portioned manner. This reduces the solvent effects and it should be possible to inject the analyte from cyclohexane into an acetonitrile/water mixture. Furthermore, it is also possible to inject a defined volume from the reaction solution into a vial and dilute it with another solvent in an automated way. The mixture can then be automatically injected onto the separation column. As a result, there are significantly more opportunities to optimize the separation conditions, with a shorter analysis time resulting in more measurement points in a shorter time.

Another way to use the multisampler is to store the reaction solutions temporarily. Currently, a relatively large amount of time is lost because the next injection cannot be performed until the separation of the sample is complete. During this time, however, catalyst poisoning progresses. Reaction solutions of heterogeneous catalysis can be stored temporarily very well, because the reaction is stopped as soon as the reaction solution leaves the reactor. In this way, it is possible to quickly test different reaction conditions and to store the solutions in vials for the time being using the multisampler. Thus, the complete time in which the catalyst is active can be used to test different reaction conditions and the analysis of the reaction solutions can be postponed to the night or the following day without any problems.

IV.2.1 References

1 I. Ryu, A. Tani, T. Fukuyama, D. Ravelli, S. Montanaro, M. Fagnoni, *Org. Lett.* **2013**, *15*, 2554–2557.

2 C. Tanielian, C. Schweitzer, R. Seghrouchni, M. Esch, R. Mechin, *Photochem. Photobiol. Sci.* **2003**, *2*, 297–305.

3 D. Ravelli, S. Protti, M. Fagnoni, *Acc. Chem. Res.* **2016**, *49*, 2232–2242.

4 E. L. Goldstein, F. Ziegler, A.-K. Beurer, Y. Traa, J. R. Bruckner, M. R. Buchmeiser, *ChemCatChem* **2022**, *14*, e202201008.

5 F. Ziegler, H. Kraus, M. J. Benedikter, D. Wang, J. R. Bruckner, M. Nowakowski, K. Weißer, H. Solodenko, G. Schmitz, M. Bauer, N. Hansen, M. R. Buchmeiser, *ACS Catal.* **2021**, *11*, 11570–11578.

V. Appendix

V.1 Curriculum Vitae

Removed from digital version for privacy reasons.

V.2 Publikationsverzeichnis

1 C. P. Haas,[+] T. Roider,[+] R. W. Hoffmann and U. Tallarek*
„Light as a reaction parameter – systematic wavelength screening in photochemical synthesis"
React. Chem. Eng., **2019**, *4*, 1912–1916. DOI: 10.1039/c9re00339h

2 F. Ziegler,[+] T. Roider,[+] M. Pyschik, C. P. Haas, D. Wang, U. Tallarek*[+] and M. R. Buchmeiser*[+]
„Olefin Ring-closing Metathesis under Spatial Confinement and Continuous Flow"
ChemCatChem **2021**, *13*, 2234–2241. DOI: 10.1002/cctc.202001993

3 T. Roider, N. Frommknecht, A. Höltzel and U. Tallarek*
"Device for automated screening of irradiation wavelength and intensity – investigation of the wavelength dependence of photoreactions with an arylazo sulfone in continuous flow"
React. Chem. Eng., **2022**, *7*, 2035–2044. DOI: 10.1039/d2re00142j

4 T. Roider, O. A. Kleykamp, S. I. Ivlev, R. W. Hoffmann and U. Tallarek*
„Catalyst-Free Indirect C–F Activation of 3-Perfluoroalkyl Indoles"
Eur. J. Org. Chem. **2022**, e202201025. DOI: 10.1002/ejoc.202201025

5 A. Böth,[+] T. Roider,[+] F. Ziegler, X. Xie, M. R. Buchmeiser and U. Tallarek*
„Olefin metathesis under spatial confinement and continuous flow: Investigation of isomeric side reactions with a Grubbs–Hoveyda catalyst"
ChemCatChem **2022**, *under review*.

[+] Die Beiträge dieser Autoren sind gleichwertig.

V.3 Erklärungen

Erklärung zum Eigenanteil

Die vorliegende Dissertation mit dem Titel „Continuous-Flow Chemistry: From the Wavelength Dependence of Photoreactions to Spatial Confinement Effects in Olefin Metathesis“ habe ich selbstständig verfasst. Der kumulative Teil dieser Arbeit (Chapter 1–5) beinhaltet veröffentlichte Fachartikel, die in Kooperation mit Koautoren verfasst wurden. Die Beiträge der einzelnen Koautoren werden im Folgenden in Anlehnung an die Contributor Roles Taxonomy (CRediT) dargestellt.

Kapitel 1: Light as a reaction parameter – systematic wavelength screening in photochemical synthesis

C. P. Haas,[+] T. Roider,[+] R. W. Hoffmann and U. Tallarek*
React. Chem. Eng., **2019**, *4*, 1912–1916. DOI: 10.1039/c9re00339h

C. P. Haas wirkte an der Konzeptualisierung, der Methodologie und der Visualisierung der Daten mit. Der erste Entwurf wurde von C. P. Haas verfasst. T. Roider wirkte an der Methodologie und der Visualisierung der Daten mit und nahm die wissenschaftlichen Daten auf. Darüber hinaus wirkte T. Roider an dem Review und der Editierung des Textes mit. R. W. Hoffman wirkte an der Konzeptualisierung sowie der Superversion mit. U. Tallarek wirkte an der Konzeptualisierung mit und stellte die wissenschaftlichen Materialien und Ressourcen bereit. Darüber hinaus wirkte U. Tallarek an dem Review und der Editierung des Textes sowie der Superversion mit.

Kapitel 2: Catalyst-Free Indirect C–F Activation of 3-Perfluoroalkyl Indoles

T. Roider, O. A. Kleykamp, S. I. Ivlev, R. W. Hoffmann and U. Tallarek*
Eur. J. Org. Chem. **2022**, e202201025. DOI: 10.1002/ejoc.202201025

T. Roider wirkte an der Konzeptualisierung sowie der Methodologie mit und nahm einen Teil der wissenschaftlichen Daten auf. Darüber hinaus übernahm T. Roider die Visualisierung der Daten und das Verfassen des ersten Entwurfs. O. A. Kleykamp wirkte bei der Methodologie mit und nahm einen Teil der wissenschaftlichen Daten auf. S. I. Ivlev vermaß den Einkristall, welcher bei der wissenschaftlichen Datenerfassung entstanden war und wertete die Messungen aus. R. W. Hoffmann wirkte bei der Konzeptualisierung sowie der Superversion als auch dem Review und der Editierung des Textes mit. U. Tallarek stellte die wissenschaftlichen Materialien und Ressourcen bereit und wirkte bei der Superversion sowie dem Review und der Editierung des Textes mit.

Kapitel 3: Device for automated screening of irradiation wavelength and intensity – investigation of the wavelength dependence of photoreactions with an arylazo sulfone in continuous flow

T. Roider, N. Frommknecht, A. Höltzel and U. Tallarek*
React. Chem. Eng., **2022**, *7*, 2035–2044. DOI: 10.1039/d2re00142j

T. Roider wirkte bei der Konzeptualisierung sowie der Methodologie mit und nahm die wissenschaftlichen Daten auf. Darüber hinaus übernahm T. Roider die Visualisierung der Daten und die Verfassung des ersten Entwurfs. N. Frommknecht wirkte bei der Entwicklung der Automatisierungseinheit mit, welche es ermöglichte, die Wellenlängen und Intensitäten automatisiert zu wechseln. Darüber hinaus wurde die Software um die Automatisierungseinheit anzusteuern von N. Frommknecht entwickelt. A. Höltzel wirkte bei der Verfassung des Entwurfs sowie dem Review und der Editierung des Textes mit. U. Tallarek wirkte bei der Konzeptualisierung sowie dem Review und der Editierung des Textes mit. Darüber hinaus übernahm U. Tallarek die Bereitstellung von wissenschaftlichen Materialien und Ressourcen sowie die Superversion.

Kapitel 4: Olefin Ring-closing Metathesis under Spatial Confinement and Continuous Flow

F. Ziegler,[+] T. Roider,[+] M. Pyschik, C. P. Haas, D. Wang, U. Tallarek*[+] and M. R. Buchmeiser*[+]
ChemCatChem **2021**, *13*, 2234–2241. DOI: 10.1002/cctc.202001993

F. Ziegler wirkte bei der Konzeptualisierung sowie der Methodologie mit und nahm einen Teil der wissenschaftlichen Daten auf. Darüber hinaus beteiligte F. Ziegler sich an der Visualisierung der Daten sowie dem Review und der Editierung des Textes. T. Roider wirkte bei der Methodologie, der Projektverwaltung, der Visualisierung der Daten sowie dem Review und der Editierung des Textes mit. M. Pyschik wirkte bei der Methodologie mit und nahm einen Teil der wissenschaftlichen Daten auf. C. P. Haas wirkte bei der Konzeptualisierung und der Methodologie mit. Die MALDI-TOF Messungen, welche notwendig waren um das Verhältnis zwischen den entstandenen Dimeren und höheren Oligomeren zu bestimmen, wurden von D. Wang durchgeführt und ausgewertet. U. Tallarek wirkte bei der Konzeptualisierung, der Methodologie sowie der Projektverwaltung und Superversion mit. Darüber hinaus wurde ein Teil der wissenschaftlichen Materialien und Ressourcen von U. Tallarek bereitgestellt und der erste Entwurf von U. Tallarek verfasst. M. R. Buchmeiser wirkte bei der Konzeptualisierung, der Superversion sowie dem Review und der Editierung des Textes mit. Darüber hinaus wurde ein Teil der wissenschaftlichen Materialien und Ressourcen von M. R. Buchmeiser bereitgestellt.

Kapitel 5: Olefin metathesis under spatial confinement and continuous flow: Investigation of isomeric side reactions with a Grubbs–Hoveyda catalyst

A. Böth,[+] T. Roider,[+] F. Ziegler, X. Xie, M. R. Buchmeiser and U. Tallarek*
ChemCatChem **2022**, *under review*.

A. Böth wirkte bei der Konzeptualisierung sowie der Methodologie mit und nahm die wissenschaftlichen Daten auf. Darüber hinaus verfasste A. Böth den ersten Entwurf und wirkte bei der Visualisierung der Daten sowie dem Review und der Editierung des Textes mit. T. Roider wirkte bei der Konzeptualisierung und der Methodologie mit und hat die Projektverwaltung übernommen. Darüber hinaus übernahm T. Roider die Visualisierung, steuerte Text zum ersten Entwurf bei und wirkte bei dem Review sowie der Editierung des Textes mit. F. Ziegler wirkte bei der Konzeptualisierung und der Methodologie mit. X. Xie übernahm die Aufnahme der NMR-Daten und wirkte bei deren Auswertung mit. Dadurch konnten die NMR-Signale exakt aufgeschlüsselt und zugeordnet werden. M. R. Buchmeiser wirkte bei der Superversion und dem Review sowie der Editierung des Textes mit. Darüber hinaus wurde ein Teil der wissenschaftlichen Materialien und Ressourcen von M. R. Buchmeiser zur Verfügung gestellt. U. Tallarek wirkte bei der Konzeptualisierung, der Superversion und dem Review sowie der Editierung des Textes mit. Darüber hinaus wurde ein Teil der wissenschaftlichen Materialien und Ressourcen von U. Tallarek zur Verfügung gestellt.

(Ort, Datum, Unterschrift des Promovierenden)

(Ort, Datum, Unterschrift des Betreuers)

Erklärung zum selbstständigen Verfassen
Ich versichere, dass ich die beiliegende Dissertation mit dem Titel:

„Continuous-Flow Chemistry: From the Wavelength Dependence of Photoreactions to Spatial Confinement Effects in Olefin Metathesis “

selbstständig und ohne fremde Hilfe verfasst und keine anderen als die angegebenen Quellen und Hilfsmittel benutzt habe. Alle vollständig oder sinngemäß übernommenen Zitate sind als solche gekennzeichnet. Die Dissertation wurde in der vorliegenden oder einer ähnlichen Form noch bei keiner anderen Hochschule anlässlich eines Promotionsverfahrens oder zu anderen Prüfungszwecken eingereicht. Ich versichere außerdem, dass diesem Promotionsverfahren keine weiteren Promotionsverfahren vorausgegangen sind.

Ort/Datum	Thomas Roider